Large Eddy Simulation of Industrially Relevant Flows

Cavar, Dalibor; Meyer, Knud Erik

Publication date:
2007

Document Version
Publisher's PDF, also known as Version of record

Link back to DTU Orbit

Citation (APA):
Cavar, D., & Meyer, K. E. (2007). Large Eddy Simulation of Industrially Relevant Flows.

MEK-FM-Ph.D. 2006-02

Large Eddy Simulation
of
Industrially Relevant Flows

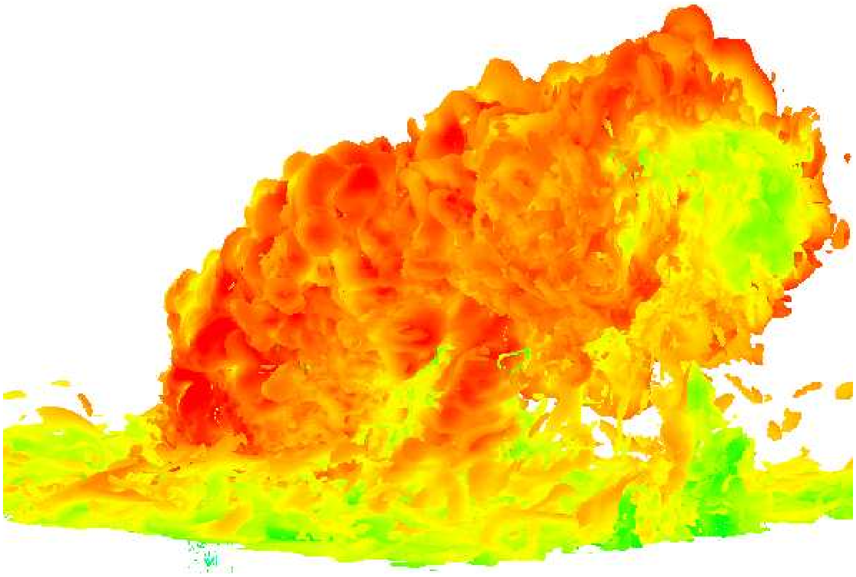

by

Dalibor Cavar

Dissertation submitted to the Technical University of Denmark in partial fulfillment of the requirements for the degree of Doctor of Philosophy in Mechanical Engineering

Fluid Mechanics
Department of Mechanical Engineering
Technical University of Denmark
October, 2006

Fluid Mechanics
Department of Mechanical Engineering
Nils Koppels Allé, Building 403
Technical University of Denmark
DK-2800 Lyngby, Denmark

Printed in Denmark by Vester Kopi, Lyngby

MEK-FM-Ph.D. 2006-02 / ISBN 87-7475-340-1

This thesis has been typeset using LaTeX2e.

Preface

This dissertation is submitted in a partial fulfillment of the requirements for obtaining the degree of Doctor of Philosophy in Mechanical Engineering. The dissertation is based on the research work carried out during the period from February 2003 to October 2006 at the Department of Mechanical Engineering, Fluid Mechanics Section, at the Technical University of Denmark. The work was carried out under supervision of Associate Professor, Ph.D. Knud Erik Meyer and Associate Professor, Ph.D. Jess A. Michelsen, and has been supported by a scholarship for the Ph.D. program in Mechanical and Civil Engineering at the Technical University of Denmark.

I would like to thank Knud Erik Meyer, Jens N. Sørensen, Jess A. Michelsen, Poul Scheel Larsen and Lars Davidson for fruitful discussions during my research.

I also thank M.Sc. Novo Karisik, for the help in the proof-reading process.

Without the love, help and support from my wife Sanja and daughter Sara none of this would have been possible.

Technical University of Denmark

Copenhagen, October 2006

Dalibor Cavar

M.Sc., Mech. Eng.

Abstract

An advanced approach to the problem of turbulence modeling - Large Eddy Simulation (LES) has been applied on two flow cases of a substantial industrial relevance: Jet in a Cross-Flow (JICF) and 2D bump flow, where the main focus has been placed on the former.

The JICF flow case has been investigated in great detail. Substantial effort has been put into generation of realistic inlet boundary conditions, which necessitated conduction of two independent pre-cursor simulations prior to the main JICF calculations. Validation of the JICF computations resulted in good agreements with available measurements on the level of various statistical flow quantities, in all flow regions but the immediate jet-to-crossflow exhaustion zone. A detailed numerical study involving 14 different cases/configurations and numerical grids of up to 15 million cells in size has then been conducted, but despite the considerable numerical effort, the observed differences could not be reduced. Results of the numerical study indicated a possible problem with the measurements in this particular region.

A direct investigation, identification and analysis of various coherent structures (CS) pertinent to the JICF flow field has been conducted utilizing a number of flow realizations (or a series of them). Most of the known coherent structures in the JICF flow were successfully identified.

A more statistically accentuated method for analysis of the CS - the Proper Orthogonal Decomposition - POD method has also been applied. In the 2D part of the POD analysis the PIV (experimental) and LES (numerical) datasets were used/compared and the obtained results identified traces of same coherent structures in both PIV- and LES- based datasets. The POD study was then extended to 3D, shedding some new light on the disputed question regarding origin of the wake vortices.

In the final stages of this project a study of a 2D Bump flow case was conducted. After an additional pre-cursor calculation of the spatially developing boundary layer flow, the obtained results, regarding both mean flow profiles and turbulence quantities, showed a very good agreement with the (LDA) measurements.

Resumé

En af de mest avancerede metoder til behandling af strømningsmekaniske problemer der involverer turbulens - Large Eddy Simulation (LES) var anvendt på to strømningstilfælde med en stor industriel relevans: Jet-i-tverstrøm (JICF) og 2D bump flow. Hovedvægten i undersøgelserne var lagt på studier af JICF strømningstilfældet.

Et stort detaljeringsniveau er opnået ved undersøgelser af JICF strømningstilfældet. Behandling af problemstillingen omkring korrekte og realistiske randbetingelser har fået den højeste prioritet, der resulterede i nødvendigheden for gennemførelse af to særskilte beregninger forinden hoved JICF beregningerne kunne fuldføres. De gennemførte valideringstests af JICF beregningerne viste gode overensstemmelser med de tilgængelige målinger, hvad det praktisk taget angik alle statistiske størrelser, i stort set alle strømningsregioner på nær den umiddelbare jet-til-tværstrøm udstødnings zone. En detaljeret numerisk undersøgelse, der involverede 14 flow-konfigurationer og beregningsnet med op til 15 millioner celler, var efterfølgende gennemført, men på trods af de store (numeriske) anstrengelser, var det ikke muligt at reducere de observerede afvigelser i resultaterne i dette område. Numeriske resultater indikerede et muligt problem med kvaliteten af målingerne i det omtalte område.

En direkte undersøgelse, identificering og analyse af forskellige aspekter af kohærente strukturer (CS) i det undersøgte jet-i-tværstrøm opstilling var foretaget, med udgangspunkt i et sæt af øjeblikkelige strømningsvisualiseringer. Mange eksperimentalt kendte kohærente strukturer kunne identificeres på denne baggrund.

En mere statistisk betonet metode til analyse af de kohærente strukturer - Proper Orthogonal Decomposition (POD) var også anvendt på dette strømningstilfælde. I 2D delen af POD analysen, to datasæt - en genereret med udgangspunkt i (PIV) målingerne og den anden genereret numerisk (LES) var anvendt og POD resultaterne tydeligvist indikerede at aftrykkene af de samme kohærente strukturer kunne spores i begge datasæt. 3D POD analysen var efterfølgende gennemført og den gav nogle nye indikationer om hvor oprindelsesstedet for såkaldte wake vortices findes i JICF strømningen.

I den afsluttende fase af projektet, en undersøgelse af 2D bump flow var foretaget. En ny forudgående beregning, hvor grænselagsstrømningen var simuleret, var gennemført og dets resultater var brugt som indløbsrandbetingelse for det undersøgte 2D bump flow tilfælde. De opnåede resultater, både med hensyn til middelstrømnings variable og størrelser der karakterisere turbulens, viste gode overensstemmelser med (LDA) målingerne.

Contents

List of Symbols . . . . **xi**

1 Introduction **1**

1.1 The present study 1

1.2 Thesis Outline 3

2 Large-Eddy Simulation (LES) **5**

2.1 The Filtering Operator 5

2.2 The Filtered Equations 7

2.3 Subgrid-Scale Models 8

2.3.1 Eddy Viscosity Models 9

2.3.1.1 Smagorinsky Model 9

2.3.1.2 The Dynamic Model 11

2.3.1.3 Mixed Scale Eddy Viscosity Models 13

2.3.1.4 One-Equation Models 14

2.3.2 Other Approaches to Modeling the SGS Stress Tensor 14

3 Channel Flow **17**

3.1 Introduction 18

3.2 Previous Investigations 18

3.3 Numerical Configuration of the Plane Channel Flow Case 19

3.4 Results and Discussions of the Plane Channel Flow Case 20

3.5 Numerical Configuration of the Rotating Channel Flow Case 27

3.6 Results and Discussions of the Rotating Channel Flow Case 28

4 Jet in a Cross Flow (JICF) 33
4.1 Previous studies 33
4.2 Flow Configuration 36
4.3 Boundary Conditions 37
4.3.1 Outflow Boundary Conditions 38
4.3.2 Inflow Conditions 39
4.4 Validation 48
4.5 Coherent structures 64
4.6 Proper Orthogonal Decomposition (POD) 73
4.6.1 Basic equations 73
4.6.2 Comparison of PIV-based and LES-based POD analyses 75
4.6.2.1 Resolved Turbulent Kinetic Energy 86
4.6.3 3D POD 89
4.7 Summary 99

5 Investigations of the 2D Bump flow 101
5.1 Previous Investigations 102
5.2 Numerical Configuration of the 2D Bump Flow Case 103
5.2.1 Boundary Conditions 106
5.3 Results and Discussions of the 2D Bump Flow Case 109

6 Summary and Conclusions 117

Bibliography 119

A Numerical Investigations of the R=3.3 Velocity Ratio Case 127
A.1 Outline of Computational Details 127
A.2 Results and discussions 133

B Numerical Investigations of the R=1.3 Velocity Ratio Case 163

C Numerical Codes and Implementations 173

List of Symbols

Symbols

$\mathbf{A}$	POD coefficient matrix containing all $\mathbf{a}^n$
$\mathbf{a}^n$	POD coefficient vector
$\mathbf{C}$	Auto-covariance matrix
$\mathbf{R}$	Two-point correlation tensor
$\overrightarrow{f_c}$	Coriolis force
C_E	Constant used in the estimate of ε
C_f	Skin friction coefficient
C_m	Constant of the Mixed Scale Eddy viscosity models
$C_{p\,(w)}$	Static pressure coefficient (in the wall-adjacent cells)
C_s	Smagorinsky constant
C_v	Constant used in the estimate of k_{sgs}
D	Jet diameter
f_i	Forcing term in N-S equations (channel flow case)
h	Bump height, Channel half-width
k_{sgs}	Subgrid scale kinetic energy
L_c	Bump chord-length
L_{x_1}	Domain extension upstream of the jet exit (inlet position)
L_{x_2}	Domain extension downstream of the jet exit (outlet position)
L_x, L_y, L_z	Computational domain extensions in respective coordinate directions
L_{z_D}	Domain extension representing jet before cross-flow entry (inlet position)
N	Number of statistically uncorrelated samples
N_x, N_y, N_z	Number of computational cells in respective coordinate directions

p_w	Static pressure in the wall-adjacent cells
R	Jet-to-crossflow velocity ratio
R_{uu}, R_{vv}, R_{ww}	Two-point or autocorrelation functions
Re_{δ}, Re_{δ^*}, Re_{Θ}	Reynolds number based on δ, δ^*, Θ
$Re_{c_{R=1.3}}$, $Re_{m_{R=1.3}}$	Reynolds number based on U_c, U_m for $R = 1.3$
$Re_{c_{R=3.3}}$, $Re_{m_{R=3.3}}$	Reynolds number based on U_c, U_m for $R = 3.3$
Re_m, Re_c, Re_{u_τ}, Re_D, Re_h	Reynolds number based on U_m, U_c, u_τ, D, h
Ro_m, Ro_{u_τ}	Rotational number - based on U_m, u_τ
U_∞	Free stream velocity
U_c	Centerline, Convective flow velocity
U_m	Mean velocity
U_{rel}, V_{rel}, W_{rel}	Relative out-of-plane POD mode velocity
y_0	Local bump height

Greek Letters

Δt	Time step size
Δt^*	Dimensionless time step size
Δ	Filter Length
$\delta^*_{(0)}$	Displacement thickness (at inlet)
$\delta_{(0)}$	Boundary layer thickness (at inlet)
$\Delta_{x,\,y,\,z}$	Local cell with
η	Kolmogorov length scale, ratio of z/δ
γ	Stretching factor, ratio of $u_{\tau,\,inlet}/u_{\tau,\,recycle}$
λ_n	Eigenvalues of $\mathbf{C}$
$\mathbf{\Phi}$	POD mode matrix containing all ϕ^n
ϕ^n	POD mode n
μ	Dynamic Viscosity
ν	Kinematic Viscosity
$\nu_{t\,(sgs)}$	Subgrid Scale turbulent viscosity
Ω	Rotational speed
ω	Vorticity vector

Π	Weighting function
ρ	Density
τ_w	Wall shear stress
τ_{ij}	Subgrid scale Reynolds stress tensor
$\Theta_{(0)}$	Momentum thickness (at inlet)
ε	Dissipation of the turbulent kinetic energy
S_{ij}	Strain Rate Tensor
u_τ	Wall-friction velocity

Indices

$(\cdot)'$	Fluctuating part of a certain statistical quantity
$(\cdot)^+$	Quantity specified in wall units
$< \cdot >$	Spatially averaged quantity
$\overline{(\cdot)}$	Filtered quantity
$\widehat{(\cdot)}$	Explicitly filtered quantity
i, j, k, m, n	Indices in tensor notation

Abbreviations

(S)CVP	(Secondary) Counter-Rotating Vortex Pair
(S)PIV	(Stereoscopic) Particle Image Velocimetry
BC	Boundary Condition(s)
BL	Boundary Layer
CDS(4)	Central Difference Scheme (4th order)
CFD	Computational Fluid Dynamics
CFL	Couran-Friedrichs-Lewy number
DES	Detached Eddy Simulation
DNS	Direct Numerical Simulation
FLT	Flow-Through Time
FVM	Finite Volume Method
JICF	Jet-in-CrossFlow
LDA	Laser Doppler Anemometry
LES	Large Eddy Simulation

N-S	Navier-Stokes equations
PISO	Pressure Implicit Split Operator
POD	Proper Orthogonal Decomposition
QUICK	Quadratic Upstream Interpolation for Convective Kinetics
RANS	Reynolds Averaged Navier Stokes
RMS	Root Mean Squared
SGS	Subgrid Scale
SIMPLE	Semi-Implicit Method for Pressure-Linked Equations
V/STOL	Vertical/Short Take-Off and Landing

Chapter 1

Introduction

One of the most challenging tasks in fluid mechanics in general is prediction of various aspects of flow phenomena, which are closely related to turbulence. As almost all flows with industrial relevance and generally encountered in nature are turbulent, the fact that turbulent flow phenomena are far from being fully understood puts some perspective on our general ability to control and predict such flows. Until recently experimental studies were the only basic tool which could be used to investigate and try to understand the phenomenology of turbulent flows. Those studies, such as Laser-Doppler Anemometry (LDA) studies, could to a certain degree elucidate several aspects of turbulent flows and they have been correspondingly used as basis for constant development of widely applied turbulence models employed in Computational Fluid Dynamics (CFD). The shortcomings of such studies are their inability to directly investigate some more dynamically accentuated aspects of turbulent flows. The advanced experimental techniques such as (Stereoscopic) Particle Image Velocimetry ((S)PIV), circumvent this problem in a way, allowing measured quantities to be obtained in a whole plane (planes) of the investigated domain at one time. Thereby, some new aspects of turbulent flows, such as investigations of coherent structures (CS) and related phenomena have the potential of being thoroughly investigated and understood.

It has long been known that some numerical methods have the potential of simulating and reproducing real turbulent flows (Direct Numerical Simulation DNS and to certain extent Large Eddy Simulation - LES), but due to extreme computational costs required to use them, they have only been utilized in investigations of some relatively simple flow cases previously. The constant increase in the computing power available has made the application of those methods on more complex and industrially relevant flows much more realistic. So at the present time it is possible to analyze some industrially relevant flows in great detail both experimentally (by use of e.g. PIV) and numerically (by use of e.g. LES) and thereby potentially gain a considerable new insight in various flow phenomena pertinent to the investigated flow cases.

1.1 The present study

In the context of this work two industrially relevant flow cases are considered and analyzed, utilizing the advanced approach to turbulence modeling - LES: Jet in a Cross-Flow (JICF) and 2D bump flow, with the main focus being placed on the former.

Jet in Cross Flow (JICF)

The Jet in Cross Flow (JICF) is a basic '*building block (canonical) flow field*' case investigated in great detail in the past, primarily due to its applicability in many engineering problems. The applications of this flow field are quite plentiful and include - mixing of gases before chemical reactions, plume dispersion, gas turbine blade film cooling, turbojet thrust vectoring for propulsive systems, reaction control for missiles and aircrafts, vertical and/or short takeoff and landing aircrafts (V/STOL), fuel injection for burners, waste disposal into rivers and many others.

Evidently, application of JICF extends throughout many different engineering areas, but despite a considerable (primarily experimental) research activity, many of the main characteristics of this complex flow field are not yet fully understood. In recent years some numerical investigations of this flow have been conducted, but they still have not completely elucidated processes of complex interaction mechanism between the jet and boundary layer cross-flow. In many of those numerical studies a clear link between numerical calculations and experimental data is not fully established, so their validity can not be easily verified.

There exists a comprehensive experimental database, comprising of both LDA (Özcan and Larsen [77]) and PIV (Meyer et al. [70, 71], Pedersen [81]) measurements of the flow set-up representing the idealized JICF flow. The basic motivation for this study is to use an advanced computation method (LES) with the purpose of attaining numerical results (data) on the same level of details as obtained by e.g. PIV. The two acquired sets of data can then be used as a suitable platform for detailed comparisons of numerical and experimental results. As an appropriate method for comparisons of various dynamic flow phenomena, the objective and un-biased method called Proper Orthogonal Decomposition (POD) can be used. Besides that, the numerically obtained 3D flow snap-shots can be used to visually identify dominant coherent structures (CS) in the JICF flow.

Thereby the basic objectives of the current JICF study can be outlined as follows:

- ▷ To validate the obtained LES results vs. mean flow data acquired utilizing LDA measurement technique (Özcan and Larsen [77])
- ▷ To investigate and identify well known dominant coherent structures in this type of the flow,
- ▷ To explore and compare dynamics of the computationally obtained flow field with the corresponding experimentally attained one (PIV of Meyer et al. [70, 71]) utilizing an appropriate method - e.g. Proper Orthogonal Decomposition (POD).

2D Bump Flow

Turbulent shear layers represented by boundary layers, mixing layers, jets etc. are frequently encountered in different industrial and natural flows. Equilibrium boundary layers are a special class of those layers which have been studied (both theoretically and experimentally) in great detail in the past. Those studies led to a substantial general ability to correctly predict characteristics of equilibrium boundary layer flows. Most of the industrially relevant flows are however subjected to different perturbations in the external conditions such as a pressure gradient, surface curvature and roughness, blowing and suction etc. In those flows, the well-defined properties of the equilibrium flow cannot be directly utilized; hence the general knowledge and general ability to predict the main features of the non-equilibrium flows are still limited. In many cases, as a consequence of encountered adverse pressure gradient, the considered flow is subjected to separation and reattachment. Predictions of correct positions of separation and reattachment in such flows have proven to be a very challenging task for numerical methods employing turbulence modes based on Reynolds Averaged Navier-Stokes (RANS) approach (see e.g. Menter [68]).

In the context of this work, a LES study of the non-equilibrium boundary layer flow over a wall mounted bump (represented by a part of a cylindrical shell) is conducted. As only a limited experimental (LDA) database of this flow case exists, the main aim of the present study is to investigate, whether a more advanced approach to turbulence modeling (LES) can reliably reproduce the main characteristics of this flow.

In order to obtain reliable LES results, the abilities of the flow solver (EllipSys) used in this study to perform general LES computations are expanded during this project by incorporating three additional Sub-Grid Scale (SGS) Models into it.

1.2 Thesis Outline

The introductory part of this thesis is followed by a chapter providing the basic theoretical foundations of the LES approach to the general problem of turbulence modeling. As some new SGS models are implemented in the flow solver utilized in this study, Chapter 3 provides the validation basis of implementation of these SGS models, where the extensively utilized flow case in the framework of LES benchmarking - the channel flow case has been used. In Chapter 4 different aspects of JICF flow case are analyzed and discussed. This includes a detailed description of numerical configuration utilized, followed by a part where LES results are validated against mean flow (LDA) data. Afterwards, various coherent structures (CS) of the JICF flow are identified and discussed and in the following part comparisons of dynamically accentuated flow characteristics of the JICF flow based on the results from this numerical study and PIV measurements are conducted. The chapter is concluded by an additional investigation of coherent structures by means of the 3D POD. In Chapter 5 different aspects of the analyzed 2D Bump Flow are discussed. In the final Chapter, the summary of the conducted work and concluding remarks are given. In Appendices A and B the results of detailed numerical studies conducted for two investigated velocity ratios (R) in the JICF flow case are presented, while in Appendix C descriptions of the CFD codes utilized in this study are given together with an overview of major new implementations incorporated in the EllipSys code.

Chapter 2

Large-Eddy Simulation (LES)

For almost four decades, LES has been a subject of considerable research activity, as it appears to be a quite promising approach to describe the turbulent flows, successfully circumventing the inherited problems concerning other methods for turbulence modeling - RANS and DNS. In fact, the method can give an accurate predictions of statistically averaged turbulent fields, as produced by RANS, utilizing considerably smaller computational effort compared to DNS.

Recent advances especially in computer technology have made the method more widely applicable and thereby more suitable for application in turbulent flows of industrial interest.

The flavor of the method can be outlined as follows:

- ▷ A filtering operator is defined aiming to decompose the velocity field into a part which is directly computed and a residual part.
- ▷ The equations of motion for the filtered velocity are derived from the Navier-Stokes equations. The new set of equations preserves the same features of the original N-S equations and contains an unknown residual stress-tensor.
- ▷ The closure to the problem is obtained by modeling the residual stress-tensor, which represents the influence of unresolved onto resolved scales.
- ▷ The modeled equations are solved numerically giving an approximate solution for the large scale motions of the turbulent flow.

In the following paragraphs the distinct features of LES are presented and different conceptual problems concerning this approach to problem of turbulence modeling are described.

2.1 The Filtering Operator

The fundamental idea behind LES lies in a separation between large- and small- scale turbulent motions. Large- scale motions are directly resolved on a given numerical grid, while the influence of small- scale on large- scale motions is modeled through the so-called subgrid (subfilter) scale models (SGS).

Formally, equations governing the larger component of the turbulent scales are derived by applying a low-pass filtering operator to Navier-Stokes equations. The filtering process decomposes any flow variable - scalar or vectorial, into two components:

$$f = \bar{f} + f' \tag{2.1}$$

where $\bar{f}$ is resolved (filtered or larger) component and f' is subgrid (subfilter or residual) component. The resolved components are originally defined by Leonard [55], and can be expressed as a convolution product between a filter kernel $G(x, \xi)$ and a flow variable f in the following way:

$$\bar{f}(x,t) = \int_{\Omega} G(x, \xi; \Delta)\, f(\xi, t)\, d\xi. \tag{2.2}$$

where Ω is the entire domain and Δ is the filter width. Filtering kernel $G(x, \xi)$ is usually a symmetric function about $\xi = x$, and the function shape remains typically constant when moving position of $\xi = x$ - see Figure 2.1(a). In such a case the filtering function is defined by a homogeneous filtering kernel, and the corresponding filtering operator is classified as homogeneous. An extension to the inhomogeneous case is not straightforward and can be done using different approaches (see e.g. Sagaut [90]).

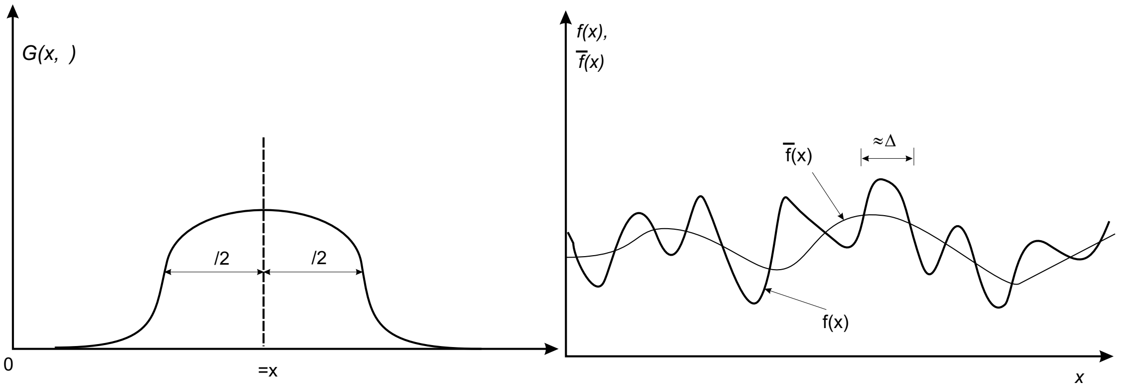

(a) 1D Filter kernel

(b) Applying filter in 1D

Figure 2.1: Applying the filtering operator on a flow variable in 1D

The effect of a filtering process is depicted on Figure 2.1(b). The Figure shows that scales of the original function are damped on the order of magnitude of the filter width, denoted as Δ. This filter width characterizes the smallest scales of turbulence, which can be resolved by the applied filter. The filtering kernel is usually scaled in such a way so that if the function to be filtered is a constant, the resulting filtered function remains the same constant.

In the general case the following relations apply:

$$\bar{\bar{f}} \neq \bar{f}, \qquad \bar{f'} \neq 0 \qquad \text{and} \qquad \overline{\bar{f} f'} \neq 0 \tag{2.3}$$

even if the flow is statistically stationary.

The most commonly used filters are the spectral cut-off filter, the Gaussian filter and the Top-Hat filter - see Table 2.1.

	Physical Space	**Spectral Space**
Spectral Cut-Off	$G(x) = \frac{\sin(\pi x/\Delta)}{\pi x/\Delta}$	$\mathcal{F}\{G(x)\} = \begin{cases} 1 & \text{if } k \leq \pi/\Delta \\ 0 & \text{otherwise} \end{cases}$
Gaussian	$G(x) = \sqrt{\frac{6}{\pi\Delta^2}} \exp(-\frac{6x^2}{\Delta^2})$	$\mathcal{F}\{G(x)\} = \exp(-\frac{k^2\Delta^2}{24})$
Top-Hat	$G(x) = \begin{cases} 1/\Delta & \text{if } \lvert x\rvert \leq \Delta/2 \\ 0 & \text{otherwise} \end{cases}$	$\mathcal{F}\{G(x)\} = \frac{\sin(k\Delta/2)}{k\Delta/2}$

Table 2.1: Typically used filters in LES and their representation in the physical and spectral space

The framework of this project is based on an in-house finite volume numerical code *EllipSys3D*. In the finite volume context the approach to filtering is based on the ideas of Deardorff [21], where the top-hat filtering of the equations of motion is implicitly done by selection of the appropriate computational grid, i.e. by the numerical discretisation. In cases where explicit filtering is necessary, the filter length on anisotropic meshes is typically found from the cell volume, i.e.:

$$\Delta = \sqrt[3]{\Delta_x \, \Delta_y \, \Delta_z}, \tag{2.4}$$

where $\Delta_{x,\,y,\,z}$ represents the local cell width in the corresponding Cartesian coordinate direction. In the rest of this chapter and thesis, it will be assumed that the filtering process is carried out based on the mentioned approach due to Deardorff [21]. The interested reader is referred to the book of Sagaut [90] among others, for discussions of further - preferably more mathematical aspects of LES.

2.2 The Filtered Equations

As stated earlier, the governing equations are filtered in space and solved numerically on a given grid in a computational LES. The classical approach here is to treat the grid and the discretisation operators as the filtering procedure of the N-S equations. Thereby an explicit definition of the filter function is not needed, or can the implicit filter be determined; hence it is very difficult to distinguish between different sources of errors implicit to this technique. This issue will be discussed briefly in the following part.

The fundamental property of the filtering operator defined in the previous paragraph is linearity i.e. $\overline{\phi + \psi} = \bar{\phi} + \bar{\psi}$. The property of commutation with respect to derivation ($\overline{\frac{\partial \phi}{\partial s}} = \frac{\partial \bar{\phi}}{\partial s}$, $s = (x, y, z, t)$) is also true for the homogeneous filter kernels. In the more general case, where the filter width is not constant (i.e. boundary layer flows) the commutation property of a given filter cannot be implicitly assumed. In fact, in a general case a form of commutation error emerges from the filtering process of the N-S equations. This issue has received a lot of attention lately and a new class of commutative filters (implies explicit filtering) aiming to diminish the influence of commutation error on LES calculations has recently been proposed (Vasilyev et al. [110], Marsden et al. [65]).

Ghosal [34] among others tried to address the general question of the numerical errors in Large Eddy Simulation. The concept of deriving governing equations for LES, with special consideration aimed at separating the effects of filtering and numerical discretisation procedures on the underlying governing equations is proposed by Carati et al. [13] and further investigated by Gullbrand and Chow [36] and Winckelmans and Jeanmart [114]. In this approach, by applying explicit filtering, the effect of the numerical error can be better isolated and hence studied in greater depth.

It should be noted that most of the issues regarding the source of errors in LES are still discussed in the framework of simple test cases for LES, like the channel flow case. Even in this context the proposed changes to the classical approach are leading to only small improvements in the computed results. Typically, a moderate increase in the number of grid points used - Lund and Kaltenbach [61], utilizing the classical approach to LES, can lead to a greater result-improvements compared to the proposed model changes, leading to the conclusion that in a sufficiently resolved LES the mentioned effects are not too significant or dominating.

As LES in the framework of this project is expected to be applied on problems with moderate Reynolds numbers, it can be reasonably assumed that the numerical grids considered, will be of sufficient quality to produce satisfactory results utilizing the classical approach to LES. For that reason the latter approach to LES, where the effects of commutation error are neglected and numerical discretisation combined with a chosen computational grid is considered as an implicit filer, will be adopted.

Utilizing the properties of linearity and commutation and applying the filter operator defined in (2.2) on the governing equations for isothermal, incompressible flows one gets:

$$\frac{\partial \overline{u}_i}{\partial x_i} = 0 \tag{2.5}$$

$$\frac{\partial \overline{u}_i}{\partial t} + \frac{\partial}{\partial x_j}(\overline{u_i u_j}) = -\frac{1}{\rho}\frac{\partial \overline{p}}{\partial x_i} + \nu \frac{\partial^2 \overline{u}_i}{\partial x_j \partial x_j}. \tag{2.6}$$

Adding the term $\overline{u}_i\overline{u}_j$ to both sides of the equation (2.6) and denoting $\tau_{ij} = \overline{u_i u_j} - \overline{u}_i\overline{u}_j$ as subgrid-scale Reynolds stress tensor, after some rearrangement it yields:

$$\frac{\partial \overline{u}_i}{\partial t} + \frac{\partial}{\partial x_j}(\overline{u}_i\overline{u}_j) = -\frac{1}{\rho}\frac{\partial \overline{p}}{\partial x_i} + \nu \frac{\partial^2 \overline{u}_i}{\partial x_j \partial x_j} - \frac{\partial \tau_{ij}}{\partial x_j}. \tag{2.7}$$

All of the terms but τ_{ij} in equation (2.7) can now be directly computed on a given grid and a closure problem in LES, expressed in a need for a suitable model for τ_{ij}, thereby emerges. It should be noted that the definition of τ_{ij} as a stress tensor stems from the way it is treated (modeled) rather than from its physical behavior. It represents the influence of the unresolved scales of motion on the resolved ones, and cannot be easily computed. In the following paragraph the problem of a suitable model for the subgrid-scale tensor τ_{ij} is discussed.

2.3 Subgrid-Scale Models

As when modeling the Reynolds stress tensor in RANS computations, a broad spectrum of different models and modeling approaches for of SGS stress tensor exists. Before proceeding to more detailed description of the latter modeling methods some physical requirements, which a successful model should comply with, are listed:

- ▷ The SGS model should be dissipative; the concept of energy transfer cascade where energy is transferred form large- to small turbulent scales should be followed. This is considered as the most important characteristic.
- ▷ The model should be able to locally mimic energy transfer from largest unresolved to smallest resolved scales (referred to as backscatter see e.g. Domaradzki and Saiki [24]).
- ▷ The model should be able to *'turn itself off'* in limiting cases of relaminarization, fully resolved flows, transition etc.
- ▷ The asymptotic decay of the small-scale growth-rate in the near-wall region should be represented correctly.

Different types of SGS models are described and discussed in the following paragraph.

2.3.1 Eddy Viscosity Models

All models of the eddy viscosity type are based on ideas known from RANS modeling. Applying the mentioned reasoning in the LES context, one can argue that the principal effects of SGS stresses are increased transport and dissipation. These phenomena are connected to the viscosity in laminar flows. Therefore a reasonable assumption for a SGS model can be expressed as:

$$\tau_{ij} - \frac{1}{3}\delta_{ij}\tau_{kk} = 2\nu_{sgs}\,\underbrace{(\frac{\partial u_i}{\partial x_j} + \frac{\partial u_j}{\partial x_i})}_{\bar{S}_{ij}/2} = \nu_{sgs}\,\bar{S}_{ij}, \tag{2.8}$$

where ν_{sgs} is the eddy viscosity and $\bar{S}_{ij}$ is the strain rate of the resolved, large scale field. Herby, the original problem of determining the SGS stress tensor is transformed to a problem of determining the scalar quantity ν_{sgs}. Using dimensional arguments one can deduce that ν_{sgs} is a product of velocity and length scales i.e. $\nu_{sgs} = u_o\, l$. As the dominating unresolved scales are assumed to be of the order of the filter size Δ, it is generally accepted to use Δ as the reasonable representative of the local length scale. The expression for the velocity scale u_o is to be determined by a particular model.

2.3.1.1 Smagorinsky Model

The earliest, simplest and most widely used eddy viscosity model is one proposed by Smagorinsky [99]. The model can be derived following the dimensional arguments.

Suppose the scale separation between large and small scales occurs in the inertial subrange region. At sufficiently high Reynolds number this range is supposed to be independent of both the large- and small- scales. The range is thus characterized by a dissipation ε and a wave number Δ. Therefore the SGS viscosity can be expressed as:

$$\nu_{sgs} = \varepsilon^a \left(C_s\Delta\right)^b . \tag{2.9}$$

Dimensional analysis yields $a = 1/3,\ b = 4/3$ leading to:

$$\nu_{sgs} = \varepsilon^{1/3} \left(C_s\Delta\right)^{4/3} . \tag{2.10}$$

The scales in the interial subrange are isotropic and thus in local equilibrium, i.e.:

$$P_{k,\,sgs} = \rho\varepsilon \qquad \Rightarrow \qquad -\tau_{ij}\bar{S}_{ij} = \varepsilon. \tag{2.11}$$

Using the approximation commonly utilized in RANS modeling, i.e. $P_k = 2\mu_t S_{ij} S_{ij}$[1], applied here on k_{sgs} equation ($P_{k,\,sgs} = 2\mu_{sgs}\bar{S}_{ij}\bar{S}_{ij}$) one gets:

$$2\nu_{sgs}\bar{S}_{ij}\bar{S}_{ij} = \varepsilon. \tag{2.12}$$

Combining equations (2.10) and (2.12) after performing some rearrangements one gets:

$$\nu_{sgs} = \left(C_s\Delta\right)^2 \sqrt{2\,\bar{S}_{ij}\bar{S}_{ij}} = \left(C_s\Delta\right)^2 \left|\bar{S}_{ij}\right| , \tag{2.13}$$

where $\left|\bar{S}_{ij}\right| = \sqrt{2\,\bar{S}_{ij}\bar{S}_{ij}}$, and C_s is the Smagorinsky constant found to be a function of Reynolds number and possibly some other dimensionless flow parameters. The value of the constant can be determined theoretically for the case of isotropic turbulence - $C_s = 0.17$, but in general cases the constant is found to vary from $C_s = 0.065$ - Moin and Kim [73] to $C_s = 0.3$ - Jones and Wille [45], so a certain a priori knowledge of some flow parameters is necessary to specify a reasonable value of C_s in most cases.

The model as such is not able to account for the previously mentioned asymptotic decay in the near-wall region. A successful recipe to circumvent this issue is to use the van Driest damping known from RANS:

$$D_{wall} = 1 - \exp(\frac{y^+}{A^+}), \tag{2.14}$$

where $A^+ = 25$, $y^+ = y\,u_\tau/\nu$, $u_\tau = \sqrt{\tau_w/\rho}$, τ_w is the wall shear-stress and y is the distance from the wall. The effective value of $C_{s,eff}$ is then obtained from $C_{s,eff} = C_s\,D_{wall}$. Other shortcomings of the model are: its inability to mimic the backscattering energy transfer process, as the constant C_s is always positive, and the inability to vanish in fully resolved and laminar flows, as the model computes non-zero SGS viscosity ν_{sgs} in those cases.

Finally it should be mentioned that the detailed tests based on DNS data (see e.g. McMillan and Ferziger [67]) revealed that the Smagorinsky model is quite poor in predicting the detailed description of subgrid scale stresses, but the pronounced dissipative nature of this model makes it reasonably successful in a broad variety of engineering problems.

---

[1] $\tau_{ij} = 2\,\mu_t\,S_{ij} - \frac{2}{3}\rho\delta_{ij}k$

2.3.1.2 The Dynamic Model

As discussed in the previous paragraph, the Smagorinsky model has some shortcomings. As a way to elude those model deficiencies, the dynamic modeling procedure, aimed to determine the Smagorinsky model constant locally, is proposed by Germano et al. [32]. Determining the coefficient locally, in the general case as a function of both space and time, allows the dynamic model to account for backscattering of energy, to vanish in laminar and fully resolved flows and even account for the asymptotic behavior in the near-wall region. Thereby the dynamic model fulfills many of the desired properties a good SGS model should posses (see section 2.3). It should be emphasized that the dynamic modeling procedure is not necessarily coupled with the Smagorinsky model; it can be based/applied on any SGS model where determination of a modeling constant(s) is necessary (see e.g. Zang et al. [119]).

The short description of the dynamic modeling procedure will be presented in the following.

Applying two filters to the Navier-Stokes equations (one implicit grid filter Δ eq. (2.4) and a second coarser, explicit test filter $\widehat{\Delta} = 2\Delta$) yields:

$$\frac{\partial \widehat{\overline{u}}_i}{\partial t} + \frac{\partial}{\partial x_j}(\widehat{\overline{u_i u_j}}) = -\frac{1}{\rho}\frac{\partial \widehat{\overline{p}}}{\partial x_i} + \nu \frac{\partial^2 \widehat{\overline{u}}_i}{\partial x_j \partial x_j}. \tag{2.15}$$

Adding the term $\widehat{\overline{u}}_i\widehat{\overline{u}}_j$ on both sides of the equation (2.15) and denoting $T_{ij} = \widehat{\overline{u_i u_j}} - \widehat{\overline{u}}_i\widehat{\overline{u}}_j$ as the subgrid-scale stress tensor at the new test level, one gets:

$$\frac{\partial \widehat{\overline{u}}_i}{\partial t} + \frac{\partial}{\partial x_j}(\widehat{\overline{u}}_i\widehat{\overline{u}}_j) = -\frac{1}{\rho}\frac{\partial \widehat{\overline{p}}}{\partial x_i} + \nu \frac{\partial^2 \widehat{\overline{u}}_i}{\partial x_j \partial x_j} - \frac{\partial T_{ij}}{\partial x_j}. \tag{2.16}$$

Applying the same procedure to already grid-filtered N-S equations (2.7) one gets:

$$\frac{\partial \widehat{\overline{u}}_i}{\partial t} + \frac{\partial}{\partial x_j}(\widehat{\overline{u}_i\overline{u}_j}) = -\frac{1}{\rho}\frac{\partial \widehat{\overline{p}}}{\partial x_i} + \nu \frac{\partial^2 \widehat{\overline{u}}_i}{\partial x_j \partial x_j} - \frac{\partial \widehat{\tau}_{ij}}{\partial x_j}. \tag{2.17}$$

Adding again the term $\widehat{\overline{u}}_i\widehat{\overline{u}}_j$ to both sides of the equation (2.17) one can write:

$$\frac{\partial \widehat{\overline{u}}_i}{\partial t} + \frac{\partial}{\partial x_j}(\widehat{\overline{u}}_i\widehat{\overline{u}}_j) = -\frac{1}{\rho}\frac{\partial \widehat{\overline{p}}}{\partial x_i} + \nu \frac{\partial^2 \widehat{\overline{u}}_i}{\partial x_j \partial x_j} - \frac{\partial \widehat{\tau}_{ij}}{\partial x_j} - \frac{\partial}{\partial x_j}(\widehat{\overline{u}_i\overline{u}_j} - \widehat{\overline{u}}_i\widehat{\overline{u}}_j). \tag{2.18}$$

From equations (2.16) and (2.18), defining $\mathcal{L}_{ij} = \widehat{\overline{u}_i\overline{u}_j} - \widehat{\overline{u}}_i\widehat{\overline{u}}_j$ as the dynamic Leonard stress tensor it follows that:

$$T_{ij} = \widehat{\overline{u}_i\overline{u}_j} - \widehat{\overline{u}}_i\widehat{\overline{u}}_j + \widehat{\tau}_{ij} = \mathcal{L}_{ij} + \widehat{\tau}_{ij}. \tag{2.19}$$

The latter equation is sometimes referred to as the Germano identity.

The basic underlying assumption in this dynamic procedure is that the subgrid scale stress tensors (τ_{ij} and T_{ij}) on both the grid and the test level can be represented by the same SGS model. Assuming that the Smagorinsky model can be used for modeling of both τ_{ij} and T_{ij} one can write:

$$\tau_{ij} - \frac{1}{3}\delta_{ij}\tau_{kk} = -2C\Delta^2 \left|\bar{S}_{ij}\right| \bar{S}_{ij}, \tag{2.20}$$

$$T_{ij} - \frac{1}{3}\delta_{ij}T_{kk} = -2C\widehat{\Delta}^2 \left|\widehat{\bar{S}}_{ij}\right| \widehat{\bar{S}}_{ij}, \tag{2.21}$$

where

$$\widehat{\bar{S}}_{ij} = \frac{1}{2}\left(\frac{\partial \widehat{\bar{u}}_i}{\partial x_j} + \frac{\partial \widehat{\bar{u}}_j}{\partial x_i}\right), \qquad \left|\widehat{\bar{S}}_{ij}\right| = \sqrt{2\widehat{\bar{S}}_{ij}\widehat{\bar{S}}_{ij}}. \tag{2.22}$$

Applying the test filter to equation (2.20) and substituting the result in equation (2.19), assuming that variations in C are slow[2] one can obtain the following expression:

$$\mathcal{L}_{ij} - \frac{1}{3}\delta_{ij}\mathcal{L}_{kk} = -2C\left(\widehat{\Delta}^2 \left|\widehat{\bar{S}}_{ij}\right| \widehat{\bar{S}}_{ij} - \widehat{\Delta^2 \left|\bar{S}_{ij}\right| \bar{S}_{ij}}\right) \tag{2.23}$$

As $\mathcal{L}_{ij}$ can be directly computed on a given grid, the equation (2.23) gives a tensor equation system (5 equations - tensor $\bar{S}_{ij}$ is symmetric and traceless) for determining the constant C, hence the problem is over-determined.

There have been several suggestions on how to close this over-determined equation system (Ghoasal et al. [33], Lilly [57], Piomelli and Liu [83] and others). The one suggested by Lilly [57] will be adapted in context of this work.

Lilly [57] suggested to use the least-square approach to satisfy the equation (2.23). Defining the error between the right- and left-hand side of eq. (2.23) as Q and denoting $M_{ij} = \left(\widehat{\Delta}^2 \left|\widehat{\bar{S}}_{ij}\right| \widehat{\bar{S}}_{ij} - \widehat{\Delta^2 \left|\bar{S}_{ij}\right| \bar{S}_{ij}}\right)$, one obtains the following expression:

$$Q = \left(\mathcal{L}_{ij} - \frac{1}{3}\delta_{ij}\mathcal{L}_{kk} + 2CM_{ij}\right)^2 \tag{2.24}$$

Now demanding that $\partial Q/\partial C = 0$, one gets a single equation for determining the constant C:

$$C = -\frac{\left(\mathcal{L}_{ij} - \frac{1}{3}\delta_{ij}\mathcal{L}_{kk}\right) M_{ij}}{2M_{ij}M_{ij}} \tag{2.25}$$

This dynamic model version gives significant improvements compared to the basic Smagorinsky model, but the method proves to be very difficult to stabilize numerically. As it turns out, the calculated coefficient is a rapidly varying quantity in both space and time and takes high values of both signs. Computations of a negative values of the coefficient, producing the negative eddy-viscosity, are believed to mimic the backscattering process, but high negative values introduce a rapid numerical instability (divergence).

For that reason, a so-called clipping of the eddy viscosity value is introduced, implemented by claiming that $\nu_{sgs} \geq -\nu$, with ν representing the molecular viscosity. In the flow cases where statistically homogeneous flow directions exist, the coefficient C is averaged in those directions to stabilize the computations. For a general flow case Davidson [20] suggested a

---

[2] C is assumed to be independent of any filtering operator

consistent method based on the use of one-equation model for the purpose of stabilizing the C coefficient.

It should be emphasized that the most methods used to stabilize the dynamic model are more based on a numerical convenience than a deeper physical reasoning.

Finally it should be noticed that the dynamic procedure for calculating the Smagorinsky constant introduces a computational overhead of about 30%, compared to the base model.

2.3.1.3 Mixed Scale Eddy Viscosity Models

Models of this type were originally developed by T. P. Loc and Sagaut [91]. They are shortly described in the book of Sagaut [90] as well.

The mixed scale eddy viscosity models exhibit a triple dependency on the large and small structures. Firstly they depend on the vorticity $\bar{\omega} = \nabla \times \bar{u}\,(x,\, y,\, z,\, t)$ or shear-strain tensor $\bar{S}_{ij}(x,\, y,\, z,\, t)$ of the resolved scales, secondly they depend on the kinetic energy of the smallest resolved scales k_{sgs} and thirdly they depend on the locally determined cut-off length scale Δ defined in equation (2.4). If the shear strain tensor $\bar{S}_{ij}$ is used in conjunction with the mixed model, it becomes a kind of extended and improved Smagorinsky model.

Formally the model is defined by the following expression:

$$\nu_{sgs}\,(\alpha,\, x,\, y,\, z,\, t) = C_m \Delta^{1+\alpha} k_{sgs}^{\frac{1-\alpha}{2}}\,(x,\, y,\, z,\, t)\,|\mathcal{F}\,(\bar{u}\,(x,\, y,\, z,\, t))|^{\alpha} \tag{2.26}$$

where $\mathcal{F}\,(\bar{u}\,(x,\, y,\, z,\, t)) = \bar{S}_{ij}(x,\, y,\, z,\, t)$ or $\nabla \times \bar{u}\,(x,\, y,\, z,\, t)$, $\alpha \in [0, 1]$ and C_m is the model constant. Setting $\alpha = 1$ and using $\mathcal{F}\,(\bar{u}\,(x,\, y,\, z,\, t)) = \bar{S}_{ij}(x,\, y,\, z,\, t)$ the Smagorinsky model is reproduced.

Using analytical theories of turbulence (see e.g. Sagaut [90]) the modeling constant C_m can be derived to depend directly on the constant in the Smagorinsky model C_s. In the context of this work the values of C_m suggested in some previous research projects will be adopted. Hence, in the case of the mixed model based on vorticity $C_m = 0.02$ will be used (Voigt [111]) and in the model version based on the shear strain tensor $\bar{S}_{ij}$ the value of $C_m = 0.06$ will be adopted (Byskov [12]).

The velocity scale here is determined through the estimate of the subgrid kinetic energy k_{sgs}. The k_{sgs} is computed utilizing the similarity approximation of Bardina et al. [9] i.e. assuming that the dominant unresolved scales are of the order of the filter width Δ and that they primarily exchange energy with the scales slightly above them - smallest resolved scales. Thereby, determining the kinetic energy contained in the smallest resolved scales a reasonable estimate of k_{sgs} can be accomplished. Then applying the explicit filter defined in the previous paragraph ($\widehat{\Delta} = 2\Delta$), one can obtain a value of $\widehat{\bar{u}}_i$. The k_{sgs} is now estimated from:

$$k_{sgs} = \frac{1}{2}(\bar{u}_i - \widehat{\bar{u}}_i)\,(\bar{u}_i - \widehat{\bar{u}}_i), \tag{2.27}$$

where $\bar{u}_i$ is the velocity resolved on the grid-filter, and $\widehat{\bar{u}}_i$ is the velocity resolved on the explicit test-filter.

As indicated the coefficient $\alpha \in [0, 1]$. For $\alpha = 0$ the model becomes $\nu_{sgs} = C_m \Delta k_{sgs}^{1/2}$ and is only dependant on the smallest resolved scales and for $\alpha = 1$ it becomes the Smagorinsky model. Hence, the parameter α defines the relative contribution of small and large scales to the model. The simulations are typically performed for $\alpha = 0.5$, where it is claimed that the model correctly predicts the asymptotic behavior in the near-wall region (see e.g. Byskov [12]).

2.3.1.4 One-Equation Models

Following an analogy known from RANS modeling, where $k - \varepsilon$ models gained significant popularity, similar methodology can be adopted for the case of modeling the SGS stresses. As stated earlier, the length scale is assumed to be of order of the filter width Δ, so an equation to determine the unknown velocity scale u_0 is required to close the equation system. For this purpose the transport equation for k_{sgs} can be derived from the filtered N-S equations yielding:

$$\frac{\partial k_{sgs}}{\partial t} + \frac{\partial}{\partial x_j}(k_{sgs}\bar{u}_j) = \frac{\partial}{\partial x_j}\left[(\nu + \nu_{sgs})\frac{\partial k_{sgs}}{\partial x_j}\right] + 2\nu_{sgs}\bar{S}_{ij}\bar{S}_{ij} - C_\varepsilon \frac{k_{sgs}^{\frac{3}{2}}}{\Delta}, \tag{2.28}$$

where the value of C_ε can be determined from Kolmogorov's $-5/3$ low to $C_\varepsilon = 0.93$ and Δ is the explicitly specified length scale.

The eddy-viscosity is calculated from:

$$\nu_{sgs} = C\Delta k_{sgs}^{\frac{1}{2}}, \tag{2.29}$$

with C being a model constant, which can either be analytically determined based on turbulence theory or dynamically adjusted, in a similar way as described in section 2.3.1.2.

This model was first introduced by Schumann [94], and later adjusted in the framework of the dynamic modeling by Davidson [20] among others.

The results obtained utilizing the one-equation model are not significantly improved compared to the ones obtained using simpler and less computationally expensive models. For that reason the model has not gained a considerable popularity in LES, but the analogous method/model is widely used in the framework of the Detached Eddy Simulation (DES).

2.3.2 Other Approaches to Modeling the SGS Stress Tensor

Of other methods used for modeling the SGS stress tensor, the method originally proposed by Bardina et al. [9] and the so-called Deconvolution method should be mentioned.

Bardina et al. [9] hypothesized that the smallest resolved scales are in many ways similar to the largest unresolved scales, assuming that the main energy interaction is taking place between the smallest eddies of the former and the largest eddies of the latter. This leads to an approach known as the Scale-similarity modeling approach. It should be emphasized that the ideas of Bardina et al. [9] have already being utilized in the framework of eddy-viscosity models leading to the dynamic modeling procedure and Mixed-Scale eddy viscosity models.

Rewriting the SGS stress tensor defined in eq. (2.7) and splitting up the unfiltered velocity field as $u = \overline{u}_i + u_i^{'}$ with $\overline{u}_i$ being the resolved and $u_i^{'}$ unresolved part, one obtains the following expression:

$$\begin{aligned}
\tau_{ij} &= \overline{u_i u_j} - \overline{u}_i \overline{u}_j = \overline{\left(\overline{u}_i + u_i^{'}\right)\left(\overline{u}_j + u_j^{'}\right)} - \overline{u}_i \overline{u}_j \\
&= \overline{\overline{u}_i \overline{u}_j} + \overline{\overline{u}_i u_j^{'}} + \overline{u_i^{'} \overline{u}_j} + \overline{u_i^{'} u_j^{'}} - \overline{u}_i \overline{u}_j, \\
&= \underbrace{\left(\overline{\overline{u}_i \overline{u}_j} - \overline{u}_i \overline{u}_j\right)}_{L_{ij}} + \underbrace{\left(\overline{\overline{u}_i u_j^{'}} + \overline{u_i^{'} \overline{u}_j}\right)}_{C_{ij}} + \underbrace{\overline{u_i^{'} u_j^{'}}}_{R_{ij}},
\end{aligned} \tag{2.30}$$

where L_{ij} denotes Leonard stresses, C_{ij} denotes cross-term stresses and R_{ij} denotes Reynolds stresses. Since L_{ij} can be directly computed, Bardina et al. [9] suggested to model C_{ij} utilizing the assumption of the scale similarity as:

$$C_{ij}^{Model} = c_r \left(\overline{u}_i \overline{u}_j - \overline{\overline{u}}_i \overline{\overline{u}}_j\right), \tag{2.31}$$

and $R_{ij}^{Model} = 0$.

Speziale [103] showed that for model to be Galilean invariant the constant must be $c_r = 1$. The model has generally proven not to be sufficiently dissipative. Therefore R_{ij} is typically modeled utilizing the Smagorinsky model to make the whole model sufficiently dissipative.

As an alternative to scale similarity and eddy-viscosity models, a model class aimed to postulate a specific form for the subgrid velocity field rather than the SGS stress tensor has drawn a lot of attention recently. The concept is known as the deconvolution concept, and is based on an attempt to estimate the unfiltered velocity from the filtered one. Having an estimate of the unfiltered velocity the residual SGS velocity can be directly computed; hence the SGS stress tensor can be straightforwardly evaluated from its definition eq. (2.7) on page 8. In estimating the unfiltered velocity, expressions of varying complexity can be utilized (see e.g. Domaradzki and Saiki [25], Stolz and Adams [106]).

It should be noted that the method is rather new, although it has been successfully applied on some benchmark test cases - see e.g. Stolz et al. [107] among others.

As testing of different models, especially different modeling approaches in the framework of LES, is both time and computationally demanding process, it is out of the scope of this work. Therefore only different versions of the SGS eddy viscosity models will be considered in the rest of this thesis.

Chapter 3

Channel Flow

Computations of the turbulent channel flow have been used as a validation and benchmark test case, especially in the framework of LES, for several decades now. Even though the flow and geometrical set up (see Figure 3.1) for this case may seem quite simple, it has proven to be a challenging task for LES computations in general. The reason for this basically lies in the fact that all turbulent structures are created in and originate from a tiny boundary layer on the channel walls. Experimental work conducted in the 1960s and 70s showed, that a quasi-cyclic (repetitive) process, called a *bursting process*, occurs in the near wall region of the boundary layer (see e.g. Hinze [39]). It is argued that a series of so called *ejection* and *in-rush* events repetitively occurring in this region are the main source of the turbulent structures in the boundary layer. Properly resolving the origin of the turbulent structures in a flow where the turbulence mainly originates from the boundary layer has therefore paramount importance, but on the other hand is very computationally costly.

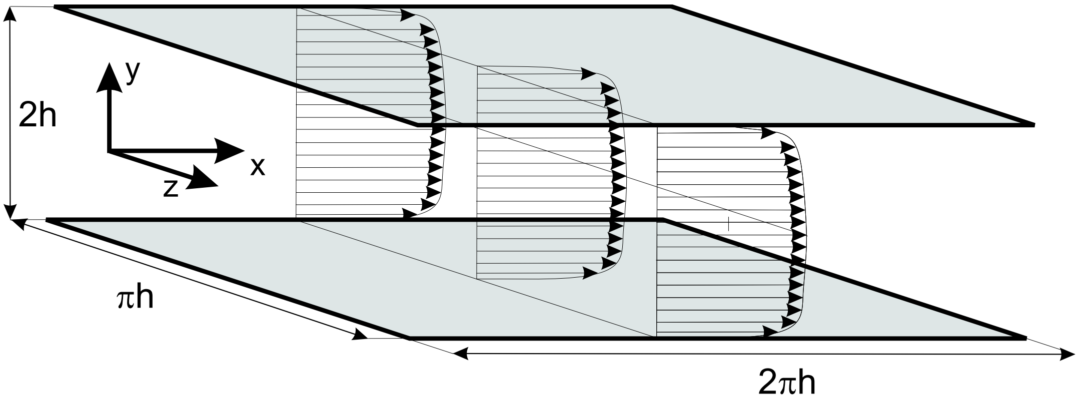

Figure 3.1: Schematic overview of the plane channel flow configuration

So despite its "*obvious simplicity*", the complexity of the physical processes in the boundary layer makes the channel flow case a good benchmark test for validation of different SGS models and modeling approaches in the framework of LES.

3.1 Introduction

Turbulence in the plane channel flow is mainly characterized by the Reynolds number based on the wall-friction velocity $Re_\tau = u_\tau h/\nu$ and Reynolds number based on the mean flow rate $Re_m = U_m h/\nu$, where h is the half channel width and the wall-friction velocity is defined as $u_\tau = \nu \left.\frac{dU}{dy}\right|_{wall}$. In the case where spanwise rotation is superimposed on the original flow, some additional contributions to the governing equations are obtained due to centrifugal and Coriolis forces. The centrifugal force is conservative and actually causes the effective static pressure to increase in magnitude, so $p_{eff} = p + \frac{1}{2}\rho\,(\Omega r)^2$, whereas one component of the Coriolis force ($\vec{f_c} = -2\rho\vec{\Omega} \times \vec{U}^1$) is acting in the wall normal direction, causing the flow in the channel to be divided into stable (eventually relaminarised) and unstable (enhanced turbulence level) sides. To quantify the importance of rotation in this flow case two rotational numbers $Ro_\tau = 2\Omega h/u_\tau$ and $Ro_m = 2\Omega h/U_m$ are introduced, where Ω is the rotational speed.

3.2 Previous Investigations

The first LES calculations on the plane channel flow case were performed in the 1970s. Deardorff [21] presented LES results based on only 6720 computational cells, performed utilizing a synthetic boundary condition in the log layer (no explicit treatment of the near-wall region). Moin and Kim [73] performed LES of the channel flow, explicitly treating the wall region and successfully reproducing experimentally observed structures in the wall-layer. Kim et al. [50] performed DNS of the channel flow utilizing a pseudo-spectral code on a domain of $4\pi h \,\mathrm{x}\, 2h \,\mathrm{x}\, 2\pi h$ and spatial resolution of $192 \,\mathrm{x}\, 129 \,\mathrm{x}\, 160$ cells in the streamwise, wall-normal and spanwise directions with Reynolds number based on friction velocity - $Re_\tau = 180$. Moser et al. [75] performed additional DNS calculations for $Re_\tau = 395$ and $Re_\tau = 590$ on a domain of $2\pi h \,\mathrm{x}\, 2h \,\mathrm{x}\, \pi h$. Databases provided by Kim et al. [50] and Moser et al. [75] are being extensively used in context of testing LES SGS models.

Numerous numerical investigations of flows determined by centrifugal and Coriolis forces are being conducted in the past. Special effort has been put into understanding the effects of rotation on turbulence quantities. Recently, a DNS study of turbulent concentric annular pipe flow was performed by Chung et al. [15], a LES study of turbulent flow in a rotating concentric annular channel was performed by Liu and Lu [59], a LES study of turbulent flow in a rotating square duct was performed by Pallares and Davidson [79] and many other related studies. In the context of the plane channel flow, Kristoffersen and Andersson [52] performed a DNS study of a rotating channel flow on a domain with same size as one used in study of Kim et al. [50], using spatial resolution of $128 \,\mathrm{x}\, 128 \,\mathrm{x}\, 128$ cells. Tafti and Vanka [109] performed a similar study utilizing only half of the mentioned domain.

In general, computations of the turbulent channel flow are being used to better understand different areas of fluid mechanics - from validation of some widely used assumptions in turbulence theory (e.g. the *Taylor hypothesis* - see Piomelli et al. [84]), through understanding of the processes in near-wall turbulence (see e.g. Chernyshenko and Baig [14]), evaluation of various SGS modeling approaches (e.g. Hartel and Kleiser [37]) to applications of POD analysis aiming to both analyze the flow structures in the channel flow (Alfonsi and Primavera [3]) and to create inflow boundary data for LES (Johansson and Andersson [44]) and many other fluid mechanics - related areas.

---

[1] $f_{c,x} = 2\rho\Omega v$, $f_{c,y} = -2\rho\Omega u$ and $f_{c,z} = 0$

In the context of this work, investigations of channel flow are entirely focused on validation of the implementation of different eddy-viscosity SGS models in the in-house finite volume CFD code EllipSys3D. Therefore, the focus is directed on comparison of LES calculations vs. the available DNS data from - AGARD [1], Moser et al. [75] and Kristoffersen and Andersson [52] for both plain and rotating channel flow. It should be noted that only low-order statistics are investigated and compared for this purpose as they are assumed to provide sufficient information to conclude whether the considered models are implemented correctly. For a deeper understanding of the underlying flow physics in the plane and/or rotational channel flow case, the interested reader is referred to the cited references.

Furthermore, it should be emphasized that no attempt to assess (study) the mutual performance of investigated models, other than the general one, will be made. Such a study will require a parametric investigation of different modeling factors, especially modeling constants used, which is out of the scope of this work. As pointed out in Sagaut et al. [92], this kind of study can help in developing techniques suitable for a particular flow case, but can not be generalized to e.g. an industrially relevant complex flow.

Therefore, some representative values for the used constants are chosen and results accomplished utilizing them are presented in the following section.

3.3 Numerical Configuration of the Plane Channel Flow Case

The computational domain is depicted on Figure 3.1. It represents two infinitely long parallel flat plates mutually divided by a distance of $2h$. Infinite extensions of the domain in the streamwise (x) and spanwise (z) directions are modeled through periodic boundary conditions. The domain extensions are chosen in order to follow the calculations from the corresponding DNS database of Moser et al. [75], AGARD [1] to $L_x = 2\pi h$, $L_y = 2h$, and $L_z = \pi h$. The validity of the chosen domain extensions will be briefly discussed in the following paragraphs. The computational mesh used in the calculations consists of 64 x 96 x 64 cells in the streamwise, wall-normal and spanwise direction, respectively. The cells are equally distributed in the x and z directions, while a stretching function is used in the wall-normal direction. The stretching function chosen is one proposed by Gullbrand and Chow [36] defined as:

$$y_j = -\frac{\tanh\left(\gamma\left(1-\frac{2j}{N_y}\right)\right)}{\tanh\left(\gamma\right)} \qquad j = 0, 1, ..., N_y, \tag{3.1}$$

with N_y representing the number of grid points in the wall-normal direction and γ is the stretching parameter. The stretching parameter used is $\gamma = 2.5$ giving $\Delta y^+_{max} = u_\tau \Delta y^{max}/\nu = 21$ and 11 grid points within $y^+ < 10$, with the first point at $y^+ = 0.55$. The dimensionless distances in the x and z directions are $\Delta x^+ = u_\tau \Delta x/\nu = 39$ and $\Delta z^+ = u_\tau \Delta z/\nu = 19.5$ respectively.

A well-resolved LES requires a mesh resolution of approximately $\Delta x^+ < 100$, $\Delta z^+ < 20$ and $\Delta y^+_{min} \leq 1$ with at least 5 grid points inside $y^+ < 10$ (see e.g. Piomelli and Balaras [82]). As it can be seen, the mesh utilized in present computations is in full compliance with those requirements.

The equations solved are given as:

$$\begin{aligned}\frac{\partial \overline{u}_i}{\partial x_i} &= 0 \\ \frac{\partial \overline{u}_i}{\partial t} + \frac{\partial}{\partial x_j}(\overline{u}_i \overline{u}_j) &= f_i \delta_{ij} - \frac{1}{\rho}\frac{\partial \overline{p}}{\partial x_i} + \nu \frac{\partial^2 \overline{u}_i}{\partial x_j \partial x_j} - \frac{\partial \tau_{ij}}{\partial x_j},\end{aligned} \tag{3.2}$$

where $f_i = [f_1, 0, 0]$ is the forcing term. Setting $u_\tau = \rho = h = 1$ the Reynolds number based on frictional velocity u_τ and half channel width h becomes $Re_\tau = 1/\nu$ yielding $\nu = 1/Re_\tau$. The forcing term in eq. (3.2) is dynamically adjusted at each time step ensuring that the mass flow rate is kept constant ($f_1 \approx 1$).

The convective term in the equation system is discretized utilizing the deferred corrected 4th order Central Difference Scheme (CDS4) and the pressure is corrected utilizing the PISO algorithm. The time step is chosen in order to obtain stable convergence in each time step to $\Delta t = 5e-4$, giving a non-dimensional time step of $\Delta t^* = u_\tau \Delta t/h = 5e-4$ and yielding a maximum CFL number of $CFL_{max} = U_{max}\Delta t/\Delta x = 0.13$. The solution is advanced in time using the 2nd order iterative dual time-stepping method. Approximately 8 subiterations were necessary for residuals to drop in order of about 10^{-4}.

At each time step during the calculations the velocity components, pressure and SGS viscosity are summed op, giving a basis for calculation of time averaged quantities. Exploiting the fact that streamwise and spanwise are the homogeneous directions, the considered quantities are additionally averaged in those 2 directions yielding a single profile dependant only on the wall-normal direction as output of the computations.

In case of the dynamic model a slightly different approach is utilized. Here, spatial averaging is undertaken at every time step, in most cases, in order to smooth out the high fluctuations in the dynamically determined C_s constant.

In order to obtain a suitable basis for comparison of LES and DNS results, the averaging process has been carried out for a period of about 25 "*Flow Through Times*" - (FLT)[2]. The averaging is typically started after the initial start-up phase of about 15-20 FLTs.

The wall friction velocity is approximated based on the following expression $u_\tau = \sqrt{\nu u/\Delta y}$, where u is the streamwise velocity at the first cell center next to the wall and Δy is the distance from the same cell center to the wall. u_τ is evaluated in each time step employing averaging in the homogeneous directions on both lateral walls. A single overall value for u_τ at a given time step is then obtained from the following expression:

$$u_\tau^2 = \frac{1}{2}\left(u_{\tau,y=-h}^2 + u_{\tau,y=h}^2\right). \tag{3.3}$$

The plane channel flow case considered in the following part is the one originally investigated by Moser et al. [75] for $Re_\tau = 395$.

3.4 Results and Discussions of the Plane Channel Flow Case

Four different SGS eddy viscosity models have been tested. A list of investigated models and their performance in form of ability to reproduce the DNS data in the wall region and in the mean flow is summarized in Table 3.1.

---

[2] A time it takes a fictive particle following the mean flow to cross the whole domain in the streamwise direction, i.e. $t_{FLT} = (x_{max} - x_{min})/U_m$

Model	Model Constant	Re_τ	Re_m	U_c/U_m	U_c/u_τ
DNS	-	395	6873	1.147	19.96
Smagorinsky	$C_s = 0.1$	415	6880	1.142	18.94
Dynam. Smagorinsky	-	380	6873	1.130	20.35
Mixed - based on Ω_{ij}	$C_m = 0.02$	391	6874	1.134	19.94
Mixed - based on S_{ij}	$C_m = 0.06$	393	6879	1.135	19.85

Table 3.1: Characteristics of the plane channel flow simulation. Mass flow rate is controlled by dynamically adjusting the forcing function from eq. (3.2). For description of the modeling constants C_s and C_m see sections 2.3.1.1 and 2.3.1.3 respectively.

The results from Table 3.1 indicate that the Reynolds number based on mean flow velocity Re_m is predicted within 0.2% of the corresponding Re_m based on DNS data, in all cases. This is a direct consequence of dynamic adjustment of the forcing function from eq. (3.2) during the calculations. The predictions of Reynolds number based on wall friction velocity Re_τ are less accurate. In the best case the predictions deviate only 0.5% (Mixed model - based on S_{ij}) and in the worst case the DNS value is overpredicted for about 5% (Smagorinsky model). Comparing the ratio between centerline and mean velocity U_c/U_m it is seen that the largest deviation from DNS data is obtained for the Dynamic Smagorinsky model - 1.5% and lowest from the Smagorinsky model - 0.5%. The same observation can be made by a closer inspection of velocity profiles shown in Figure 3.2(a). Finally, a comparison of the ratio between centerline and friction velocity U_c/u_τ reveals that Mixed model based on Ω_{ij} is the best in resembling the DNS data, whereas on the other hand Smagorinsky model produces an underprediction of about 5.6%.

Summarizing results from Table 3.1 one can state that the obtained LES results deviate in general less then 6% from the corresponding DNS data. The general good agreement between LES and DNS is probably due to a reasonable grid resolution used in the calculations.

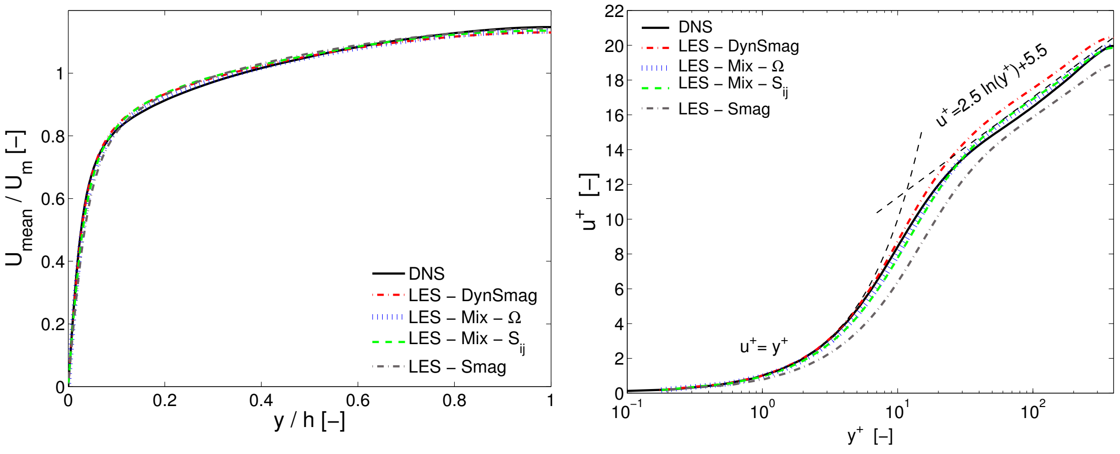

(a) Global units (b) Wall units

Figure 3.2: Mean streamwise velocity profiles normalised by mean flow velocity (a) and wall-friction velocity (b).

Figure 3.2 shows the computed mean flow profiles presented in both global and wall units vs. the DNS data. From Figure 3.2(a) it is observed that the mean LES profiles generally underpredict the DNS data in region $y/h \leq 0.1$ overpredict it in region $0.1 \leq y/h \leq 0.5 - 0.65$ and again underpredict the DNS profile in region from $y/h \geq 0.5 - 0.65$ towards the middle of the channel. Only the Smagorinsky model shows a different behavior as it does not underpredict the DNS profile in region $y/h \geq 0.5 - 0.65$ and generally has the largest deviations from DNS. Considering semi-log plot of u^+ vs. y^+ in Figure 3.2(b) the deviations of Smagorinsky model from DNS data become even more apparent. It is evident that Smagorinsky model significantly underestimates the DNS profile throughout the whole channel. It should be noted that the Smagorinsky constant used here is about factor 2 larger than the one proposed by Moin and Kim [73] for the channel flow case. Lowering the constant to more appropriate value would decrease the SGS viscosity considerably and probably lead to much better agreement with DNS data. Furthermore, from Figure 3.2(b) it is seen that the Dynamic Smagorinsky model follows DNS profile closely, especially in region $y^+ < 10$, but it overpredicts it in $y^+ > 15$ region. Both Mixed models show a similar behavior. They underpredict the DNS data in a region close to the wall and overpredicts it in a region where $y^+ > 30$, though the overpredictions are considerably smaller than ones computed with Dynamic Smagorinsky model.

Figure 3.3 shows the root-mean-square velocity fluctuations u_{rms} and v_{rms} normalized by the wall friction velocity u_τ.

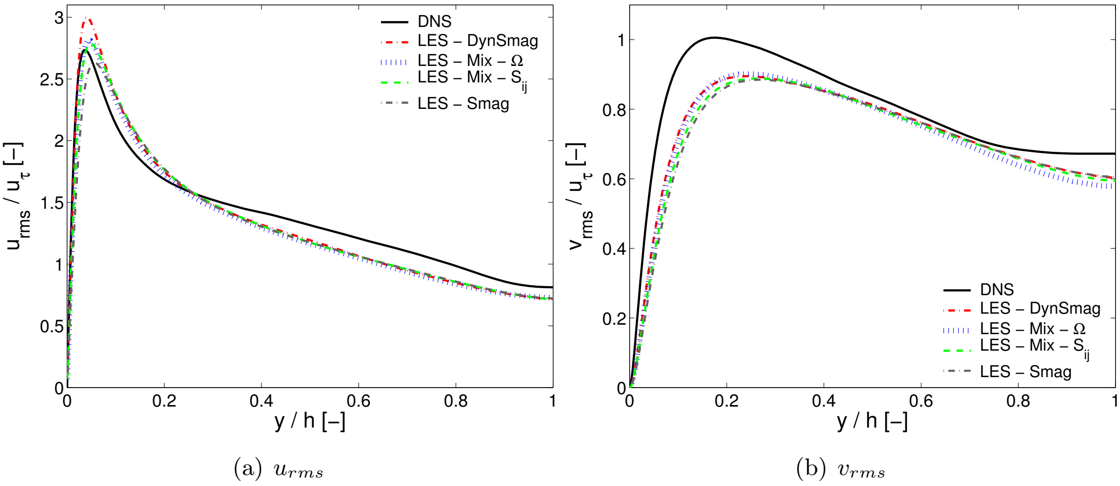

(a) u_{rms} (b) v_{rms}

Figure 3.3: Root-mean-square velocity fluctuations u_{rms} and v_{rms} normalized by the wall friction velocity.

Figure 3.3 shows that the general shape of DNS profiles is reproduced by LES. A position of the peak in u_{rms} profile is correctly reproduced only by the Dynamic model, however the magnitude of the peak itself is overpredicted - see Figure 3.3(a). Mixed models overpredict the magnitude of u_{rms} peak as well, but they are not reproducing the peak position correctly. Predictions given by the Smagorinsky model deviate significantly from DNS data in the near wall region. Moving towards the center of the channel the models tend first to overestimate and then underestimate the DNS profile.

Figure 3.3(b) indicates that only the shape of the DNS profile for v_{rms} is correctly reproduced by LES. None of the LES models are capable of correctly reproducing either the magnitude or the position of the peak in the v_{rms} DNS profile. Moreover, it is seen that all LES SGS models produce v_{rms} profiles of similar shape and magnitude.

Figure 3.4 shows the root-mean-square velocity fluctuations w_{rms} and Reynolds shear stress $\overline{u'v'}$ normalized by the wall friction velocity u_τ.

Agreements between DNS and various LES SGS models considered for the case of w_{rms} and $\overline{u'v'}$ are similar to the previously discussed findings (see Figure 3.4). Profile shapes and peak positions are correctly reproduced but the peak magnitude is generally underestimated. Disagreements are most pronounced in the near-wall region, while a reasonable agreement between LES and DNS is obtained in the rest of the channel, especially for the Reynolds shear stress $\overline{u'v'}$ - Figure 3.4(b).

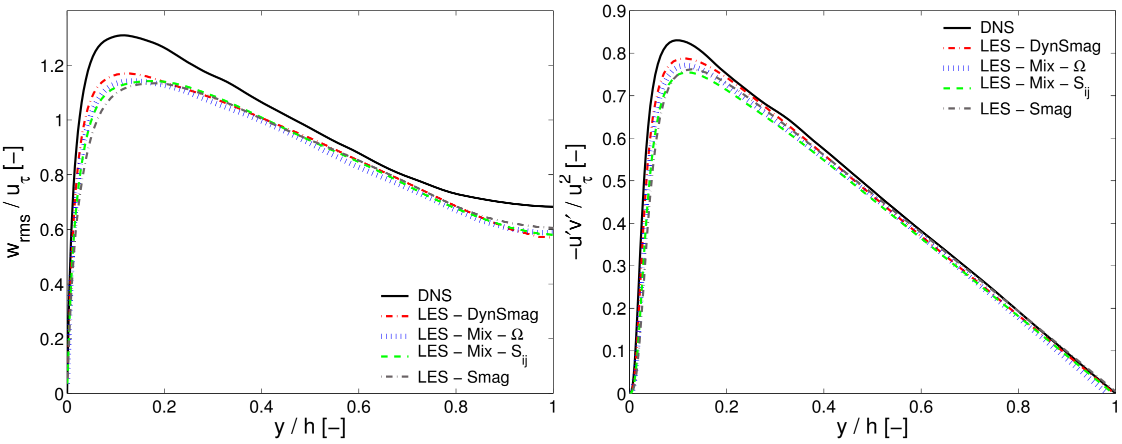

(a) w_{rms} (b) $\overline{u'v'}$

Figure 3.4: Root-mean-square velocity fluctuation w_{rms} and Reynolds shear stress $\overline{u'v'}$ normalized by the wall friction velocity.

Figure 3.5 depicts a ratio of the computed SGS viscosity ν_{sgs} vs. molecular viscosity ν. Profiles are calculated in a similar way as the rest of the profiles previously discussed in this chapter, i.e. time averaging is conducted first followed by the spatial averaging in the homogeneous directions at the end of calculations. The Dynamic Smagorinsky profile is obtained based on calculation of the C_s constant, which is on-line spatially averaged in each time step.

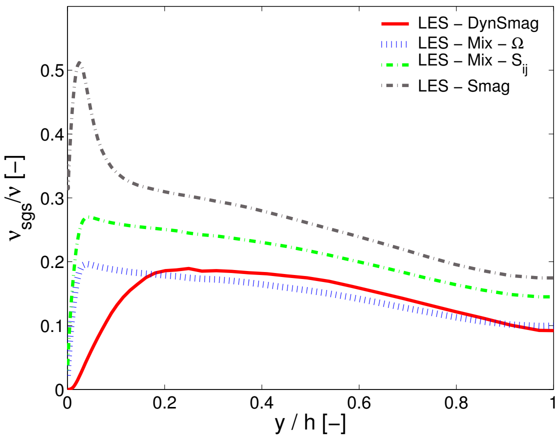

Figure 3.5: Ratio between SGS viscosity ν_{sgs} and molecular (kinematic) viscosity ν

It is seen that the Smagorinsky model produces an extensive (unphysical) peak in the near-wall region, so a use of the van Driest damping function in order to reduce ν_{sgs} viscosity in this region would be advantageous. The Dynamic model is seen to produce a smooth decay form about $y/h \approx 0.2$ towards the wall. Recalling that the Dynamic model proved to be capable of reproducing the DNS profile in the buffer layer region (see Figure 3.2), it can be concluded that the Dynamic model shows the desired *"self-adaptive"* behavior in the near-wall region. Mixed models seem to generate ν_{sgs} profiles of similar shape. They do not produce as smooth decay in the near-wall region as the Dynamic model, but on the other hand they do not create an excessive peak in ν_{sgs} as seen in Smagorinsky model either. It should be noted that by adjusting constants in the considered mixed models, the computed ν_{sgs} profiles would probably end up having similar magnitudes as well.

Turbulence Quantities

To quantify the distinct characteristics of the considered turbulent channel flow, some relevant turbulence quantities are extracted and discussed in this subsection. As all SGS models proved to be efficient in creating a real turbulent flow in the channel, investigating results based on only one of them seems both sufficient and reasonable. The SGS model chosen for this analysis is the Dynamic Smagorinsky model.

The use of periodic boundaries in the statistically homogeneous directions is typically justified if the domain considered is sufficiently large to accommodate the largest eddies in the flow (see e.g. Kim et al. [50]). A fundamental way to investigate whether the considered domain extent is suitably chosen, is through the analysis of two-point correlations. A sample two point correlation for 3 $y-$locations placed in different parts of the domain is presented in Figure 3.6. Corresponding one-dimensional spectra are depicted on Figure 3.7.

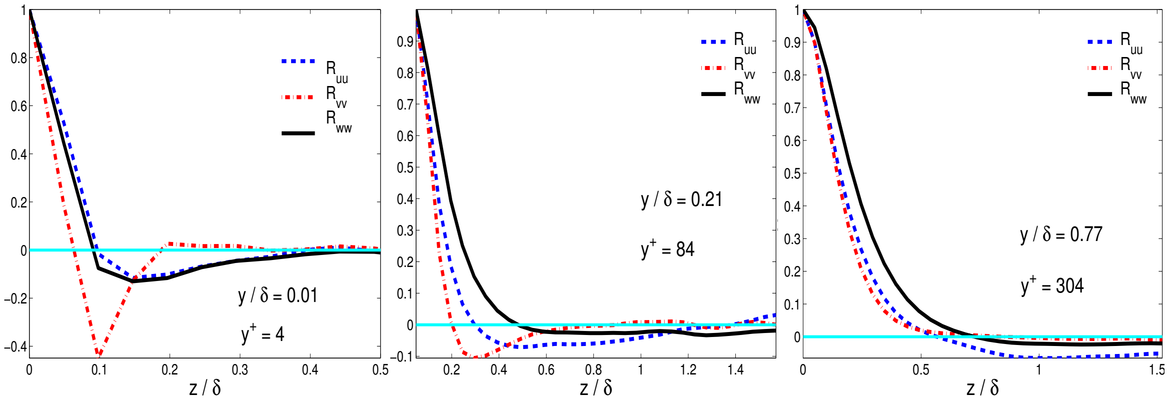

Figure 3.6: Two-point correlations R_{uu}, R_{vv} and R_{ww} in the spanwise direction

As pointed out in Frohlich et al. [31] the domain extent is considered to be sufficient, if the two-point correlation crosses the zero-line inside the domain half-width (length). Considering the correlation coefficient for $u-$, $v-$ and $w-$fluctuations for different locations in the boundary layer - $y^+ = 4$, 84 and in the bulk flow - $y^+ = 304$ presented in Figure 3.6, it is seen that the spanwise extension of the considered computational domain is adequate.

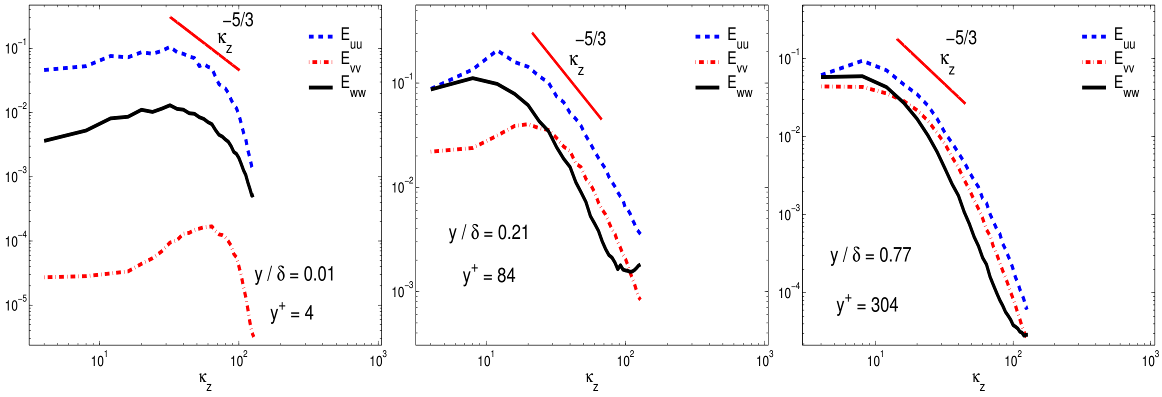

Figure 3.7: One-dimensional energy spectra E_{uu}, E_{vv} and E_{ww} in the spanwise direction

Analyzing the energy spectra shown in Figure 3.7, it can be observed that there is no sign of energy accumulation at high wave numbers, indicating that the SGS model used is acting as an effective energy drain. The figure illustrates also that the inertial subrange (Kolmogorov $-5/3$ range) is well reproduced. A difference in energy content of $u-$, $v-$ and $w-$ fluctuations, showing the local anisotropy is evident at the $y-$location very close to the wall (buffer-layer $y^+ = 4$). Local isotropy is reestablished as the location moves towards the middle of the channel.

Inspecting the two-point correlations in the streamwise direction, shown in Figure 3.8, it can be concluded that the domain extent in this direction might not be sufficient to accommodate eddies of all sizes.

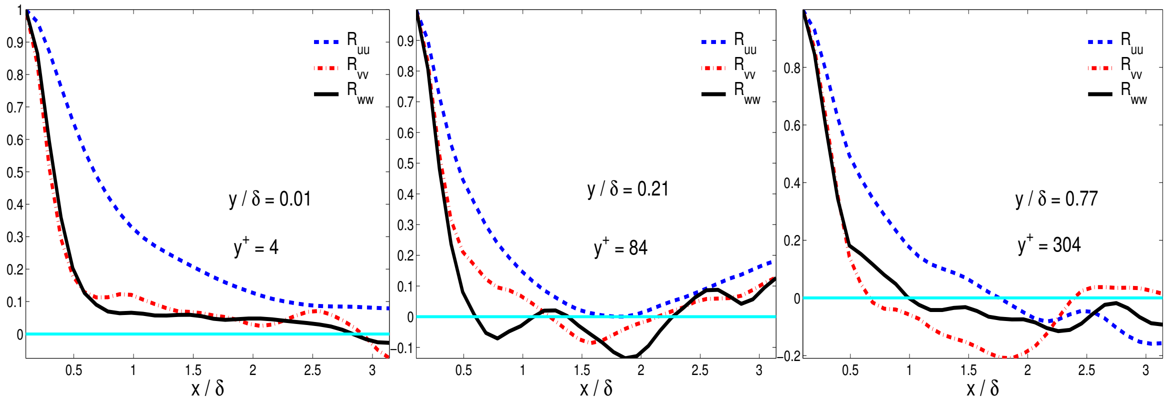

Figure 3.8: Two-point correlations R_{uu}, R_{vv} and R_{ww} in the streamwise direction

As reported in many bifurcation studies and pointed out in Frohlich et al. [31], inadequate domain extension tends only to compress the largest flow structures. It is emphasized further in [31], that in cases where LES and DNS are conducted on a domain of the same extent, the underlying comparison of the computed results is not generally affected by the insufficient domain size. Therefore, an inadequate streamwise domain extension should not have a significant impact on the presented result comparisons.

Figure 3.9 shows the autocorrelation function for $u-$, $v-$ and $w-$velocity fluctuations at four different $y-$locations.

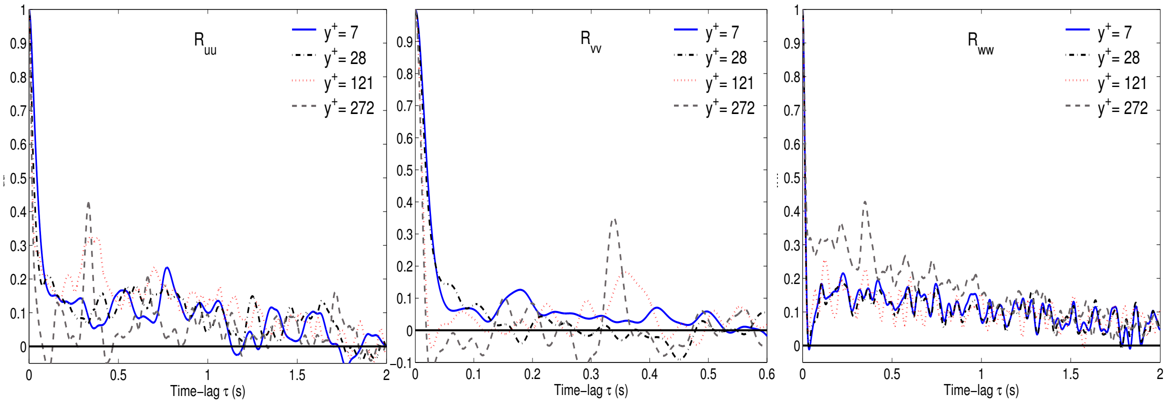

Figure 3.9: Autocorrelation function for $u-$, $v-$ and $w-$velocity fluctuations at four $y-$locations

The integral time scale, defined as an area under the autocorrelation curve, is a typical measure of the time a velocity component is correlated with itself. In a simplified form the zero-crossing of the autocorrelation function, depicted in Figure 3.9, can be taken as an indicator of the integral time scale size. The Figure shows that the $w-$ component of the velocity tends to stay correlated with itself for almost 2 seconds, leading to a considerable overall integral time scale.

Finally, histograms of all velocity fluctuations, with superimposed Normal (Gaussian) distribution, which fits the underlying data series best, for two $y-$locations, one in the boundary layer and the other in the bulk flow are presented in Figures 3.10 and 3.11.

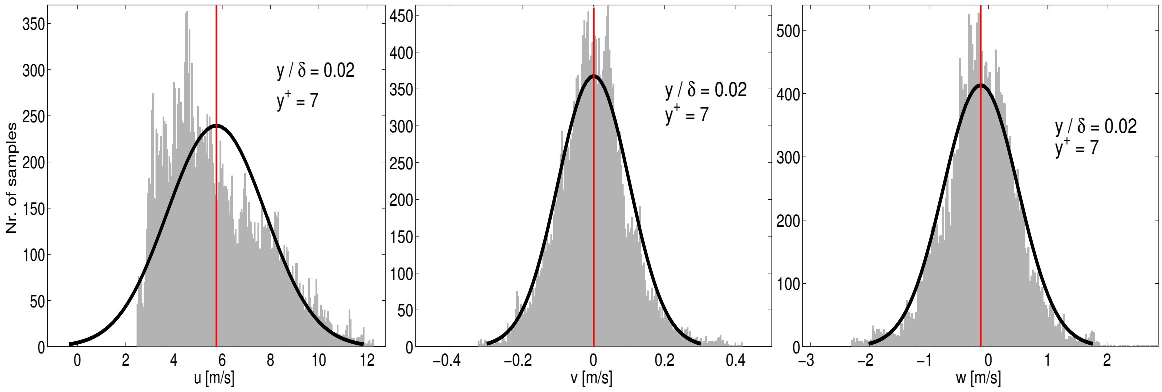

(a) $u_{mean} = 5.75\, m/s$ (b) $v_{mean} = 0.0009\, m/s$ (c) $w_{mean} = -0.13\, m/s$

Figure 3.10: Histograms of $u-$, $v-$ and $w-$ velocity fluctuations, with superimposed Normal (Gaussian) distribution, which best fits the underlying data series for a $y-$location in the boundary layer. Position of the mean is illustrated by a red solid line.

Figures 3.10 and 3.11 show that the $u-$velocity fluctuation exhibits a pronounced skewness for the point located in the boundary layer, considerably deviating from the corresponding Gaussian distribution. Other fluctuating components, including all velocity components placed in the bulk flow, seem to resemble the Gaussian distribution to a high extent. Non-zero skewness of fluctuating velocity components in the near-wall region have been reported in many experimental investigations of boundary layers (e.g. Eckelman [27]) and is probably directly linked to occurrence of the previously mentioned bursting events in the near-wall area.

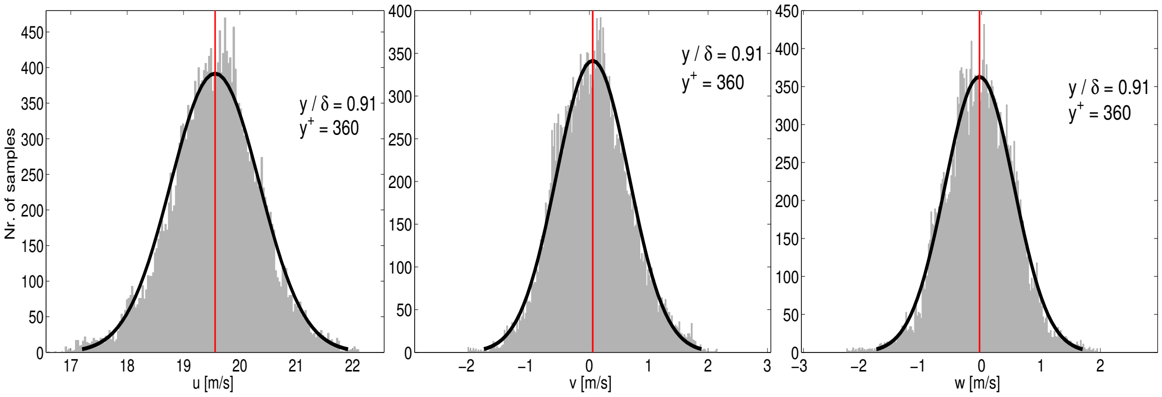

(a) $u_{mean} = 19.56\,m/s$ (b) $v_{mean} = 0.057\,m/s$ (c) $w_{mean} = -0.036\,m/s$

Figure 3.11: Histograms of $u-$, $v-$ and $w-$ velocity fluctuations, with superimposed Normal (Gaussian) distribution, which best fits the underlying data series for a $y-$location in the bulk flow. Position of the mean is illustrated by a red solid line.

3.5 Numerical Configuration of the Rotating Channel Flow Case

A numerical setup for the rotating channel flow case is very similar to the one used in the plane case (see Figure 3.12). The grid size is unchanged, but the domain considered is expanded in the streamwise and spanwise directions to mimic the conditions used to obtain the DNS results i.e. $L_x = 4\pi h$, $L_y = 2h$, and $L_z = 2\pi h$.

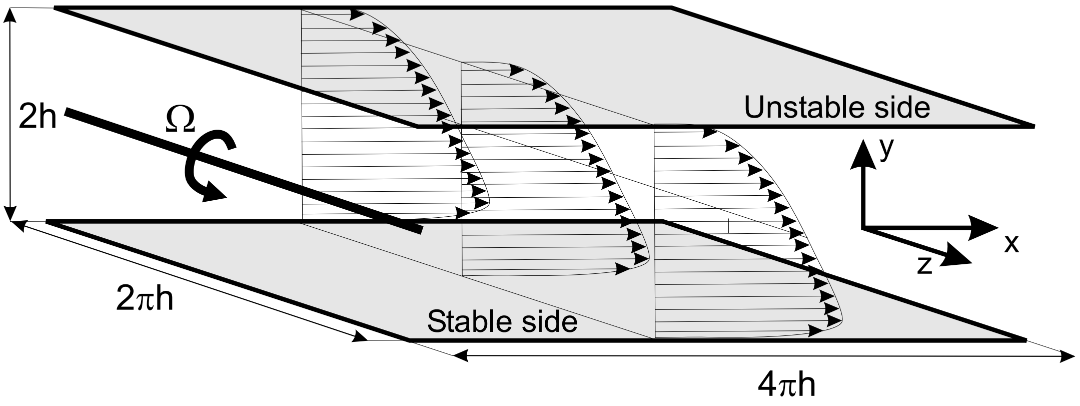

Figure 3.12: Schematic overview of the rotating channel flow configuration

The Reynolds number based on wall-friction velocity is slightly decreased in this case to $Re_\tau = 194$. A numerical grid is created using the same stretching parameter in the wall-normal direction as before ($\gamma = 2.5$) giving now $\Delta y^+_{max} = 11$ and 16 grid points within

$y^+ < 10$, with the first point at $y^+ = 0.29$. Dimensionless distances in x and z directions are now $\Delta x^+ = 38$ and $\Delta z^+ = 19$ respectively. Thereby, the criteria for well-resolved LES stated by Piomelli and Balaras [82] are fulfilled for this case as well.

Governing equations determining the flow physics have now an additional term due to effects of the Coriolis forces and are given as:

$$\begin{aligned} \frac{\partial \overline{u}_i}{\partial x_i} &= 0 \\ \frac{\partial \overline{u}_i}{\partial t} + \frac{\partial}{\partial x_j}(\overline{u}_i \overline{u}_j) &= f_i \delta_{ij} - \frac{1}{\rho}\frac{\partial \overline{p}_{eff}}{\partial x_i} + \nu \frac{\partial^2 \overline{u}_i}{\partial x_j \partial x_j} - \frac{\partial \tau_{ij}}{\partial x_j} + \vec{f}_{c,i}, \end{aligned} \tag{3.4}$$

where $f_{c,x} = 2\rho\Omega v$, $f_{c,y} = -2\rho\Omega u$ and $f_{c,z} = 0$, Ω is the rotational speed and the effect of centrifugal forces is absorbed in the effective pressure term $p_{eff} = p + \frac{1}{2}\rho\,(\Omega r)^2$.

All other parameters in this calculation are unchanged compared to computations of plane channel flow (see section 3.3).

Introduction of spanwise system rotation has a great impact on both the mean flow properties and the turbulent quantities. The flow is actually supposed to relaminarize on the stable side of the channel at a sufficiently high rotational number Ro_m. As the dynamic model is claimed to be "*self-adaptive*", it is interesting to investigate whether this model is capable of correctly predicting relaminarization in the mentioned region.

For this reason, the rotational channel flow case investigated in the following section is one with considerable system rotation introduced and originally studied by Kristoffersen and Andersson [52] for $Re_\tau = 194$ and $Ro_m = 0.5$.

3.6 Results and Discussions of the Rotating Channel Flow Case

In case of the rotating channel only two SGS models are tested - Mixed model based on Ω_{ij} and Dynamic Smagorinsky model. Previous tests conducted on the plane flow case showed that the implemented models performed in an expected way. As indicated by Kim [48], adding system rotation to the flow should not affect the smallest scales of turbulence; hence as the latter is modeled in LES, a general SGS model is expected to perform reasonably for the rotational flow case without additional modifications. Therefore, considering only two SGS models seems sufficient for the present purpose of validation of the SGS model implementations.

LES- and corresponding DNS- results from Kristoffersen and Andersson [52] are summarized in Table 3.2.

Model	Re_τ	Re_m	U_m/u_τ	$u_{\tau_{y=-h}}/u_\tau$	$u_{\tau_{y=h}}/u_\tau$
DNS	194	2948	15.25	0.679	1.207
Dynam. Smagorinsky	191	3078	16.15	0.711	1.223
Mixed - based on Ω_{ij}	197	3051	15.52	0.706	1.226

Table 3.2: Characteristics of the rotating channel flow simulation

The results from Table 3.2 indicate that Reynolds number Re_m based on the mean flow velocity U_m is not predicted as well as in case of the plane channel - an overprediction of up to 4.5% is seen here. A reason for this lies in the fact that dynamic forcing was not applied in this test case, as one of components of the Coriolis force is acting in the streamwise direction and calculations with attempted forcing have not shown satisfactory results. On the other hand the deviations between LES and DNS for the case of Reynolds number Re_τ based on friction velocity u_τ are on the order of about 1.5% i.e. better than findings for the case of the plane channel.

Wall-friction velocity u_τ on two channel walls in this rotating case is not equal. Therefore, two values $u_{\tau_{-h}}$ and u_{τ_h} at opposite channel walls are presented in Table 3.2. Overall u_τ is calculated according to equation (3.3).

Generally, the results from Table 3.2 indicate that LES results predict DNS data within an error-margin of 5% and that Mixed model is giving a slightly better agreements with DNS data compared to the Dynamic Smagorinsky model.

Figure 3.13 shows mean velocity- and turbulent kinetic energy- profiles for the rotating channel flow. Mean velocity profiles are normalized by the mean flow velocity rate U_m and turbulent kinetic energy profiles are normalized by wall friction velocity u_τ.

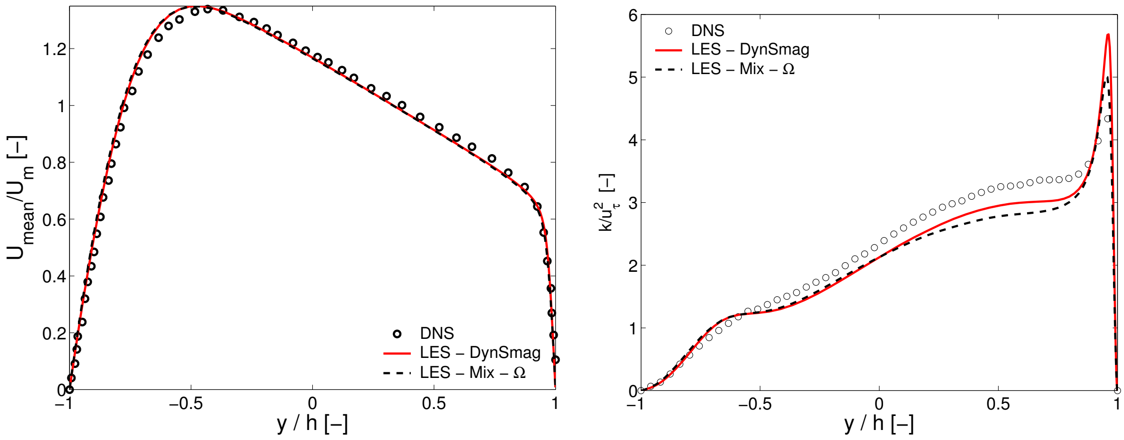

(a) (b)

Figure 3.13: Mean velocity- (a) and turbulent kinetic energy- (b) profiles for the rotating channel flow case

Figure 3.13(a) shows that the asymmetrical shape of the mean velocity profile is generally well-reproduced by LES calculations. Only in the region where $y/h \approx -0.45$ the velocity peak is slightly overpredicted by LES. The profile of the turbulent kinetic energy (Figure 3.13(b)) is highly influenced by system rotation as well. Figure 3.13(b) shows that flow is actually relaminarizing at $y = -h$ (stable side), and that LES is able to correctly predict this behavior. On the other wall (unstable side) the turbulence level is increased, but the peak value given by DNS is overpredicted by LES, especially by the Dynamic Smagorinsky model. Throughout the domain it is seen that LES profiles follow the DNS data closely with a slight underprediction in the region where $-0.5 \leq y/h \leq 0.7$. Generally, the Dynamic model tends to mimic the DNS data slightly better than the Mixed model.

Figure 3.14 shows the computed SGS viscosity ν_{sgs} normalized by the molecular viscosity ν. Figure 3.14(a) shows profiles for the two considered SGS models. The Mixed model tend to compute a higher values of ν_{sgs} in the region where $-1 \leq y/h \leq 0.5$ while Dynamic model produces the highest overall value of $\nu_{sgs}/\nu = 0.35$ in the vicinity of the wall. A smooth transition towards the wall is again observed in dynamic model profile at the upper wall (see Figure 3.5 for comparison). Furthermore, from Figure 3.14(a) it is seen that the Dynamic model is able to predict the flow relaminarization correctly, as the model "*turns off* " the viscosity on the stable channel side in the region of$-1 \leq y/h \leq -0.45$, whereas the Mixed model is not capable of predicting the relaminarization correctly.

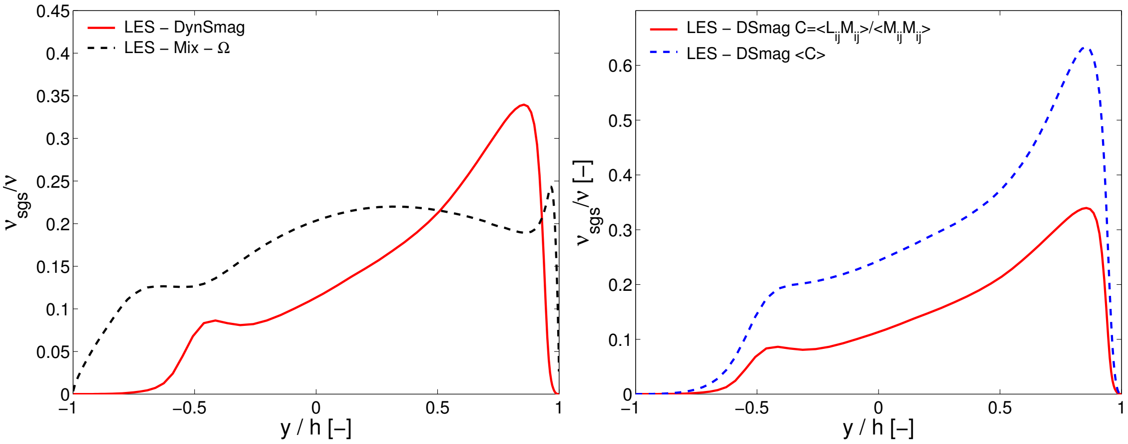

(a) (b)

Figure 3.14: Ratio between SGS viscosity ν_{sgs} and molecular (kinematic) viscosity ν for the rotating channel flow case

Several additional computations of both rotating and plane channel flow have been carried out. Since they generally do not introduce a new insight in the problems considered, they have not been included in the previous analysis. However, an interesting observation on the levels of turbulent viscosity computed by the Dynamic Smagorinsky model can be made. As explained before, ν_{sgs} profiles for the Dynamic model have been computed based on spatially (in each time step) and time averaged constant C_s. The profile computed in this way is depicted on Figure 3.14(b) by a red solid line. $< \cdot >$ stands for the spatial averaging in the homogeneous directions, showing that both numerator and denominator are averaged separately as suggested by Lilly [57]. The dashed line in the same Figure represents results from the Dynamic model, where spatial averaging is not undertaken during the calculations. This profile is obtained by sampling C_s values in time and conducting spatial averaging at the end of calculations (similar to calculation of U_{mean}, u_{rms}, etc.). A profile obtained in this way corresponds to a higher degree to a computation of a flow where no statistically homogeneous directions exist, i.e. a general flow case.

Comparing these two profiles it becomes apparent, that they compute turbulent viscosity profiles of similar shape but quite different magnitude, with a difference in magnitude being almost factor 2. In general, the results based on low-order statistics, from computations based on the Dynamic model, where no on-line spatial averaging is conducted, are similar to the ones discussed previously in this chapter. So a distinct influence of the observed difference in ν_{sgs} profiles cannot be directly quantified for this flow case, but this shows a potential weakness of the Dynamic approach (with/without spatial averaging) in a general sense. It should be noted that the similar findings can be obtained by a posteriori tests, i.e. taking an instantaneous flow realisation and calculating C_s and ν_{sgs} in the described way.

As originally proposed by Germano et al. [32], C_s in the Dynamic model is $C_s(x,\, y,\, z,\, t)$, i.e. a function of both space and time. A rationale behind applying averaging in any flow direction is actually more based on a numerical convenience than on a deeper physical reasoning, but as shown here can have a significant impact on the calculated SGS eddy viscosity and potentially on computed results in a general flow case.

Lastly, it should be emphasized that the results presented in the current work are in good qualitative agreement with numerical findings - obtained utilizing LES of [12, 83, 109, 111, 118] in both the plane and rotating channel flow case.

As pointed out many times (e.g. Byskov [12]) a direct comparison of performance of any SGS model in the framework of LES has to be taken in context of a numerical method used, grid size and domain extension utilized and many other factors of influence. For that reason, comparing directly e.g. the level of SGS viscosity introduced by Smagorinsky model with results obtained by other authors using the same model, can be quite ambiguous, potentially misleading and has to be undertaken bearing the mentioned issues in mind.
Therefore, it is only underlined here that the present LES findings are in good qualitative agreement with the previously conducted similar numerical investigations of the plane and rotating channel flow.

Finally, summarizing the results presented in this chapter, it can be concluded that all SGS models considered are successfully implemented in the in-house numerical solver EllipSys3D, as they all produce expected and satisfactory results, both with regards to the underlying DNS database and previous findings by other authors conducting similar LES analyses.

Chapter 4

Jet in a Cross Flow (JICF)

The Jet in Cross Flow (JICF) is a basic flow case investigated quite thoroughly in the past, primarily due to its applicability in an extensive array of engineering problems. Basic applications of this '*building block (canonical) flow field*' include - plume dispersion, gas turbine blade film cooling, turbojet thrust vectoring for propulsive systems, reaction control for missiles and aircrafts, vertical and/or short takeoff and landing aircrafts (V/STOL), fuel injection for burners, waste disposal into rivers, mixing of gases before chemical reactions in e.g. air pollution control systems and many others.

It is evident that application of JICF extends throughout many different engineering fields, but it should be noted, that the largest single application, which was the driving force behind the JICF research in the Cold War period, was a military related investigation of V/STOL aircrafts and its different variants. In the post Cold War period the research focus shifted towards more basic understanding of various flow structures dominating the JICF near- and far- field. For a comprehensive review of research activity in the field of JICF up to early 1990's, the interested reader is referred to the article of Margason [64].

4.1 Previous studies

The evolution of vertical flow in and around a JICF has thus been subjected to several experimental and numerical investigations from a variety of research groups, which aimed towards a better understanding of a complex interaction mechanism between the jet and the cross-stream. This interaction creates a set of coherent structures, which dominate the flow over much of the flowfield, and consist basically of a horseshoe vortex system that forms upstream of the jet exit, the jet-shear-layer spanwise vortical rollers formed primarily at the upstream jet-to-cross-flow interface, the counterrotating vortex pair (CVP), and the unsteady tornado-like wake vortices emerging downstream of the jet orifice - as shown by the experimental investigations of Fric and Roshko [30] and Kelso et al. [47] - see Figure 4.1.

The horseshoe-formed vortex around a wall mounted obstacle in a uniform flow is known to be a dominant vortical structure for this type of flow and has been studied in great detail by many investigators (see e.g. Seal et al. [95], Baker [7]). The presence of a similar vortical structure in the upstream area of the transverse jet, formed from an interaction between the jet and the oncoming cross-flow boundary layer, has been reported in experimental studies of Krothapalli et al. [53, 54], Andreopoulos [5], Fric and Roshko [30], Kelso and Smits [46], Shang et al. [96]

among others. Krothapalli et al. [53, 54] studied interaction of rectangular jets with cross-flow boundary layer and observed that a horseshoe vortex system is created upstream of the jet orifice. They found that creation of this vortex system is presumably governed by periodic phenomena, occurring at frequencies comparable to those of periodic vortical structures in the wake. Kelso and Smits [46] observed furthermore that formation of the horseshoe vortex system is dependant on important flow parameters such as Reynolds number and jet-to-cross-flow velocity ratio and can be classified in three general regimes - steady, oscillating and coalescing, according to the choice of the previously mentioned flow parameters. Their results suggest also a strong connection between unsteadiness of the horseshoe vortex and unsteady tornado-like vortices in the wake.

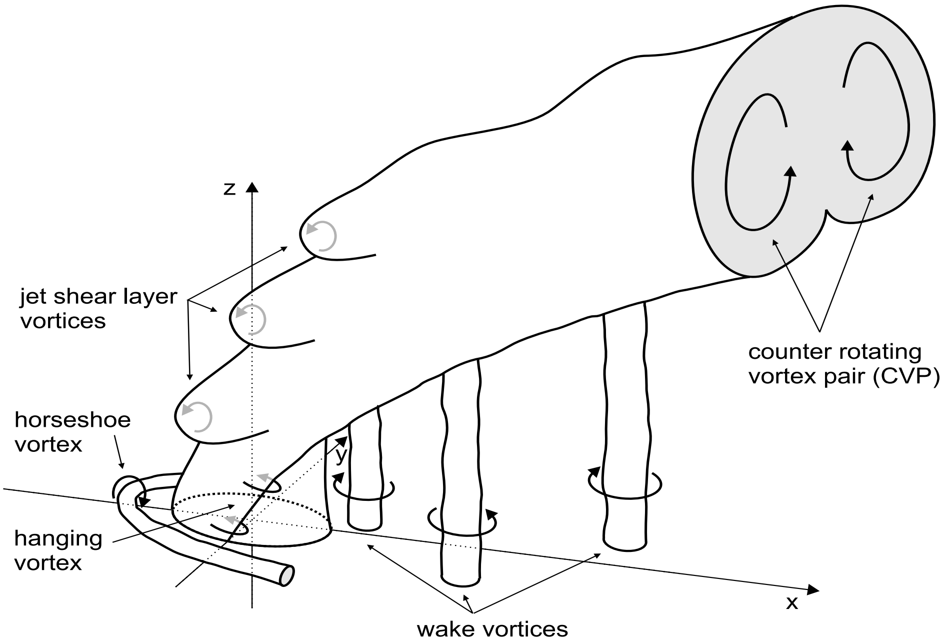

Figure 4.1: Schematic illustration of vortical structures pertinent to near-field of the JICF flow. Taken with permission from Meyer et al. [69].

The instability induced leading edge jet-shear-layer loop- like vortices (see Figure 4.1), created along jet-to-cross-flow interface, are also among dominating structures of the near-field of this flow. Flow visualizations performed by Kelso et al. [47], Fric and Roshko [30] and Lim et al. [58] and numerical investigations of Yuan et al. [117] indicate that instability of the annular shear layer emerging from the jet orifice causes the creation of those characteristic vortical structures on both the leading- and trailing- edges of the jet-to-cross-flow interface.

The counter-rotating vortex pair (CVP) - see Figure 4.1, has long been accepted as the most dominant feature of this type of flow, emerging in the near field and persistently dominating the flow field far downstream of the jet orifice. The length scales of these vortices are considerably larger than those of energetic eddies generated by turbulence itself, so CVP is actually considered to be associated with the mean flow rather than the turbulence (Morton and Ibbetson [74]).

Many of the early experimental studies focused on the time-averaged properties of the CVP (e.g. Moussa et al. [76]) but its origins have ever since been subjected to a considerable debate. The early consensus of opinion agreed that the original source of vorticity in the CVP is the jet shear layer, but the realignment of this initially azimuthally oriented vorticity at the jet exit into the streamwise vorticity of the CVP is still not fully understood. Most researchers argued that the series of vortex rings emanates from the jet orifice, and upon entrainment into the cross-flow those vortex rings are reoriented on their edges to streamwise vorticity of the CVP. The particular mechanism controlling the way in which vortex rings coalesce into the line vortices of CVP differ from one author to another. Andreopoulos [5] postulated that the lee-side edges of each vortex ring are compressed by the mean strain, which thereby causes elimination of the spanwise vorticity and promotes emanation of the CVP. Sykes et al. [108] suggested that an interaction of the upstream edge of one vortex ring with the downstream edge of the following ring causes the proper reorientation of the vorticity in the CVP, while Coelho and Hunt [17] proposed that entrainment of the cross-flow fluid forces the azimuthally oriented vorticity in the jet shear layer to redistribute into the streamwise vorticity of the CVP.

A recent numerical study of Yuan et al. [117] and the experimental flow visualization study of Lim et al. [58] in particular showed however, that vortex ring stretching and deformation might not provide an appropriate description of the CVP initialization. Lim et al.'s studies showed no sign of complete vortex ring structures, but rather showed that upstream- and lee-side vortices are created on corresponding sides of the jet-to-cross-flow interface, and they proposed a model to describe how the side arms of those vortices merge into the CVP. They indicated furthermore, that the cylindrical vortex sheet, immediately upon entrainment into the cross-flow, gets folded on both lateral edges, thereby forming the CVP. Similar findings of the CVP origin are reported by Yuan et al. [117]. They postulate that breakdown of the quasi-steady (hanging) vortices (see Figure 4.1), formed in the skewed mixing layer on the lateral edges of the jet, are the origin of the CVP. Their study showed no evidence to support the theory that the closed circumferential vortex rings exist in this type of flow either. Clearly a full consensus on proper formation mechanism of CVP is yet to be achieved.

It should be noted, that the existence of a secondary pair of CVP (SCVP) on top of the primary one was already observed by Moussa et al. [76] in their experimental setup consisting of an unskirted[1] round jet. This CVP structure was further investigated by Haven and Kurosaka [38] among others. Their results suggest that a double-decker CVP structure clearly exists in JICF cases, where jet geometries are elliptical or rectangular but are not that distinguishable for round jet geometries. The SCVP structure was also observed in the experimental data of Özcan and Larsen [77] and further discussed in Özcan et al. [78].

Vortical structures in the wake region of the transverse jet have been studied in the past too. The initial studies of Moussa et al. [76], McMahon et al. [66] among others were not able to provide a satisfactory explanation as to what the source of the vorticity in this wake region is, nor provide an adequate answer to how the tornado-like wake vortices (see Figure 4.1) are created. Recent visualization studies of Fric and Roshko [30] showed however, that for JICF with jet-to-cross-flow velocity ratio between 2 and 10, the flat plate boundary layer is the main source of vorticity in the wake region. This study reiterated a known postulate that the vorticity can not be generated anywhere within the interior of the homogeneous fluid (see Morton and Ibbetson [74]), underlining that the wake vortex formation mechanism in JICF is fundamentally different from one that produces the periodic von Karman vortex-street in the wake of a cylinder. Fric and Roshko's study showed also, that the boundary layer fluid, by wrapping around the jet and separating on its lee side, is actually creating the well known tornado-like wake vortices. It should be noted however, that Smith and Mungal [100] in their

---

[1] jet-pipe penetrates into and extends beyond the cross-flow boundary layer flat plate

JICF study with jet-to-crossflow ratios R from 5 to 25 report that the jet fluid entrains the wake region for $R > 10$. Similarly Gopalan et al. [35] report in their experimental JICF study, that properties of the wake region for low velocity ratios $R < 2$ are conceptually different from ones observed for $R > 2$, i.e. no traces of the tornado-like vortices are observed in the wake for $R < 2$ and they state furthermore, that vorticity in this region is mainly supplied by the jet shear layer in the case of low velocity ratios.

Concerning recent experimental investigations, a detailed experimental study of the JICF flow conducted by Özcan and Larsen [77] utilizing LDA measurement technique and Meyer et al. [70, 71], Pedersen [81] utilizing SPIV, should be mentioned.

Several numerical investigations of the JICF flow case have been conducted in the past as well. From initial attempts of numerical simulations based on vortex methods of Margason [63] and (more recently) Coelho and Hunt [17], Cortelezzi and Karagozian [18] among others to RANS based calculations of e.g. Sykes et al. [108], Alvarez and Jones [4] Claus and Vanka [16], Demuren [22] and more recent LES based computations of e.g. Jones and Wille [45], Yuan et al. [117] and DNS studies of e.g. Rudman [89]. As already discussed, many of the conducted numerical studies shed new and valuable insight into the complex dynamics of the JICF flowfield.

The brief review of research activity in the JICF flow case presented above shows that numerous, primarily experimental investigations, were conducted in the past. While experimental studies are quite plentiful, the numerical counterparts, especially ones who describe the flow on equivalent level of details as experiments, are still limited. As underlined earlier (e.g. AGARD [2]), only DNS and potentially LES can numerically reveal the inherit complexity (3D) and sensitive nature of the complex unfolding process and interaction between the jet and the oncoming cross-flow.

Regarding the above, the present study therefore aims to:

- ▷ establish a clear link between (validation of) numerical (LES) findings and experimental results by comparing computations and experimentally obtained mean-flow quantities,
- ▷ investigate and identify well known dominant coherent structures in this type of flow,
- ▷ explore and compare the dynamics of the computationally obtained flow field with the corresponding experimental one (obtained utilizing PIV) by use of an appropriate method e.g. Proper Orthogonal Decomposition (POD).

4.2 Flow Configuration

The present work is based on an experimental investigation of an idealized jet in a crossflow, carried out originally as a set of measurements of mean flow properties utilizing LDA measurement technique by Özcan and Larsen [77] and further investigated by a stereoscopic PIV measurements in works of Meyer et al. [70, 71] and Pedersen [81].

A fully developed turbulent pipe flow, penetrating the turbulent flat plate boundary layer through an orifice positioned perpendicular to the flat plate, creates the investigated, idealized jet in crossflow (see Figure 4.2).

Figure 4.2 shows the placement of the coordinate system- origo and the domain extensions used in the calculations.

The domain size in z and y direction is fixed for all investigated cases to $L_z = 10D$ and $L_y = 12D$, respectively. The original wind tunnel test facility has a cross section of $12.5D \, \mathrm{x} \, 25D$ in z and y direction, respectively. As the state of the boundary layer is only known on the $z = 0$ wall, it was decided not to include a part of the cross section in z direction, where boundary layer from the upper wall presumably exists (last $2.5D$ out of $12.5D$). The spanwise domain extensions are chosen in order to fully accommodate the jet entrainment into the boundary layer to $L_y = 12D$. Previously conducted similar numerical investigations (Yuan et al. [117]) showed that domain extension of $8D$ in spanwise direction actually might suffice.

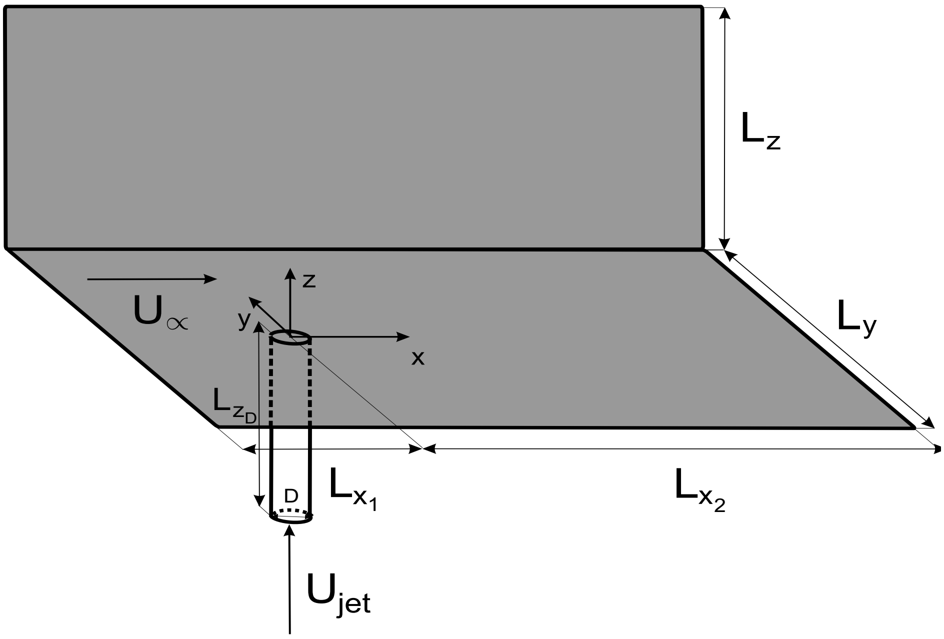

Figure 4.2: Flow configuration. The domain dimensions - $L_{x_1} = 5D \, \mathrm{or} \, 10D$, $L_{x_2} = 12D \, \mathrm{or} \, 25D$, $L_{z_D} = 3D \, \mathrm{or} \, 6D$, $L_y = 12D$, $L_z = 10D$

In order to realistically describe the process of jet entrainment into the flat plate turbulent boundary layer, a cylindrical domain extension located below the main domain is included in the computations (see Figure 4.2). This domain extension is varied in size from $L_{z_D} = 3D$ to $L_{z_D} = 6D$, in order to clarify its influence on the realistic jet inflow condition.

Domain extensions in streamwise direction have been changed in various calculations too. As different types of outflow boundary conditions have been tested, the position of the outflow boundary is varied accordingly ($L_{x_2} = 12D \, \mathrm{or} \, 25D$). Aiming to investigate the influence of the oncoming boundary layer on the computed results, the location of the inflow boundary is changed in different simulations as well ($L_{x_1} = 5D \, \mathrm{or} \, 10D$).

4.3 Boundary Conditions

The flow configuration consists of two main flow streams, one coming from the fully developed turbulent pipe flow creating the jet and the other one approaching the jet from a wind tunnel side as a spatially developing turbulent boundary layer. As both inflow conditions are turbulent, they demand a special attention and therefore are discussed separately in the following paragraphs.

On the lateral sides of the domain, periodic boundary conditions proved to interfere least with the near-boundary flow and therefore are chosen for the main calculations. At the top domain-surface the symmetry boundary condition is applied - see Figure 4.3. As stated earlier, the boundary layer emerging on the top surface of the wind-tunnel experimental configuration is assumed to be thinner[2] than $2.5\,D$ so a free stream flow is assumed to exist in the region where the top boundary in the z direction is located. On the bottom wall and the cylindrical part of the domain placed beneath the main flow set-up, the no-slip wall boundary condition has been applied - see Figure 4.3.

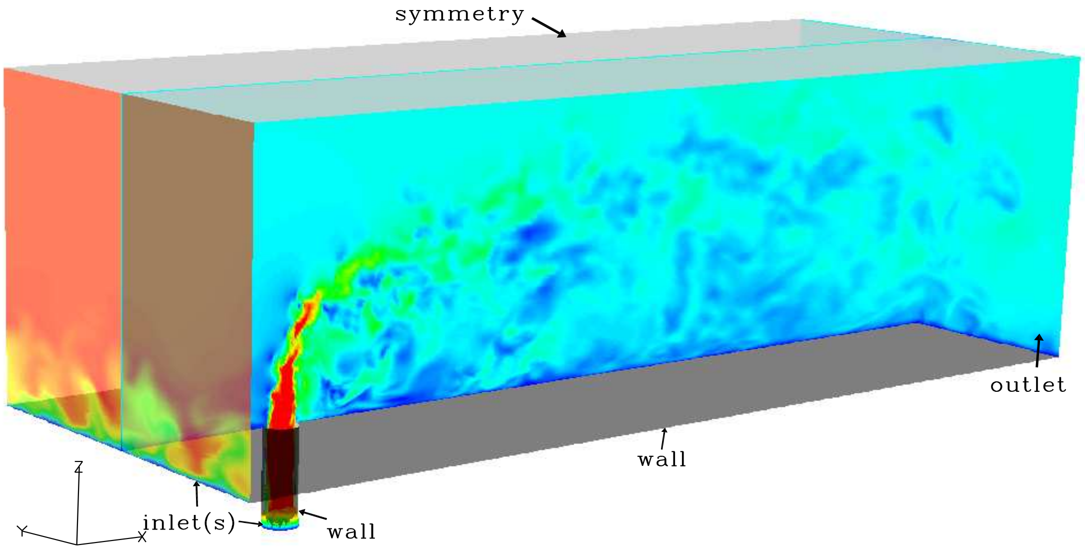

Figure 4.3: Outline of the computational set-up corresponding to the analyzed JICF flow case. An instantaneous snap-shot of the velocity magnitude from the investigated flow is visualized on three different planes - inlet, outlet and plane corresponding to the symmetry ($y/D = 0$) plane. Note that positions of some domain boundaries, with the corresponding boundary conditions applied in the computations, are included in the Figure. Periodical boundary conditions are applied in the spanwise (y) direction - they are not illustrated in the Figure.

4.3.1 Outflow Boundary Conditions

As LES computations are based on the solution of the 3D and unsteady Navier-Stokes equations, a suitable non-intrusive method for the exit boundary should be utilized. It is generally accepted that the best method for moving structures out of the computational domain in LES calculations is the convective outflow condition, which is directly derived from the one-dimensional wave equation, and is defined by:

$$\frac{\partial \phi}{\partial t} + U_c \frac{\partial \phi}{\partial n} = 0, \tag{4.1}$$

---

[2] Boundary layer flow on the bottom wall is experimentally achieved utilizing vortex generators in order to accelerate *"the state of fully turbulent spatially developing boundary layer"*. Its thickness is $\delta_{Bottom} \approx 3\,D$ (Özcan and Larsen [77]) so assuming BL thickness to be smaller $\delta_{Top} < 2.5\,D$ on the top wall, where no vortex generators are used, seems to be reasonable.

where ϕ is any scalar or velocity component considered, U_c is the convective velocity and n is the coordinate in the direction of the outward normal at the exit boundary. This method has been implemented and tested in the flow solver *EllipSys3D* as a part of this study and therefore was only included in the computations in the final phase of this project.

In the initial phase of this work the zero-gradient condition was applied to any flow variable at the exit boundary, i.e.:

$$\frac{\partial \phi}{\partial n} = 0, \tag{4.2}$$

where ϕ and n are the same quantities as previously described.

It should be noted that the zero-gradient outflow condition proved to influence the flow upstream of the exit boundary position strongly. The formation of unphysical structures was observed in a region of up to $10D$ upstream of the exit boundary. Therefore a streamwise domain extension used in the cases where zero-gradient condition was applied ($25D$ from the jet exit) is chosen based on a need to include a sort of *buffer-near-outflow-zone*, introduced as a way of diminishing the influence of the observed unphysical structures on the base flow configuration.

4.3.2 Inflow Conditions

Preliminary calculations conducted on the JICF computational set-up immediately showed that turbulent inflow conditions are necessary in order to obtain a proper turbulent flow in the computational domain. As the Reynolds numbers on both the pipe flow side as well as on the wind tunnel side are comparably low, just disturbing the mean flow at inlets in any way (e.g. randomly perturbing the initial flow, super-imposing random fluctuations with a given probability distribution to a targeted mean profile, etc.) never led to a sustainable turbulent flow in the main computational domain.

For that reason a set of separate simulations aiming to generate a realistic inflow data for both the pipe flow and the spatially developing boundary layer flow have been conducted. The results of those computations are presented in the following paragraphs.

Pipe Flow

The idea behind a precursor computation of fully developed pipe flow is to extract an instantaneous flow *"snap shot"* at some streamwise location and save it to a database, which then can be used to specify a realistic turbulent inlet condition for the main calculations.

The precursor calculations are conducted allowing the specified experimental mass flow rate to be kept constant. In order to obtain this the magnitude of the streamwise pressure gradient was adjusted iteratively until a targeted mass flow rate was achieved. Furthermore, the initial phase of the simulations was carried out until a flow reached a statistically steady state. Small oscillations of the temporal mass-flow rate (in order of less than 2% of the targeted rate) were observed at the point where a flow reached the statistical steady state. Those oscillations have not been filtered out at this point but they were rather treated at the point where the inflow condition was applied to the main calculations. The reason for this lies in the fact that the precursor simulations were performed on a finer grid than the one applied in the main JICF computations and a certain error due to interpolation of the inflow data was therefore expected. For those reasons, it was decided to address any issue regarding the pipe mass flow rate at the point where the inflow condition was applied to the main JICF calculations.

The domain extensions for the precursor computations are basically predefined. Only the streamwise domain length can be freely adjusted. Basic DNS calculations performed under similar conditions by Eggels et al. [28] showed that a streamwise domain extension of $5D$ is sufficient to accommodate almost all of the largest structures in the domain.

In order to follow the notion in the already described channel flow case (see Chapter 3) the streamwise domain extension here is chosen to be $L_z = 2\pi D \approx 6.3\,D$.

The equations are solved in the Cartesian coordinate system, but the grid sizes and other relevant quantities are best expressed in cylindrical coordinates for this particular case. Converting the quantities into cylindrical coordinates the computational mesh is approximately defined by 72 x 192 x 96 cells in r, θ and z-direction respectively. The cells are equally distributed in the z direction, while a stretching function is used in the wall-normal radial direction in order to adequately resolve the flow in the near-wall area. A so called *"butterfly or O- grid"* (see e.g. [6]) is utilized in the computations giving a non-constant grid spacing in the θ direction, but its variations are very small - practically negligible.

The dimensionless grid spacing parameters, expressed in cylindrical coordinates and wall units (ν/u_τ), for both considered cases are summarized in Table 4.1.

Case	Δz^+	$(r\Delta\theta)^+$	Δr^+	y_1^+	Nr. of grid points inside $y^+ < 10$
R=1.3	14.5	$[0.06 - 3.5]$	$[0.16 - 2.9]$	0.08	22
R=3.3	32	$[0.11 - 8]$	$[0.35 - 6.5]$	0.18	14

Table 4.1: Characteristics of the fully developed pipe flow simulations corresponding to two investigated jet-to-crossflow ratios. The values in parentheses represent the interval the corresponding quantity can assume throughout the domain. y is a distance from the wall, y_1 is the distance from the first cell center to the wall.

Considering values from Table 4.1 it can be concluded that the requirements for well-resolved LES in a wall bounded flows stated in e.g. Piomelli and Balaras [82] (see Section 3.3 on page 19) are well fulfilled for both cases considered here. Regarding the general computational details it is stated that the convective term in the N-S equation system is discretized utilizing the deferred corrected 4th order Central Difference Scheme (CDS4). Pressure is corrected utilizing the PISO algorithm and solution is advanced in time using the 2nd order iterative dual time-stepping method. The Mixed scale eddy viscosity model of Sagaut [91] (based on Ω) is utilized for modeling the SGS stresses.

The mean flow statistics computed by LES calculations compared with the available LDA measurements and the DNS simulations of Eggels et al. [28] for fully developed pipe flow are presented in Figures 4.4 and 4.5. The Reynolds number used in Figures - Re_c is based on the mean centerline velocity U_c and the pipe diameter D.

Figure 4.4 shows the mean axial velocity profiles and profiles of the streamwise RMS velocity fluctuation.

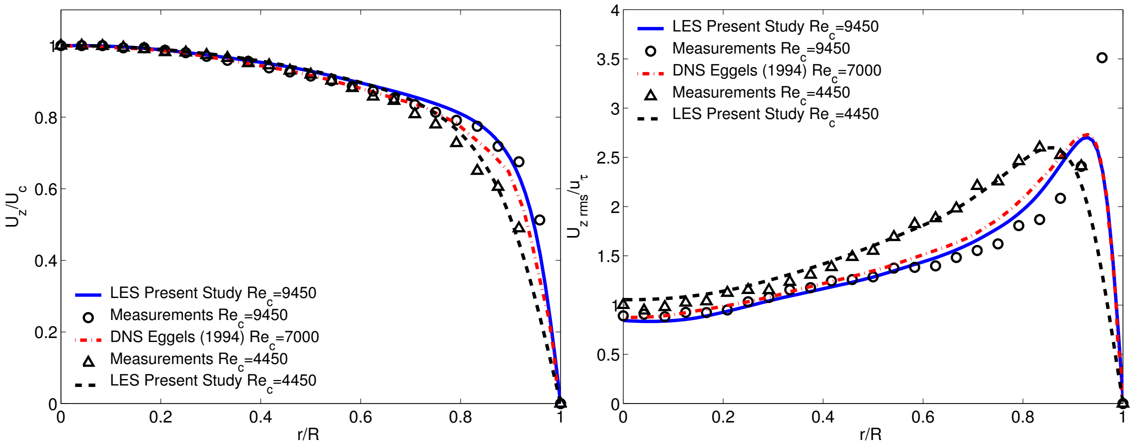

Figure 4.4: Axial mean velocity U_z normalized by the centreline velocity U_c and root-mean-square velocity fluctuation $u_{z\,rms}$ normalized by the wall friction velocity u_τ. Measurements refer to the experiment of Özcan and Larsen [77].

From Figure 4.4 it is seen that the experimental mean velocity profiles are well reproduced by LES computations in both pipe center- and near wall- region. Also it is observed that the DNS profile lies as expected between the Re_c for $R = 1.3$ and Re_c for $R = 3.3$ profiles - referred to as $Re_{c_{R=1.3}}$ and $Re_{c_{R=3.3}}$ in the following, which is in agreement with findings of den Toonder and Nieuwstadt [23].

In the case of streamwise RMS velocity component $u_{z\,rms}$, Figure 4.4 shows that the experimental profiles are reasonably reproduced by the LES. For $Re_{c_{R=1.3}} = 4450$ the agreement between LES and measurements is very good in all parts of the domain. For $Re_{c_{R=3.3}} = 9450$ the measured values are slightly overpredicted by LES in region $r/R > 0.6$, and the disagreement becomes most pronounced for the measurement point closest to the wall. From Figure 4.4 it is seen further that the DNS profile closely follows the LES profile for $Re_{c_{R=3.3}}$, indicating peek values virtually at the same position and showing similar behavior in the near-wall region.

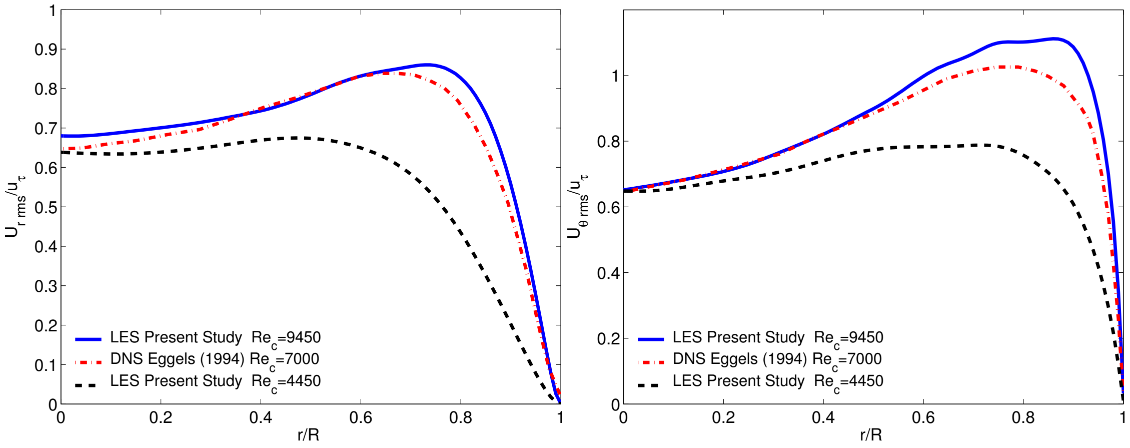

Figure 4.5: Root-mean-square velocity fluctuations $u_{r\,rms}$ and $u_{\theta\,rms}$ normalized by the wall friction velocity u_τ

A series of LDV measurements conducted by den Toonder and Nieuwstadt [23] showed that the peak magnitude and its position in the $u_{z\,rms}/u_\tau$ profile (magnitude of app. 2.75) are virtually independent of the Reynolds number in a range $4900 \leq Re_m \leq 24600$ where Re_m is based on the bulk velocity. Figure 4.4 shows that LES and DNS results here confirm this behavior. Findings of den Toonder and Nieuwstadt [23] indicate further that general disagreement between LES (DNS) and measurements can probably be attributed to a problem with the measurements of Özcan and Larsen [77] in the near wall region, as the corresponding Re_m for $R = 3.3$ i.e. $Re_{m_{R=3.3}} = 7200$ in this case.

Figure 4.5 shows the RMS profiles of radial $u_{r\,rms}$ and azimuthal $u_{\theta\,rms}$ velocity fluctuations normalized by u_τ. The direct measurements of those quantities are not available.

Figure 4.5 illustrates a certain Re-number dependence of both $u_{r\,rms}$ and $u_{\theta\,rms}$ in the considered Re-number range. The same kind of Re-number dependence is reported by den Toonder and Nieuwstadt [23] in the case of radial velocity fluctuation, indicating that LES here computes reasonable profiles of those statistical quantities as well.

Spatially Developing Boundary Layer Flow

Generating inflow data for the case of a spatially developing boundary layer flow is more complex and involved than the previously described pipe flow case. The main difficulty in this type of simulation emerges from the fact that the mean flow is evolving in the streamwise direction, making the use of periodic boundary conditions unfeasible. Therefore a different approach has to be adopted.

A detailed description of different methods which can be used for generation of suitable inflow boundary conditions for LES calculations can be found in e.g. Johansson and Andersson [44]. A short description of various methods for generating inflow data for the case of spatially developing boundary layers can be found in Sagaut [90]. Two of the methods described in [90] are of special interest (Lund et al. [62] and Spille-Kohoff and Kaltenbach [104]) as the numerical test conducted utilizing them proved to efficiently reproduce the targeted boundary layer flow.

In the context of this work the method of Lund et al. [62] is implemented in the *EllipSys3D* code and used for the precursor simulations of the boundary layer flow. The ideas behind this method will be briefly outlined in the following part.

The method's first step consists of decomposing the instantaneous flow field as a sum of mean and a fluctuating part i.e.:

$$u_i'(x, y, z, t) = u_i(x, y, z, t) - U_i(x, z), \tag{4.3}$$

where x, y and z are the streamwise, spanwise and wall-normal directions respectively. Note that the spatial averaging in the spanwise direction is implicitly included in the flow-decomposition process.

Utilizing a well-known boundary layer theory (see e.g. Hinze [39]) the mean streamwise velocity profile at the inlet boundary can be determined from the mean velocity profile at the recycle plane position. Dividing the mean streamwise velocity profile into the inner boundary layer (BL) region part, governed by the law of the wall theory and the outer BL region part, governed by defect law theory one gets:

Law-of-the wall

$$U^{inner} = u_\tau(x)\, f_1(z^+), \tag{4.4}$$

Defect-law

$$U_\infty - U^{outer} = u_\tau(x)\, f_2(\eta), \tag{4.5}$$

where $u_\tau = \sqrt{\nu\, \partial u/\partial z|_{wall}}$ is the friction velocity, $z^+ = \frac{u_\tau z}{\nu}$, $\eta = \frac{z}{\delta}$, δ is the boundary layer thickness, U_∞ is the free-stream velocity and f_1, f_2 are two universal functions to be determined. According to the mentioned scaling laws, the streamwise mean velocities at the recycling- and inlet- position are related in the following way:

$$U^{inner}_{inlet} = \gamma U_{recycle}(z^+_{inlet}), \tag{4.6}$$

$$U^{outer}_{inlet} = \gamma U_{recycle}(\eta_{inlet}) + (1-\gamma)\, U_\infty, \tag{4.7}$$

with $\gamma = \frac{u_{\tau,\, inlet}}{u_{\tau,\, recycle}}$. z^+ and η are evaluated at the inlet plane, while $U_{recycle}(\eta_{inlet})$ and $U_{recycle}(z^+_{inlet})$ are computed at the recycle-plane position. A direct linear interpolation has been applied for calculating the grid points between the two planes.

Similarly, utilizing the same technique the mean wall-normal velocity component can be expressed as:

$$W^{inner} = U_\infty\, f_3(z^+) \Rightarrow W^{inner}_{inlet} = W_{recycle}(z^+_{inlet}), \tag{4.8}$$

$$W^{outer} = U_\infty\, f_4(\eta) \Rightarrow W^{outer}_{inlet} = W_{recycle}(\eta_{inlet}), \tag{4.9}$$

where f_3, f_4 are two universal functions determined in the same way as before. The spanwise velocity component should be zero in mean; hence no mean spanwise velocity rescaling is necessary.

In the next step, the fluctuating velocity components are rescaled according to the following expressions:

$$\left(u'_i\right)_{inner} = u_\tau(x)\, g_i(x,\, y,\, z^+,\, t) \Rightarrow \left(u'_i\right)^{inlet}_{inner} = \gamma\, \left(u'_i\right)_{recycle}(y,\, z^+_{inlet},\, t) \tag{4.10}$$

$$\left(u'_i\right)_{outer} = u_\tau(x)\, h_i(x,\, y,\, \eta,\, t) \Rightarrow \left(u'_i\right)^{inlet}_{outer} = \gamma\, \left(u'_i\right)_{recycle}(y,\, \eta_{inlet},\, t) \tag{4.11}$$

where g_i and h_i are approximately homogeneous (periodic) functions in the streamwise x direction, as the streamwise inhomogeneity is isolated in the explicit determination of u_τ.

The last step now consists of prescribing a composite profile for the complete instantaneous velocity at the inlet plane, through the weighted average of the inner and outer profiles:

$$(u_i)_{inlet} = \left[U^{inner}_{inlet} + \left(u'_i\right)^{inlet}_{inner}\right](1-\Pi(\eta_{inlet})) + \left[U^{outer}_{inlet} + \left(u'_i\right)^{inlet}_{outer}\right]\Pi(\eta_{inlet}), \tag{4.12}$$

where weighting function $\Pi(\eta)$ is defined as:

$$\Pi(\eta) = \frac{1}{2}\left\{1 + \tanh\left[\frac{\alpha\,(\eta - b)}{(1-2\,b)\;\eta + b}\right] / \tanh\,(\alpha)\right\}, \tag{4.13}$$

and $\alpha = 4$ and $b = 0.2$.

The rescaling process involves specification (knowledge) of two parameters - δ and u_τ, at inlet- and recycle- plane position. In general they can be directly computed at the recycle-plane position, assuming the proper averaged quantities are available at that position. But the computation of averaged quantities is an integral part of the whole recycling procedure, i.e. the velocity decomposition relies upon it etc. and those quantities become available only after the long initial computational phase has been completed. To find a suitable way to circumvent this, a series of trial-and-error based computations was conducted. Computations showed that the best results are achieved by specifying a δ value at the inlet followed by use of a well-known power-low approximation for obtaining the δ value at the recycling position, while u_τ at the recycle-plane position is directly computed and the same power-low approximation is used to obtain a proper value for u_τ at the inlet. In this way the recycling parameters are partially directly specified from the beginning of the computations and partially dynamically adjusted throughout the computation process.

A contour plot of the streamwise velocity U at the inlet- and recycle- plane, showing the basic set-up of the described method, is presented in Figure 4.6. From the Figure it can be observed how the structures from the recycle-plane are slightly "*compressed*" by the Lund et al.'s method and reintroduced at the inlet boundary. Figure 4.6 illustrates also the position of the recycle-plane in the computational domain. The recycle-plane is placed in the vicinity of the outflow boundary, sufficiently far from the latter in order to avoid any outflow boundary (convective/zero-gradient) related errors.

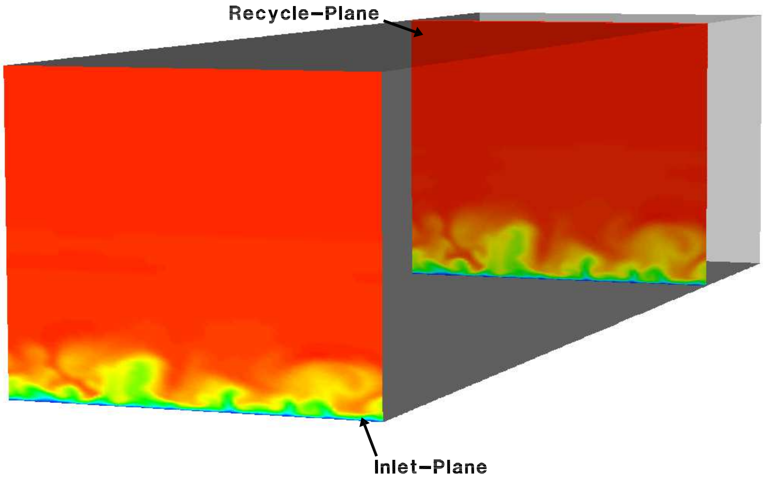

Figure 4.6: Contour plot of the instantaneous streamwise velocity U at the inlet- and recycle-plane. Grey surfaces represent the domain boundaries.

The described BL rescaling procedure introduces a sort of spurious coupling in the computed solution through the described quasi-periodical recycling process (see e.g. [44, 90]). A way to diminish this coupling is to use a domain of a sufficient streamwise extent, which allows the largest structures to be enclosed by a domain before recycling takes place (here $L_x = 18\,\delta_0$ is used). An even better way to eliminate the mentioned coupling is to split the computations into two phases. In the first phase the computations are conducted in the described way and an instantaneous flow realization at a plane with a lower δ value than targeted is saved in a database. In the second phase this database is used as a valid inflow condition for the computation of the boundary layer flow, from where the data are extracted to a new database based on targeted values for δ and u_τ. This procedure is utilized in the present work.

The targeted boundary layer parameters used to characterize the investigated flow are listed in Table 4.2, where δ^* is the displacement- , δ is the boundary layer- and θ is the momentum-thickness.

u_τ	δ_0^*	δ_0	θ_0	$Re_{\delta^*} = \frac{U_{duct}\,\delta^*}{\nu}$	$Re_{\delta^*,1} = \frac{u_\tau\,\delta^*}{\nu}$	$Re_\theta = \frac{U_{duct}\,\theta}{\nu}$
$0.07\,m/s$	$10.8\,mm$	$70\,mm$	$7.7\,mm$	1080	327	770

Table 4.2: Targeted boundary layer parameters

The computational grid used in the calculations consists of 192 x 96 x 96 cells in streamwise, spanwise and wall-normal direction respectively, while the domain extensions are specified as $L_x \,\mathrm{x}\, L_y \,\mathrm{x}\, L_z = 18\,\delta_0 \,\mathrm{x}\, 4\delta_0 \,\mathrm{x}\, 3.5\delta_0$. The cells are equally distributed in x and y directions, while a stretching function is used in the wall-normal z direction. The stretching function used here is a modified version of the function described by equation (3.1). The used function gives $1.2 \leq \Delta z^+ \leq 20$ in region $z < 2\ \delta_0$ and 7 grid points within $z^+ < 10$, with the first point at $z^+ = 0.62$. The dimensionless distances in x and y directions are $\Delta x^+ = 28$ and $\Delta y^+ = 14$ respectively.

Thereby, the requirements for well-resolved LES in a wall bounded flows, already discussed in Section 3.3, seem to be well fulfilled for the flow case investigated here. The general computational details are analogous to ones previously described in the pipe flow case. The only difference, besides using inflow/outflow BC conditions instead of the periodical ones, is utilization of the QUICK scheme for the convective term in N-S equations, which turned out to be necessary in order to stabilize the calculations.

It should be noted that the domain sizes in spanwise and wall-normal directions are predetermined by the chosen geometry of the JICF computational set-up. The streamwise domain extent is chosen in order to diminish the spurious coupling in the computed solution to $L_x = 18\,\delta_0$. Previous, similar investigations (Lund et al. [62]) showed that even smaller domain length of $L_x = 10\,\delta_0$ can provide satisfactory results.

Figure 4.7 shows the results obtained by LES simulation of a spatially developing boundary layer compared to available measurements from Özcan and Larsen [77] and well-known DNS database of Spalart [102]. The DNS data are included here in order to have an additional result-reference on one hand and on the other hand in order to illustrate the effects of Re_θ based flow dependence. Moreover it should be emphasized, that LES has been performed in a way that the mass flow rate was kept constant and equal to a mass flow rate determined by integration of the experimentally obtained mean streamwise velocity profile of Özcan and Larsen [77]. This approach is used in order to properly control the governing parameters in the JICF simulation.

The results from Figure 4.7 can be generally classified as typical LES results for the wall-bounded flows, where by controlling the mass flow rate, the friction velocity u_τ becomes under-predicted, streamwise velocity fluctuations u_{rms} (Figure 4.7(c)) in the wall region becomes over-predicted and the spanwise - v_{rms} (Figure 4.7(d)) and wall-normal- w_{rms} (Figure 4.7(e)) fluctuations become under-predicted, when LES is compared to DNS[3] data.

Considering the non-dimensional mean velocity profiles (Figures 4.7(a) and (b)) it can be seen that measurements are slightly over-predicted by LES (Figure 4.7(a)) in a region $0.4 \leq z/\delta_0 \leq 0.8$, but the under-prediction of the LES computed u_τ leads to a distinct over-predictions of measurements in the outer BL region (Figure 4.7(b)), when the profiles are compared in wall-unit coordinates. The inner BL region seems to be well-reproduced by the LES results.

---

[3] Figure 4.7 illustrates that the Re_θ- number dependence in interval $670 \leq Re_\theta \leq 1410$ causes only minor changes in the profile shapes for the velocity fluctuations.

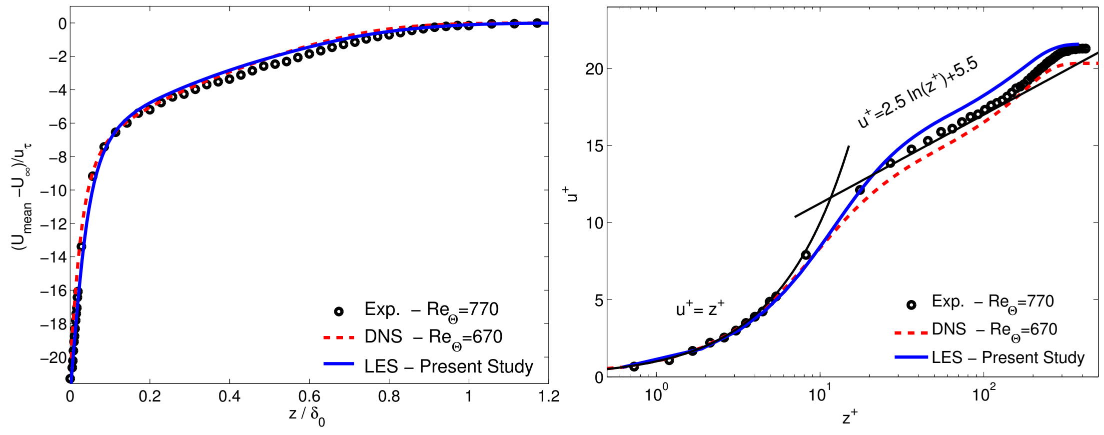

(a) U_{mean} (b) u^+

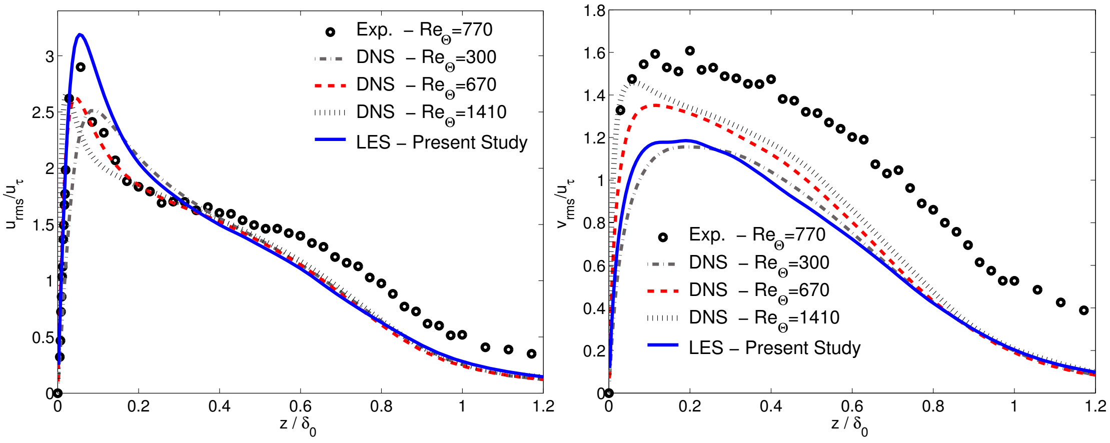

(c) u_{rms} (d) v_{rms}

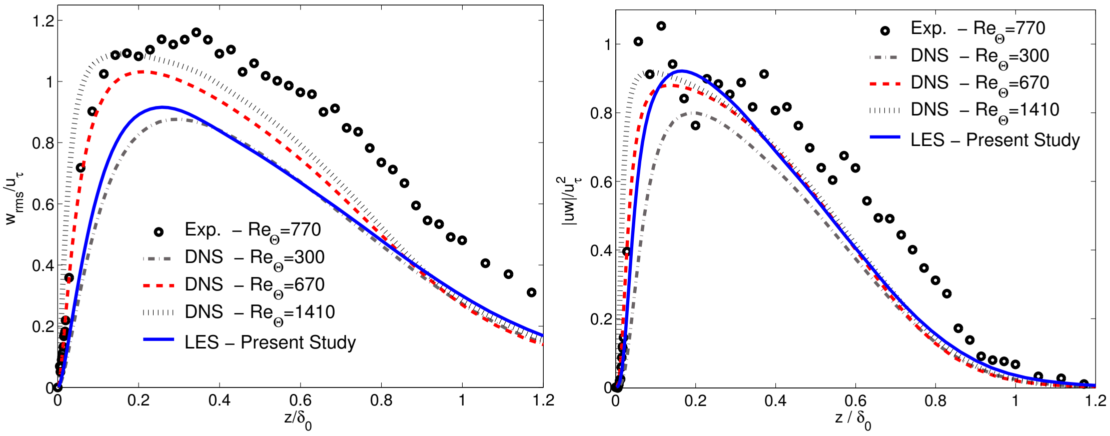

(e) w_{rms} (f) $\overline{uw}$

Figure 4.7: Streamwise mean velocity U normalized by the centerline velocity U_∞ and the wall friction velocity u_τ, and root-mean-square velocity fluctuations u_{rms}, v_{rms}, w_{rms} and shear stress $\overline{uw}$ normalized by the wall friction velocity u_τ

Comparing the available measurements with the DNS data, one can observe some distinct differences in the profiles of normal Reynolds stresses and the non-zero Reynolds shear-stress. DNS profiles presented for three different Re_θ can give an idea of profile-shape changes caused by the increase in Re_θ. It is observed that measurements do not follow this concept as a constant overshoot in v_{rms} and w_{rms} profiles is evident from Figure 4.7 while u_{rms} and $\overline{uw}$ profiles actually deviate significantly in shape from corresponding DNS (LES) profiles. Some of the observed dissimilarities can probably be related to the determination of a skin-friction velocity or possibly to the procedure of artificial enhancement of the turbulent BL utilized in the experiments of Özcan and Larsen [77].

A sufficient refinement of a grid utilized in LES will eventually lead to the presented DNS results. Considering the differences between the measurements and DNS, it is concluded that this procedure generally will not improve the overall agreement between the computations and experimental results. Therefore, the author feels confident that the presented LES boundary layer simulation can be assumed as satisfactory and correspondingly used as a suitable basis for the final JICF computations.

4.4 Validation

As stated earlier, one of the objectives of this study is to explore and compare the flow dynamics of the computationally and experimentally obtained JICF fields, while another one is based on the establishment of a clear general analogy between the LES computed results and experiment. An important step in accomplishing both of these objectives is achieved by insuring that the agreement between numerically and experimentally obtained flow fields, on the level of mean-flow statistical quantities, is satisfactory.

Therefore, the computations are validated against the experimentally obtained (LDA) measurements of mean flow quantities of Özcan and Larsen [77] on the symmetry ($y/D = 0$ - see Figure 4.3 on page 38) plane. It should be noted for the sake of completeness, that experimental data are partially available on 4 other planes - $z/D = [0.17,\ 1.3,\ 3.0]$ and $x/D = 2.4$. It is however chosen only to compare datasets on the symmetry plane, as the experimental data on these 4 planes are only available as contour plots, so only qualitative comparisons between computations and experiment can be made. Besides that, the initial comparisons of results on these planes showed similar tendencies as ones based on data sets from $y/D = 0$ plane (to be presented in the following) and therefore are not included in this report.

On the other hand, during the course of this JICF study different SGS models were utilized in the computations, different discretization schemes were used, different positions of inflow and outflow boundaries in the computational domain were considered etc.. In spite of the considerable number of computations on the correspondingly adjusted numerical setups, the calculated results showed no decisive/distinct differences, when compared against the experimental data, and for the sake of brevity, only the representative computational set is included in the main rapport. A numerical study involving comparisons of 14 different computations/cases, where influence of various numerical parameters on the obtained results was investigated, can be found in Appendix A. Based on this analysis the representative computational case is chosen (case LES 6 from Appendix A) and subsequently included in this report.

On the following Figures 4.8 and 4.9 vertical profiles of streamwise (U) and wall-normal (W) velocity components and the corresponding r.m.s fluctuations are presented. The shear stress component uw and the spanwise velocity fluctuation v_{rms} are shown on Figure 4.10. The results are presented for 16 different streamwise x/D stations in the symmetry plane[4]. Note that velocities, r.m.s. fluctuations and shear stress are rescaled with an appropriate factor on many subfigures in order to accommodate a better comparison basis between LES results and experiment. The scale is adjusted at the first four ($x/D = [-1.00,\ -0.83,\ -0.67,\ -0.5]$) positions in the case of mean wall-normal velocity W, the first three positions ($x/D = [-1.00,\ -0.83,\ -0.67]$) are adjusted in the case of the r.m.s fluctuations and uw shear stress, while only the first position ($x/D = -0.67$) is adjusted in the case of v_{rms} velocity fluctuation. As an extension of the presented profile comparisons, in Figures 4.12 and 4.13 the mean streamwise and wall-normal velocity contours and contours of velocity fluctuations and shear-stress at the symmetry plane are presented. Note that, subfigures on the left hand-side in Figures 4.12 and 4.13 are based on LDA measurements of Özcan and Larsen [77], while subfigures on the opposite side are calculated based on LES computations. Thereby, both qualitative and quantitative assessment of the computed LES results vs. LDA measurements can be established.

---

[4] v_{rms} profiles are presented for 5 streamwise locations, where the measurements are available.

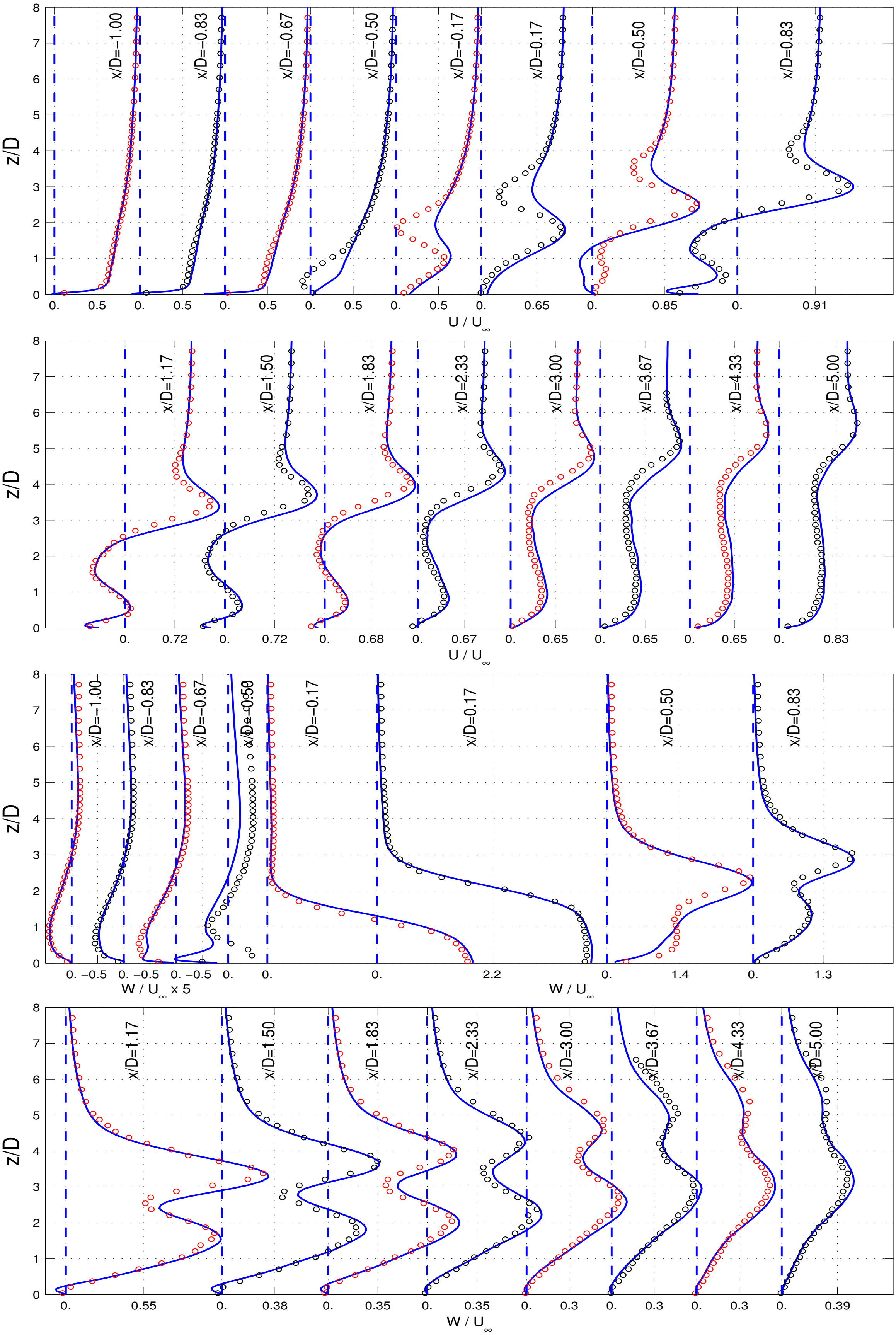

Figure 4.8: U/U_∞ and W/U_∞ for $R = 3.3$ case, at $y/D = 0$ plane. Solid lines - LES computations, open circles - Özcan and Larsen [77].

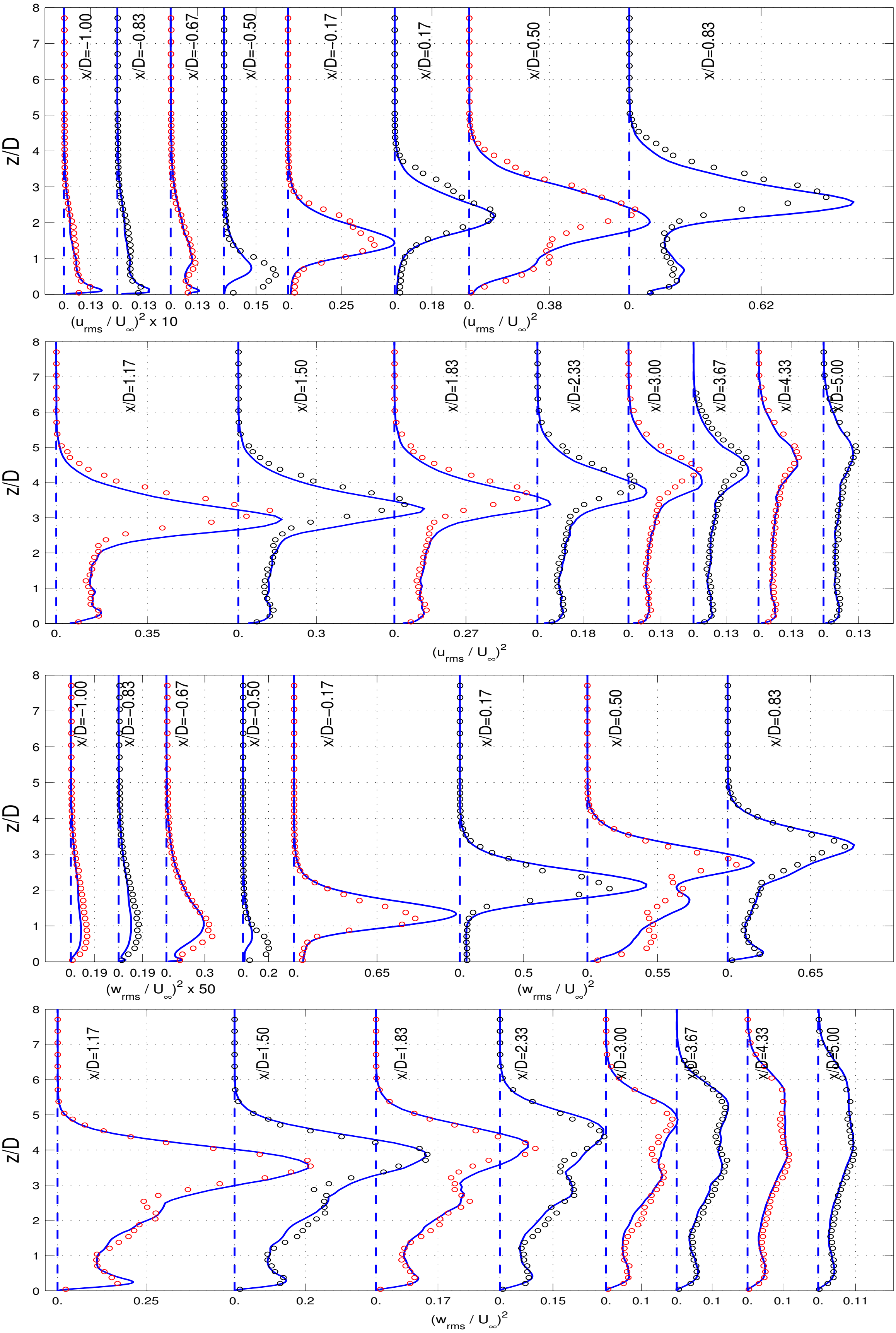

Figure 4.9: $(u_{rms}/U_\infty)^2$ and $(w_{rms}/U_\infty)^2$ for $R = 3.3$ case, at $y/D = 0$ plane. Solid lines - LES computations, open circles - Özcan and Larsen [77].

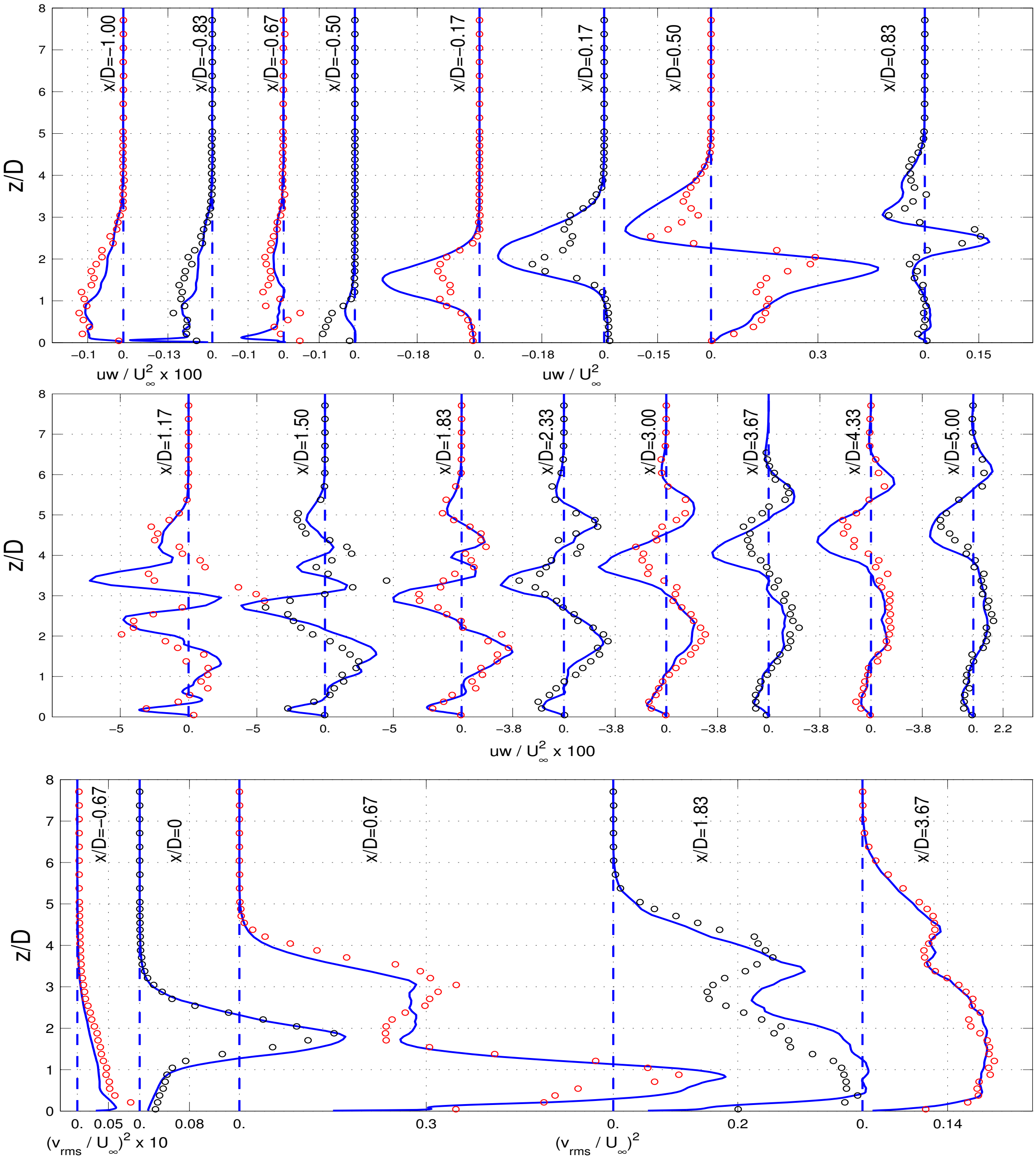

Figure 4.10: $(v_{rms}/U_\infty)^2$ and uw/U_∞^2 for $R = 3.3$ case, at $y/D = 0$ plane. Solid lines - LES computations, open circles - Özcan and Larsen [77].

Considering the overall agreement between LES and measurements, it can be concluded that LES is quite capable of capturing almost all flow features revealed by the experiment. However some differences do exist.

The most distinct difference can be observed in the case of streamwise velocity component in the '*jet exhaustion*' area - $-0.5 \leq x/D \leq 0.5$, Figure 4.8 - upper part. Here, LES is clearly producing gradient magnitudes in the U-velocity profile considerably smaller than ones given by the measurements. Actually, this discrepancy appeared in all conducted calculations and was the driving force behind several grid refinement investigations, inflow/outflow boundary position studies etc. - but none of those changes in the computational setup quantitatively improved the agreement between LES and experiment (see Appendix A). Considering the contour plots of U-velocity in Figure 4.12(a) and (b) it becomes clear, that difference between profile shapes observed in Figure 4.8 is a direct consequence of different form of the upstream jet-to-cross-flow interface revealed by LES and experiment.

While LDA measurements reveal some clear traces of shear-layer loop-like vortical structures along the jet-to-cross-flow interface (Figure 4.12(a) - region $-1 \leq x/D \leq 0$, $0 \leq z/D \leq 3$) the same is not true for the LES calculated contours. Evidently, a low-velocity pockets visible on the Figure 4.12(a) in the mentioned area are the main cause of the distinct gradients in the measured U-velocity profiles observed in the Figure 4.8.

As the main reason for the inability of LES to produce a distinct flow feature is generally connected to an insufficient grid resolution, several computations with grids of up to 15 mill. cells in size were conducted aiming, among other tings, to investigate the observed disagreement. As seen from e.g. Figure A.9 in Appendix A, none of those computations were able to produce better agreements with the measurements in the mentioned region. In Appendix A, an estimate of grid resolution quality in form of comparison of the local grid size Δ and the Kolmogorov length scale η (Figures A.19, A.20) is also shown indicating (see e.g. Frohlich et al. [31]) that already a grid of app. 4.7 mill. cells should be quite capable of producing reliable results.

Besides LDA measurements, a set of PIV measurements, aimed to investigate the flow dynamics in the JICF flow field have been conducted on the same experimental set-up. The results, comparing LES computations vs. LDA and PIV measurements are shown in Figure 4.11. It should be noted that LES- and LDA- data are obtained at $x/D = 0$ position, while the PIV measured data are available at $x/D = -0.05$ position. Inspecting the Figure 4.8 again, it is evident that LDA measurements have a considerable second (negative) peak in all velocity profiles in the area $-0.5 \leq x/D \leq 0.5$ so a direct comparison of PIV, LES and LDA can be assumed appropriate even thought the PIV measurement position is not completely aligned with LES and LDA positions. It is noted furthermore that the LDA measurement method is generally accepted as providing more reliable mean flow statistical data than PIV

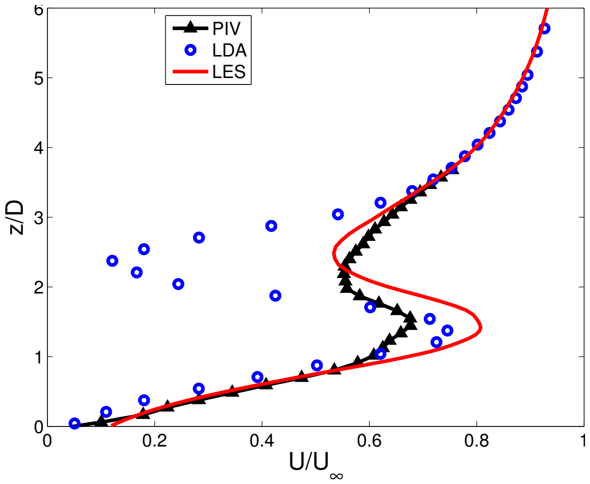

Figure 4.11: U/U_∞ for $R = 3.3$ case, at $x/D = 0$ position in the $y/D = 0$ plane. Solid line - LES computations, open circles - LDA measurements of Özcan and Larsen [77], filled triangles - PIV measurements of Meyer et al. [70].

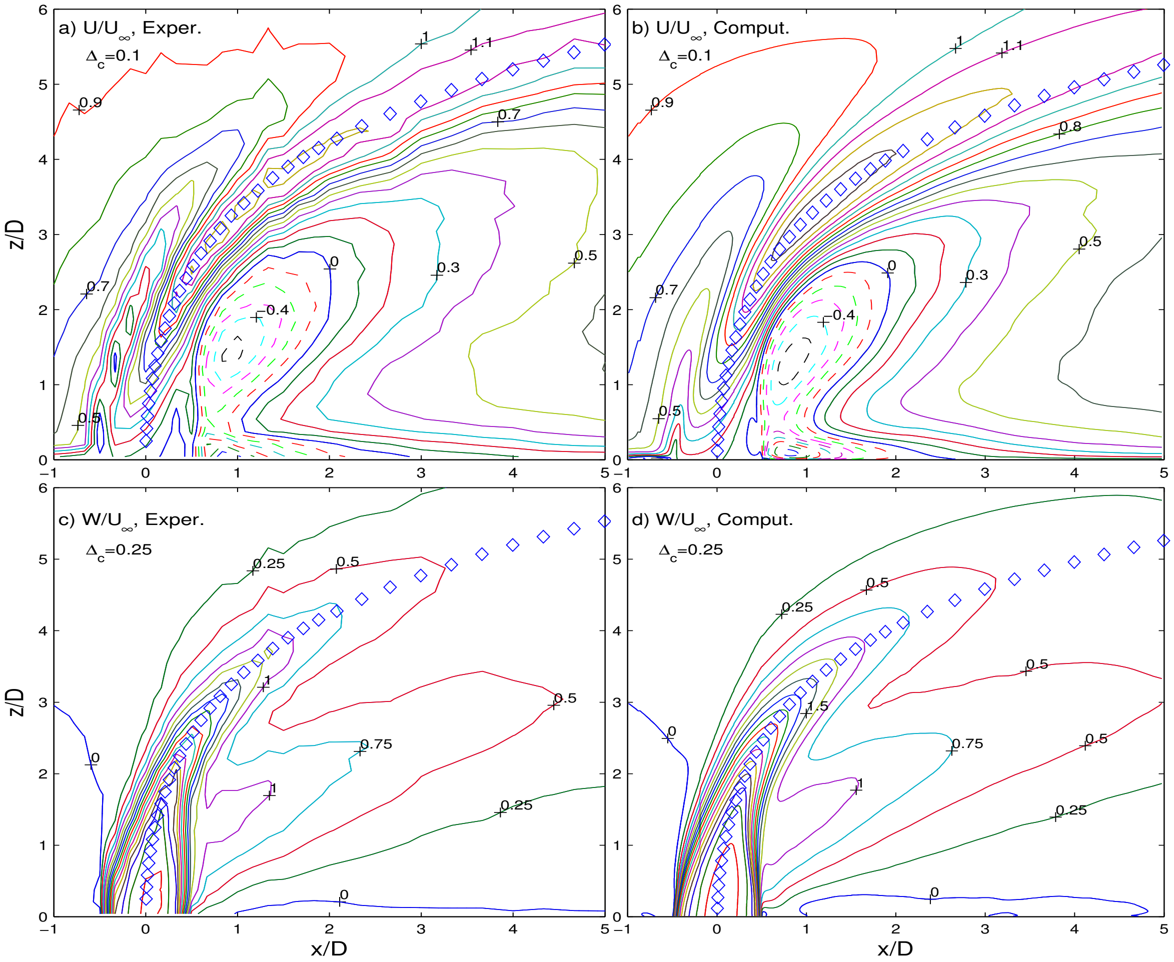

Figure 4.12: U/U_∞, W/U_∞ for $R = 3.3$ case, at $y/D = 0$ plane. Subfigures (a) and (c) are experimentally determined, while subfigures (b) and (d) are based on LES computations. Curves depicted by the same color in comparable subfigures (i.e. (a) - (b), etc.) represent the same contour level. Dashed lines represent negative contour levels. Δ_c refers to difference between plotted contour levels. Diamonds depict jet trajectories, estimated as mean streamlines emerging from the point $x/D = z/D = 0$ in the symmetry plane following the definition of Yuan et al. [117].

measurements, due to the limited resolution capabilities and a certain area averaging of the measured quantities implicit to the PIV method.

Figure 4.11 indicates clearly, that LES and PIV agree much better on the magnitude of the second peak in the U-velocity profile and shows furthermore very significant disagreement between PIV and LDA measurements for the streamwise velocity profiles. A private communication with Prof. Özcan, who was in charge of the LDA measurements and participated in obtaining the PIV data, did not reveal the reason for the observed discrepancies. It showed however that LDA measurements were repeated several times on different occasions, leading always to the profiles presented in this report. Considering the results of Yuan et al. [117] obtained for the same jet-to-cross-flow velocity ratio (cross-flow in their study was however laminar) reveals no traces of shear-layer vortices in the contour plot of the streamwise velocity component (Figure 21 in their paper) either. Generally, the shear-layer vortices are considered to be intrinsically unsteady (Fric and Roshko [30]) and subsequently they typically do not have a mean flow definition.

Therefore the observed differences do not necessarily reflect an inability of LES computations to capture a distinct flow feature, but according to the results presented in Figure 4.11, can as well be connected to a possible biasing or seeding error/problem in LDA measurements.

The U-velocity profile at $x/D = 0.5$ (Figure 4.8 the uppermost subfigure) shows an additional disagreement between LDA and LES in the near-wall jet exit area. Here, LES profile indicates that recirculating zone created on the jet lee side (clearly visible for profiles $0.83 \leq x/D \leq 1.83$) is entraining the jet, while LDA measurements show no negative streamwise velocities at this position. Again all LES runs showed the same tendency at this position (see Appendix A).

LDA and LES U-velocity profiles, at positions $1.83 \leq x/D \leq 3.67$ show a slight disagreement in the area $3 \leq z/D \leq 5$, i.e. after the second (negative) velocity peak. This discrepancy proved to be directly connected to the numerically achieved jet-to-cross-flow velocity ratio R. A detailed explanation on how the numerical velocity ratio is determined is provided in Appendix A. On Figures A.12-A.14 (cases LES 6, 10 and 11) in Appendix A the results obtained from an investigation of a moderate change in the numerical velocity ratio are presented. It can be seen that the result-agreements between cases LES 11 ($R = 3.61$), LES 10 ($R = 3.41$) and measurements in this particular region are somewhat improved compared to the LES 6 case, but result-disagreements in other areas (the most of the W-velocity profiles) for those cases are also obvious from Figure A.12. It is seen furthermore that best overall agreements with the measurements are obtained for the case LES 6. This clearly indicates that an ideal numerical velocity ratio, which will fit the measured profiles in all regions, is practically impossible to obtain on the utilized numerical set-up leading to the conclusion that a certain basic difference in the numerical and experimental flow set-up do exist. The observed result-disagreements in region $1.83 \leq x/D \leq 3.67$ become much more pronounced in the velocity ratio case of $R = 1.3$ (to be discussed in the following) indicating that differences in the state of the boundary layer at inflow, between measurements and precursor computations, may play a significant role here (see Section 4.3). From Figures A.12-A.14, especially from comparisons of jet trajectories in Figure A.14 in Appendix A, it can be seen that the synthetic jet flow calculated by LES behaves in an expected manner (note the change in slope of the computed jet trajectories, which corresponds to the velocity ratio increase) pointing out that upper wind-tunnel boundary condition chosen (as symmetry or slip-wall boundary) for LES does not influence the calculated results significantly, and can be assumed to reasonably reflect the experimental conditions at this position (discussed previously in paragraph 4.3). Note that jet-trajectories presented in Appendix A are estimated as mean streamlines emerging from the point $x/D = z/D = 0$ in the symmetry plane following the definition of Yuan et al. [117].

LDA and LES W-velocity profiles in Figure 4.8 show a quite good agreement. Some differences can however be observed at $x/D = \pm 0.5$, and can have a similar basis as discussed in the case of U-velocity profiles. On the other hand the measured and calculated profiles show a very good agreement throughout the jet body, compared to the same positions in the U-profiles. Profiles of u_{rms} and w_{rms} velocity fluctuations (Figure 4.9) illustrate similar tendencies. The jet-to-cross-flow velocity ratio sensitivity is most likely the reason for a slight over-prediction of u_{rms} values in $0.83 \leq x/D \leq 3.00$ and $2 \leq z/D \leq 5$ zone. The w_{rms} profile in the jet area shows a slight overshoot of the measured quantities. The v_{rms}-velocity profile

(Figure 4.10) shows some disagreement in magnitude between the values predicted by LES and measurements at $x/D = 1.83$ (the measured profile shape is correctly predicted however).

This disagreement can, among other things, be connected to the uncertainty in the determination of the mean spanwise velocity (should be zero due to symmetry[5]). In Figures A.6-A.8 in Appendix A the results of case LES 7, which have the highest overall number of samples included into the statistics, are presented. In Figure A.14, the velocity ratio effect on the computed profiles at $x/D = 1.83$ position is illustrated. Accounting for the velocity ratio effect, from Figures A.6-A.8 it can be observed that general differences (including profile differences of v_{rms} fluctuations) between results of cases LES 6 (presented here) and 7 are comparatively small, indicating that further increase in the number of samples included into the statistics will generally not improve the agreement between computed and measured v_{rms} profile at this position. Results from the mentioned Figures indicate furthermore that the convergence levels of the presented statistics (case LES 6) can be assumed as satisfactory.

uw shear stress profiles illustrate similar trends (Figure 4.10) as U-velocity profiles. Again in the jet exhaustion zone $-0.5 \leq x/D \leq 0.5$ some significant differences between LES and measurements are visible. This is the only case where trends in the LES predicted profiles are substantially different from the measured ones, as the three peak structure at $x/D = \pm 0.17$, and four peak structure in the measured uw shear stress profile at $x/D = 0.5$ position is evidently not reproduced by LES. As previously discussed, general disagreement between LES and LDA exist in this zone at same vertical positions in the case of the mean streamwise velocity. So the observed differences in the uw shear stress profiles are most likely directly connected to the differences in U-profiles. In other areas, the profile shapes are correctly reproduced by LES, although at some positions the disagreements in magnitude are present.

Generally it should be noted that LES agrees well with the experiment in the most part of the upstream jet region, both with regards to mean velocities and turbulence quantities. However some disagreements, like flow deceleration in vertical velocity component (at $x/D = -0.67$, near wall-region) computed by LES and not visible in measurements, do exist. The general impression is that the turbulent inflow boundary condition used, reasonably resembles the experimental flow state, despite some of the differences observed and commented previously in this section and section 4.3.2.

Examining the contours of streamwise and wall-normal velocities, presented in Figure 4.12, it can be observed that LES captures and reproduces the experimental flow structure well. The main difference, as previously discussed, is at the upper jet-to-cross-flow interface. The shape and size of the recirculating zone existing on the jet lee-side and consisting of two areas - one directly adjacent to the main jet body and the other in the vicinity of the wall is well reproduced. Actually a small pocket of the negative streamwise velocity entraining the main jet body in the near wall area is also visible on LES based contour plots in Figure 4.12(b) - see Figure 4.8, $x/D = 0.5$. Considering the overall structure of the streamwise velocity contours, it is evident that LES contours are more '*compressed*' in $x/D > 2$ and $z/D < 4$ (jet lee-side) area indicating a faster recovery of U-velocity in the wake zone. This indicates that simulated jet rises more slowly, compared to the experimental one. As shown in Appendix A, a better agreement between measured and computed jet trajectory, with the corresponding faster rise of the synthetic jet, can be obtained for the numerical velocity ratio of $R = 3.41$ (case LES 10) - see Figures A.12 - A.14, but results of the $R = 3.41$ case show some distinct disagreements with the measured profiles in other regions, indicating that the overall improvement of computational results vs. measurements is not obtained for

---

[5] This is only accomplished when the complete convergence of statistics is achieved

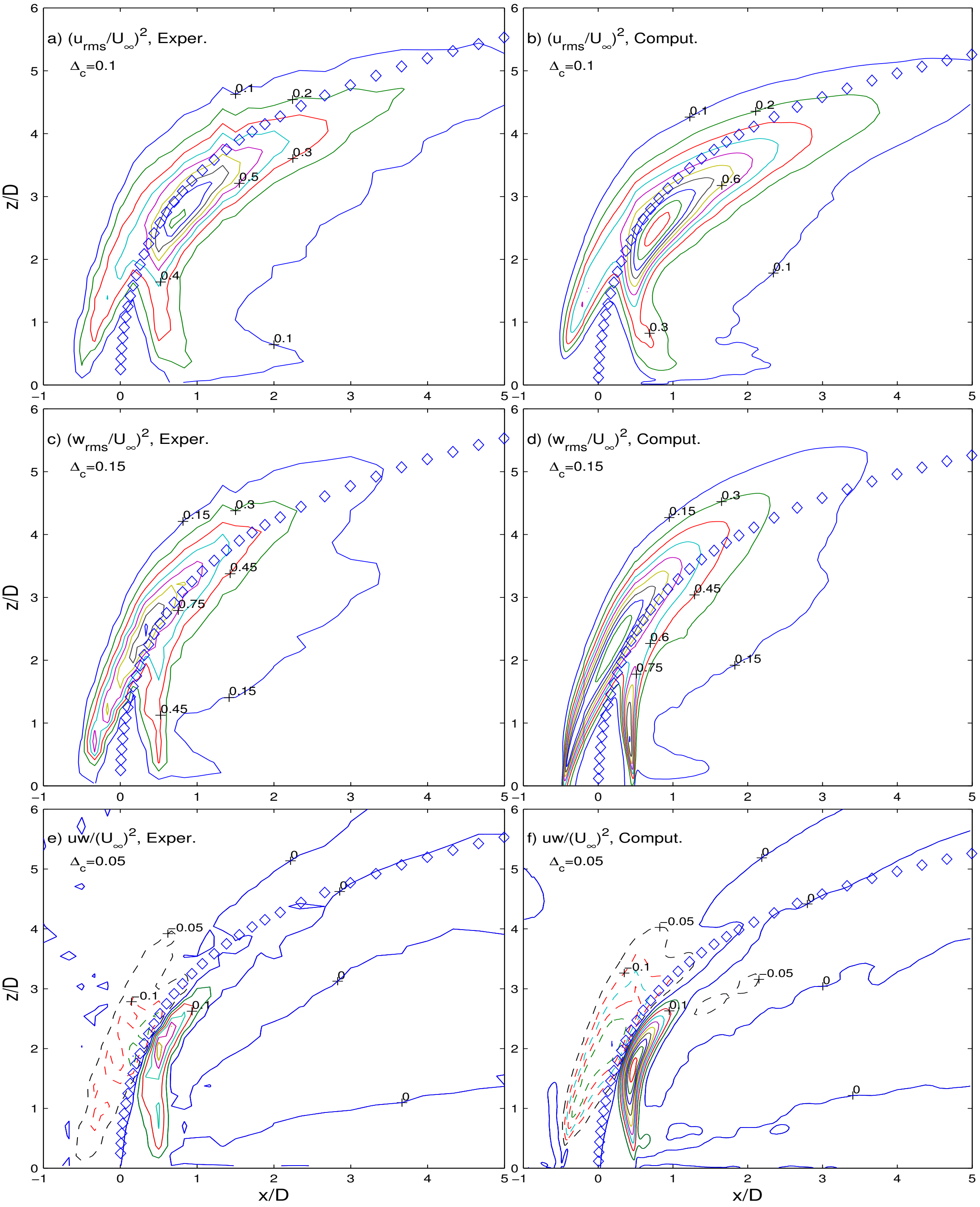

Figure 4.13: $(u_{rms}/U_\infty)^2$, $(w_{rms}/U_\infty)^2$ and uw/U_∞^2 for $R = 3.3$ case, at $y/D = 0$ plane. Subfigures (a), (c) and (e) are experimentally determined, while subfigures (b), (d) and (f) are based on LES computations. Curves depicted by the same color in comparable subfigures (i.e. (a) - (b), (c) - (d), etc.) represent the same contour level. Dashed lines represent negative contour levels. Δ_c refers to difference between plotted contour levels. Diamonds depict jet trajectories, estimated as previously following the definition of Yuan et al. [117].

this numerical velocity ratio. Similar observation concerning agreements of numerical and computational results can be made by examination of the wall-normal velocity contours in the symmetry plane - Figure 4.12(c) and (d). All contour shapes are correctly reproduced by LES, but it is evident that the simulated jet is bending more rapidly in the area above the position of the mean jet trajectory, while the entrainment of the wall-normal velocity on the jet lee-side spans over a wider zone - i.e. opposite to the behavior of the streamwise velocity component. Comparing the results of Yuan et al. [117] (Figure 21 and 22 in their article) with the present study, it can be seen that the recovery of streamwise velocity is even more rapid and the entrainment of the vertical velocity spans over even wider zone on the jet lee-side in the flow case of Yuan et al. [117], compared to present LES and specially LDA measurements. Accounting for the fact that the boundary layer was laminar in Yuan et al.'s study, the overall influence of the general boundary layer state becomes apparent. As previously discussed, the experimentally achieved boundary layer showed some distinct differences, when compared to the present LES and DNS data of Spalart [102]. This can again lead to the conclusion that the observed differences in general boundary layer state may contribute significantly to the mentioned disagreements.

Examining now contour plots of r.m.s. velocity fluctuations and uw shear stress depicted on Figure 4.13, a good qualitative agreement between measurements and computations can again be observed. From Figure 4.13 it is evident that LES based contours are revealing much more detailed description of the turbulence quantities throughout the considered part of the flow field, so a direct comparison other than the general one, is therefore difficult. However, the position of main zones existing in the measured contours can easily be identified on the corresponding LES subfigures.

LES results and LDA measurements, compared above for the case of jet-to-cross-flow velocity ratio of $R = 3.3$, proved that a good qualitative and quantitative agreement between computations and experiment exist. It showed that LES undoubtedly is capable of capturing the main mean flow features revealed by the experiment, indicating that the simulated flow should also be able to capture more dynamically accentuated flow features, i.e. vortical structures. Those characteristic vortical structures are examined in greater detail in the following paragraphs.

Before proceeding further, a similar comparison of mean flow properties, for the case of a lower jet-to-cross-flow velocity ratio of $R = 1.3$ is presented. Gathered experience from the $R = 3.3$ velocity ratio case was in a way directly transferred to this $R = 1.3$ case, so only a limited number of computations was performed here. However, some initial tests showed even more pronounced differences between measurements and computations than encountered previously in the $R = 3.3$ case, which necessitated a velocity ratio sensitivity study presented in Appendix B. Based on comparisons of the obtained results presented in Appendix B, the computational set presented here is chosen. The structure of the material presented in the following is the same as previously described for the higher velocity ratio flow, so the presented results in Figures 4.14 - 4.17 correspond to results in Figures 4.8 - 4.13. As many of the relevant flow features are the same across the investigated velocity ratios, only the instances where some additional differences are observed will be discussed in the following.

Examining the U-velocity profiles in Figure 4.14, it is seen that the pronounced difference between LES and measurements in the *'jet exhaustion'* zone $-0.5 \leq x/D \leq 0.5$ does not occur in the case of the lower velocity ratio. However, a noteworthy difference in the peak

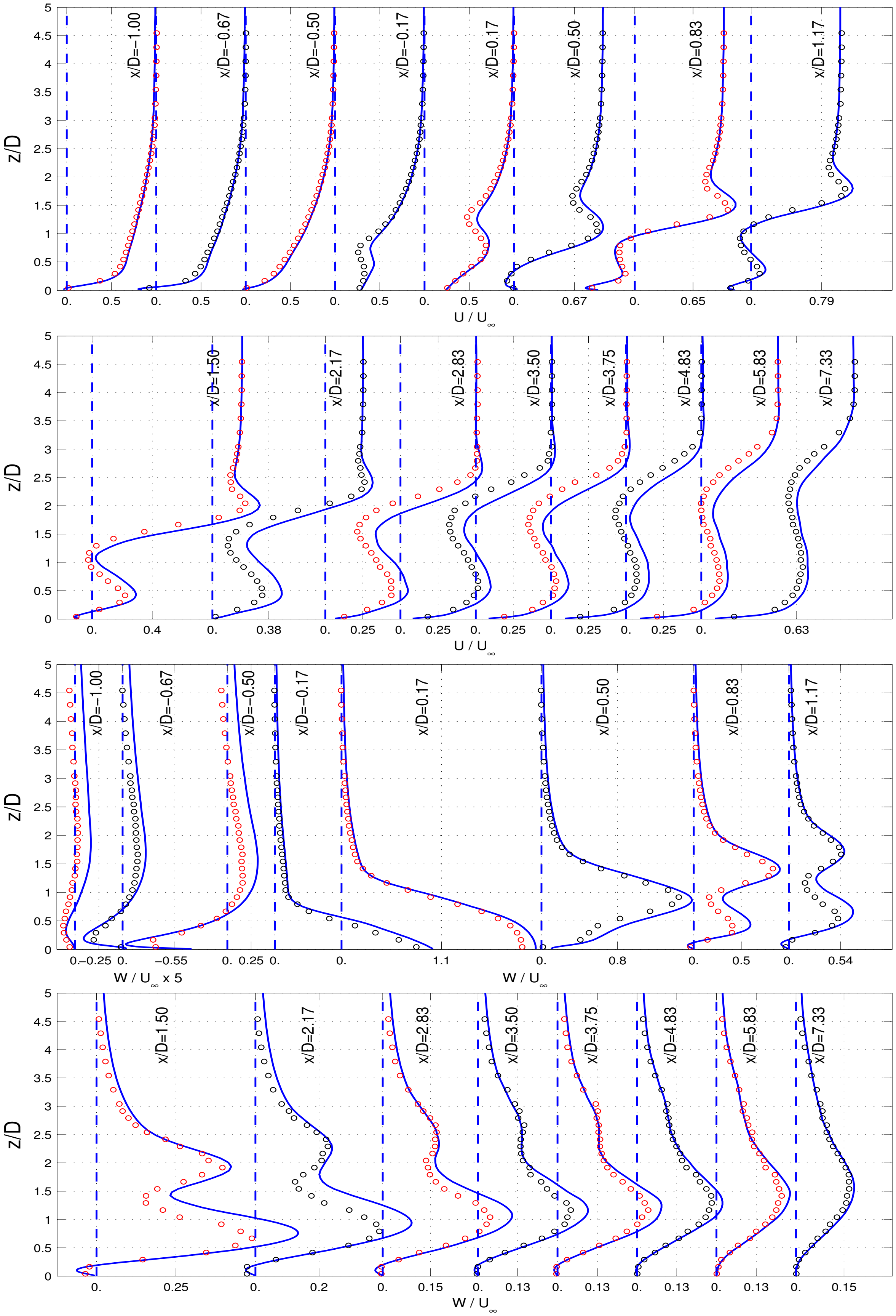

Figure 4.14: U/U_∞ and W/U_∞ for $R = 1.3$ case, at $y/D = 0$ plane. Solid lines - LES computations, open circles - Özcan and Larsen [77].

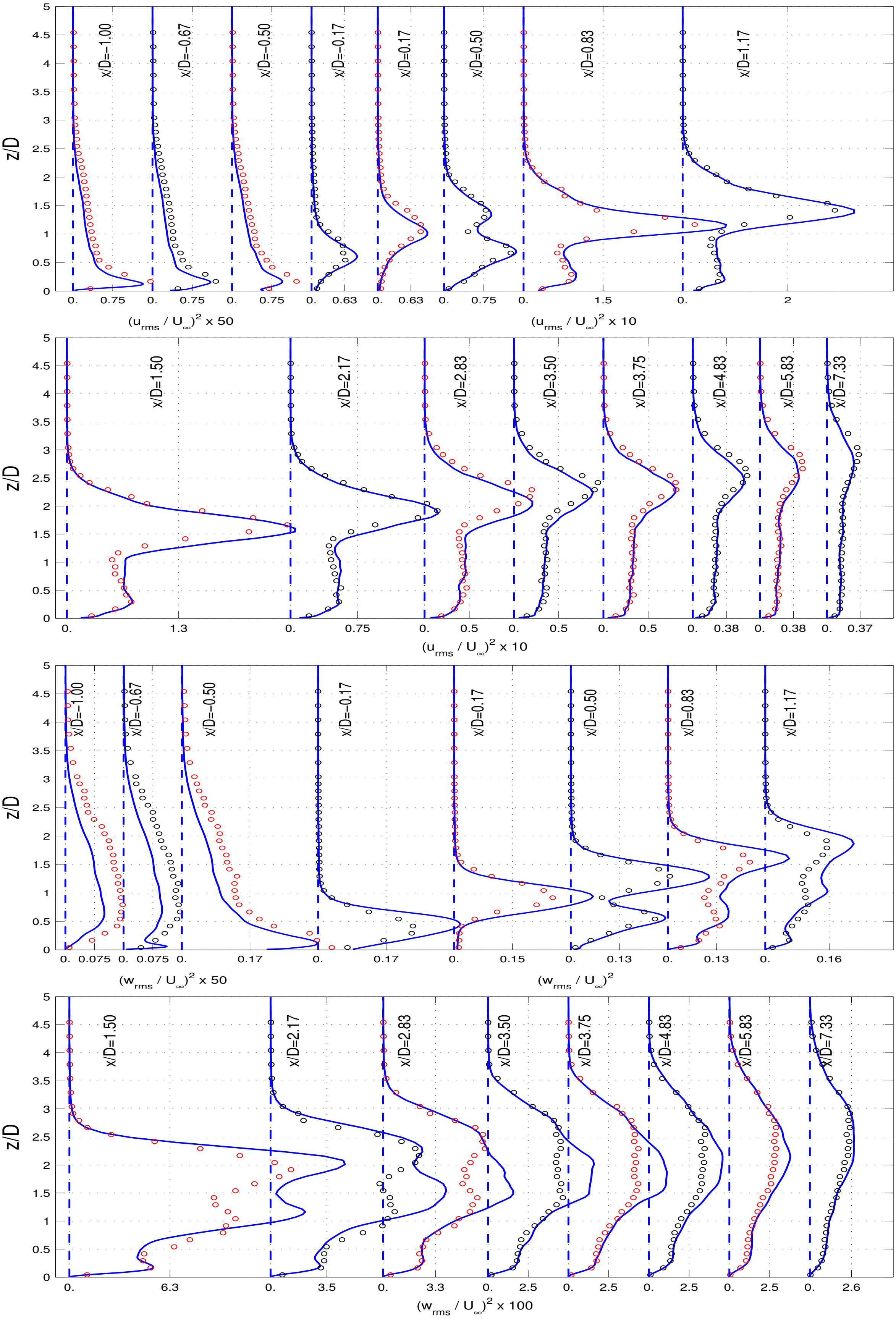

Figure 4.15: $(u_{rms}/U_\infty)^2$ and $(w_{rms}/U_\infty)^2$ for $R = 1.3$ case, at $y/D = 0$ plane. Solid lines - LES computations, open circles - Özcan and Larsen [77].

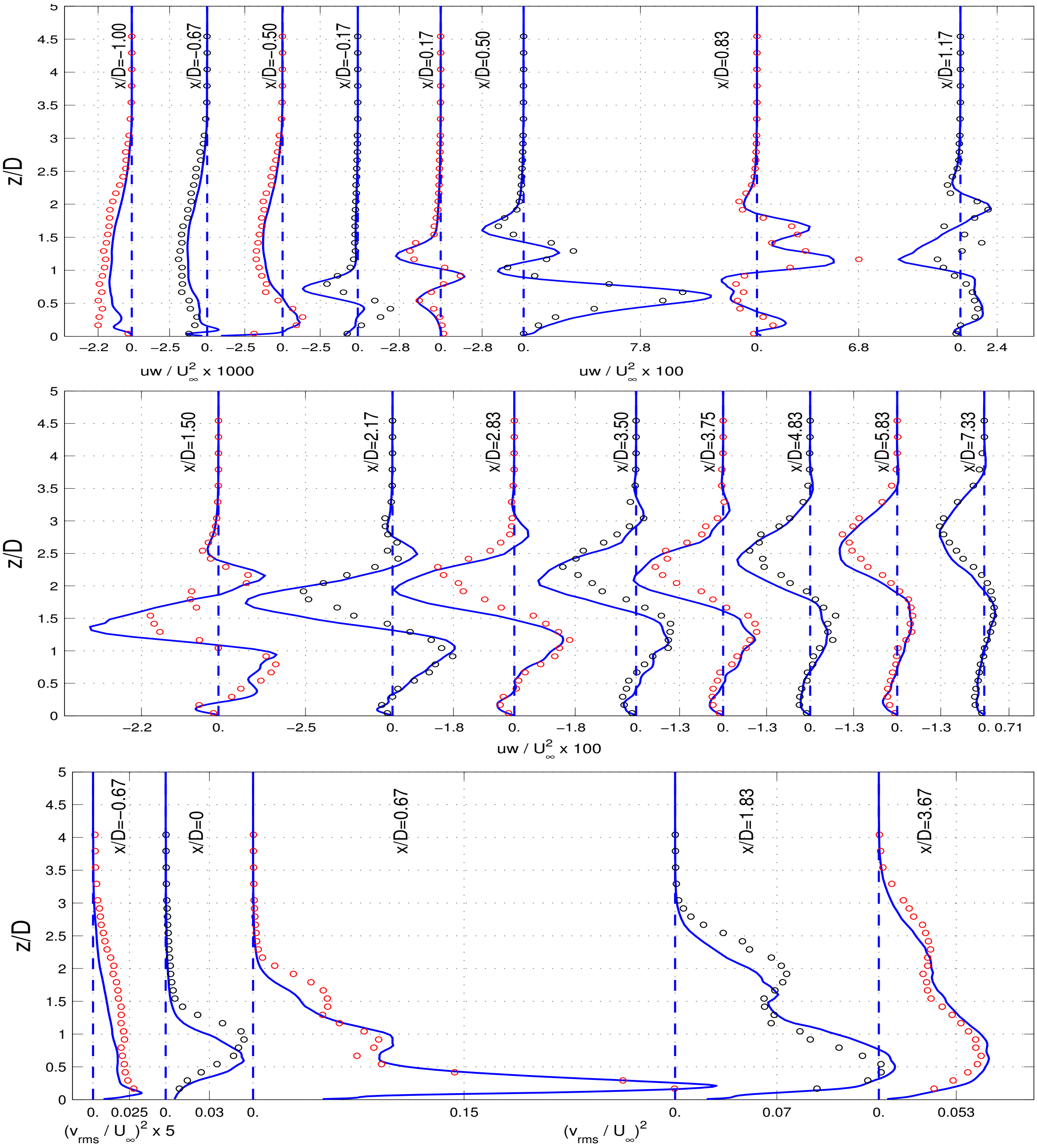

Figure 4.16: $(v_{rms}/U_\infty)^2$ and uw/U_∞^2 for $R = 1.3$ case, at $y/D = 0$ plane. Solid lines - LES computations, open circles - Özcan and Larsen [77].

magnitude at $x/D = \pm 0.17$ positions is still present. A major discrepancy between LES and experiment in this case actually occurs in the wake region, namely for profiles in the $2.17 \le x/D \le 7.83$ zone. Here, clear overpredictions of the measured streamwise velocities are visible, while the shapes of the computed profiles resemble the measured data well.

The same is true for the vertical velocity component. Clear overpredictions of the first peak in the W-velocity profiles followed by underpredictions of the subsequent velocity minima are visible in Figure 4.14. However, this behavior starts and ends a bit earlier; it starts at

$x/D = 0.83$ and diminishes significantly from $x/D > 4.83$ onward, compared to the U-velocity component.

A velocity ratio sensitivity study presented in Appendix B indicates even more clearly than in the $R = 3.3$ case, that an ideal numerical velocity ratio, which will match the measured profiles in all regions, can not be found on the present LES flow set-up. This study showed that the best fit with the measured quantities is obtained for the numerical velocity ratio of $R = 1.45$.

As indicated in experimental study of Gopalan et al. [35], the structure of the wake region is conceptually different for velocity ratios $R < 2$, compared to $R > 2$ cases. Gopalan et al. observed that in case of $R < 2$, the vorticity in the wake region is mainly supplied from the jet shear layer and no traces of the wake- vortices were found, i.e. contrary to findings of Fric and Roshko [30] for $2 < R < 10$.

It was previously underlined that some distinct differences in the computed and measured wind tunnel boundary layer flow exist. Influence of the oncoming boundary layer flow have in this lower velocity ratio case comparably larger effect on the resultant flow field than in the $R = 3.3$ case.

From results of Gopalan et al.'s study one can deduce that even small differences in basic configurations used to obtain a low velocity ratio JICF flow can impact the resultant flow field significantly. Therefore the observed differences in mean velocity profiles are most probably associated with the outlined basic differences between the numerical and experimental flow configurations utilized in obtaining the presently investigated JICF flow.

A distinct difference in the computed and measured w_{rms} fluctuation component can be observed from Figure 4.15 in region $x/D \geq 2.17$. Here, a difference in profile shapes is evident. A similar discrepancy in profile shapes was only observed in the $R = 3.3$ case for the uw shear stress. As previously, it is here assumed that the observed differences are directly linked to the mentioned discrepancies in the mean (W-) velocity profiles.

uw shear stress and u_{rms}, v_{rms} profiles of velocity fluctuations in Figures 4.15, 4.16 and contour plots presented in Figure 4.17 underline a good overall agreement between computations and measurements.

Generally, results presented in this section show that LES predicted mean flow quantities are in good agreement with their experimentally obtained counterparts. The observed differences are mostly related to discrepancies in magnitudes at various positions in the considered $y/D = 0$ plane, whereas in only two cases the distinct difference in the predicted and measured profile shapes was observed.

Considerable numerical effort was particularly focused on the higher velocity ratio - $R = 3.3$ case. Computed results proved to be very sensitive to even minor changes in the general computational flow set-up and on the other hand uncertainties in both the computationally and experimentally obtained results (see Appendix A) could not be assumed as negligible. Therefore despite the considerable numerical effort, the observed disagreements in results at certain locations, between LDA measurements and the present LES study, could not be improved.

On the lower velocity ratio case only a smaller amount of the computational time was used. As the numerical setup was unchanged across the computed velocity ratios, i.e. grid size, domain extension etc., it was expected to obtain even better agreements with the measurements here,

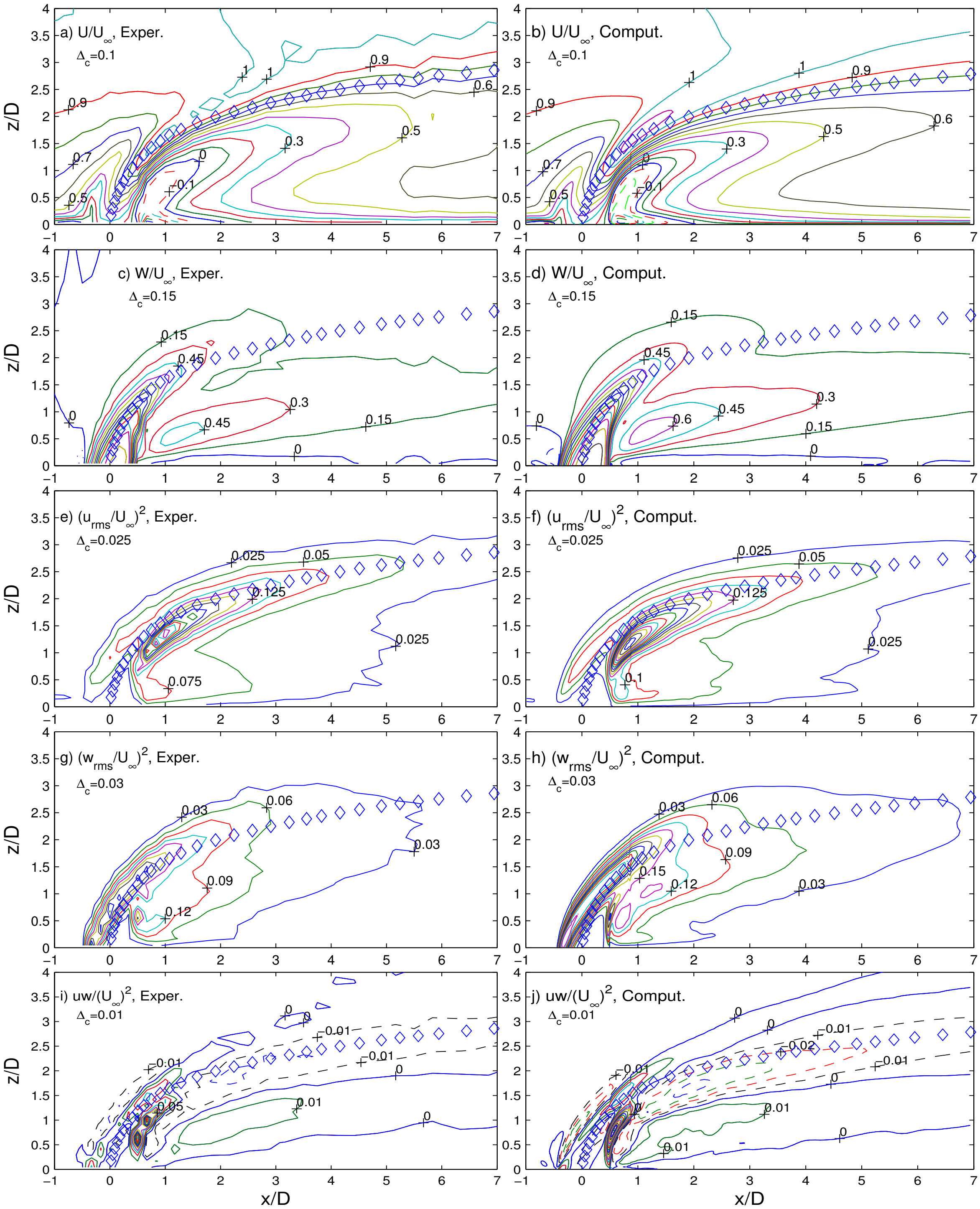

Figure 4.17: U/U_∞, W/U_∞, $(u_{rms}/U_\infty)^2$, $(w_{rms}/U_\infty)^2$ and uw/U_∞^2 for $R = 1.3$ case, at $y/D = 0$ plane. Subfigures (a), (c), (e), (g), (i) - Experiment and subfigures (b), (d), (f), (h), (j) - Computations. Coloring scheme - the same as one described on Figure 4.12. Δ_c refers to difference between plotted contour levels. Diamonds depict jet trajectories, estimated as previously following the definition of Yuan et al. [117].

but as the flowfield apparently goes through a transitional phase in the vicinity of the jet-to-cross-flow velocity ratio of $R = 2$ - Gopalan et al. [35], some basic differences between numerical and experimental flow configurations seem to have a significant impact on the corresponding agreements between experimental data and computational results, especially in the wake region.

Nevertheless, the presented LES results show that both simulated jets realistically represent the general JICF flow field.

In the following paragraphs some distinct features of the JICF flow field will be examined and identified. Even though some conceptual differences across compared velocity ratios were observed, the basic structure of the general JICF flow can be obtained by focusing on only one of the considered velocity ratios. As the main part of the experimental investigations of the flow dynamics of the JICF flow are available for the $R = 3.3$ case, it is chosen to examine this case in greater detail in the following paragraphs.

4.5 Coherent structures

Various experimental investigations of the JICF flow field conducted in the past showed that some distinct flow structures, which exist in a flow for a certain period of time and can be directly identified and followed throughout the flowfield, do exist in this complex flow. The mentioned structures are often referred to as coherent structures.

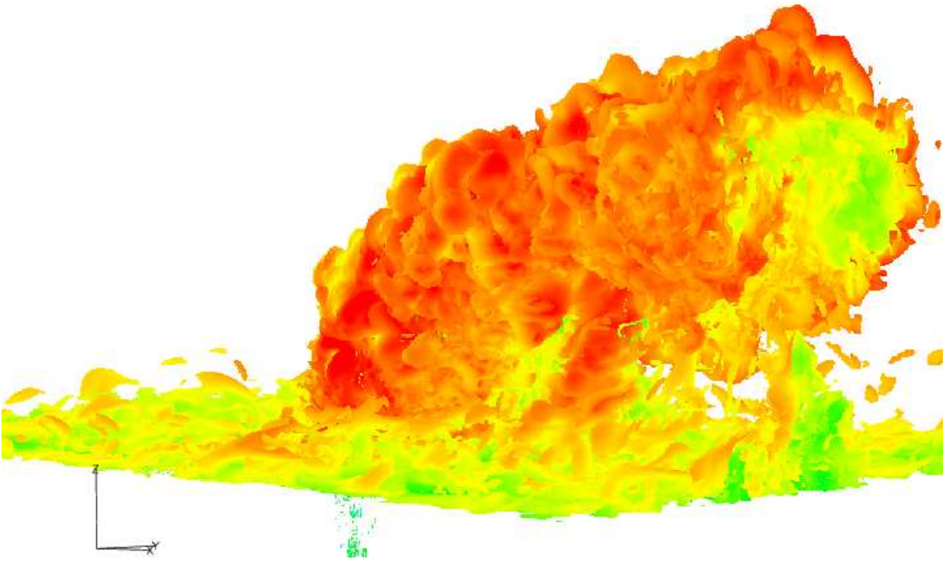

Figure 4.18: Iso-surface of the vorticity magnitude colored by the instantaneous streamwise velocity.

In the previous section it was shown that the numerically achieved JICF flow, both qualitatively and quantitatively resembles the mean flow properties of the corresponding experimental JICF flow case well, indicating that experimentally observed coherent structures should exist in the computationally obtained synthetic jet flow as well.

Identifying coherent structures is, on the other hand, a quite complex issue.

The basic way to identify a vortical structure is of course by examining the vorticity field (see Figure 4.18). Combining different components of the vorticity vector with iso-surfaces of the instantaneous pressure field can give some indication of the coherent structures in the JICF flow (see e.g. Yuan et al. [117]), but generally it is very difficult to isolate a specific flow structure in this way, and even separate the main flow structures from e.g. non-dominant vortical structures of the boundary layer flow. Considering the iso-surface of the vorticity magnitude shown in Figure 4.18, it is clear that some main flow structures of the JICF flow are revealed here. The basic jet structure is clearly visible and the shapes of the wake vortices can faintly be identified as well. But it is evident from Figure 4.18, that other distinguished characteristics of the JICF flow, like the horseshoe vortex-system, are deeply covered into the small-scale vortices of e.g. the cross-flow boundary layer.

Therefore in order to better identify the distinguished features of the JICF flow some other methods are used in the context of this work.

Many experimental investigators injected dye or smoke into the JICF flowfield in order to reveal the complex vortical structures of this flow. In this LES study, massless particles are seeded (injected) on two locations - one in the jet shear layer and the other in the cross-flow

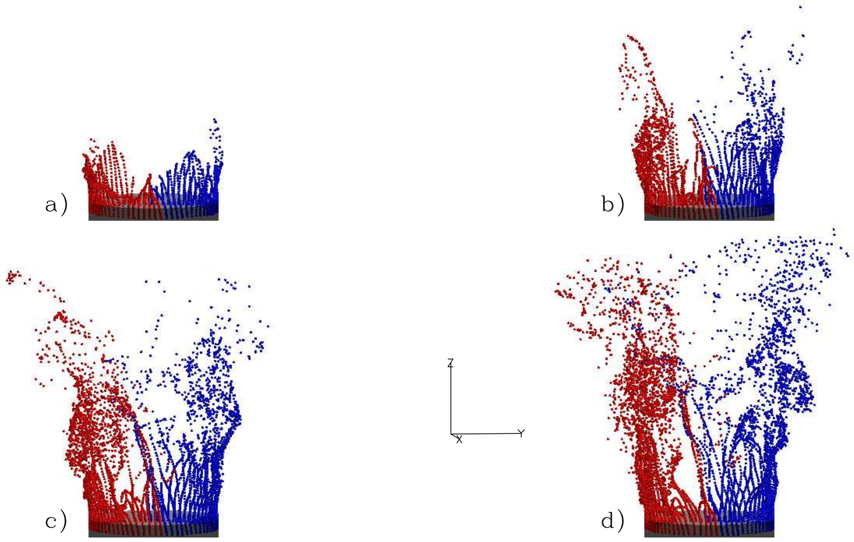

Figure 4.19: Structure of the Counter-Rotating Vortex Pair (CVP) build-up process depicted by instantaneous particle paths (streaklines) of massless particles - PART I. Coordinate system orientation shown in subfigure (d) is the same on all subfigures. Zero-point is placed in the jet center (see Figure 4.2 on page 37). Particles originating from $y < 0$ zone are depicted in red color, correspondingly particles originating from $y > 0$ zone are colored blue. Particle-seeding position is the jet shear-layer - at radial position of 0.49 D and vertical position of $z/D = -0.08$ and the time interval between subfigures is $\Delta t^* = \Delta t / (D/U_\infty) = 0.3125$.

boundary layer in order to obtain similar flow visualizations. The results of those visualizations are presented in the following Figures 4.19 - 4.23.

Figures 4.19 and 4.20 represent a series of instantaneous visualizations of the seeded massless particles. Particles are seeded in the jet shear-layer just beneath the jet entry point and the time difference between the shown frames is $\Delta t^* = 0.3125$. The Figure orientation for all subfigures is shown on subfigures 4.19(d) and 4.20(f) i.e. the jet direction is out of the paper; hence the jet is viewed from its lee side.

Following the movement of particles originating in the jet shear-layer one can actually follow the deformation process of the this cylindrical shear-layer and its roll-up into the counterrotating vortices. As the massless particles are seeded in the area where vorticity is generated it is assumed that they can reasonably depict vortical structures, at least in the jet-vicinity area and in the early stages of the flow development process.

Inspecting the mentioned series of visualizations the sense of creation and (counter) rotation of the CVP can almost be felt. It is clearly seen that particles originating on each lateral side of the cylindrical shear-layer contribute directly to the creation of one of the CVP rollers on the corresponding lateral edges.

It is seen furthermore that no sign of a vortex ring structure is visible on the jet lee side, whereas a clear two branch CVP structure is evident from those Figures. Inspecting closely, especially subfigures 4.20(b), (c) and (d), the sense of CVP counterrotation can be observed.

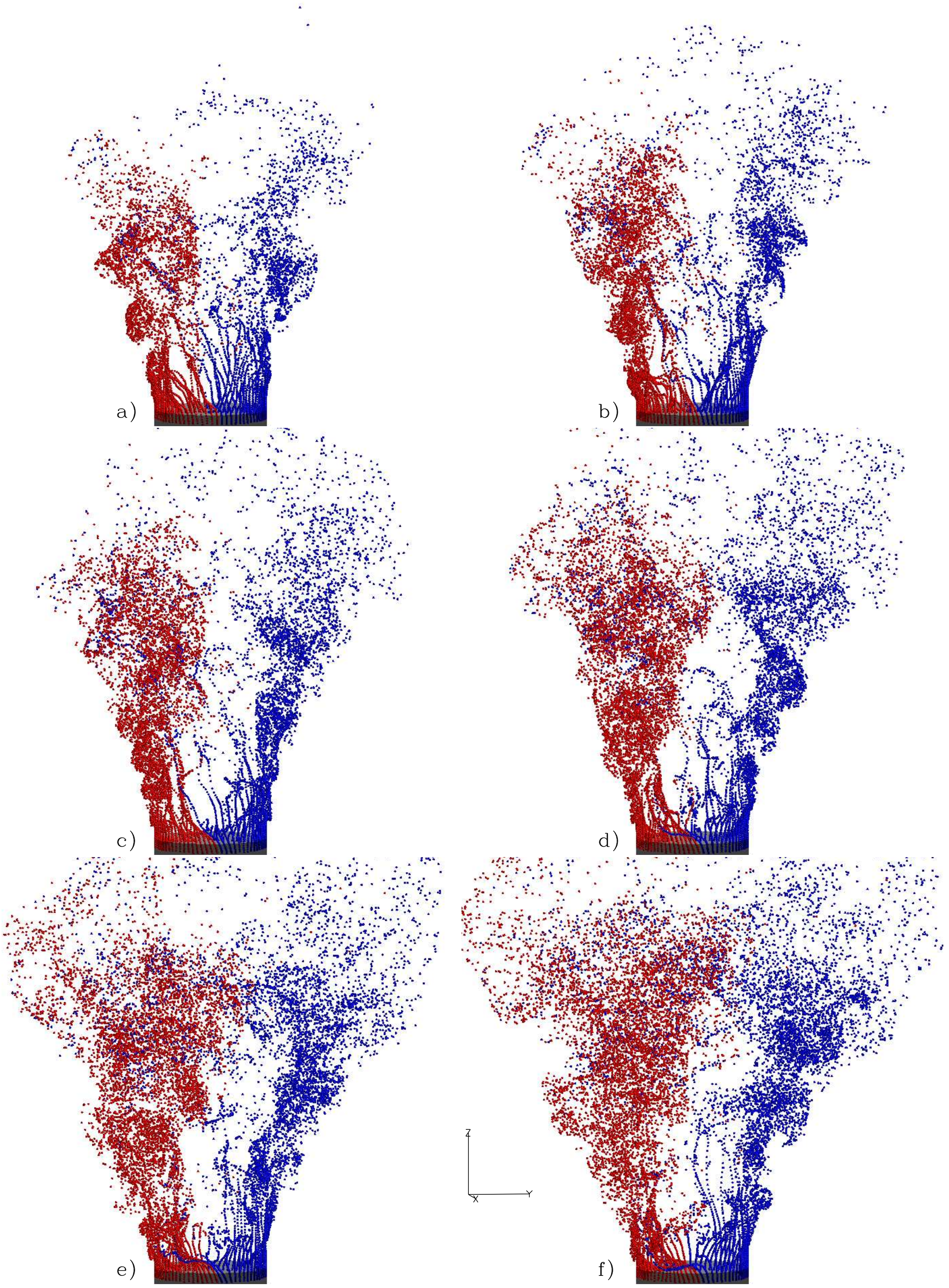

Figure 4.20: Structure of the Counter-Rotating Vortex Pair (CVP) build-up process depicted by instantaneous particle paths (streaklines) of massless particles - PART II. Coordinate system orientation shown in subfigure (f) is the same on all subfigures. For further description see the caption of Figure 4.19.

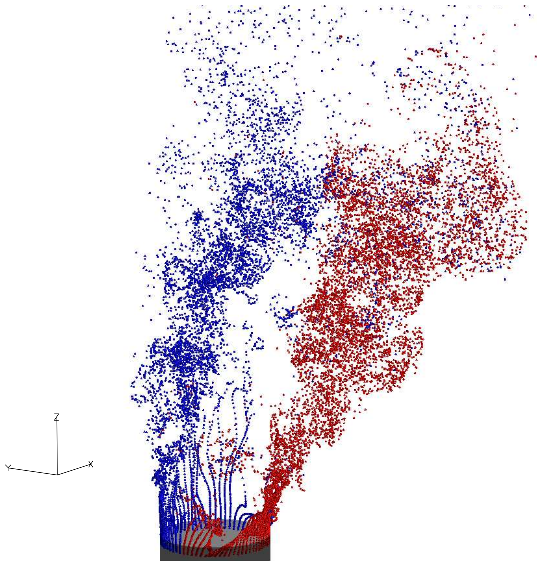

Figure 4.21: Structure of the Counter-Rotating Vortex Pair (CVP) depicted by instantaneous particle paths (streaklines) of massless particles. Particle paths shown correspond to paths presented in Figure 4.20(f) - here the coordinate system orientation is changed.

On the following subfigures 4.20(e) and (f) particles start the mixing process in the outer area, so following particle paths further downstream will only bring up a more blurred depictions of the flow field.

In Figure 4.21 a rotated view of particle paths presented in Figure 4.20(f) is shown. By inspecting the particle paths in this way some additional insight into the CVP creation process can be obtained. From this slightly rotated side view of the jet entrainment process one can follow paths of particles on the front side of the jet. Following those particle signatures it is seen that most particle paths originating from $y < 0$ side (depicted red in Figure 4.21) are quite swiftly turned directly into one branch of the CVP, while some of those particles (those facing the upstream jet area) follow the bended cylindrical jet shear-layer in the initial phase - forming the upstream loop-like roller, before they finally turn towards the corresponding branch of the CVP further downstream - see Figure 4.21.

The observations presented here agree quite well with recent experimental flow visualization study of Lim et al. [58]. Lim et al.'s study showed that cylindrical jet shear-layer, after emerging into the cross-flow, undergoes three distinct folding processes - one leading to creation of vortices on the upstream side of the jet, second creating vortices on the jet lee side and third creating two CVP branches on the lateral sides of the jet. This study confirmed that CVP creation process actually inhibits the formation of vortex ring structures known from the "*Free Jet*" flowfields.

The presented particle visualizations confirm at least two of Lim et al.'s observations - the upstream side vortices (Figure 4.21) and the CVP creation and fold-up process (Figure 4.19 and 4.20) in the investigated synthetic flow correspond well with Lim et al.'s (velocity ratio - $R \approx 4.4$) study. On the other hand, corresponding formation of lee-side vortices could not be directly confirmed in this way. It should be moreover noted that Yuan et al. [117] identified standing vortical structures on the lateral sides of the jet as hanging vortices. The present particle visualization confirms the existence of standing vortical structures reminiscent of the

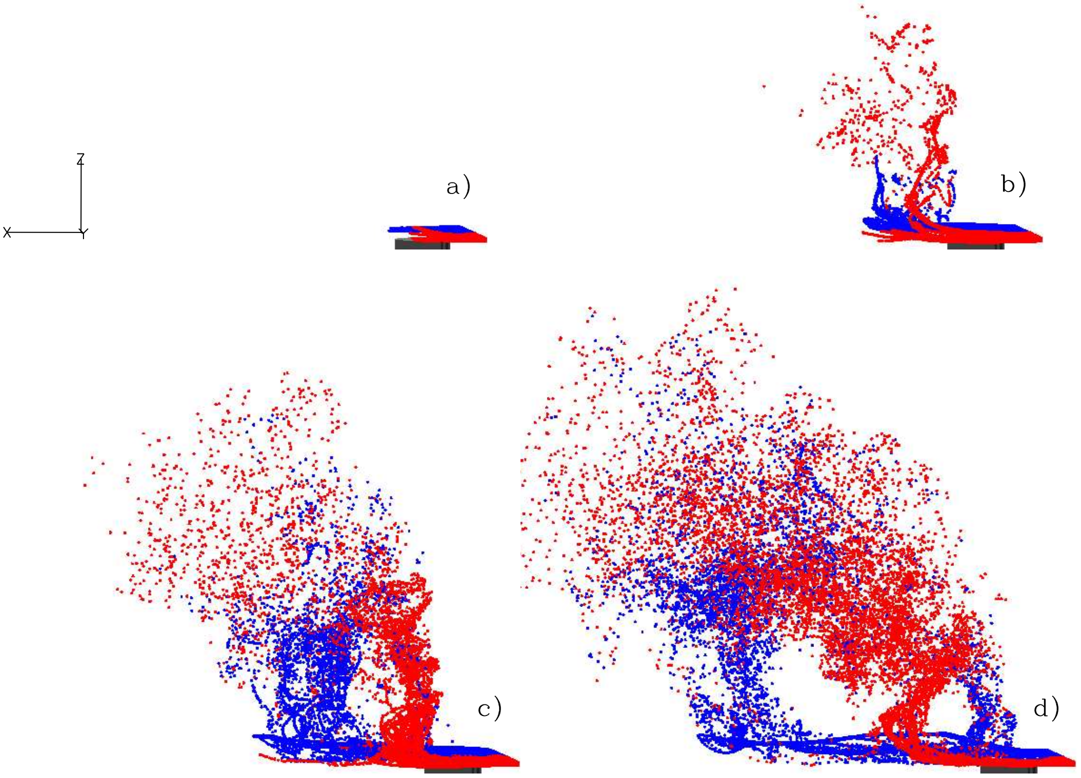

Figure 4.22: Structure of the wake region depicted as a series of instantaneous particle paths originating from the cross-flow boundary layer at vertical position of $z = 0.1\,D$, streamwise position of $x/D = -0.9$ and spanwise positions - $-2 \leq y/D \leq 2$ - PART I. Particles originating from $y < 0$ zone are colored blue and particles originating from $y > 0$ zone are colored red. Δt^* between subfigures is $\Delta t^* = 3.125$. Coordinate system orientation shown in subfigure (a) is the same on all subfigures.

hanging vortices in this region - e.g. in Figure 4.21 the high particle density of red particles on a lateral side closest to the viewer indicates existence of a strong coherent structure at this position, which looses some of its coherence as particles are diffused downstream. In the following section the vortex identification Q-criterion will be applied on the mean flow data combined with the results of POD analysis in order to identify and even better visualize existence and dynamics of the hanging vortex structure in the currently investigated JICF flow.

Figures 4.22 and 4.23 depict a series of instantaneous flow visualizations of the wake region. Here, a particle seeding position is the cross-flow boundary layer $x = -0.9\,D$ upstream of the jet orifice and $z = 0.1\,D$ above the wall. The Figure orientation shown on subfigure 4.22(a) is the same for all subfigures in Figures 4.22 and 4.23, i.e. the wake region is visualized from the spanwise direction and the main flow direction is from right to left.

A clear alternating structure of the wake region, governed by the so-called separation events (Fric and Roshko [30]) is depicted by the used particle paths. Following the frame sequence

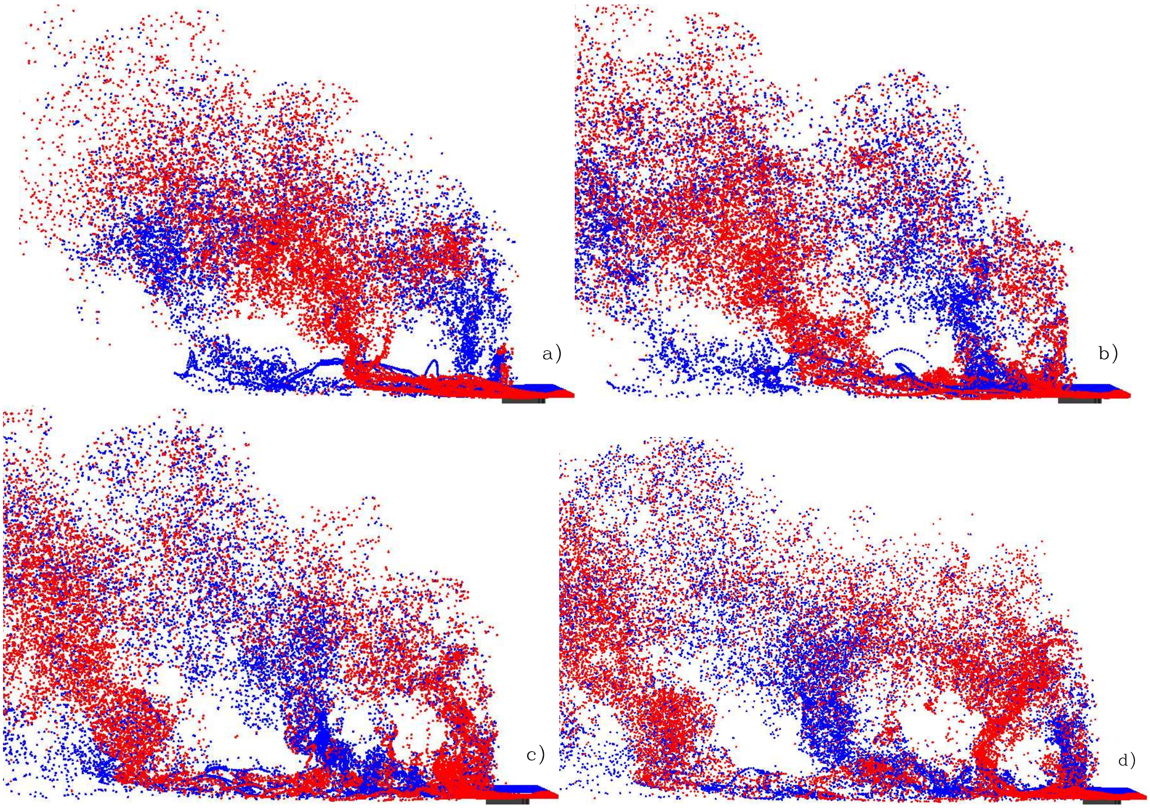

Figure 4.23: Structure of the wake region depicted as a series of instantaneous particle paths - PART II. Coordinate system orientation shown in Figure 4.22(a) is valid for all subfigures presented here. For further description see the caption of Figure 4.22.

presented, a wake vortex formation process can be identified. It is seen that particles originating from different spanwise zones either directly sweep around the jet and contribute to the CVP formation on the jet lee side (particles colored red on Figure 4.22) or contribute to the formation of the instantaneous wake vortex (particles colored blue). From frame (d) on Figure 4.22 through frames (a) and (b) on Figure 4.23 it is seen that relative particle contribution from different spanwise flow regions exchanges place, i.e. blue particles supply CVP and red particles follow the wake vortex, indicating that new separation event has occurred between frames (c) and (d) in Figure 4.22.

This alternating wake structure, reminiscent of von Karman vortex street formation in the wake of a cylinder - but fundamentally different in its origin from the latter (Morton and Ibbetson [74]), was thoroughly investigated by Fric and Roshko [30]. A clear link between the presented wake formation process and e.g. wake structure presented in Figure 27 ($R = 4$) of Fric and Roshko's article can directly be made. Although several attempts were made in order to directly visualize the horseshoe vortex formation on the front side of the jet, the visualization of the latter by particle paths did not give satisfactory results. Despite that, a clear link between flow dynamics dominating the flowfield in the upstream-jet-area and formation of the wake vortices is visible from the presented visualizations. Similar connections between flow dynamics of the upstream-jet-area and the wake vortex structure dominating the flow downstream of the jet orifice in a zone between the cross-flow boundary layer and the main jet body have been previously experimentally obtained by e.g. Krothapalli

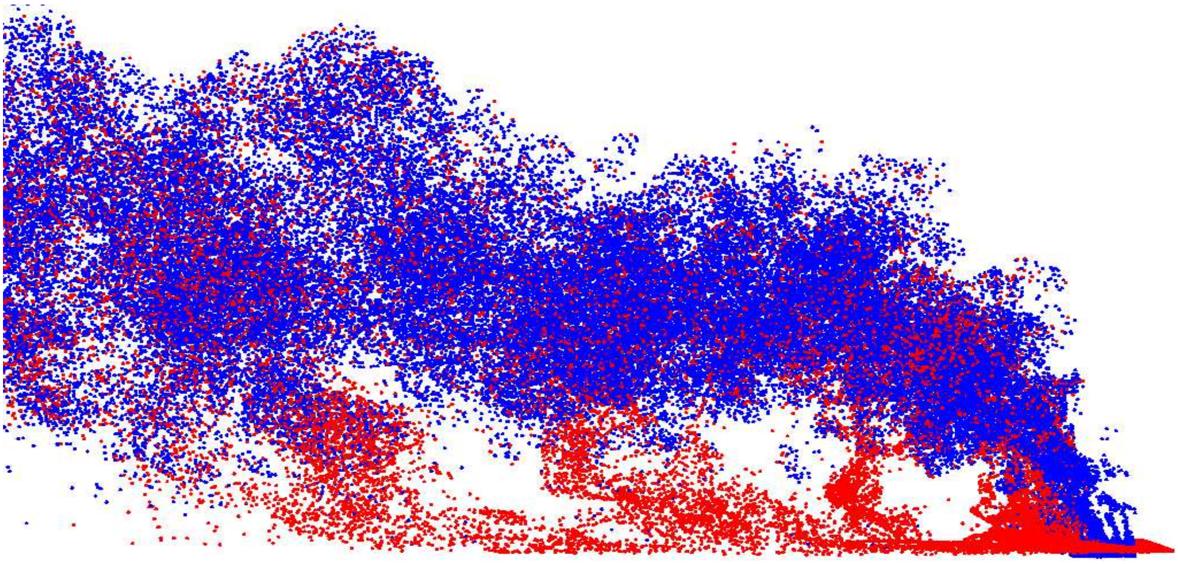

Figure 4.24: Structure of the wake region illustrated by particle paths of massless particles. Particles originating from the pipe shear-layer are colored blue, while particles originating from the cross-flow boundary layer are depicted red. Particle-seeding positions are the jet shear-layer at radial position of 0.49 D, vertical position of $z/D = -0.08$ and cross-flow boundary layer at vertical position of $z/D = 0.1$, streamwise position of $x/D = -0.1$ and spanwise positions - $-2 \leq y/D \leq 2$. Figure represent instantaneous particle paths taken $\Delta t^* = 25$ after the initial release. Coordinate system orientation shown in Figure 4.22(a) is valid here as well.

et al. [53, 54], Kelso and Smits [46] among others.

Figures 4.22 and 4.23 illustrate that the wake - "*tornado like*" vortices supply the boundary layer vorticity to the CVP vortex system. In the experimental work of Fric and Roshko [30] ($2 < R < 10$), it was argued that the exclusive source of vorticity in the wake region is the cross-flow boundary layer.

In Figure 4.24 particle paths originating from the jet shear layer (colored blue) and paths originating from the cross-flow boundary layer (colored red), at an instant $\Delta t^* = 25$ after the initial release, are depicted.

Figure 4.24 illustrates clearly that in a present synthetic jet with $R = 3.3$ the cross-flow boundary layer is basically the main source of vorticity in the wake region. However it should be noted, that in the upper connection areas between the main jet body and the wake vortices and regions relatively far downstream, considerable concentration of particles originating from the jet shear layer seem to exist in the wake vortical structures. This indicates that vorticity originating from the jet shear layer may contribute and noticeably supply the vorticity into the wake vortical structures, at least in the mentioned flow regions. In the following paragraph, by means of the POD analysis, it will be shown that the upper connection region between the main jet body and wake vortices may play a crucial role in the creation process of the wake vortices.

As shown in Figure 4.18, identification of coherent structures (vortices) based on plots

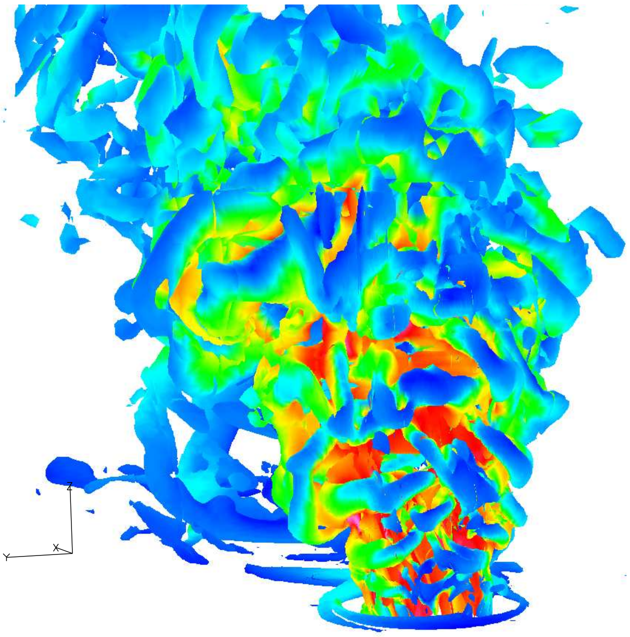

Figure 4.25: Instantaneous iso-surface, colored by the velocity magnitude, of a Second Invariant of the Velocity Gradient Tensor - $Q = -\frac{1}{2}\frac{\partial u_i}{\partial x_j}\frac{\partial \bar{u}_j}{\partial x_i} = 5$.

of the vorticity field can be quite difficult. Therefore some other vortex identification criteria have been suggested in the past in order to better and easier identify various vortical structures in different flow fields.

Two most widely used criteria are the Q-parameter criterion of Hunt et al. [41] and λ_2 criterion of Jeong and Hussain [43]. Initially, both of those criteria have been used in the present study, but it turned out that they produce similar results. As the Q-parameter criterion is easiest to directly apply on a given flow case it will be used in the course this study.

In Figures 4.25 and 4.26 iso-surfaces of the Q-parameter, applied on instantaneous and mean flow field respectively, are presented.

Inspecting the Q-parameter surface based on the instantaneous flow field (Figure 4.25), a clear indication of a horseshoe vortex system (surrounding the jet-entry area) is visible. Furthermore many of the shear-layer rollers on the front side of the jet are visible too. Actually a wake vortex system connecting the main jet body and the cross-flow boundary layer is illustrated by the presented iso-surface as well. Comparing Figures 4.18 and 4.25 it becomes clear that Q-parameter criterion successfully removes shear induced vorticity of the boundary layer flow thereby revealing many of the characteristic coherent structures of the JICF flow.

On Figure 4.26 the same criterion is applied on the mean flow field. An easily distinguishable CVP structure becomes quite apparent. As suggested by Rivero et al. [88] the dominant CVP structure is not a steady feature of the instantaneous JICF flow but can fluctuate strongly and is dependant on the wake vortex system. Figure 4.26 support Rivero et al.'s findings as the CVP structure in the presently simulated flow could only be structurally identified using the Q-parameter criterion based on the averaged flow field. Furthermore, some clear traces of vortical structures in the near-wall area, reminiscent of wall-vortex pair struc-

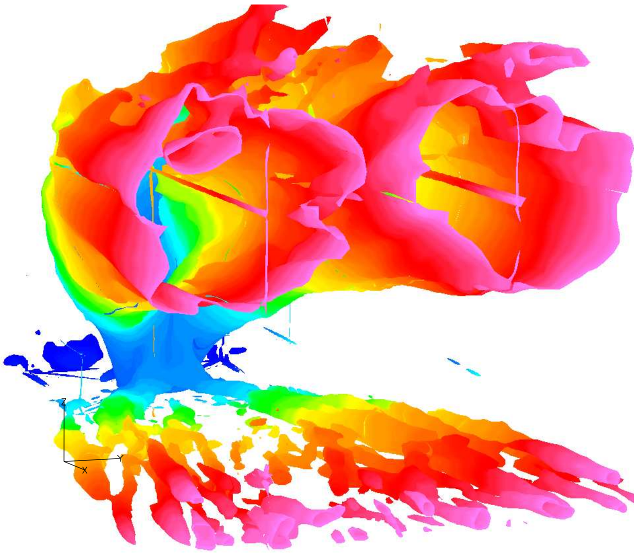

Figure 4.26: Mean iso-surface of a Second Invariant of the Velocity Gradient Tensor - $Q = 0.01$. In order to enhance the visibility of the CVP the coloring scheme used here follows the streamwise (x) direction.

tures (with several branches) identified by e.g. Yuan et al. [117], are also visible in Figure 4.26.

The presently used methods, directly applied on a number of flow realizations (or on a series of them) - the Q-parameter criterion and massless particle tracking throughout the flow field, have been able to successfully identify many of the known coherent structures pertinent to the JICF flow field. In the next section the POD method will be applied on several, both PIV and LES based datasets, in order to further investigate the agreement between experimental and computational findings and in order to additionally analyze the coherent structures of the JICF flow field utilizing a more statistically accentuated tool for identification of the latter.

4.6 Proper Orthogonal Decomposition (POD)

In the previous paragraph different methods were used in order to identify coherent structures in the JICF flow. The method which gave the best visual depictions of the JICF flow field was based on use of massless particle paths and an assumption that those paths can track deformation of vorticity into vortical structures, in a similar way as most of the experimental flow visualizations are conducted. It should be mentioned that most of the experimental studies conducted in the past used setups with laminar inflow condition(s), where the process of tracking of the vorticity is substantially simplified compared to the corresponding turbulent inflow cases. However, even though both the cross-flow boundary layer and the jet flow are turbulent in the present study, the applied method satisfactorily gave some indications of the vortical structures in the JICF flow.

A more objective and unbiased method, which can be used to identify flow structures in a given flow, is Proper Orthogonal Decomposition - POD. In POD a series of flow visualizations is decomposed, using some mathematical tools, into a set of orthonormal basis functions, which span the given dataset in the most "*optimal*" way. The definition of optimality in POD is based on energy considerations, as POD eigenvalues, which represent the relative contribution of a given POD mode to the overall resolved kinetic energy, can be arranged in a descending order, so the most energetic i.e. largest flow structures are captured in the first couple of POD modes. Therefore in cases where the flow dynamics are dominated by some distinct coherent structures, it should be possible to capture them by considering a relatively small number of POD modes.

4.6.1 Basic equations

POD was introduced in the context of turbulence by Lumley in 1967 [60]. Before that time the same method, known as Karhunen-Loève expansion, was used in probability theory and statistics. In the context of this work the method known as *"snapshot POD"* of Sirovich [98] will be used. In the following a brief description of basic equations, which constitute a mathematical foundation of the applied method, will be given. For a detailed description of a general POD methodology, an interested reader is referred to the book of Holmes et al. [40].

Following the basic (classical POD) ideas of Lumley [60], the equation for determination of the POD eigenvalues and eigenfunctions can be derived (see e.g. Pedersen [81]):

$$\int_{\Omega} \mathbf{R}(\mathbf{x}, \mathbf{x}')\mathbf{\Phi}(\mathbf{x}')d\mathbf{x}' = \lambda\mathbf{\Phi}(\mathbf{x}), \tag{4.14}$$

where Ω denotes the spatial domain ($\mathbf{x} = \{x,\, y,\, z\} \in \Omega$) considered, $\mathbf{R}$ is the two-point correlation tensor and λ and $\mathbf{\Phi}$ are POD- eigenvalues and eigenfunctions respectively.

Considering an ensemble of uncorrelated flow realizations, where a single realization - representing the fluctuating part of e.g. the velocity field, is written as:

$$\mathbf{u^n} = \mathbf{u}(\mathbf{x}, t^n), \qquad n = 1, ..., N, \tag{4.15}$$

one can approximate the two-point correlation tensor (assuming the ensemble is sufficiently large - see Sirovich [98]) as:

$$\mathbf{R}(\mathbf{x},\mathbf{x}') = \frac{1}{N}\sum_{n=1}^{N}\mathbf{u}(\mathbf{x},t^n)\mathbf{u}^{\mathbf{T}}(\mathbf{x}',t^n). \tag{4.16}$$

Assuming furthermore that the basis modes can be written in terms of the original dataset as:

$$\mathbf{\Phi}(\mathbf{x}) = \sum_{n=1}^{N} A(t^n)\mathbf{u}(\mathbf{x},t^n), \tag{4.17}$$

and inserting (4.16) and (4.17) into (4.14), after some rearrangements it yields:

$$\sum_{n=1}^{N}\left(\frac{1}{N}\int_{\Omega}\mathbf{u}^{\mathbf{T}}(\mathbf{x}',t^n)\mathbf{u}(\mathbf{x}',t^n)d\mathbf{x}'\right)A(t^n) = \lambda A(t^n). \tag{4.18}$$

Denoting

$$\mathbf{C} = C(i,\, j) = \frac{1}{N}\,\left(u^T(\mathbf{x},\, t^i)u(\mathbf{x},\, t^j)\right), \qquad i,\, j = 1, ..., N, \tag{4.19}$$

and

$$\mathbf{A} = A(t^n) \qquad n = 1, ..., N, \tag{4.20}$$

the equation system (4.18) can be written in a compact form as:

$$\mathbf{CA} = \lambda\mathbf{A}. \tag{4.21}$$

Solving the eigenvalue-problem in eq. (4.21) one gets a set of N mutually orthogonal eigenvectors, which then can be used to construct the POD modes according to eq. (4.17). The POD modes are typically normalized giving the orthonormal basis of the considered dataset, as:

$$\mathbf{\Phi}^i(\mathbf{x}) = \frac{\sum_{n=1}^{N}\ A^i(t^n)\mathbf{u}(\mathbf{x},t^n)}{\left\|\sum_{n=1}^{N}\ A^i(t^n)\mathbf{u}(\mathbf{x},t^n)\right\|} \qquad i = 1, ..., N. \tag{4.22}$$

In practice the method is applied on either experimental or numerical - i.e. discrete datasets. Considering a POD analysis of N 2D datasets, which corresponds to N planes consisting of $\mathrm{k\,x\,m} = \mathrm{M}$ data points, by subtracting the mean value of the considered quantity e.g. velocity component, its fluctuating parts can be arranged in a matrix $\mathbf{U}$ as follows:

$$\mathbf{U} = \left[\mathbf{u}^1\,\mathbf{u}^2 \,..........\, \mathbf{u}^{N-1}\,\mathbf{u}^N\right] = \begin{bmatrix} u_1^1 & u_1^2 & ...... & u_1^{N-1} & u_1^N \\ \vdots & \vdots & \vdots & \vdots & \vdots \\ u_{\mathrm{M}}^1 & u_{\mathrm{M}}^2 & ...... & u_{\mathrm{M}}^{N-1} & u_{\mathrm{M}}^N \\ v_1^1 & v_1^2 & ...... & v_1^{N-1} & v_1^N \\ \vdots & \vdots & \vdots & \vdots & \vdots \\ v_{\mathrm{M}}^1 & v_{\mathrm{M}}^2 & ...... & v_{\mathrm{M}}^{N-1} & v_{\mathrm{M}}^N \end{bmatrix}.$$

Correspondingly, the auto-covariance N x N matrix **C** is formed as:

$$\mathbf{C} = \mathbf{U}^T\mathbf{U}.$$

Solving the eigenvalueproblem (4.21) and arranging solutions in a descending order one gets:

$$\lambda^1 > \lambda^2 > .... > \lambda^{N-1} > \lambda^N = 0.$$

Corresponding POD modes are then created, typically using the discrete 2-norm $\|z\| = \sqrt{z_1^2 + z_2^2 + ... + z_{2M-1}^2 + z_{2M}^2}$ as:

$$\phi^i(\mathbf{x}) = \frac{\sum_{n=1}^{N} A_n^i \mathbf{u}^N}{\left\|\sum_{n=1}^{N} A_n^i \mathbf{u}^N\right\|} \qquad i = 1, ..., N. \tag{4.23}$$

One of the basic properties of POD is that each original snapshot can be reconstructed from the calculated POD modes. In order to do that the expansion coefficients, called POD coefficients have to be calculated first.

Basically,

$$\mathbf{u}^n = \sum_{i=1}^{N} a_i^n \phi^i = \mathbf{\Psi}\mathbf{a}^n, \tag{4.24}$$

where $\mathbf{\Psi} = \left[\phi^1\, \phi^2 \,......\, \phi^{N-1}\, \phi^N\right]$ and the POD coefficient vector for a given snapshot is defined by $\mathbf{a}^n = \left[a^n\left(t^1\right)\, a^n\left(t^2\right) ...... a^n\left(t^{N-1}\right)\, a^n\left(t^N\right)\right]^T$.

Once the POD modes are calculated the unknown POD coefficients can be determined from:

$$\mathbf{a}^n = \mathbf{\Psi}^T\mathbf{u}^n. \tag{4.25}$$

An important property of POD coefficients $a^n(t)$ is that they represent the amount of energy of $\mathbf{u}^n(\mathbf{x}, t)$ in the "*direction*" of ϕ^n. Therefore the size of a given POD coefficient indicates directly the significance of the corresponding POD mode for the considered instantaneous flow realisation.

4.6.2 Comparison of PIV-based and LES-based POD analyses

In section 4.4 the LDA acquired mean flow data was compared to data from the present LES study. As an extension to this comparison of statistical flow quantities, the described POD analysis has been applied on the two datasets - one originating from the PIV measurements (Meyer et al. [70, 71]) and the other from the present LES calculation. Comparison of the achieved results from both analyses is presented in the following.

In both cases the POD analysis is conducted utilizing 1000 instantaneous flow realizations, with the exception of the $z/D = 1.33$ plane where PIV based analysis has been conducted on the available set of 658 flow realizations. It should be noted that PIV obtained data are statistically uncorrelated, while the same demand in the LES case could not be met for the obvious reasons of extreme computational overhead connected with it.

As a large number of different computations have been conducted in order to be able to state, with a reasonable certainty, that the computed JICF flow realistically resemble the flow case in the experimental set-up of Özcan and Larsen [77], Meyer et al. [70, 71], the current 2D POD analysis has been carried out after the completion of all of the mentioned numerical studies. Therefore the current LES based POD study is conducted based on the results of case LES 6 from Appendix A and datasets extracted on 3 investigated planes during the overall time period corresponding to 30 FLTs.

The turbulence time scale is increasing with the downstream distance in the JICF flow. Assuming that the average integral time scale in the near-field flow is $3\,D/U_\infty$ (obtained from autocorrelation function R_{uu} at Point 1 in Figure A.1 on page 129), the present LES dataset will only contain app. 90 statistically uncorrelated samples. The initial analysis was conducted on these 90 uncorrelated flow realizations showing qualitatively similar results to those based on 1000 samples. The main difference was that some structures were significantly "*blurred*" and not easily identifiable in the small dataset analysis. So despite the fact that the LES dataset contained statistically correlated data, it was decided to conduct the main LES analysis on the full dataset in order to accommodate comparison of PIV and LES data up to a similar level of detail.

The POD analyses are compared on three mutually perpendicular planes in the jet near-field - $y/D = 0$ the symmetry plane, $x/D = 1$ and $z/D = 1.33$ planes.

Before preceding further, a comment on the data plotting method should be given. As the POD method is based on solution of an eigenvalueproblem, the resulting eigenvectors, called POD modes are only determined up to a constant by this analysis. Scaling the POD modes to make an orthonormal basis addresses this issue only partially, as the sign of eigenvectors, resulting from the solution of the underlying POD problem, may still strongly depend on the solution procedure. This implies that PIV-based POD mode 1 and LES-based POD mode 1 in Figure 4.30 are in very good agreement and represent a trace of a similar flow structure - only both the in-plane and out-of-plane POD mode velocities are simply mirrored (have an opposite sign) in those two contour/vector plots.

In should be noted furthermore that in-plane POD mode velocities (illustrated as vectors) in all subsequent Figures are scaled by factor of 2 in order to better visualize the existing flow structures in the corresponding planes, while coordinate axes are normalized by the pipe diameter D. Assessment of a relative influence of the in-plane-velocity POD mode component vs. out-of-plane-velocity POD mode component is basically done by introducing a parameter:

$$V_{rel} = \frac{\sum_i |v_i|}{\sum_i \sqrt{u_i^2 + w_i^2}}, \quad U_{rel} = \frac{\sum_i |u_i|}{\sum_i \sqrt{v_i^2 + w_i^2}}, \quad W_{rel} = \frac{\sum_i |w_i|}{\sum_i \sqrt{u_i^2 + v_i^2}}, \tag{4.26}$$

which is used in $y/D = 0$, $x/D = 1$ and $z/D = 1.33$ planes respectively. In this way a size of the "*mean*" POD mode in- vs. out-of-plane velocity is evaluated. It proved to be meaningful to use a fixed scaling of the POD out-of-plane velocity component contours in all presented Figures, as the fixed scaling combined with the relative size of the out-of-plane POD velocity component from eq. (4.26) gives both visual and quantitative estimate on which part of the POD based velocity component predominantly influences the considered mode.

Finally it should be noted that LES-based analysis is conducted on the PIV-based grid in order to facilitate a reasonable basis for the conducted comparisons. The data are interpolated from the numerical LES grid to the PIV-based grid prior to POD analysis using a second order inverse distance interpolation technique.

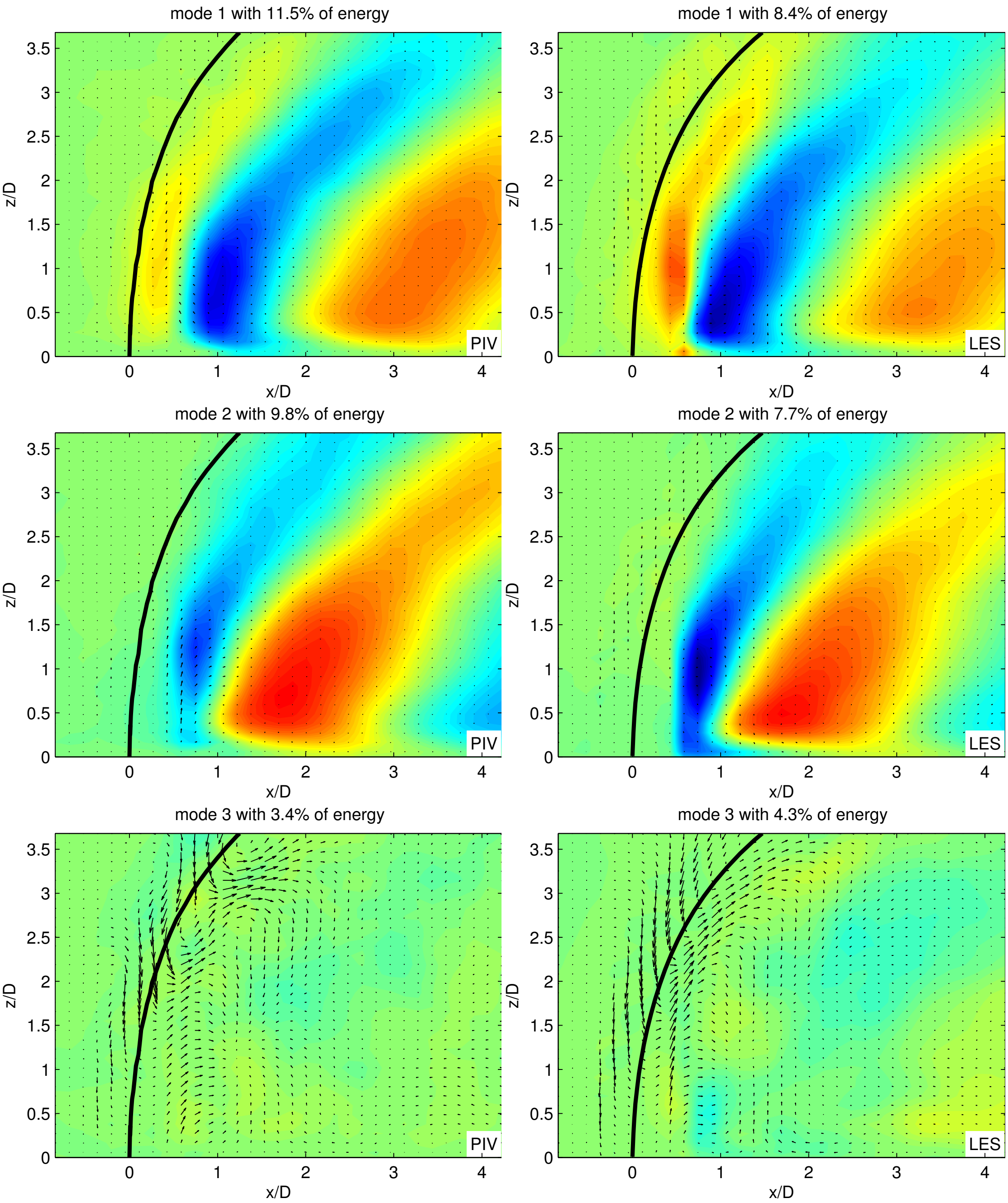

Figure 4.27: Plane $y/D = 0$, POD - modes 1, 2 and 3. All subfigures in the left-hand side column are based on PIV measurements and correspondingly all subfigures in the right-hand side column are based on the present LES calculations. Contour level scales are identical in all subfigures and equal to the scales presented in Figure 4.30(a) and (b).

In the following, the results of the conducted POD analyses are presented and compared in such a way that the first 6 POD modes on the three investigated, mutually perpendicular planes are directly compared. Besides that, the relative energy content in the first 20 modes for both PIV- and LES- based POD analysis is presented together with an estimate of the

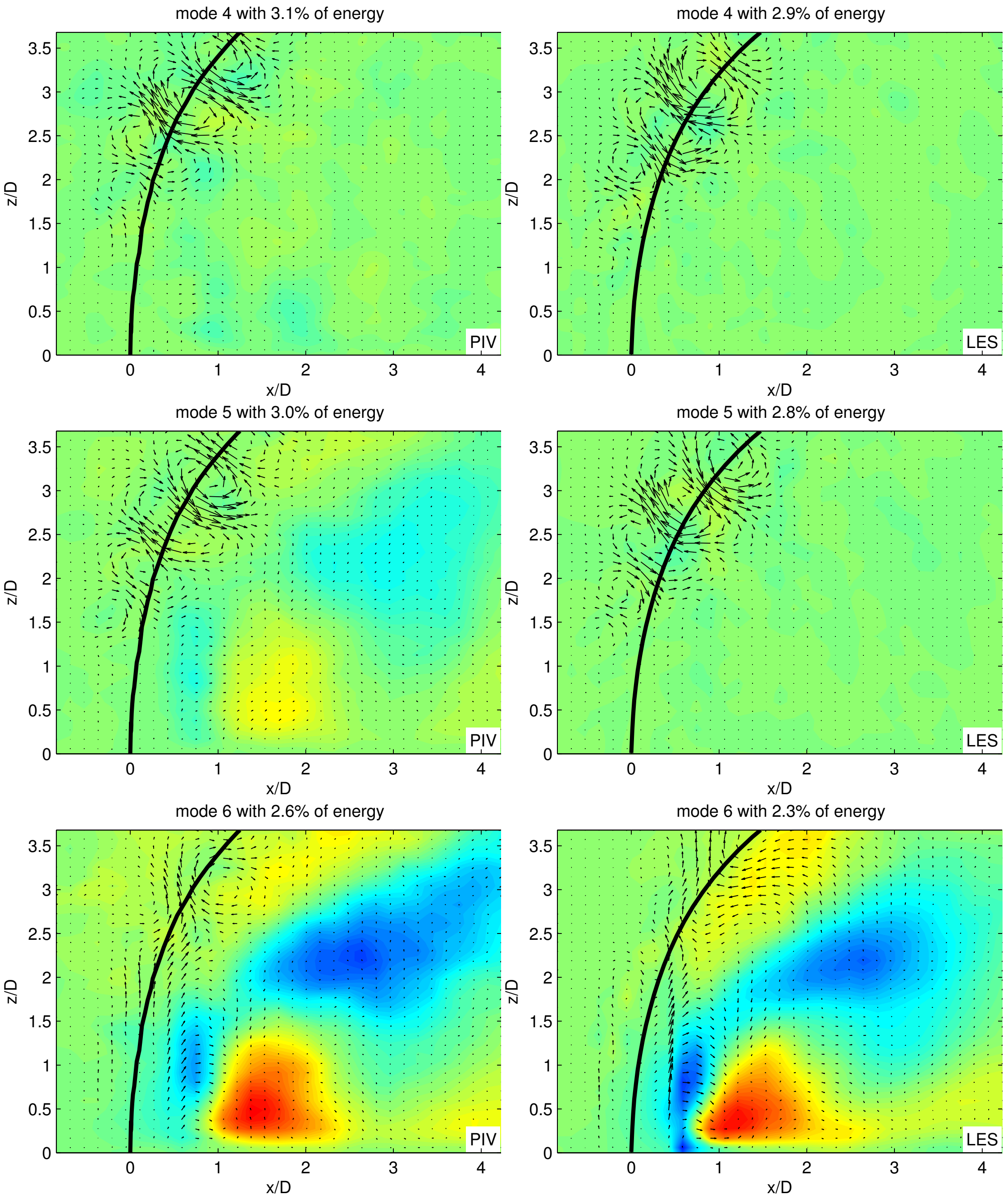

mode 4 with 3.1% of energy

mode 4 with 2.9% of energy

mode 5 with 3.0% of energy

mode 5 with 2.8% of energy

mode 6 with 2.6% of energy

mode 6 with 2.3% of energy

Figure 4.28: Plane $y/D = 0$, POD - modes 4, 5 and 6. Subdivision of PIV- and LES- based subfigures follows the description from Figure 4.27. Contour level scales are identical in all subfigures and equal to the scales presented in Figure 4.30(a) and (b).

relative size of the out-of-plane POD velocity component from eq. (4.26) for each of the regarded planes.

Results from the POD analyses based on datasets corresponding to the symmetry plane are presented in Figures 4.27 - 4.29. Results are presented "*in pairs*" - so each column in the following Figures represent POD modes based on PIV data (left column) and LES calculations

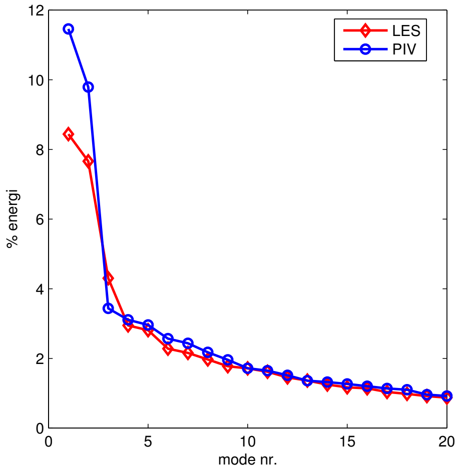

Figure 4.29: Relative energy content in the first 20 POD modes in the $y/D = 0$ plane.

(right column). A thick black line indicated on all subfigures for $y/D = 0$ plane represent the jet trajectory, defined as previously according to Yuan et al. [117] - see e.g. Figure 4.12 on page 53.

Mode number	1	2	3	4	5	6
V_{rel} - PIV	7.66	6.75	0.16	0.17	0.46	1.50
V_{rel} - LES	4.75	4.89	0.26	0.10	0.11	1.13

Table 4.3: Extent of the relative out-of-plane motion in the first 6 POD modes in the $y/D = 0$ plane

From Figures 4.27 - 4.29 and Table 4.3, a general good agreement between POD modes calculated from PIV and LES datasets can be observed.

It is evident that the first two POD modes in both analyses show a clear dominance of the out-of-plane POD mode velocity component, where 3 dominant and almost parallel structures placed downstream of the jet trajectory are clearly visible. Besides a general good agreement between the two analyses in the case of the first two modes, some differences in the near-wall region at position $x/D \approx 0.5$ can be observed. In section 4.4, a disagreement between LDA measurements and LES has been observed on this particular location too - see Figure 4.12(a) - (b) on page 53. It should be noted furthermore that PIV method introduces erroneous results, caused by a velocity bias towards zero, in the immediate vicinity of the jet entry point in region $-0.5 < x/D < 0.5$ - see Pedersen [81]. Therefore it is difficult to estimate whether the observed differences between LES and PIV results are reflecting a real discrepancy in the obtained results or they are simply a product of the mentioned biasing error. One should also note a difference in the extension of the first dominant out-of-plane structure for POD mode 2 in the near-wall region $0.5 < x/D < 1.25$, between PIV- and LES- based results.

The third POD mode shows similar tendencies in both analyses as well. Here, significantly more dominant in-plane velocities a basically arranged in a way that two distinct areas with uniform vector orientations are placed on each side of the jet trajectory.

Analyzing the results further, it is evident that POD modes 4 and 5 (Figure 4.28) from LES and PIV based datasets show a good agreement too. Here, the most dominant is the in-plane motion, where some distinct traces of shear-layer vortical structures are visible in the vicinity of the jet trajectory. It seems that both modes 4 and 5 represent a similar vortical structure, which is just slightly shifted in the downstream direction. It should be noted here, that the out-of-plane motion is more significant in the PIV based POD mode 5 than in its LES based counterpart.

A general good agreement between POD mode 6 from both analyses is visible from Figure 4.28, where very similar structures are reviled by the slightly dominant out-of-plane motion. However, some differences in the less dominant in-plane motion pattern can be seen as well.

Considering the relative energy content in the first 20 POD modes and comparing it between the two analyses (Figure 4.29), some differences can be observed, although the general energy distributions seem quite similar. In the PIV based analysis the first 2 modes contain more than 20% of the overall resolved kinetic energy. The energy distribution has a substantial drop in energy content from the second to the third mode and a much lower rate of energy decay from mode 3 onward is observed. In the LES based analysis the first 2 modes are clearly more energetic than the rest of the modes. A substantial drop in energy content is seen between modes 2 and 3 here as well, but the third POD mode is evidently more energy containing than the rest of the higher POD modes.

Thereby it is evident that the general energy distribution between POD modes is quite similar regardless of the basis for the conducted analyses, but some distinct differences do exist. In section 4.6.2.1 the overall kinetic energy resolved by PIV measurements and LES computation is compared and discussed. There it will become apparent, that discrepancies observed here can probably be attributed to those overall kinetic energy differences.

Turning the attention to the results from $x/D = 1$ plane - Figures 4.30-4.32 and Table 4.4, a reasonably good agreement between conducted analyses is observed. It is seen that traces of similar two-branch structures are detectable from the out-of-plane velocity component in POD mode 1 in both cases. It is seen further that a similar and dominant in-plane velocity pattern is visible in subfigures depicting POD mode 1. Also in- and out- of-plane based structures represented by POD mode 2 are evidently similar in both analyses. Especially from POD mode 2 it is observed, that LES based out-of-plane structures are more “*compressed*” indicating, as previously discussed, that the synthetic jet is bending faster than the corresponding experimental jet. Besides that, the non-dominant out-of-plane POD mode velocity component in the LES based POD mode 1 seems to depict traces of some vortical structures in region $-0.5 < x/D < 0.5$ and $0 < z/D < 1.1$, whereas the same structures can not be seen in the PIV based subfigure. It should be noticed also, that a similar reverse in the in-plane flow pattern from mode 1 ($z/D < 1.5$) to mode 2 ($1 < z/D < 2$) is visible in both analyses from Figure 4.30.

Considering the in- and out- of-plane based structures represented by POD mode 3 (Figure 4.30), a good agreement is observed. Comparing furthermore POD modes $4-6$ (Figure 4.31), it is seen that PIV based mode 4 and LES based mode 5, PIV based mode 5 and LES based mode 6 and PIV based mode 6 and LES based mode 4 seem to be in a reasonable agreement. Considering the relative influence of the in- vs. out- of-plane velocity components (Table 4.4) this observation is further supported, as the relative influence factors agree much better if e.g. the PIV based mode 6 and LES based mode 4 are compared etc.. As the relative energy content in POD modes $4-6$, especially in the LES based analysis, are almost equal, it can be expected that some of the (higher) modes resulting from this analysis can swap places.

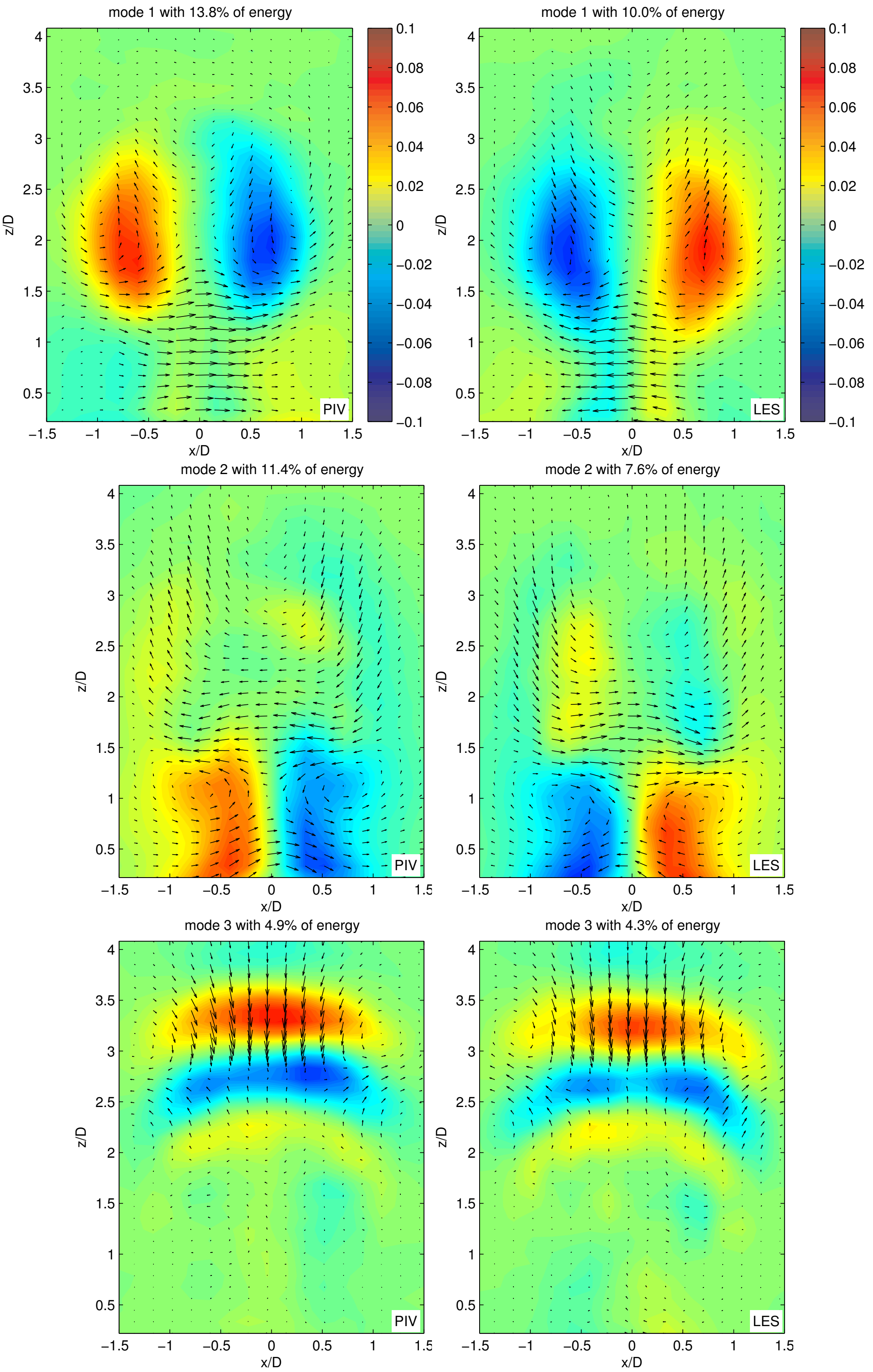

Figure 4.30: Plane $x/D = 1$, POD - modes 1, 2 and 3. Subdivision of PIV- and LES- based subfigures follows the description from Figure 4.27. Contour level scales are identical in all subfigures and equal to the scales presented in subfigures (a) and (b).

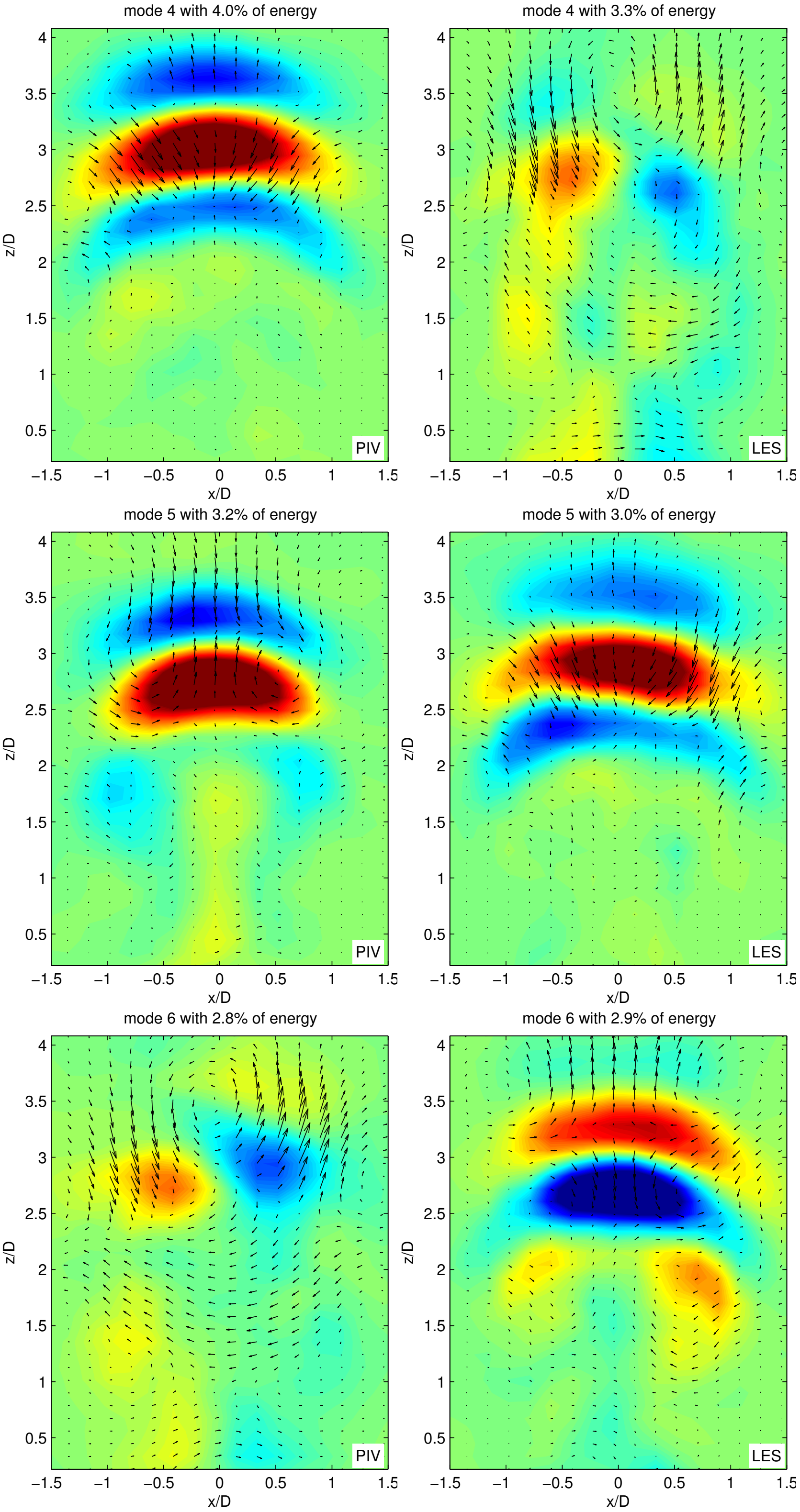

Figure 4.31: Plane $x/D = 1$, POD - modes 4, 5 and 6. Subdivision of PIV- and LES- based subfigures follows the description from Figure 4.27. Contour level scales are identical in all subfigures and equal to the scales presented in Figure 4.30(a) and (b).

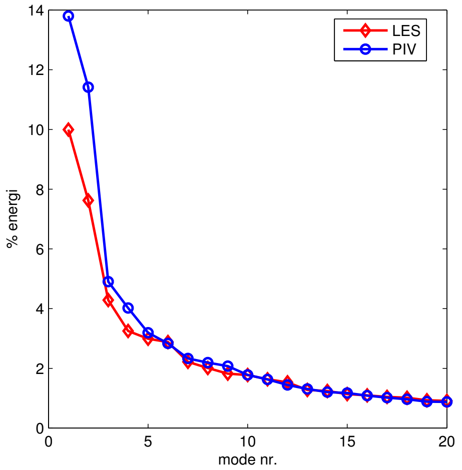

Figure 4.32: Relative energy content in the first 20 POD modes in the $x/D = 1$ plane.

Mode number	1	2	3	4	5	6
U_{rel} - PIV	0.55	0.44	0.52	1.07	0.86	0.35
U_{rel} - LES	0.53	0.43	0.44	0.31	0.91	0.89

Table 4.4: Extent of the relative out-of-plane motion in the first 6 POD modes in the $x/D = 1$ plane.

The relative energy content in the first 20 POD modes shown on Figure 4.32, indicates that the first 2 modes are the dominant ones in this case too. Here, the energy content in the first two LES based modes is again lower than in the PIV based ones and some dissimilarities between PIV- and LES- based energy contents are generally seen in the case of the first 6 modes.

Analyzing results from the $z/D = 1.33$ plane (Figures 4.33 - 4.35 and Table 4.5) a relatively good agreement is observed in the case of the first 3 POD modes, while agreements in the rest of the depicted modes are not particularly evident. Considering immediately the energy distribution between POD modes $1 - 20$ (Figure 4.35) it is clear that the first two modes represent almost 35% (PIV case) and 25% (LES case) of the total kinetic energy resolved. As the rest of the modes only represent less than 3.5% of the total energy each, a small scale structures can be expected to play a dominant role in these POD modes. As various parameters can influence structures at the smallest resolved scales, a better general agreement between present analyses for those POD modes can therefore not be expected.

Mode number	1	2	3	4	5	6
W_{rel} - PIV	0.27	0.25	0.35	0.38	0.33	0.34
W_{rel} - LES	0.24	0.25	0.39	0.42	0.39	0.44

Table 4.5: Extent of the relative out-of-plane motion in the first 6 POD modes in the $z/D = 1.33$ plane

Considering structures described by the in-plane velocities in the first two POD modes one can observe traces of two vortices centered at $y/D = 0$ and $x/D = 0.5$, $x/D = 1.5$ (PIV case); $x/D = 0.6$, $x/D = 1.75$ (LES case) in the POD mode 1. In the POD mode 2 traces of

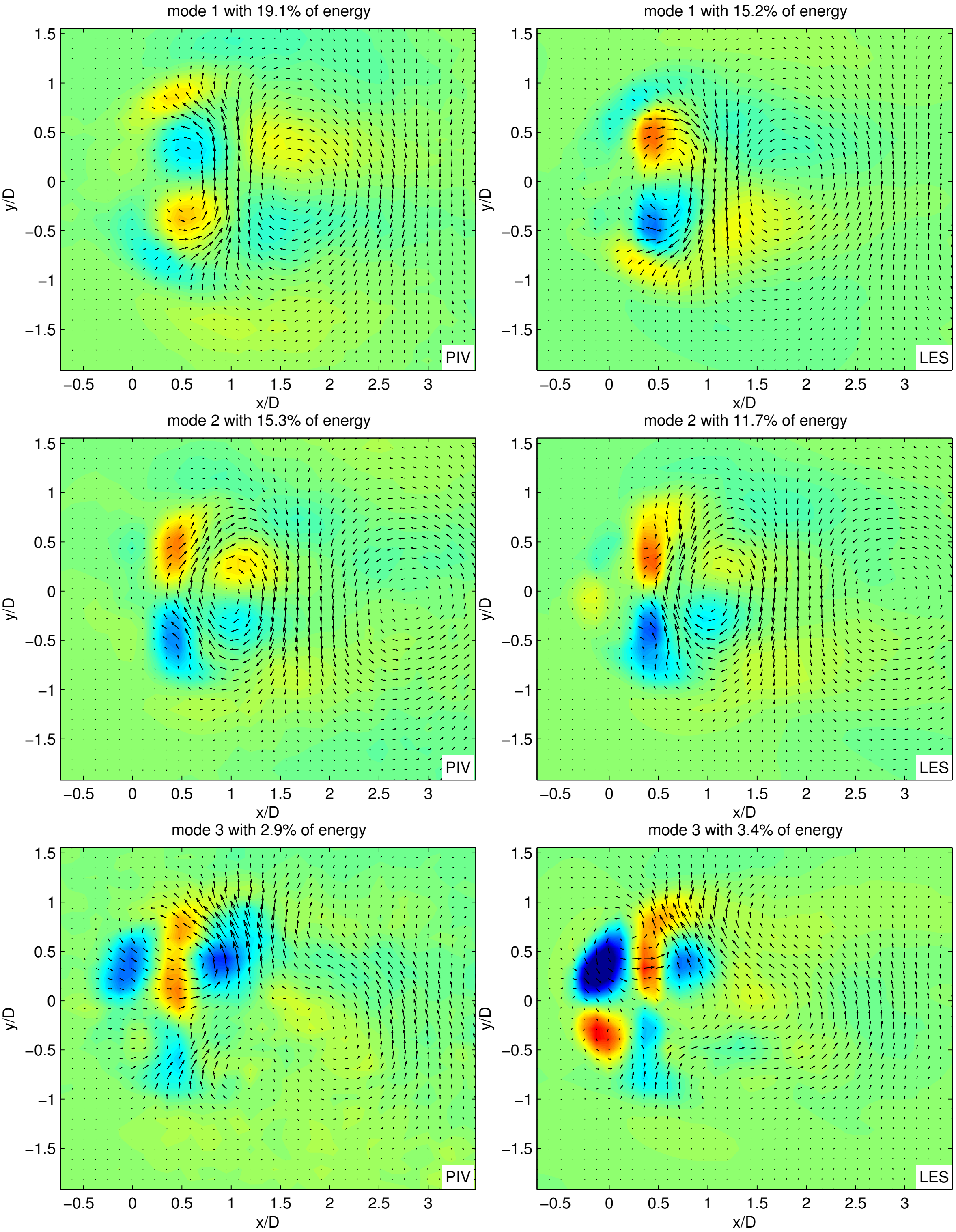

Figure 4.33: Plane $z/D = 1.33$, POD - modes 1, 2 and 3. Subdivision of PIV- and LES-based subfigures follows the description from Figure 4.27. Contour level scales are identical in all subfigures and equal to the scales presented in Figure 4.30(a) and (b).

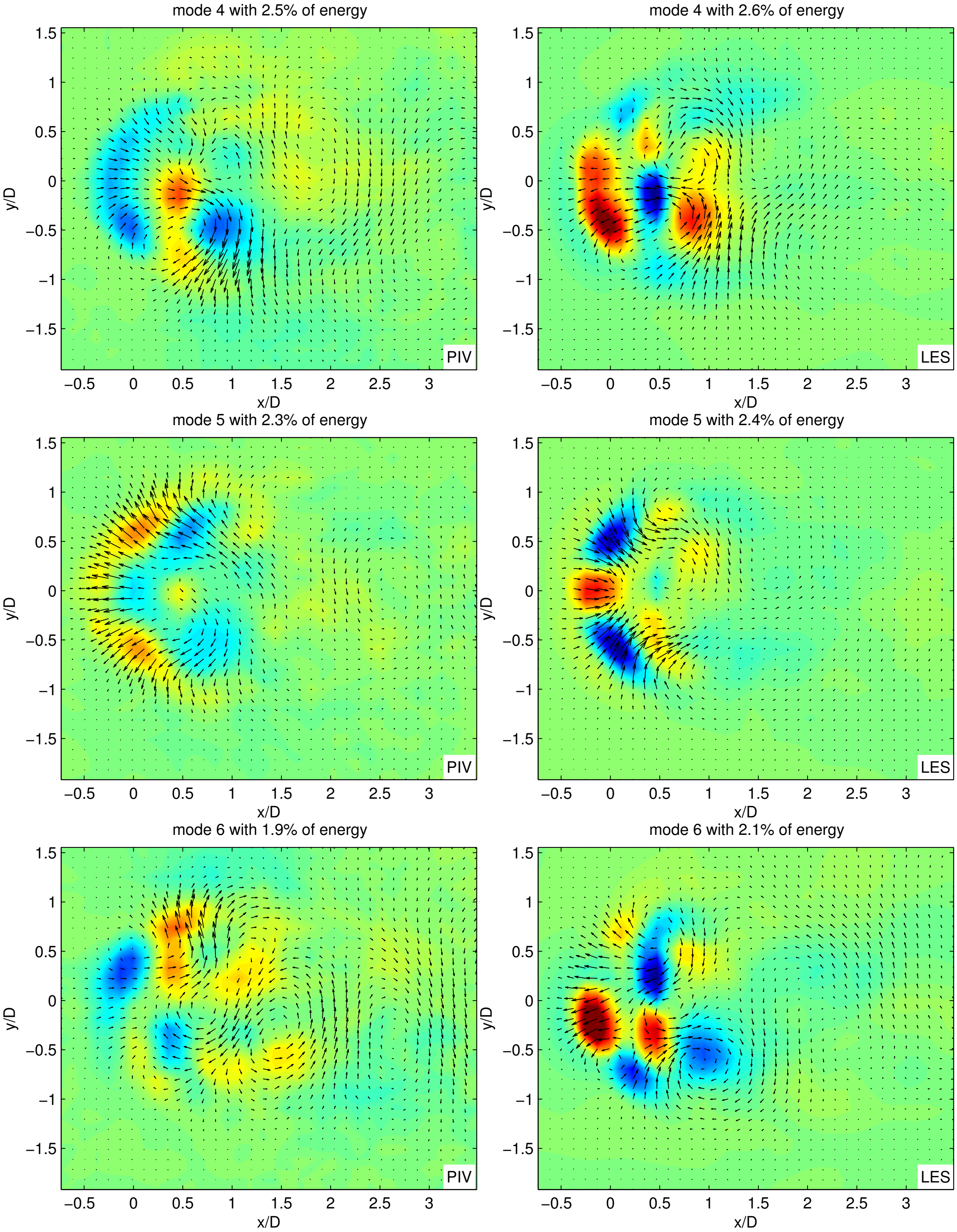

Figure 4.34: Plane $z/D = 1.33$, POD - modes 4, 5 and 6. Subdivision of PIV- and LES-based subfigures follows the description from Figure 4.27. Contour level scales are identical in all subfigures and equal to the scales presented in Figure 4.30(a) and (b).

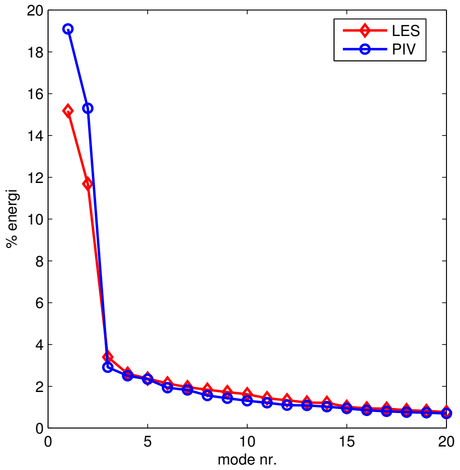

Figure 4.35: Relative energy content in the first 20 POD modes in the $z/D = 1.33$ plane.

two vortices, but now centered at $y/D = 0$ and $x/D = 1$, $x/D = 2.7$ (PIV case); $x/D = 1.1$, $x/D = 3$ (LES case) can be observed. The out-of-plane velocities play a less significant role in those modes (Table 4.5), but nevertheless contour shapes of the out-of-plane velocity components in LES- based and PIV- based analyses are in good agreement. As seen previously, LES- and PIV- based energy distribution between the first 20 POD modes are qualitatively similar, with consequently lower energy content in the first 2 LES- based modes, compared to the PIV- based ones.

4.6.2.1 Resolved Turbulent Kinetic Energy

The underlying basis for the conducted POD analyses is turbulence i.e. the fluctuating part of the considered velocity field. The POD results presented in this section showed that many structures revealed by the analysis of POD modes are similar, regardless of the data acquiring procedure (experimental or numerical) used, but some differences in the obtained results have been observed too.

As the turbulent kinetic energy is a general way of quantifying turbulence levels in any analyzed flowfield, comparing levels of the resolved kinetic energy in the two underlying datasets used in the POD analyses, can actually give an indication of an extent to which the results from the conducted POD analyses can be expected to match.

The resolved turbulent kinetic energy in PIV- and LES- based datasets used in the described POD analyses is presented on Figure 4.36. Note that contour levels and colorbars shown in subfigures 4.36(a) and (b) are valid for all investigated planes.

Analyzing the results from Figure 4.36 it is clear that some differences in levels of the resolved turbulent kinetic energy by PIV and LES do exist. It should be noticed, that LES results are obtained on the PIV- based grid points, so the shown results are directly comparable.

The agreement between experimental and numerical results, on a general level, seems to be satisfactory, as similarly shaped high- and low- turbulence intensity areas can be identified on both PIV- and LES- based subfigures for all considered planes. However, differences in the general level of the resolved turbulent kinetic energy (basically visible in all areas of the considered planes and especially noticeable inside the jet core) do exist, as LES consequently

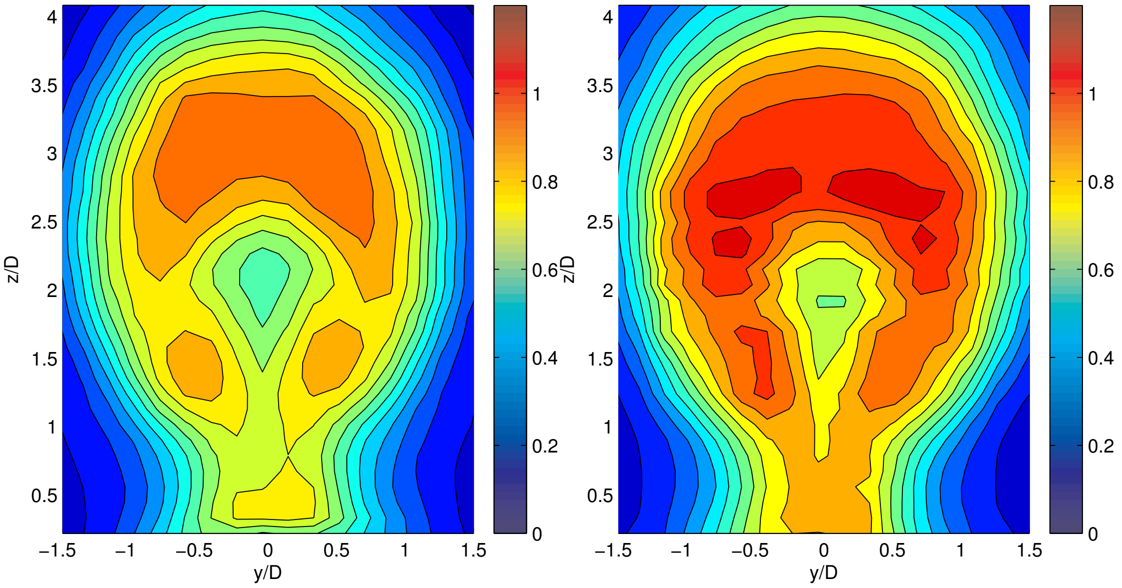

(a) x/D=1 - PIV

(b) x/D=1 - LES

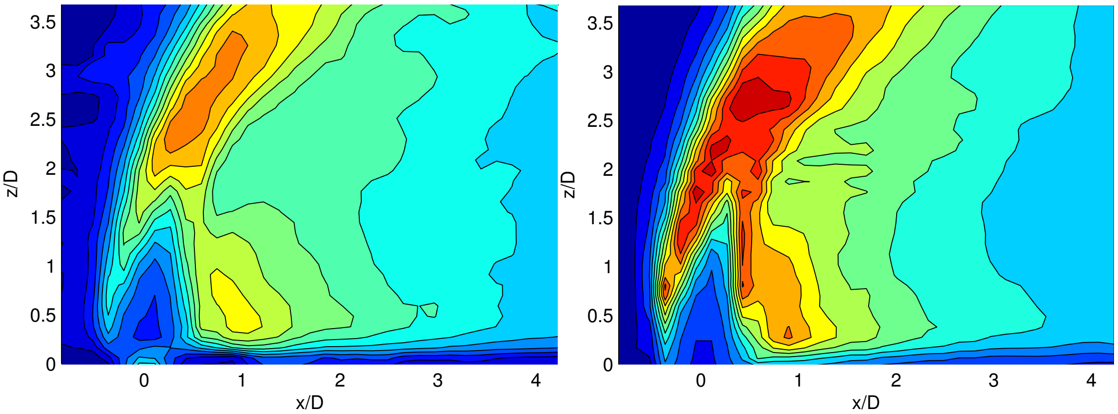

(c) y/D=0 - PIV

(d) y/D=0 - LES

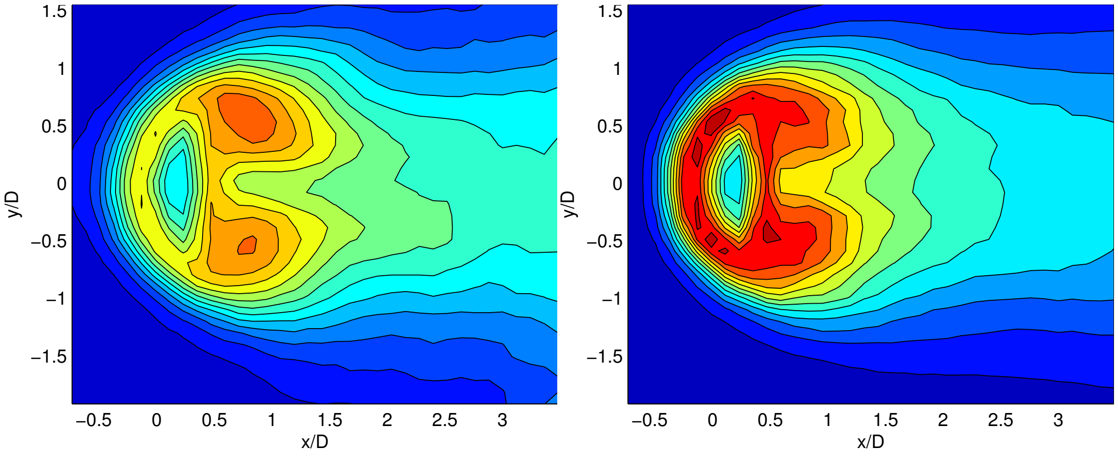

(e) z/D=1.33 - PIV

(f) z/D=1.33 - LES

Figure 4.36: Turbulent kinetic energy k/U_∞^2 in the considered planes resolved by PIV and LES. Contour level scale used in subfigures (a) and (b) is applied on all other subfigures and the difference between two contour levels in all subfigures is $0.1\,U_\infty^2$.

indicates higher turbulence intensities, than those revealed by the PIV. This difference can in principle be implicit to the applied analysis, as an interpolation of velocities from the numerical LES grid to the grid used in the present POD analysis will include the effect of all scales resolved by the numerical grid used in the basic computations, while limited resolution capabilities, a sort of low-pass filtering and area averaging implicit to PIV measurements will practically "*remove*" the smallest scales from the measured dataset.

Each POD analysis relies on the kinetic energy contained in the underlying dataset considered. Previously it was shown that the first 2 POD modes in all investigated planes represent similar flow structures regardless the dataset used. Therefore it seems reasonable to assume that the first modes represent similar levels (on the absolute basis) of the total turbulent kinetic energy resolved. At the same time the total (absolute) amount of the kinetic energy in the PIV- based dataset is lower than in its LES- based counterpart; hence it can be expected that the dominant structures in the PIV- based analysis contain relatively more energy than the relative energy contained in the same LES- based structures. This can most probably explain the qualitative but not quantitative agreement between energy distributions in the first couple of POD modes presented in this section.

From the above argumentation it can be deduced further, that general agreement between the present PIV- and LES- based POD analyses can only be expected on the level of dominant flow structures; hence only the agreement between the most energetic (the first couple of) modes can therefore be expected.

4.6.3 3D POD

In the previous paragraph the POD method has been applied on datasets from three mutually perpendicular planes in the near-field flow of the jet. Two different sequences of data were used in those analyses (numerically and experimentally obtained ones) and the achieved 2D results were compared and discussed. Even though many relevant flow features can be revealed by this type of analysis, a generally better understanding of different flow structures can be obtained by studying results of a corresponding 3D analysis. For that reason a new 3D POD analysis has been conducted.

The investigated near-flow JICF region ($-1 < x/D < 4$,$-1.5 < y/D < 1.5$ and $0 < z/D < 4$) was discretized by app. 500 000 points, where points in the considered domain were mutually equidistantly displaced by 0.05 D. The underlying LES dataset comprised of app. 1.2 million points in the regarded region. Data points for POD analysis were correspondingly interpolated, using the second order inverse distance interpolation technique. Results of this analysis are presented in the following.

Numerical investigations of the JICF flow case presented in Appendix A, showed that it was very difficult to obtain a perfect correspondence between LES results and experimental (LDA) measurements. As argued in section 4.4, majority of the observed (relatively small) discrepancies can be attributed to some differences in the numerical and experimental flow configurations. So relatively early in the course of this project, it became clear that the synthetic LES based JICF flow can realistically resemble the main characteristics of a general JICF flow case, which was later fully confirmed by e.g. comparisons of the 2D POD results presented in the previous paragraph. Whereas in the case of the 2D POD analysis it was highly important to consider the experimental flow case and its best numerical counterpart (case LES 6), the present 3D POD analysis is not bound by the same constraints. Therefore the underlying dataset used in this 3D POD analysis has been attained simultaneously with the studies presented in Appendix A, i.e. much earlier then the corresponding dataset used in the 2D POD analysis. In this way the computational overhead (in terms of the necessary CPU time) could be distributed over a longer time period. Thus the 3D POD analysis is based on case LES 7 from Appendix A and the longest (in time units) overall computation conducted in the course of this whole project.

The dataset used in the 3D analysis was extracted during the total time period corresponding to 100 FLTs. Making the same estimates as previously, the present 3D dataset (comprising 1000 samples) will contain app. 300 statistically uncorrelated samples. As the agreements between PIV and LES based 2D POD analyses showed good general agreement despite the fact that the underlying LES dataset contained only app. 90 uncorrelated samples, the present 3D analysis is conducted on the full set of 1000 samples.

Results of the 2D POD analyses had some distinct characteristics - e.g. the first two POD modes, at all examined locations were noticeably dominant, as they represented significantly larger amount of the total turbulent kinetic energy compared to the remaining modes. As all three 2D POD analyses were separately conducted i.e. a single analysis took into account only the "*local*" dataset in the examined plane, it is interesting to investigate whether the first two 2D POD modes in reality represent traces of the same 3D structure(s). In order to do this, the results of the 3D POD analysis are extracted on locations corresponding to the planes considered in the 2D POD analyses. Results are presented on Figures 4.37 and 4.38 and Table 4.6. It should be noted that different scaling factors, compared to ones used in the

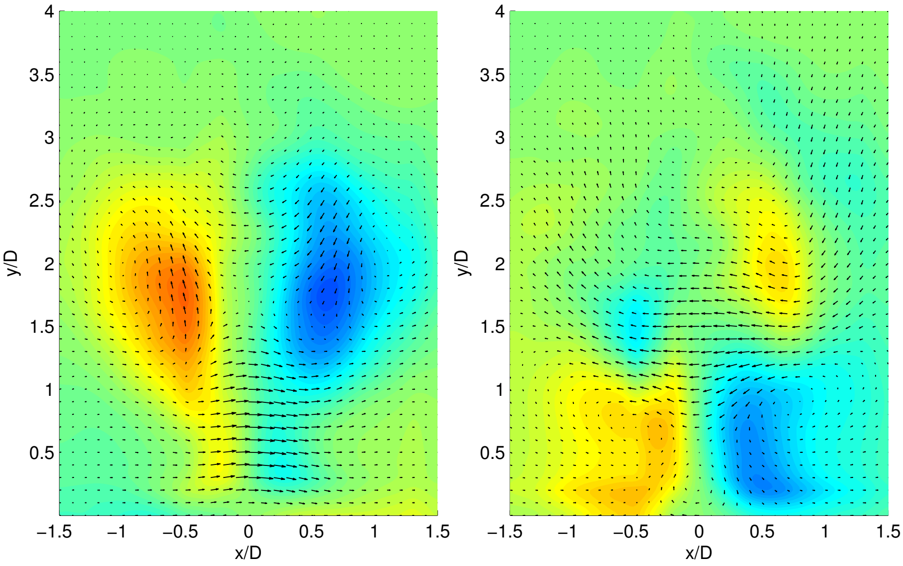

(a) x/D=1 - Mode 1 (b) x/D=1 - Mode 2

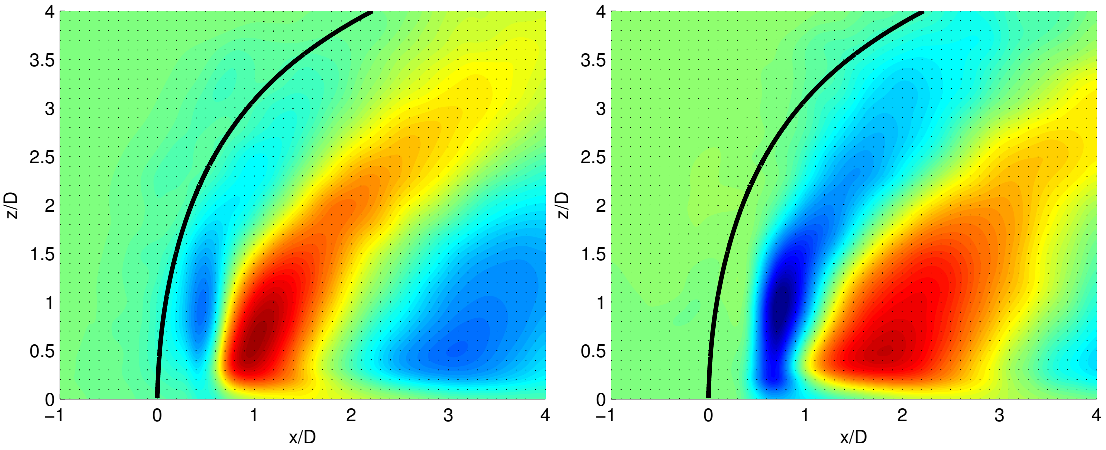

(c) y/D=0 - Mode 1 (d) y/D=0 - Mode 2

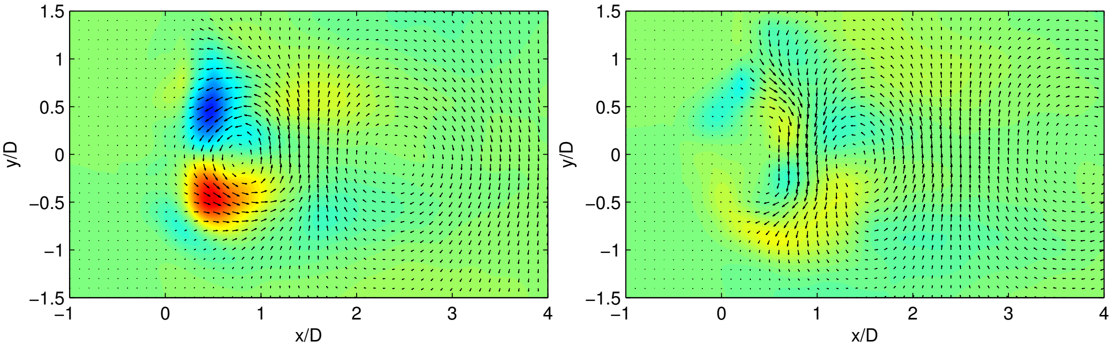

(e) z/D=1.33 - Mode 1 (f) z/D=1.33 - Mode 2

Figure 4.37: Results of the 3D POD analysis extracted on locations corresponding to the planes of 2D POD analysis.

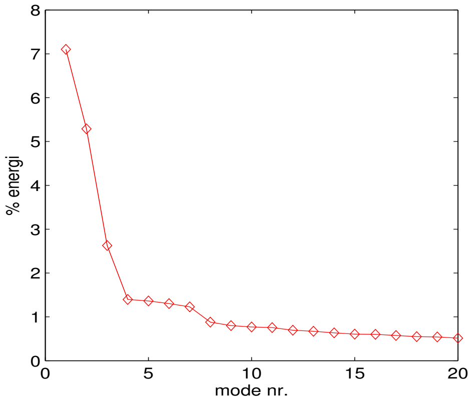

Figure 4.38: Relative energy content in the first 20 POD modes in the 3D POD analysis.

Mode number	1	2
V_{rel} - $y/D = 0$ plane	10.56	8.60
U_{rel} - $x/D = 1$ plane	0.64	0.54
W_{rel} - $z/D = 1.33$ plane	0.22	0.17

Table 4.6: Extent of the relative out-of-plane motion in the first two POD modes in planes corresponding to the 2D POD analysis.

previous paragraph, are used in the contour/vector plots in Figure 4.37 in order to obtain a suitable basis for comparisons with the 2D POD results.

Inspecting the results from Figures 4.37 and 4.38 and Table 4.6, many similarities between 3D and 2D POD analyses can be observed. First, the 3D analysis clearly produces two dominant modes as well (Figure 4.38) and the ratio of out- vs. in- plane velocities in all investigated planes (Table 4.6) match closely with the corresponding 2D results (Tables 4.3, 4.4 and 4.5).

A general good agreement between 3D and 2D results from $x/D = 1$ plane is visible from Figures 4.37(a) - (b) and Figure 4.30. Clearly, the traces of vortical structures in mode 1 and a similar in-plane motion pattern in both modes is seen in both analyses.

The dominant out-of-plane motion in modes 1 and 2 in $y/D = 0$ plane shows a very good agreement (Figures 4.37(c) - (d) and Figure 4.27) while traces of two vortices in the dominant in-plane motion in modes 1 and 2 in $z/D = 1.33$ plane (Figures 4.37(e) - (f) and Figure 4.33) also agrees well across the considered analyses.

From the above considerations it is evident that results regarding the first two POD modes in both 2D and 3D analyses agree well. Therefore it can be concluded that the dominant modes revealed by the 2D POD analysis do represent traces of the same 3D coherent structures.

On the other hand it is interesting to investigate what kind of 3D structures are revealed by the 3D POD analysis. Results of this study are presented in the following.

It should be noted that a full 3D POD flowfield analysis has not been applied often in the past. The main reason for this is a considerable computational effort connected with it, especially in cases where a direct (classical) POD analysis is utilized. However in the work of Rempfer and Fasel [87] a full 3D snapshot POD analysis was applied in order to investigate dominant structures in a transitional flowfield of a boundary layer. Results of Rempfer and Fasel's

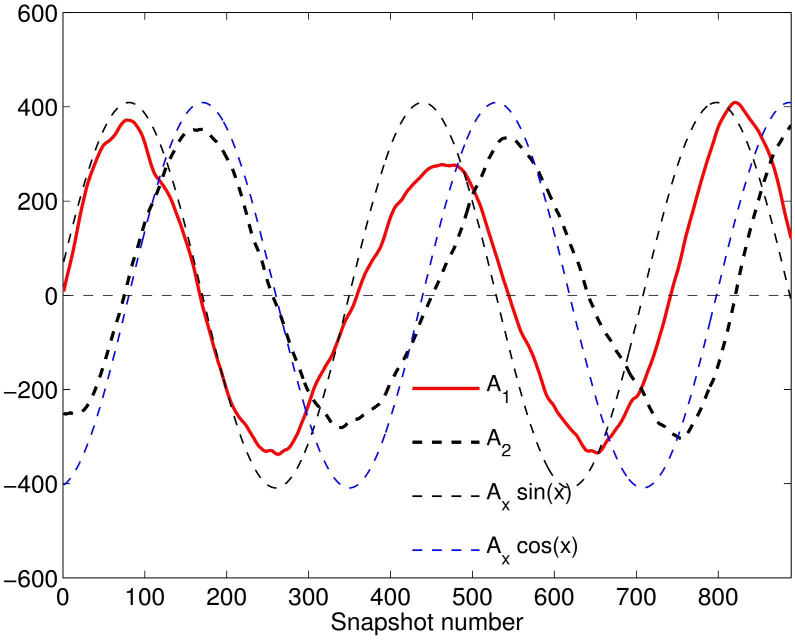

Figure 4.39: Time history of the first two POD coefficients in the 3D analysis. Δt^* between the snapshots is $\Delta t^* = \Delta t U_\infty / D = 0.0313$. x refers in this context to a variable which follows the number of snapshots, while $A_x = (A1_{max} + A2_{max})/2$.

analysis showed that POD modes appeared in pairs i.e. two subsequent modes appeared to represent almost equal levels of energy and that the corresponding POD coefficients, besides having a similar maximal magnitude appeared as phase-shifted in time. All of this indicated that both considered modes represented the same "*spatially displaced*" coherent structure. They suggested therefore that a better way of representing a coherent structure at a time t^n on the energy level contained in those two modes ($\lambda_i \approx \lambda_{i+1}$) is given by their superposition as:

$$a_i^n \phi^i + a_{i+1}^n \phi^{i+1}, \tag{4.27}$$

where a_i^n is the considered POD coefficient and ϕ^i is the corresponding POD mode.

In Figure 4.39 the time evolution of the first two POD coefficients of the 3D POD analysis is presented. From the Figure it is clear that the coefficients behave in a very similar way, have a small difference in maximal magnitude and are practically phase-shifted in time. The period can be app. estimated to $T^* = T\,U_\infty/D = 11.25$ corresponding to $f^* = 1/T^* = 0.09$. To emphasize the mentioned observation further, the sine and cosine functions, with an average of the maximum values of A_1 and A_2 coefficients as amplitude, are superimposed the analyzed coefficients in Figure 4.39, clearly underlining the phase shifted coefficient behavior. Utilizing the results of Rempfer and Fasel's analysis, this indicates that both mode 1 and 2 are directly connected to the same 3D coherent structure, which changes its shape (degenerate) and is convected downstream in time.

In the final part of this 3D POD analysis it will be shown that the first two POD modes are directly connected to the CVP and wake vortex structures. As CVP has a mean flow definition - see Figure 4.26 on page 72 and e.g. Rivero et al. [88], it is difficult to interpret the first POD modes on their own without relating them directly to the mean flow field. However

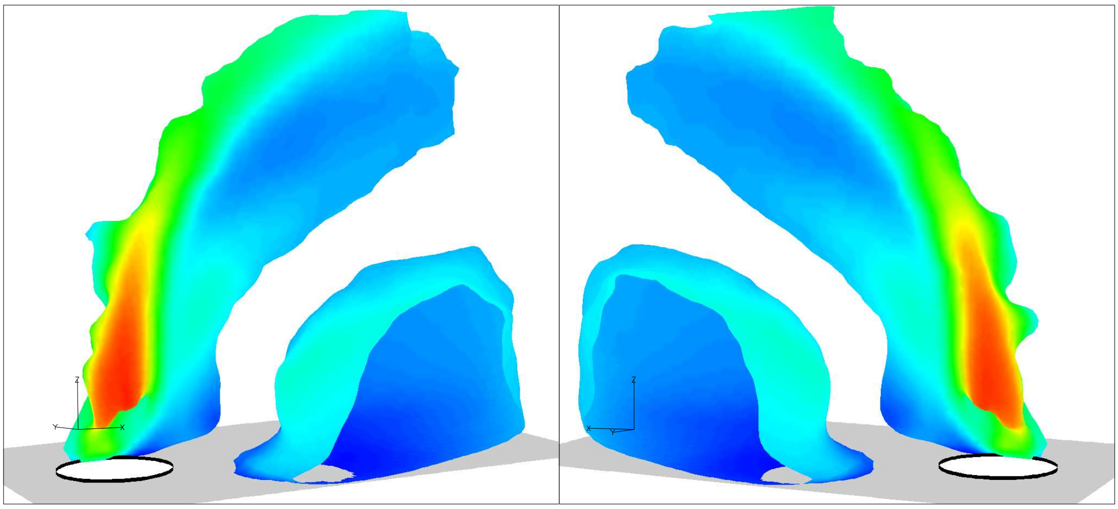

(a) U - Mode 1, IsoSurface = u_{1_0} (b) U - Mode 1, IsoSurface = $-u_{1_0}$

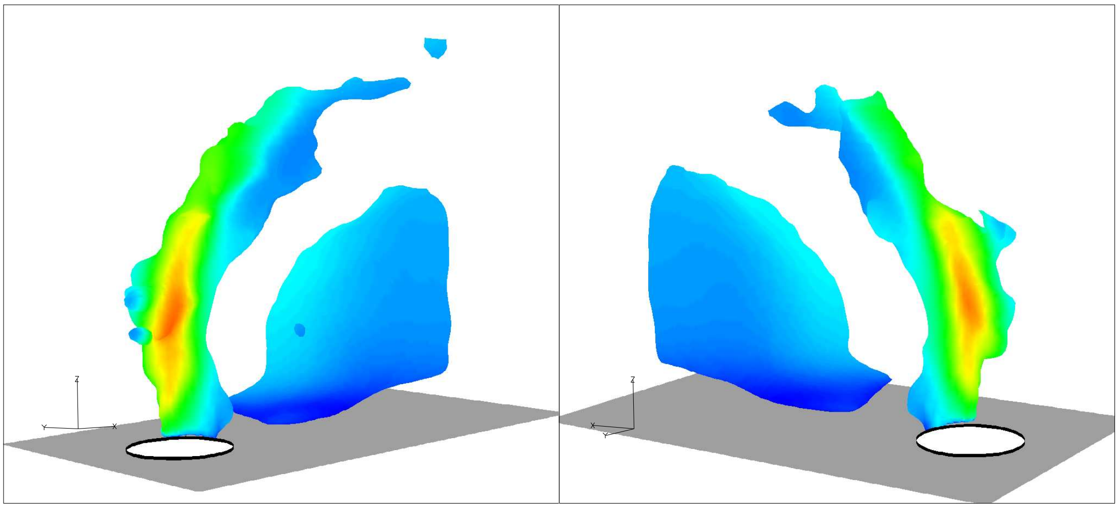

(c) U - Mode 2, IsoSurface = u_{2_0} (d) U - Mode 2, IsoSurface = $-u_{2_0}$

Figure 4.40: Isosurfaces, colored by the velocity magnitude, representing structures revealed by $U-$ velocity component of POD modes 1 and 2. Two isosurfaces of mode 1 - (a), (b) and mode 2 - (c), (d) have the same magnitude but the opposite sign - u_{1_0} and u_{2_0} refer to two chosen plotting values.

inspecting the first POD modes alone gives some interesting depictions of flow structures in the JICF flow field. The first two POD modes, shown as isosurfaces of $U-$ and $W-$velocity POD components are presented in Figures 4.40 and 4.41. It should be noted that isosurfaces presented in the following are chosen in such a way that the presented structures are visualized most clearly.

In Figures 4.40(a) - (b) two isosurfaces colored with the velocity magnitude, with same magnitude and opposite sign, of the U-velocity POD component from mode 1 are depicted. A clear standing structure, originating at the lateral sides of the jet is detectable from those subfigures. Besides that, another structure located in the jet-wake region is clearly visible. In a similar way two isosurfaces of the U-velocity POD component from mode 2, having the

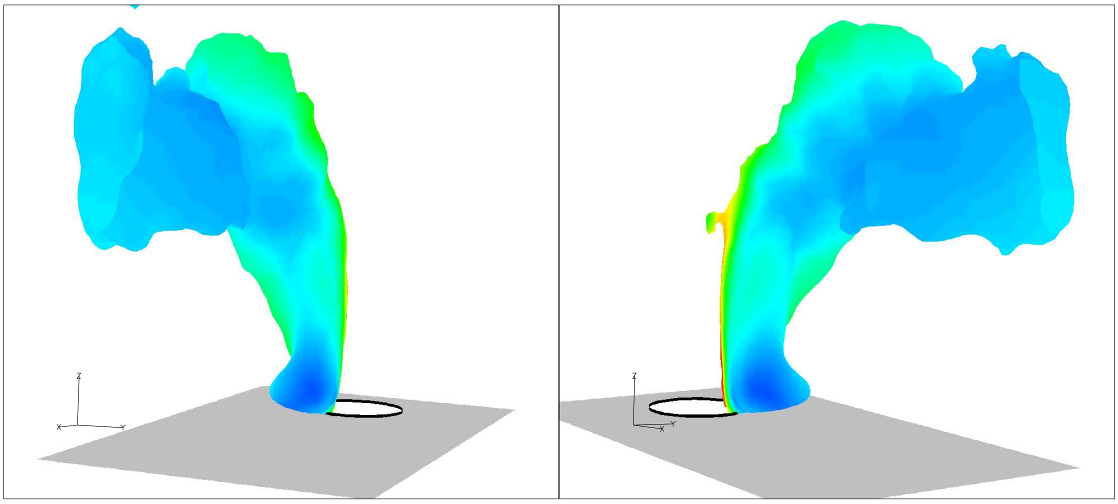

(a) W - Mode 1, IsoSurface = w_{1_0} (b) W - Mode 1, IsoSurface = $-w_{1_0}$

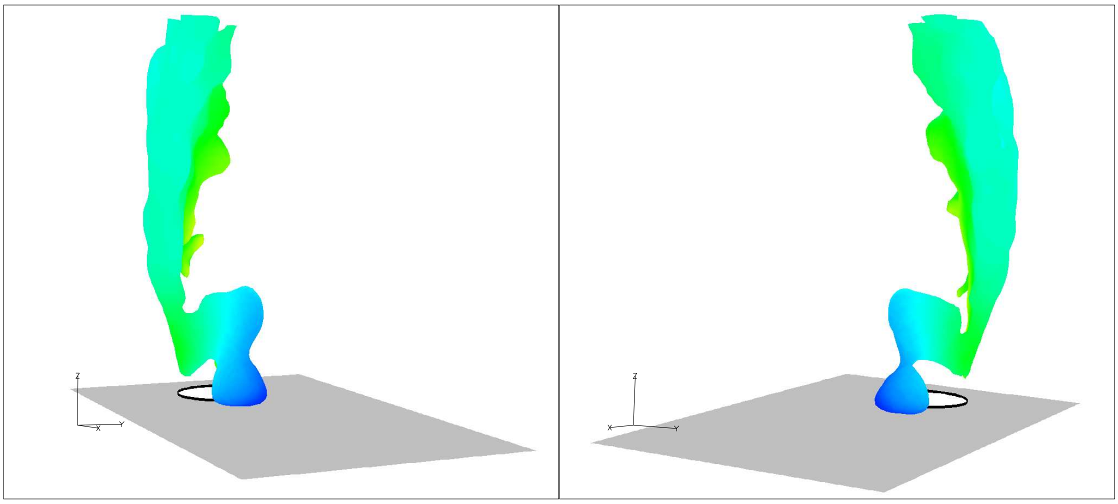

(c) W - Mode 2, IsoSurface = w_{2_0} (d) W - Mode 2, IsoSurface = $-w_{2_0}$

Figure 4.41: Isosurfaces, colored by the velocity magnitude, representing structures revealed by $W-$ velocity component of POD modes 1 and 2. Two isosurfaces of mode 1 - (a), (b) and mode 2 - (c), (d) have the same magnitude but the opposite sign - w_{1_0} and w_{2_0} refer to two chosen plotting values.

same magnitude and opposite sign, are depicted in subfigures 4.40(c) - (d). Again two clear structures, one originating at the lateral side of the jet and another residing in the jet-wake region are detectable here.

Similarly, $W-$velocity POD component isosurfaces of modes 1 (subfigures (a) and (b)) and 2 (subfigures (c) and (d)) are presented in Figure 4.41. Yet again, two isosurfaces colored with the velocity magnitude, with same magnitude and opposite sign are depicted in corresponding subfigures. Here, some structures placed at the position where CVP resides in the mean JICF flow field can be seen from the Figure. Considering both Figures 4.40 and 4.41 it becomes clear that POD modes 1 and 2 are directly associated with the dynamics of the CVP and wake vortex related structures in the currently investigated JICF flow.

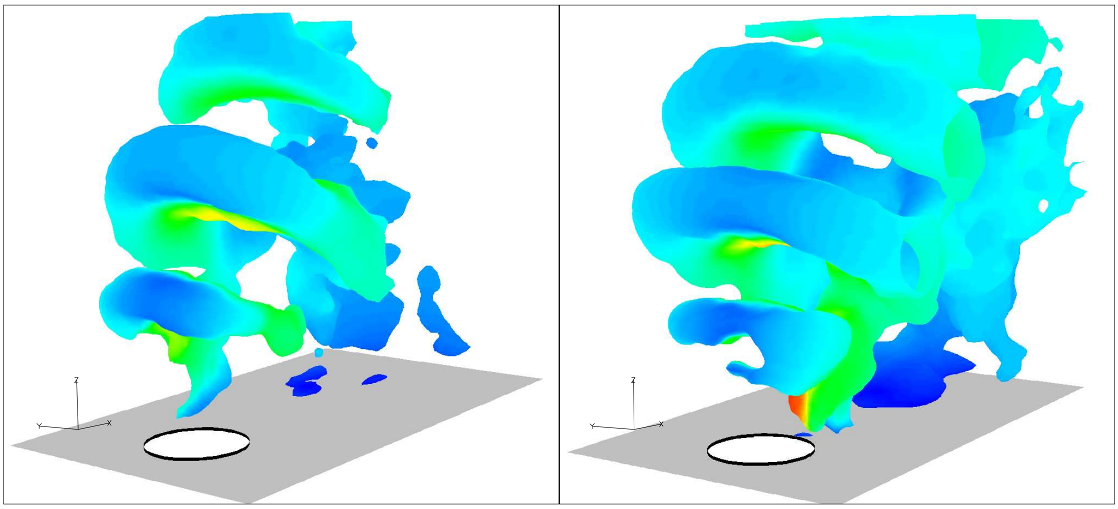

(a) Constant U IsoSurface - Mode 4 (b) Constant U IsoSurface - Mode 5

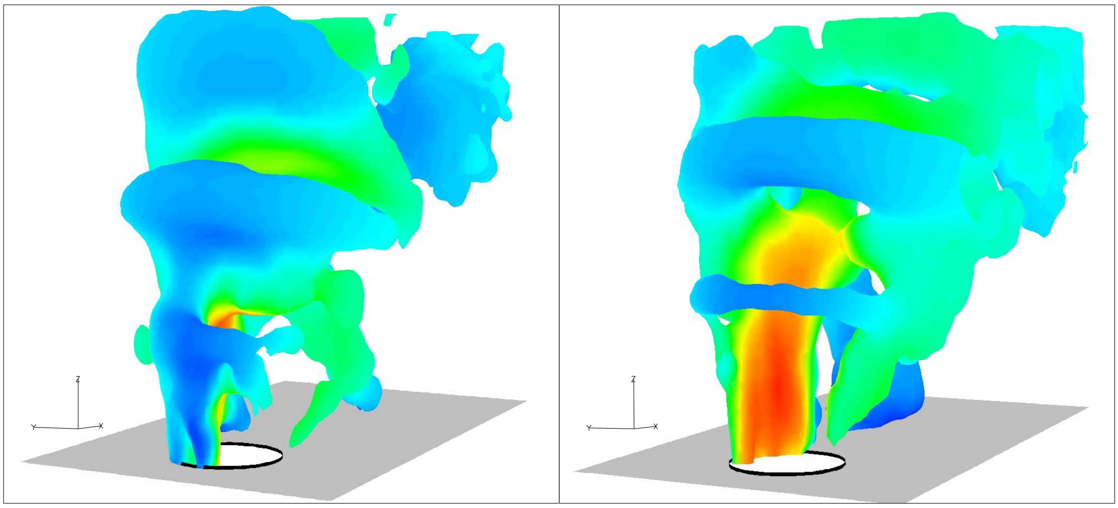

(c) Constant W IsoSurface - Mode 4 (d) Constant W IsoSurface - Mode 5

Figure 4.42: Isosurfaces, colored by the velocity magnitude, representing the coherent structures revealed by $U-$ and $W-$ velocity component of POD modes 4 and 5.

Figure 4.42 depicts structures revealed by modes 4 and 5. It is evident that the dominant structures depicted are the jet shear-layer vortices (see also Figure 4.28). A closer inspection of the results indicates that the same shear-layer vortices are practically spatially displaced in the streamwise direction while moving from mode 4 to mode 5 - from subfigures 4.42(a) to (b) and from 4.42(c) to (d).

From Figures 4.40 and 4.41, where structures depicted by modes 1 and 2 are presented, it is evident that those modes are connected to CVP and wake vortex related structures, but it is generally difficult to directly relate structures presented in those Figures to coherent structures of the JICF flow field. In the recent work of Meyer et al. [69], who analyzed experimentally obtained data of the currently investigated JICF flow, some indications of an interaction between different vortices in the wake region are given. Based on their 2D POD analysis, Meyer et al. [69] argues that interaction between the standing (hanging) vortex of

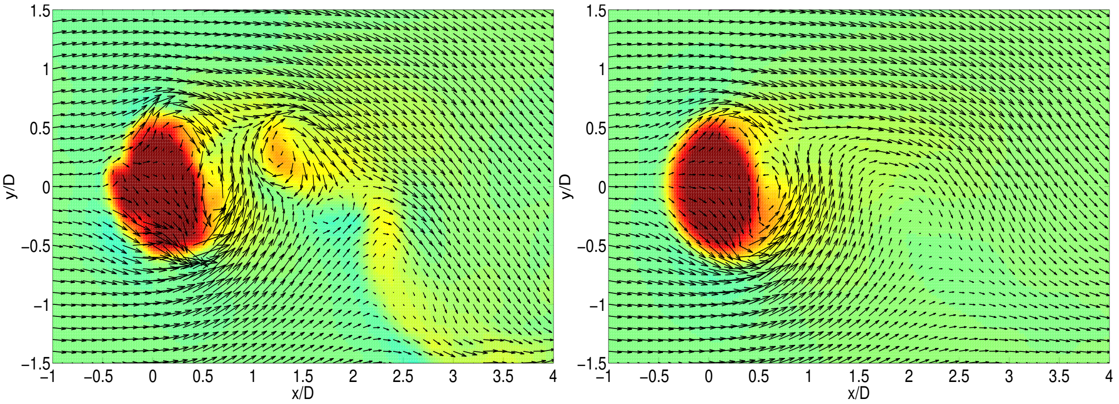

(a) Snapshot

(b) Reconstruction

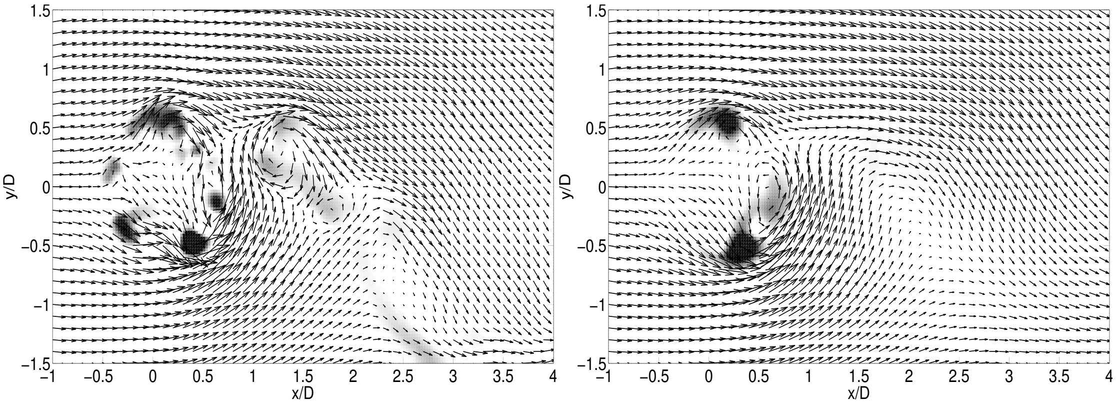

(c) Q-criterion applied on the Snapshot

(d) Q-criterion applied on the Reconstruction

Figure 4.43: Snapshot of the $z/D = 0.55$ plane (a) and its reconstruction (b). Q-criterion applied on the snapshot (c) and its reconstruction (d). The reconstruction is based on the first two POD modes.

Yuan et al. [117] (see Figure 4.1 on page 34) and wake vortices in the downstream region of the jet entry point can be identified by analyzing a POD based flow reconstruction of the JICF flow field. This analysis showed also that the best depictions of the interaction process can be obtained by analyzing $z/D =$ const. planes.

Figure 4.43 depicts several aspects of a representative snapshot of the JICF flow field at $z/D = 0.55$ position. From subfigure 4.43(a), where snapshot of the velocity field is presented showing the in-plane velocity components as vectors and out of plane velocity component as contour plot, various vortical structures can be identified. A vortex positioned at $(x/D,\ y/D) = (0.6,\ -0.1)$ another one at $(x/D,\ y/D) = (1.25,\ 0.3)$ and third one at $(x/D,\ y/D) = (1.75,\ -0.2)$ can be clearly recognized indicating that a continuous vortex-shedding process takes place in the wake region. On the corresponding POD based reconstruction, which is obtained by adding only the first two POD modes to the mean flow field, - subfigure 4.43(b), it is seen that only vortices in the vicinity of the jet can be identified. Significant variations in position of shaded vortices in the wake region (this can be visualized by inspection of several snapshots of the $z/D = 0.55$ plane - not shown here), indicate that the downstream transport of the wake vortices do not follow a regular pattern; hence each of the mentioned vortices singly is not capable of leaving a clear trace in the first POD modes.

It has been shown in section 4.5 that a vortex-identification method such as Q-criterion (Hunt et al. [41]) can be used as a superior vortex-identification tool. In subfigures 4.43(c) and (d) results of an application of the Q-criterion on the snapshot from subfigure 4.43(a) and its reconstruction from subfigure 4.43(b) are presented. As seen form the subfigure 4.43(c), various vortices on the upstream side of the jet, actually not directly seen in the snapshot itself (traces of shear-layer vortices) as well as vortices in the wake region can be identified. However, the most interesting part here is represented by three vortices seen on both subfigures 4.43(c) and (d) positioned at $(x/D,\ y/D) = (0.45,\ -0.5)$, $(x/D,\ y/D) = (0.4,\ 0.5)$ and $(x/D,\ y/D) = (0.65,\ -0.2)$. As hypothesized in Meyer et al. [69], the first two vortices should represent traces of standing (hanging) vortices of Yuan et al. [117], while the last one should represent traces of a wake vortex.

From Figure 4.39 it is seen that time variation of A_1 and A_2 coefficients closely follow a phase shifted pattern of sine and cosine functions. Small variations in amplitude and period of both coefficients seen in Figure 4.39 can probably be attributed to some random flow variations. In order to diminish the effect of random variations on the present analysis, coefficients are in the following part assumed to follow an idealized sine and cosine patterns indicated in Figure 4.39.

In order to better analyze vortical structures seen in subfigures 4.43(c) and (d) the present investigation is continued in 3D - Figure 4.44. Subfigures of Figure 4.44 illustrate iso-surfaces, colored by ω_z, of the same positive Q value, where Q-criterion has been applied on flow reconstructions based on the first two POD modes with idealized coefficients (the modes are as previously added to the mean flow field). Moreover, subfigures of Figure 4.44 actually follow the development of structures depicted in subfigure 4.44(a) throughout approximately half of the periodical cycle of coefficients A_1 and A_2 (180 snapshots - cf. Figure 4.39).

Generally, in Figure 4.44 three to four distinct vortical structures can be identified. Two of them, positioned on lateral edges of the jet, are visible on all subfigures. They slightly change their inclination angle with the z-axis (or jet trajectory) but always appear at approximately same domain position. According to the definition of Yuan et al. [117] they can be identified as hanging vortices.

Inspecting the subfigure 4.44(a) in a more detailed manner two additional structures, both attached to the corresponding hanging vortex can be identified. The process of continuous and alternating creation and destruction of these structures can be followed throughout subfigures 4.44(a)-(f). In subfigure 4.44(a) it is seen that one of the mentioned structures is attached to the left hanging vortex, while the other one is just about to be created in the close proximity of the right hanging vortex. Following the vortex dynamics further - subfigure 4.44(b), one can observe that the vortex connected to the left hanging vortex become detached from it, while the vortex connected to the right hanging vortex grows in size, while it is convected downstream.

The growth and downstream convection of the vortex attached to the right hanging vortex can be followed through subfigures 4.44(c)-(e) and subfigure 4.44(f) depicts a mirror image of subfigure 4.44(a), indicating that a new analogous process of creation and destruction of the attached/detached vortices from the hanging vortices takes place.

The described process clearly elucidates the process of a dynamical interaction of wake vortices and corresponding hanging vortices in the JICF flow. Furthermore, from subfigures 4.44(a) and (f) a clear indication of the significant role the hanging vortex plays in the creation process of wake vortices is underlined. It is seen that the wake vortex practically originates

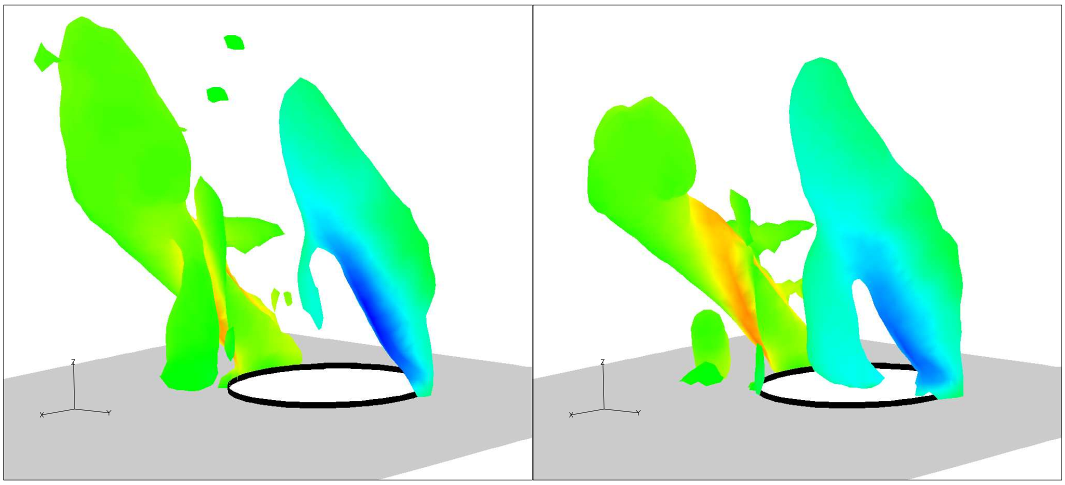

(a) $(A_1,\ A_2) = (281.0,\ 263.1)$

(b) $(A_1,\ A_2) = (78.6,\ 376.9)$

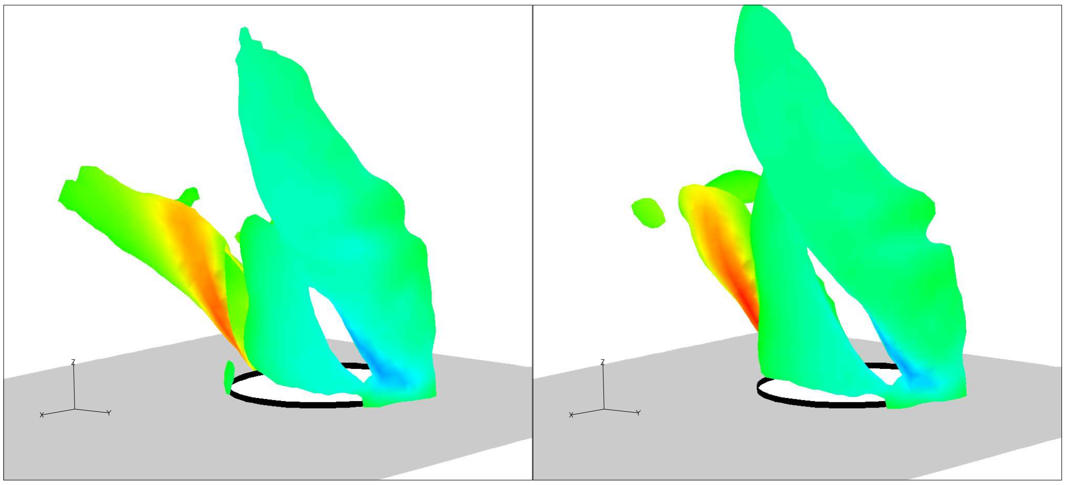

(c) $(A_1,\ A_2) = (-152.4,\ 353.6)$

(d) $(A_1,\ A_2) = (-327.9,\ 201.7)$

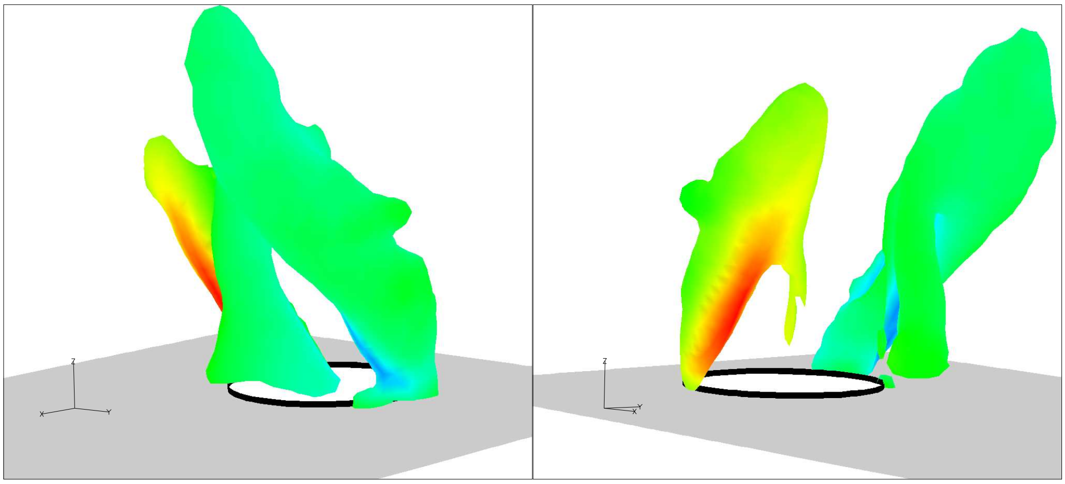

(e) $(A_1,\ A_2) = (-384.3,\ -23.6)$

(f) $(A_1,\ A_2) = (-244.2,\ -297.7)$

Figure 4.44: Iso-surfaces, colored by ω_z, of the same positive Q value, with Q-criterion being applied on flow reconstructions based on the first two POD modes with idealized coefficients. Subfigures (a)-(f) follow the development of structures depicted in subfigure (a) throughout approximately half of the periodical cycle of coefficients A_1 and A_2 (180 snapshots - cf. Figure 4.39). A_1- and A_2-coefficient values are indicated in the corresponding subfigures.

from the hanging vortex and grows in size in a tornado vortex like manner by "*sucking up*" the boundary layer fluid.

The current findings are in close agreement and provide an additional support to the recent investigations of Meyer et al. [69].

Finalizing the presentation of various POD analyses, it can be concluded that LES results combined with the POD method can be a powerful tool in the investigation of different coherent structures in an analyzed flow field.

4.7 Summary

In the present Chapter an extensive investigation of various characteristics of the JICF flow field have been conducted. After considerable effort has been put into generation of realistic boundary conditions, both on the jet and on the cross-flow side, the LES results have been successfully validated against the available LDA measurements. As the validation basis between experiment and LES calculations has been established, the analysis of various coherent structures pertinent to the JICF flow have been carried out, which led to identification of many coherent structures previously experimentally visualized in the corresponding JICF fields. In the last part of this Chapter a POD analysis of the JICF flow was conducted. In the 2D part of the POD analysis, the results of comparable investigations performed on the experimentally (PIV) and numerically attained datasets, showed a good overall agreement. The POD analysis was then extended to 3D, shedding some new light on the disputed question of the origin of the wake vortices.

Chapter 5

Investigations of the 2D Bump flow

Turbulent shear layers represented by boundary layers, mixing layers, jets etc. are frequently encountered in different industrial and natural flows. Equilibrium boundary layers are a special class of those layers in which the production and dissipation of turbulent kinetic energy remain in balance for a major part of the layer. In the context of both experimental and numerical investigations, those layers proved to provide a suitable framework for continuous progress in understanding the various properties of turbulent flows. However most of the industrially relevant flows are in general subjected to different perturbations in the external conditions such as a pressure gradient, surface curvature and roughness, blowing and suction etc. In those flows, the well-defined properties of the equilibrium flow cannot be directly utilized; hence general knowledge and the general ability to predict the main features of non-equilibrium flows are still limited.

In the context of this work, a LES study of the non-equilibrium boundary layer flow over a wall mounted bump (represented by a part of a cylindrical shell) is conducted - Figure 5.1. The underlying experimental data used for comparisons are LDA measurements of Jensen [42].

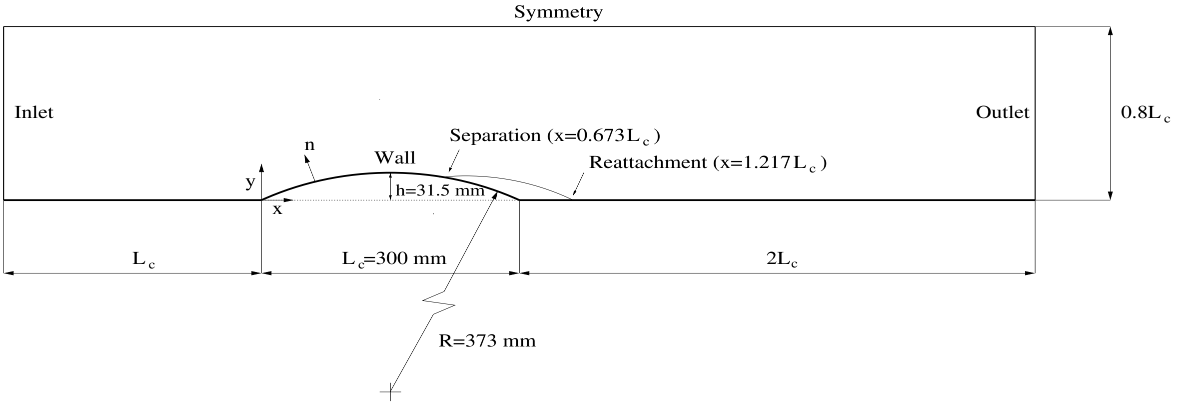

Figure 5.1: Schematic description of the analyzed $2D$ bump flow geometry. Coordinate system origo is, as indicated, located at the bump leading edge. n refers to a coordinate direction perpendicular to the wall surface. Extension of the spanwise domain - not indicated on the Figure, is L_c. Periodic boundary conditions are applied in this direction.

The turbulent boundary layer passing over a bump has quite complex flow characteristics, despite the apparent geometrical simplicity of the considered system (cf. Figure 5.1). The sharp and abrupt perturbations in the longitudinal surface geometry (flat to convex to flat) cause changes in the streamwise pressure gradient i.e. an adverse pressure gradient in the bump upstream region which changes to a favorableone in the flow region approaching the bump apex, which returns to an adverse one in the downstream region of the bump apex and finally turns to a favorable one over the flat plate downstream of the bump.

5.1 Previous Investigations

Effects of streamline curvature on the boundary layer flow have been extensively investigated in the past (e.g. Bandyopadhyay and Ahmed [8], Patel and Sotiropoulos [80] among others). Many of those experimental investigations were designed in a way that a considerable effort has been put into elimination of the additional effects (like the streamwise pressure gradient) from the considered flow cases. On the other hand the effects of a streamwise pressure gradient on the boundary layer flow have been studied by various investigators (e.g. Spalart and Watmuff [101], Fernholz and Warnack [29], Warnack and Fernholz [112] among others), but as pointed out in Webster et al. [113], there is no evidence that the response of the boundary layer to a series of external perturbations can be regarded as a simple superposition of the responses originating from independent perturbations.

The response of a boundary layer flow to the combined effects of surface curvature and pressure gradient in the flow over a two-dimensional curved hill has been the subject of several experimental (e.g. Baskaran et al. [10, 11], Webster et al. [113]) and numerical (e.g. Wu and Squires [115], Kim and Sung [49]) investigations with flow geometries and general flow set-up relatively comparable to the one examined in the present study. The study of Baskaran et al. [10], who examined a 2D hill consisting of two small concave and a prolonged convex surface and a wing section corresponding to the convex surface of the 2D hill (height-to-chord ratio was 0.1 in both cases), showed that an *"internal layer"*, typically triggered by the discontinuity in the surface curvature, emerges in the flow over the hill. This layer is best visualized through the profiles of turbulence quantities, where so-called *"knee points"* can be identified. The studies of Webster et al. [113] (height-to-chord ratio was 0.08 in this case) showed furthermore that pressure gradient effects are the main reason for initiation of the internal layer, while Wu and Squires [115], who numerically examined the flow configuration of Webster et al. [113], suggested that the pressure gradient, by causing abrupt changes in magnitude of the wall-friction, enhances the near-wall turbulent stresses and significantly impacts the creation process of the internal layer.

It should be noted that the present study, with height-to-chord ratio of ≈ 0.1, has a similar geometrical set-up as the mentioned studies, but the Reynolds number, based on the bump height h and the free-stream velocity U_∞ - $Re_h = U_\infty \, h/\nu = 1950$ is much lower in the present case, than in the corresponding studies of Webster et al. [113] - $Re_h = 20\,000$ and Baskaran et al. [10, 11] - $Re_h = 270\,000$.

The motivation behind the present LES investigation of the $2D$ bump flow is further enhanced by the recently conducted LES study of Reck [86], where a set of delta wings resembling the vortex generator system, was mounted on the same geometrical set-up of the present $2D$ bump flow case. This numerical study of a highly complex flow did not reproduce various experimentally measured quantities satisfactorily. As many different parameters can directly contribute and basically cause a failure of LES to reproduce different measured quantities well, the current study can be regarded as a precursor or baseline flow case study of a more complex flow analysis of the $2D$ bump flow with mounted vortex generator system.

The general ability of LES to resemble experimental measurements in already complex and challenging flow passing a $2D$ bump can then be regarded as direct indicator of how well LES in general can be expected to reproduce basic characteristics of an even more demanding $2D$ bump flow, which includes vortex generators.

5.2 Numerical Configuration of the 2D Bump Flow Case

Outline of the computational domain is illustrated on Figures 5.1 and 5.2. It is seen that the domain extensions chosen are $L_x = 3L_c$, $L_y = 0.8L_c$ and $L_z = L_c$ where L_x, L_y and L_z refer to streamwise, wall-normal and spanwise directions respectively. Comparing the chosen computational geometry with calculation domains of Wu and Squires [115] and Kim and Sung [49], it can be observed that all domain extensions in the present study are at least 30% larger than geometrical extensions in the mentioned studies.

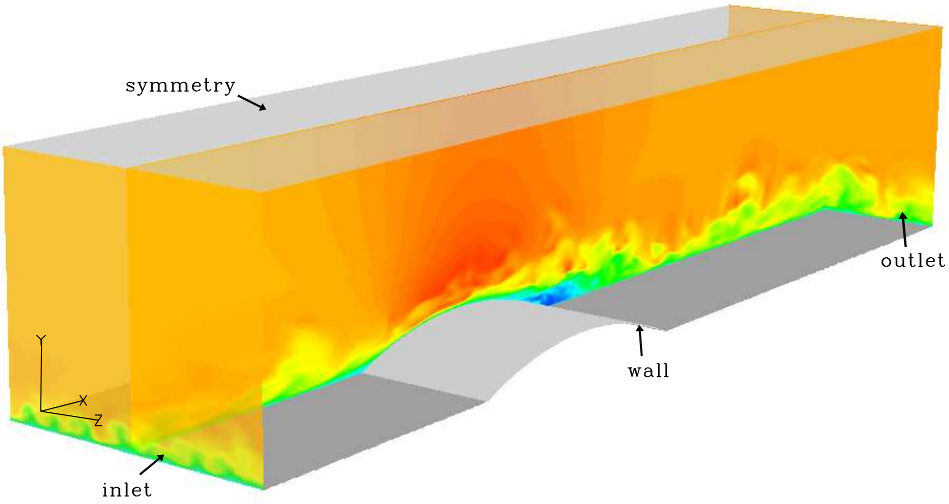

Figure 5.2: Outline of the computational set-up corresponding to the considered flow case. An instantaneous snap-shot of the streamwise velocity component from the investigated flow is visualized on three different planes - inlet, outlet and plane corresponding to the half domain width in the spanwise direction. Note that positions of some domain boundaries, with the corresponding boundary conditions applied in the computations, are included in the Figure. Periodical boundary conditions are applied in the spanwise direction - they are not illustrated in the Figure.

The computational mesh chosen consists of 576x128x128 cells in streamwise, wall-normal and spanwise directions respectively. The cells are equally distributed only in the z direction, while stretching functions are applied in both streamwise and wall-normal directions. Outline of the two basic grid configurations, in a flow region representing vicinity of the bump ($x - y$ plane), is presented in Figure 5.3. Both grids shown have a resolution of 576x128 cells in the $x - y$ plane, but the meshing strategy utilized in generating them is different. In the first case (Figure 5.3(a)) the grid is considerably distorted in the most of the $x - y$ plane in order to accommodate a full grid-surface-orthogonality in the bump region. Here, the stretching function is applied in the streamwise (x) direction at the bottom wall but the grid distances at the upper symmetry boundary are kept constant. In the second case (Figure 5.3(b)) the meshing strategy at the upper symmetry boundary was the opposite of the one used previously. Here, both the bottom wall and upper symmetry boundary have the same distribution of cells in x direction and only a slight grid distortion is applied to accomplish a local grid-surface-orthogonality in the vicinity of the wall mounted bump. It should be noted that the distribution in the wall-normal direction (y) was the same in both cases and based on the equation (3.1) on page 19. Furthermore the grid-surface-orthogonality was fulfilled on the top symmetry surface in both cases too.

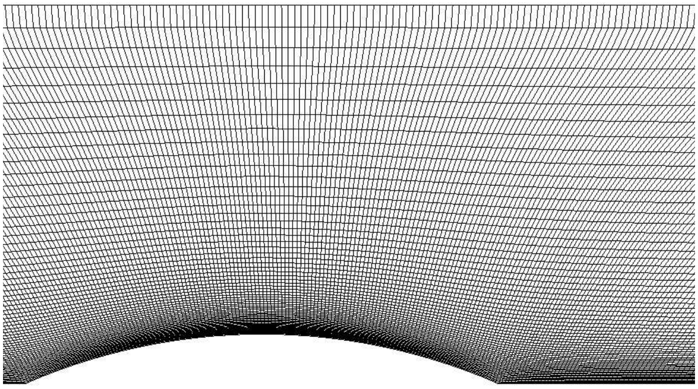

(a)

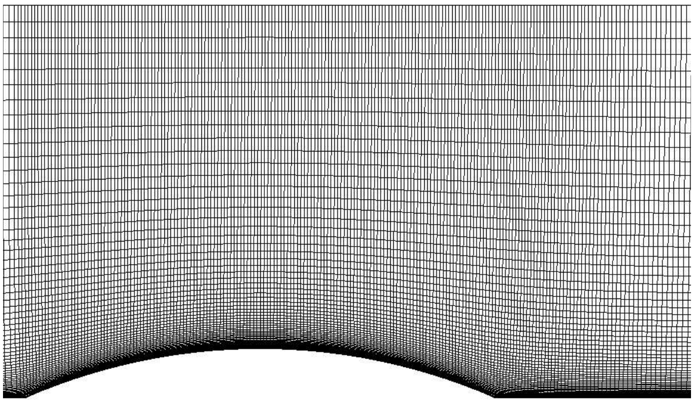

(b)

Figure 5.3: Sections of a grid region in the vicinity of the bump utilized in the computations of the $2D$ bump flow. Note that only every second grid point is illustrated in the Figure.

It turned out that computational results obtained utilizing the described grids did not show any significant differences, so only results based on the grid illustrated in Figure 5.3(a) will be presented in the following.

Expressing the grid distances in wall-units, the utilized grid have $3 < \Delta x^+ < 23$, with $3 < \Delta x^+ < 10$ in domain region $-0.1 < x/L_c < 1.33$, $\Delta y^+_{max} = 12$ in region $y < 2\ \delta_0$-

with 22 points within $y^+ < 10$, the first point at $y^+ = 0.44$ and 100 points inside $y^+ < 300$ corresponding to $y < 1.5\ \delta_0$ and $\Delta z^+ = 7$. Note that all wall units based distances presented here are based on the inflow friction velocity u_τ. δ_0 is the inlet BL thickness.

It is seen that resolution requirements for wall bounded flows (see e.g. Piomelli and Balaras [82]) are well fulfilled by the grid used in this study.

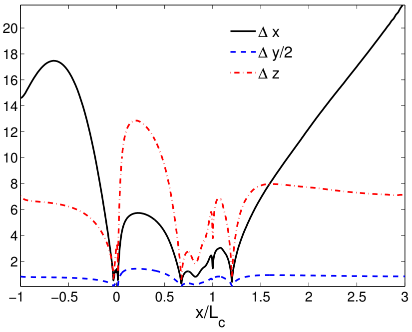

Figure 5.4: Grid distances in the wall-adjacent cells along the bottom boundary expressed in wall-units based on locally calculated friction velocity u_τ.

As an additional test of the general grid quality, the grid distances can be calculated based on locally determined friction velocities on the a-posteriori basis, i.e. after the computation has finished. Results, illustrated as grid distances in all directions, for the wall-adjacent cells along the bottom wall boundary, are presented in Figure 5.4. It is seen that grid distance-values calculated based on the inlet friction velocity are locally overestimated, but the resolution demands for obtaining a reliable LES results are clearly fulfilled by values presented in the Figure as well.

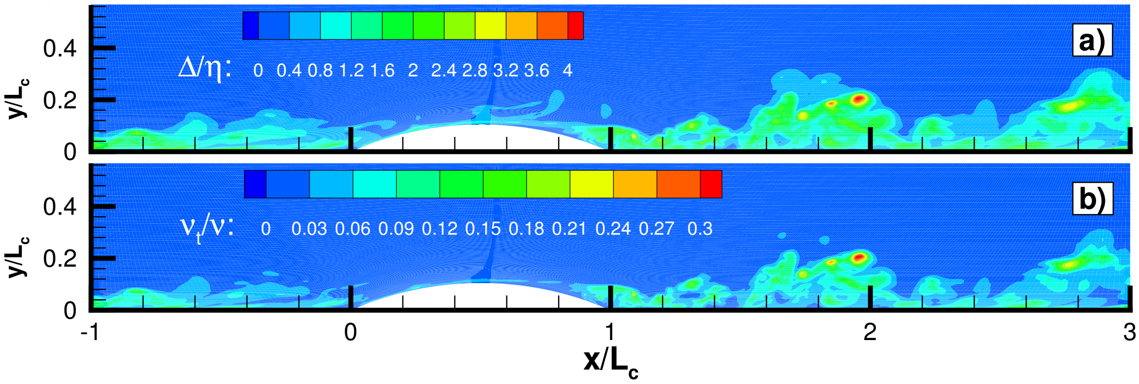

Figure 5.5: (a) Estimate of the Δ/η ratio based on k_{sgs} from Eddy Viscosity model of Sagaut [91] and (b) Ratio of the instantaneous subgrid-scale viscosity ν_t and the kinematic viscosity ν.

As previously discussed in the JICF case (see Figures A.19, A.20 and A.22 in Appendix A), a grid quality assessment in the interior of the calculation-domain can be made by comparing the local grid size Δ and an estimate of the Kolmogorov length scale η. Estimating η based on equations (A.3), (A.3) - page 156 in Appendix A, where k_{sgs} is determined directly from the Mixed Scale eddy viscosity model, the Δ/η ratio presented in Figure 5.5(a) is obtained.

Analogously the instantaneous ν_t/ν ratio is directly determined and presented in Figure 5.5(b). Analyzing the obtained ratios from Figure 5.5, it becomes apparent that the present study can be regarded as a highly resolved LES study (for further discussions see Appendix A, especially discussions in connection with Figures A.19, A.20 and A.22).

Basic computational details can be summarized as follows:

Convective term in the N-S equation system is discretized utilizing the deferred corrected 4th order Central Difference Scheme (CDS4). Pressure is corrected utilizing the PISO algorithm. Time step is chosen in order to obtain stable convergence in each time step to $\Delta t^* = \Delta t\, U_\infty / L_c = 0.0033$, yielding a maximum CFL number of $CFL_{max} = 0.91$. Solution is advanced in time using the 2nd order iterative dual time-stepping method. Approximately 6 subiterations were necessary for residuals to drop in order of about 10^{-3}. The Mixed scale eddy viscosity model of Sagaut (Sagaut [91]) (based on Ω) is used for modeling the SGS stresses.

At each time step during the calculations the velocity components, pressure and SGS viscosity are summed op, giving a basis for calculation of time averaged quantities. Exploiting the fact that spanwise is the homogeneous direction, the considered quantities are additionally averaged in this direction, basically yielding results on a single $2D\ x-y$ plane (see Figure 5.1) as an output of the computations.

In order to obtain a suitable basis for comparison of LES and measurements of Jensen [42], the averaging process has been carried out, after the statistically steady flow state has been reached, for a period of 10 "*Flow Through Times*" - FLTs (see definition on page 20). As turbulent inflow conditions were used, a period of additional 3 FLTs was necessary to achieve the statistically steady flow state.

5.2.1 Boundary Conditions

Illustrations of the basic boundary condition configuration have already been given in the previous paragraph. Standard BC's are applied at the upper-domain boundary (symmetry), at two lateral domain borders (periodic) and at the bottom boundary surface, where the bump is mounted (no-slip wall). Besides those BC's, inlet and outlet boundary conditions are applied at two domain edge-surfaces, as indicated in both Figures 5.1 and 5.2.

Regarding the outflow boundary condition, the non-intrusive method for the outlet boundary - the convective outflow condition given by equation (4.1) on page 38 and described in section 4.3.1 is utilized. As illustrated by Figure 5.2, the basic flow structures are allowed to *"pass through"* the domain outlet, without being noticeably influenced by the chosen boundary condition. This indicates directly that the chosen boundary condition has only a negligible impact on the flow upstream of the exit-surface, reiterating again that the convective outflow condition, which is implemented in the course of this project, functions properly and is a suitable choice for the outflow boundary condition in this flow case.

Regarding the inflow boundary condition, similar types of problems to the ones discussed in the Jet-in-Cross-Flow case are encountered here. Actually, the same wind tunnel is used in both the JICF and the 2D bump experimental configurations, with the basic difference being expressed in the utilized free-stream velocities. The utilized $U_\infty = 1.0\,\mathrm{m/s}$ in the present case vs. $U_\infty = 1.5\,\mathrm{m/s}$ used in the JICF study. As the general flow configuration in the 2D bump case can be regarded as even lower Re number flow, than the one encountered in the JICF study, the problem of generating a sustainable turbulent flow in the computational domain is emphasized even further in this case.

The first approach in an attempt to create the turbulent inflow was to try to reuse the data gathered for the JICF study. From the JICF inflow dataset the fluctuating part of the U, V and W velocity components have been extracted and added to the mean profiles of experimentally measured (Jensen [42]) profiles of U and V (W is zero in mean) velocities, thereby creating an inlet dataset comparable to the one used in the JICF study. It should be noted that no rescaling of the turbulence quantities has been attempted in the described process, as the rescaling procedure is generally assumed to "*destroy*" the turbulence scales. The effect of artificial turbulence scales can be correspondingly felt for long distances from the inlet position in the computational domain[1]. Anyhow this approach did not produce satisfactory results, as all statistical quantities appeared considerably overpredicted, when LES was compared to measurements of Jensen [42]. Furthermore, this initial calculation clearly indicated that the best approach here would be to conduct a new precursor calculation of the spatially developing boundary layer flow, where all flow parameters are adjusted to the original configuration of the 2D bump flow. Accordingly this was done in the next step.

The basic parameters, which characterize the conducted precursor calculation of the boundary layer flow are listed in Table 5.1.

u_τ	δ_0	θ_0	$Re_\theta = \frac{U_\infty \theta}{\nu}$
$0.05\,m/s$	$65\,mm$	$5.5\,mm$	365

Table 5.1: Targeted boundary layer parameters

The general computational layout of the considered boundary layer flow is almost completely identical to the one used in the precursor calculations of the JICF flow. This means that the computational grid used in the calculations consists again of 192 x 96 x 96 cells in streamwise, wall-normal and spanwise directions respectively, while the domain extensions are specified as $L_x \,\mathrm{x}\, L_y \,\mathrm{x}\, L_z = 16\,\delta_0 \,\mathrm{x}\, 3.5\delta_0 \,\mathrm{x}\, 4\delta_0$. The cells are equally distributed in x and z directions, while a stretching function is used in the wall-normal (y) direction. The stretching function used is based on the equation (3.1) on page 19, which yields $0.95 \leq \Delta y^+ \leq 15$ in region $y < 2\,\delta_0$ and 9 grid points within $y^+ < 10$, with the first point at $y^+ = 0.46$. The dimensionless distances in x and y directions are $\Delta x^+ = 20$ and $\Delta z^+ = 11$ respectively.

This implies that the requirements for well-resolved LES in a wall bounded flows (see e.g. Piomelli and Balaras [82]) are fulfilled in the computations conducted here. For further details regarding the general numerical configuration utilized here the interested reader is referred to section 4.3.2 on page 42.

Figure 5.6 presents the results obtained from LES computations compared to available measurements of Jensen [42] and the well-known DNS database of Spalart [102].

By inspecting the results shown on Figure 5.6 and comparing them to the results of precursor calculation of the JICF flow case - Figure 4.7 on page 46, a direct analogy between the presented results can immediately be established, especially when LES is compared to the DNS data. This implies further that result-discussions already given in section 4.3.2 on page 42 fully apply in the case of the precursor calculation of the 2D bump flow as well, so

---

[1] The present comment is based on private communication with Prof. Lars Davidson, Division of Fluid Dynamics, Chalmers University of Technology, Gothenburg, Sweden

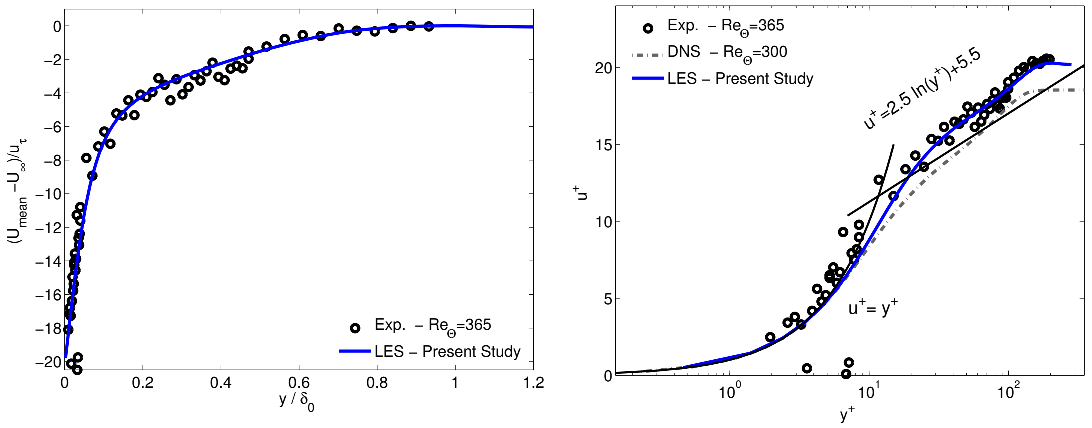

(a) U_{mean} (b) u^+

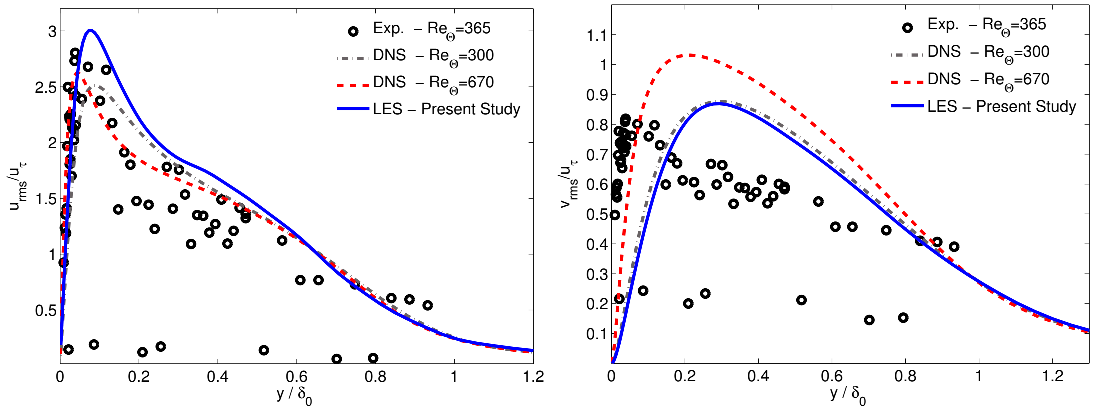

(c) u_{rms} (d) v_{rms}

Figure 5.6: Boundary Layer Simulation - $u_\tau = 0.05\ m/s$, $\delta = 65\ mm$, $\Theta = 5.5\ mm$ and $Re_\Theta = 365$

the interested reader is referred to the mentioned section for further remarks regarding the obtained results. Here it is only noted, that the inlet data for the 2D bump case have a very similar quality as it was the case in the basic JICF computations.

Moreover it should be noticed that the greatest difference in the two compared boundary layer cases is actually the quality of the experimental data. Clearly, a high degree of scattering of the measured data points is seen on Figure 5.6, where measurements of Jensen [42] are presented, which can implie a questionable quality of the latter. This is most obviously elucidated in Figure 5.6(c) where u_{rms} profiles are presented.

Finally a remark on the specific position, where the measurements shown in Figure 5.6 are taken, is given. As in the JICF case the promotion of the fully turbulent boundary layer state have been experimentally attempted by positioning the vortex generator system at a bump-upstream position in the wind tunnel - referring to the coordinate system origo illustrated in Figure 5.1 this position is $x = -3.44\,L_c$ (upstream of the bump leading edge). The position in this coordinate system where the shown measurements are taken is unfortunately not $x = -L_c$ or relatively close to this position (see Figure 5.1) but rather at the position corresponding to $x = 0.24\,L_c$. This leads to a certain inconsistency in the basic state of the boundary layer between the precursor and the main 2D bump flow computations. Actually the general state of the boundary layer at the proper bump-upstream position (where the actual inlet in the calculations is positioned) could not be directly estimated or assumed, as it was not clear whether the fully developed turbulent boundary layer state was experimentally completely established there. For that reason it is assumed that LES results presented above are representative for the general flow state in the investigated flow and can be used as an appropriate inflow condition in the present case. Formulating this in other words, it means that better agreements with the measurements in the 2D bump flow case could not be expected if the inlet data set was created based on velocities taken on a upstream plane distanced $1.24\,L_c$ from the targeted values.

5.3 Results and Discussions of the 2D Bump Flow Case

In this section results of the conducted computations are presented and compared with the available measurements of Jensen [42]. On Figures 5.7 - 5.10 the profiles of mean velocity components U and V and the corresponding r.m.s. velocity fluctuations u_{rms} and v_{rms}, on 36 different streamwise positions in the considered domain, are presented and compared. It should be noted that measurements of shear stress and w_{rms} velocity fluctuation are not available; hence the computational results of those quantities are not included in this presentation.

Furthermore it should be underlined that all coordinate axes on the shown Figures are normalized by the bump cord-length L_c. Correspondingly all mean velocities and velocity fluctuations are normalized by the free-stream velocity U_∞. In order to enhance visibility of the bump position in the presented profile plots a quantity referred to as y_0 is introduced. $y_0 \neq 0$ only at positions in the domain where bump resides ($0 < x/L_c < 1$) and corresponds to the local wall location at a given x/L_c position on the bump - e.g. $y_0/L_c = 0.08$ for $x/L_c = 0.25$ etc.. Coordinate direction n refers to the normal distance from the wall surface in a coordinate system defined to follow the bottom wall surface geometry - see Figure 5.1. Finally it should be pointed out that two presented profiles at streamwise positions $x/L_c = [0, 1]$ are taken in a direction perpendicular to the flat plate, while measurements at two other positions $x/L_c = [0.00033, 0.9997]$ are taken in a direction normal to the bump.

Inspecting results of the presented computations and comparing them to the measurements of Jensen [42] - Figures 5.7 - 5.10, a general good agreement between the two can be observed. It is seen that the LES calculated profiles do resemble almost all experimentally measured profile characteristics fairly well, but some differences can be seen too.

A quite distinct difference in the magnitude of all presented statistical quantities in the near-wall region, at streamwise locations $x/L_c < 0$ - i.e. $x/L_c = [-0.33, -0.25, -0.17, -0.083]$, upstream of the bump leading edge, are apparent in all shown Figures 5.7 - 5.10. Whereas the mean streamwise velocity U appears underpredicted (Figure 5.7), the mean wall-normal velocity V (Figure 5.8) is overpredicted by the LES calculations in this region. On the other hand the streamwise velocity fluctuations u_{rms} (Figure 5.9) are clearly overpredicted, while the wall-normal velocity fluctuations v_{rms} (Figure 5.10) are underpredicted in the mentioned region. The observed discrepancies between the measured and computed profiles are most likely related to the difference in the general boundary layer state at the computational inlet position. This issue was discussed in the previous section and is basically caused by the fact that no reliable measurements exist at the position where the computational inlet is placed. It should be noted that differences in the state of the BL at inlet seem to have a quite local effect, as most of the observed differences disappear rapidly, once the flow encounters the strong influence of the bump presence in the domain - i.e. $x/L_c \geq 0.083$.

Regarding the general agreements between the measurements and computations at other streamwise positions, it is seen that mean streamwise velocity profiles and corresponding streamwise velocity fluctuations have a quite good agreement with the experiment in region $x/L_c \geq 0.083$, while the agreements of the wall-normal statistical quantities in the same region are not of the same quality. It is seen furthermore from Figures 5.7 - 5.10 that data scattering and even clustering is much more noticeable in measurements of the wall-normal statistical quantities, especially for v_{rms}, than in corresponding profiles of U and u_{rms}, so a difference in the experimental data quality can be a part of the explanation for this behavior.

From Figure 5.7 it can be observed that LES based profiles are able to predict the real flow behavior in the region where separation occurs. It is seen that all U profiles, at positions where the negative streamwise velocity occur, are estimated well by LES, both with regards to the size and shape of the separation zone.

Turning the attention to profiles of the streamwise velocity fluctuations (Figure 5.9) some interesting observations can be made. Besides a relatively good agreement of LES with the measurements, inspecting the u_{rms} profile shapes one can observe the distinct *"knee points"* in those profiles starting from position $x/L_c = 0.17$ on-wards. The mentioned *"knee points"* are identified and defined by Baskaran et al. [10] and also observed by Webster et al. [113] and Wu and Squires [115] in their 2D hill flows. From Figure 5.9 it is seen that u_{rms} profile structure have a distinct peek in the near-wall region followed by an additional peak further away from the wall at streamwise positions $x/L_c \geq 0.17$. Following the definition of Baskaran et al. [10], this kind of profile shapes characterizes flows where development of a so-called internal layer takes place. The first maximum in the u_{rms} profile moves away from the wall, while the second local maximum defining the *"knee point"* at the local position, diminishes in magnitude, while it moves away from the wall for increasing streamwise stations in region $x/L_c \geq 0.17$. The structure of LES calculated profiles changes again starting from $x/L_c = 0.75$ on-wards, where an additional peak in the near-wall region starts to develop, while position of the overall profile maximum turns rapidly further away from the wall. The latter behavior is characteristic for boundary layers experiencing strong adverse pressure gradient (see e.g. Simpson [97], Wu and Squires [115]).

One of the computationally challenging tasks in flows that encounter separation and reattachment is a proper determination of the positions where they experimentally occur. Unfortunately the quality of measurements conducted by Jensen [42] is not sufficiently reliable to make a basis for comparisons with the conducted LES computations. For that reason the measurements of Schmidt [93], who used an almost identical experimental setup as Jensen [42], but utilized a considerably different inlet conditions (Schmidt [93] used fully developed channel flow with $Re_h = 1850\,(3700)$ vs. spatially developing BL flow of Jensen [42] and $Re_h = 1950$) are included here as they can give a general idea of the size and proper position of the separated region in the investigated flow. The separation zone is visualized through plots of the wall-friction coefficient defined as:

$$C_f = \frac{\tau_w}{\frac{1}{2}\rho U_\infty^2}, \tag{5.1}$$

where τ_w is the skin friction at the wall, approximated in the computations based on following

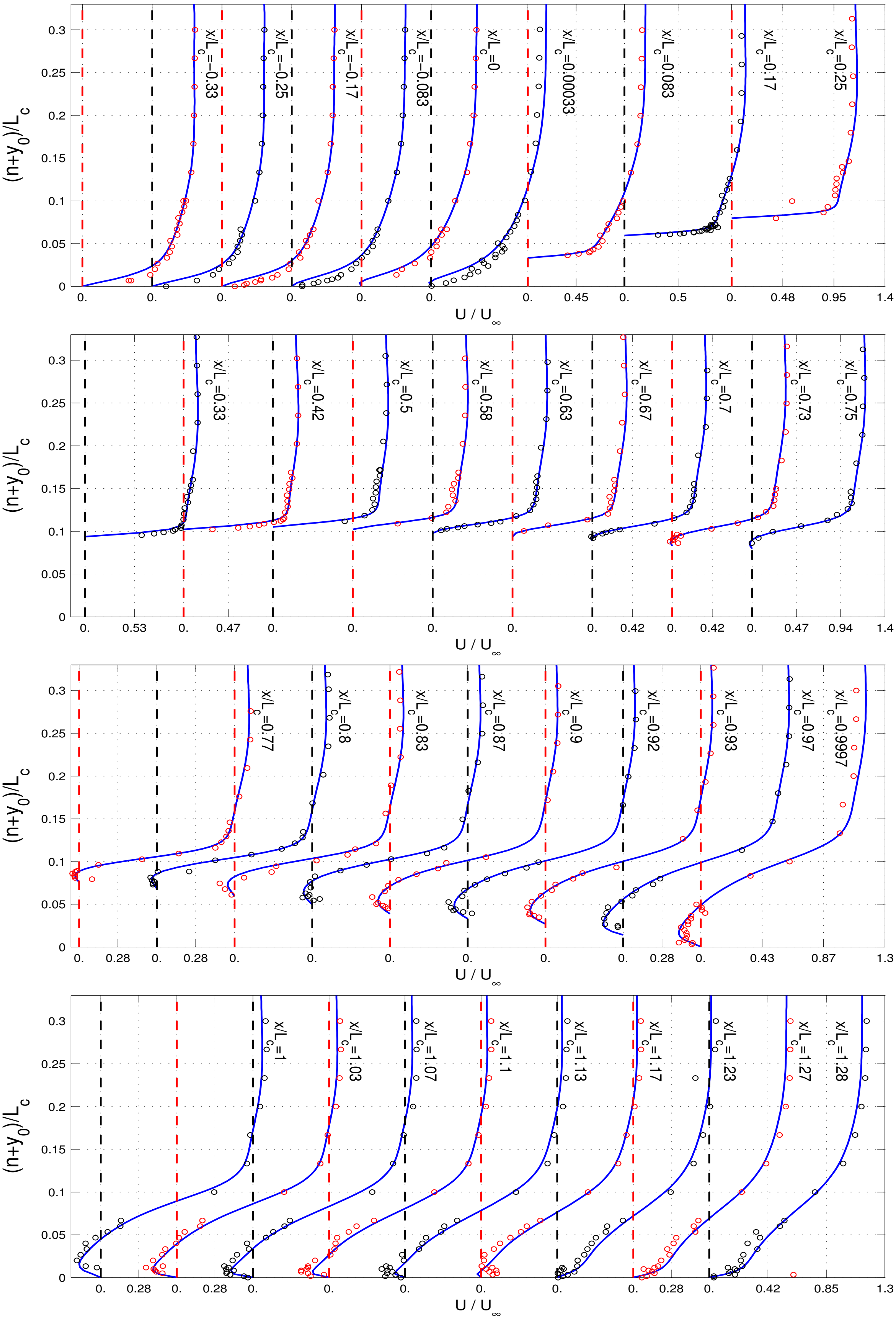

Figure 5.7: U/U_∞. Solid lines - LES computations, open circles - LDA data of Jensen [42].

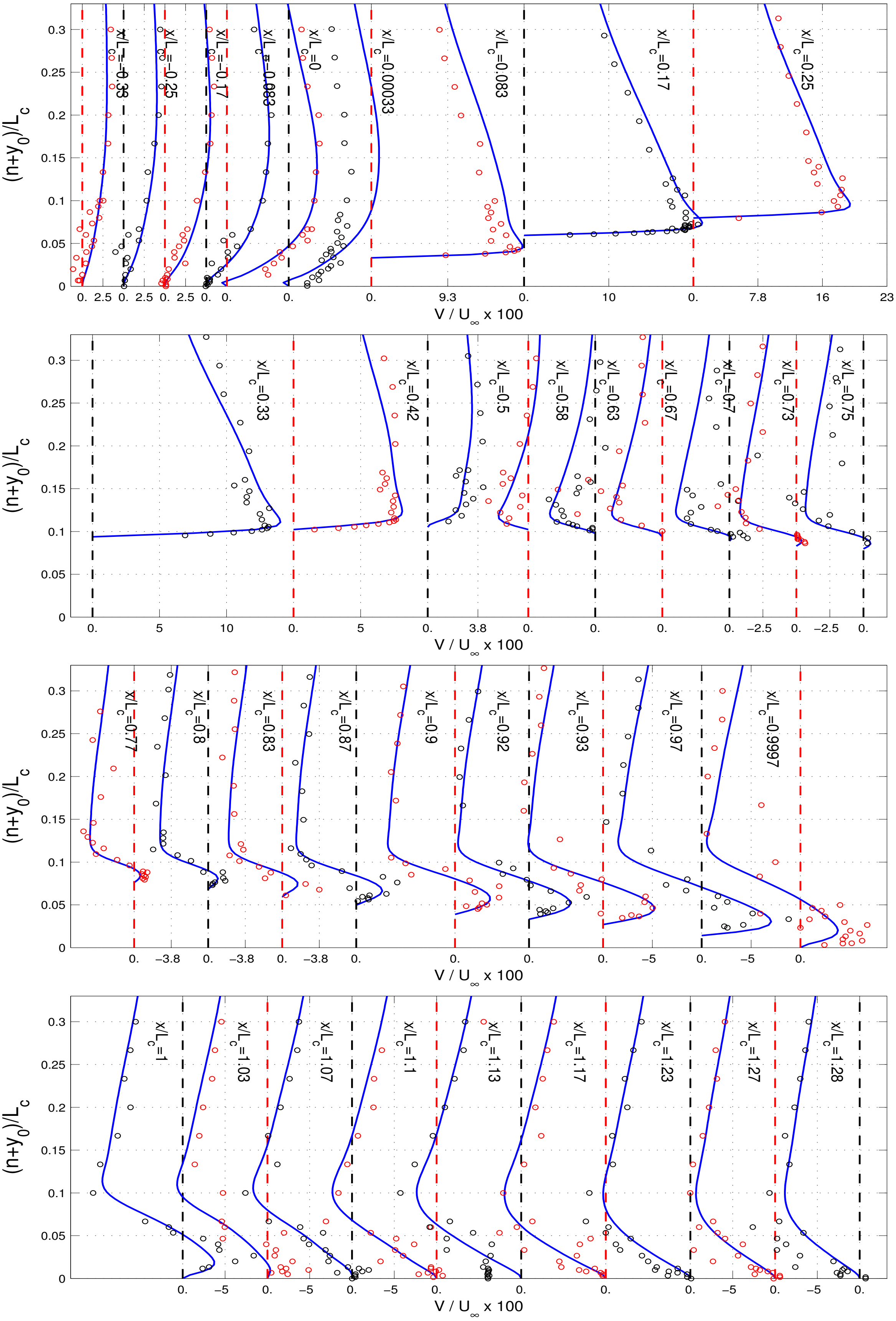

Figure 5.8: V/U_∞. Solid lines - LES computations, open circles - LDA data of Jensen [42].

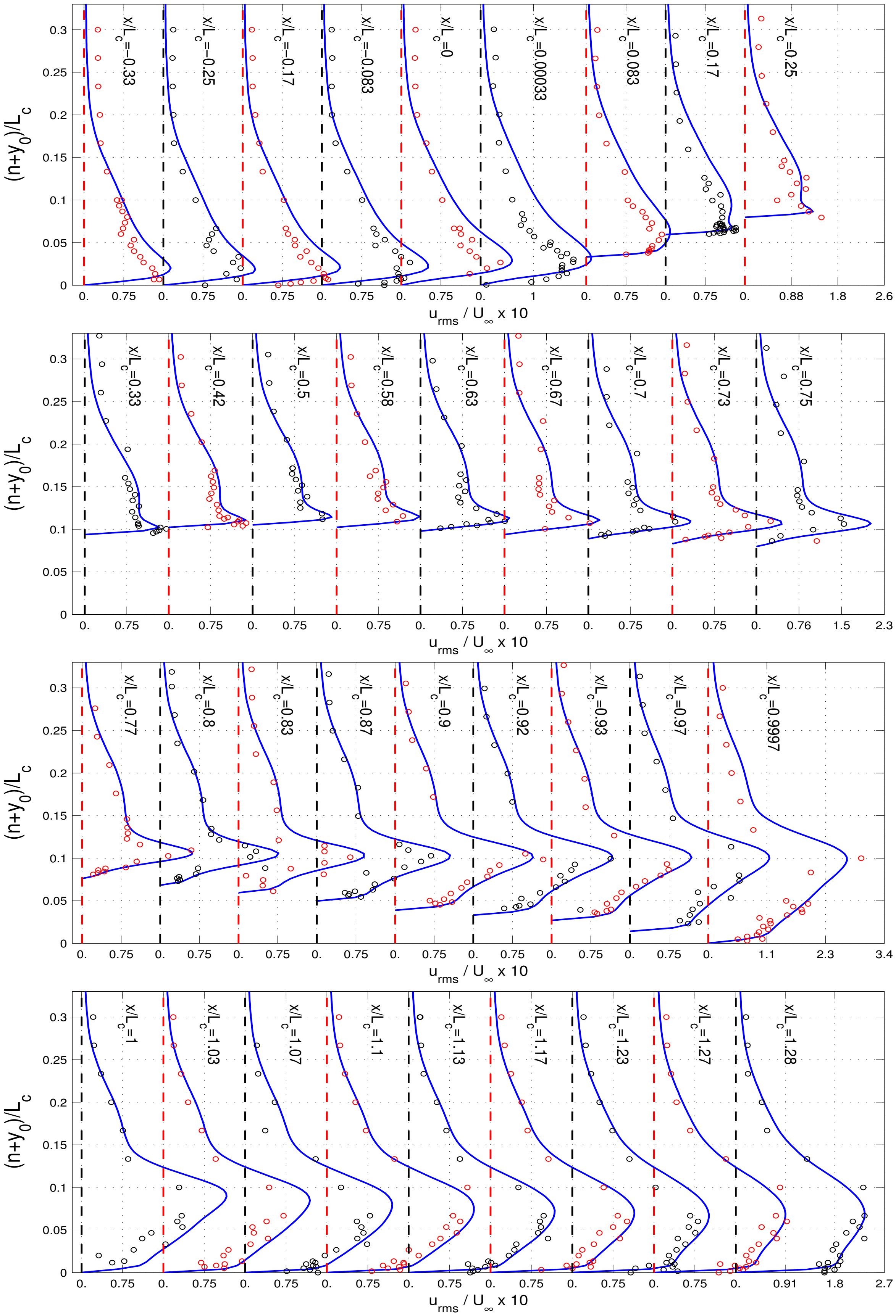

Figure 5.9: u_{rms}/U_∞. Solid lines - LES computations, open circles - LDA data of Jensen [42].

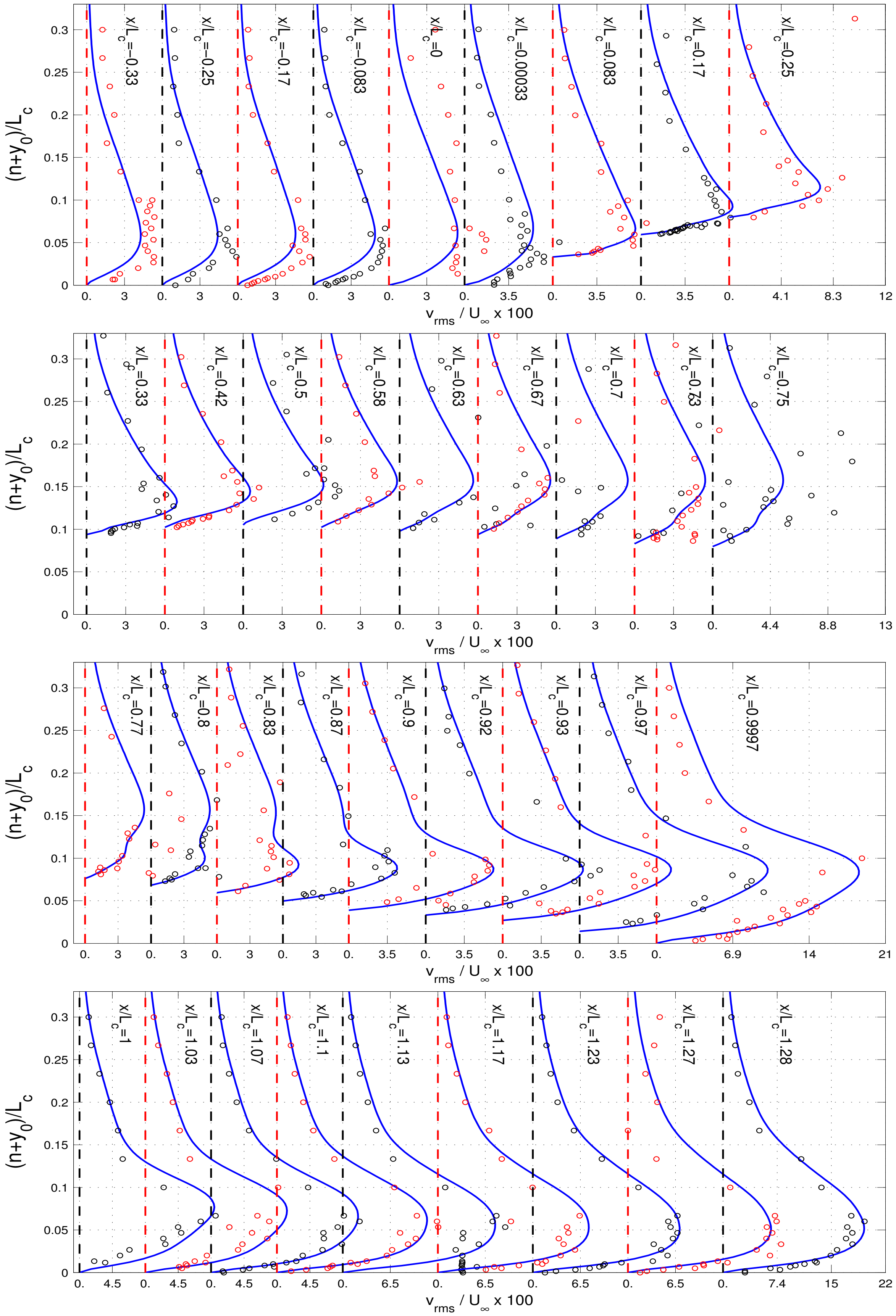

Figure 5.10: v_{rms}/U_∞. Solid lines - LES computations, open circles - LDA data of Jensen [42].

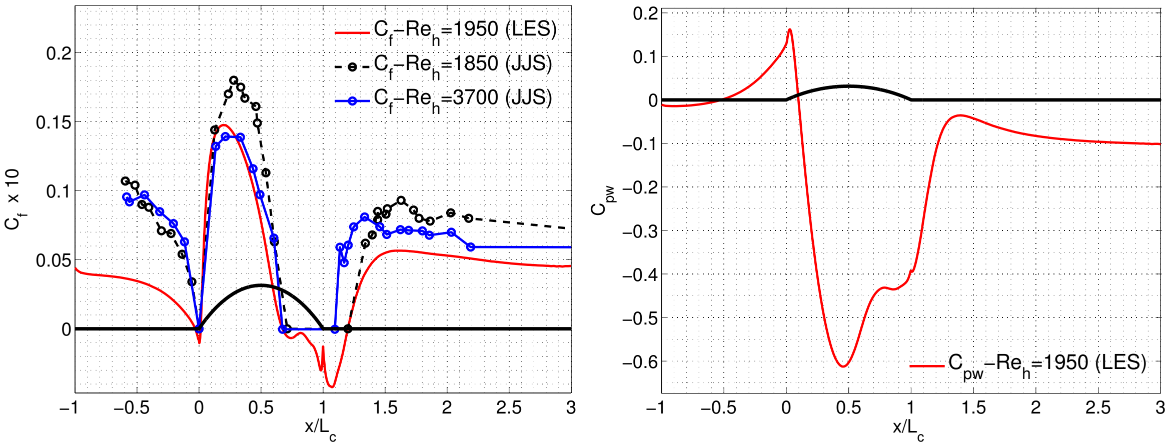

(a) C_f (b) C_{pw}

Figure 5.11: C_p, C_f - Skin friction and Static Pressure Coefficients. JJS refers to Experimental data of Schmidt [93]. The black solid line indicates the bottom wall surface geometry, including the bump.

expression - $\tau_w = \mu \langle u \rangle / \Delta y$, where $\langle u \rangle$ is the mean streamwise velocity at the first cell center next to the wall and Δy is the distance from the same cell center to the wall.

The results are presented on Figure 5.11(a). The results of Schmidt [93] indicate that separation point changes slightly from $x/L_c = 0.683$ to $x/L_c = 0.693$ by doubling the Re_h from 1850 to 3700, while the reattachment position changes significantly from $x/L_c = 1.217$ to $x/L_c = 1.070$ for the same Re_h values. The LES results are seen to generally deviate considerably from the closest $Re_h = 1850$ case of Schmidt [93] - both in the bump upstream region, on the bump before separation and after the reattachment. Most of those dissimilarities can probably be attributed to differences in inlet boundary conditions. Whereas the separation point in current LES study occurs at $x/L_c = 0.673$ vs. $x/L_c = 0.683$ in the study of Schmidt [93] for $Re_h = 1850$, the reattachment point occurs at almost identical position in both cases.

From Schmidt [93] study it can be deduced, that by increasing the Re_h, position of the separation point shifts in the positive x direction and position of the reattachment point shifts in the negative x direction, thereby diminishing the size of the separated flow region with increasing Re_h. This behavior in not generally followed by the present LES study. Regarding the measurements of Jensen [42] - Figure 5.7, it is seen that separation in his study occurs between positions - $x/L_c = 0.67$ and $x/L_c = 0.70$, and the reattachment occurs between positions - $x/L_c = 1.17$ and $x/L_c = 1.23$. This indicates that predictions of the present LES study lies in the region where separation and reattachment in reality occurs, but based on Jensen's measurements it is difficult to deduce, whether the disagreement between LES and tendencies deduced from Schmidt's study are solely attributed to differences in the inflow conditions utilized in those studies or an inability of LES to reproduce the experimental results correctly.

On Figure 5.11(b) profile of the surface static pressure $C_{pw} = (\langle p_w \rangle - \langle p_{w,ref} \rangle)/(\frac{1}{2}\rho U_\infty^2)$ is presented. C_{pw} and thereby also p_w are evaluated at the same grid points as τ_w. Thus, a general surface pressure distribution in the streamwise direction is visualized. As expected C_{pw} profile reveals the region of an adverse pressure gradient in the bump-upstream region, followed by the favorable pressure gradient zone in the region approaching the bump apex.

After the apex position an adverse pressure gradient is observed, while a favorable pressure gradient is seen in the flat plate region after the bump. One should note a region between $x/L_c \approx 0.67$ and $x/L_c \approx 1.22$ where the C_{pw} coefficient clearly indicates existence of the separation zone.

Finally it should be noted that a kink in LES profiles of both C_f and C_{pw} are observed in Figure 5.11 at positions of the abrupt changes in the surface curvature - i.e. $x/L_c = 0$ and $x/L_c = 1$.

Based on the presented results it can be concluded that present LES study is capable of predicting the main features of the $2D$ bump flow fairly well. Due to an insufficient experimental data quality it was not possible to fully investigate the ability of LES to correctly predict positions of the experimental separation and reattachment points, but nevertheless the present results indicate that the highly resolved LES conducted in the course of this study is in general very much able to predict the real $2D$ bump flow behavior. This indicates further that a similar LES study applied on a flow configuration, where vortex generators are mounted on the $2D$ bump, can be expected to reproduce the basic characteristics of that flow reasonably well.

Chapter 6

Summary and Conclusions

The basic topic of this dissertation was an advanced approach to the problem of turbulence modeling (LES) and its applicability on flow cases of industrial relevance. In order to be able to perform general LES computations during this study, the main focus in its initial phase was directed on the enhancement of general capabilities of the utilized flow solver (EllipSys) to perform LES calculations. This was done by implementing three new SGS models into the code and validating the implementations on a well-known benchmark test case for LES computations - the channel flow case.

The LES method was then applied on one of the basic flow cases with a significant industrial relevance - The Jet-in-Cross-Flow (JICF) flow case. A comprehensive experimental database, comprising of both LDA (Özcan and Larsen [77]) and (S)PIV (Meyer et al. [70, 71], Pedersen [81]) measurements on the flow set-up representing the idealized JICF flow was selected to be used as a comparison basis for the conducted numerical JICF study. As the experimental data were attained in a low speed wind tunnel, the experimentally attained JICF flow case could be in general regarded as a relatively low Reynolds number (Re_D) flow. This fact allowed the present LES investigation to be performed on a high-resolution meshes, so the present numerical study of the JICF flow case can in general be regarded as a highly-resolved LES investigation of the JICF flow.

The fact that the overall Reynolds number (Re_D) in the investigated flow case was relatively low led to some other major difficulties, basically expressed in an absolute necessity of treating inlet boundary conditions (at least one) explicitly. So in the first phase of JICF calculations, the pre-cursor computations of the jet (pipe) flow were performed and some initial results comparing mean flow (LDA) measurements and LES results were obtained. Already these comparisons showed good overall agreement in areas downstream of the jet entry region in the cross flow boundary layer. But at the same time they showed some discrepancies in profiles of mean streamwise velocity component in a jet-to-cross-flow exhaustion region, which could at that point be attributed to many different parameters, including the non-turbulent flow of the on-coming boundary layer. Further investigations of JICF flow included an additional pre-cursor simulation of the spatially developing boundary layer flow.

Performing computations in the case of spatially developing boundary layer flow was more complex and involved than the firstly performed computations of the jet (pipe) flow. The main difficulty was expressed in the existence of the mean flow gradient in the streamwise direction, which made the use of periodic boundary conditions unfeasible. Therefore the method of Lund et al. [62] was implemented in the EllipSys code. Actually the method proved to be quite difficult to implement due to some basic constraints (like grid structure) of the EllipSys solver.

Based on two inlet databases new computations of the JICF flow were performed in the next phase. They still showed same considerable discrepancies between measured and calculated streamwise velocity profiles in a jet-to-cross-flow exhaustion region, so an almost parametric numerical study involving 14 different cases and meshes of up to 15 million cells in size was subsequently conducted. The major outcomes of this study can be summarized as follows:

- ▷ None of the conducted LES calculations could resemble the measured gradients in the streamwise velocity profiles in the jet-to-cross-flow exhaustion region,
- ▷ Overall agreement between LDA measurements and basically all computations, with regards to both mean flow and turbulence quantities, in all other regions was good,
- ▷ The grid denoted as baseline grid with 4.7 millions cells could be regarded as one producing reliable LES results,
- ▷ The influence of various numerical parameters (SGS models, domain extensions and positions of inflow/outflow boundaries etc.) on the computed results was almost negligible,
- ▷ There might be a problem with the quality of the (LDA) measurements in the jet-to-cross-flow exhaustion region.

So despite some discrepancies between measurements and computation, localized at certain position in the flow domain, it can be generally stated, that LES results obtained in the course of this study were in good agreement with LDA measurements of various mean-flow statistical quantities.

After the validity of numerical calculations was established, some more dynamically accentuated characteristics of the JICF flow were investigated. Based on use of some known tools (Q-criterion, seeding of massless particles) various coherent structures pertinent to the JICF flow were successfully analyzed and identified.

The last part of the JICF analysis comprised of a study which involved use of the Proper Orthogonal Decomposition (POD) technique. Two datasets, each including 1000 $2D$ snapshots of the JICF flow on the 3 mutually perpendicular planes ($y/D = 0$, $x/D = 1$ and $z/D = 1.33$), where one was obtained experimentally (Meyer et al. [70, 71]) and the other was obtained numerically (LES), were analyzed using the POD method. The POD results showed a high level of resemblance, as they virtually identified traces of same coherent structures in both the PIV- and LES- based datasets. The POD study was then extended to 3D, shedding some new light on the disputed question regarding origin of the wake vortices.

In the final stages of this project a study of a 2D Bump flow case was conducted. In many ways the gathered (LES) experience from the JICF case was directly applied here, so after an additional pre-cursor calculation of the spatially developing boundary layer flow, the obtained results, regarding both mean flow profiles and turbulence quantities, showed a very good agreement with the (LDA) measurements.

Based on the results of this study it can be concluded that the LES method does not only have a potential, but it is a method capable of producing results of broad engineering interest and at the same time a method which can be used as a significant scientific tool in the persistent and ongoing quest to increase our general ability to understand and predict turbulent flows.

Bibliography

[1] AGARD. *A selection of Test Cases for the validation of Large Eddy Simulation of Turbulent Flows*, pages 119–120. AGARD Advisory report 345, 1998.

[2] AGARD. *Computational and Experimental Assessment of Jets in Cross Flow*, pages GD–1 – GD–13. AGARD Conference proceedings 534, 1993.

[3] G. Alfonsi and L. Primavera. Coherent structure dynamics in turbulent channel flow. *Journal of Flow Visualization and Image Processing*, 9(1):89–98, 2002.

[4] J. Alvarez and W. Jones. Predictions of Momentum and Scalar Fields in a Jet in Cross-Flow using First and Second Order Turbulence Closures . In *Computational and Experimental Assessment of Jets in CrossFlow, AGARD-CP-534*, Nov. 1993.

[5] J. Andreopoulos. On the structure of jets in a crossflow. *Journal of Fluid Mechanics*, 157:163–197, 1985.

[6] ANSYS. *ICEM CFD Hexa v 5.1 -Tutorial/User Manual.* ANSYS Inc., 2004.

[7] C. J. Baker. The laminar horseshoe vortex. *Journal of Fluid Mechanics*, 95:347–367, 1979.

[8] P. Bandyopadhyay and A. Ahmed. Turbulent boundary layers subjected to multiple curvatures and pressure gradients. *Journal of Fluid Mechanics*, 246:503–527, 1993.

[9] J. Bardina, J. H. Ferziger, and W. Reynolds. Improved subgrid scale models for Large-Eddy Simulations. *AIAA paper No. 80-1357*, 1980.

[10] V. Baskaran, A. J. Smits, and P. N. Joubert. Turbulent flow over a Curved Hill: Part 1. Growth of an Internal Boundary Layer. *Journal of Fluid Mechanics*, 182:47–83, 1987.

[11] V. Baskaran, A. Smits, and P. Joubert. Turbulent flow over a Curved Hill. Part 2. Effects of Streamline Curvature and Streamwise Pressure Gradient. *Journal of Fluid Mechanics*, 232:377–402, 1991.

[12] R. K. Byskov. *Large-Eddy Simulations of Flow Structures in a Centrifugal Pump Impeller, Part II.* PhD thesis, Ålborg University, 2000.

[13] D. Carati, G. Winckelmans, and H. Jeanmart. On the modelling of the subgrid-scale and filtered-scale stress tensors in Large-Eddy Simulations. *Journal of Fluid Mechanics*, 441:119–138, 2001.

[14] S. Chernyshenko and M. F. Baig. The mechanism of streak formation in near-wall turbulence. *Journal of Fluid Mechanics*, 544:99–131, 2005.

[15] S. Y. Chung, G. H. Rhee, and H. J. Sung. Direct numerical simulation of turbulent concentric annular pipe flow : Part 1: Flow field. *International Journal of Heat and Fluid Flow*, 23(4):426–440, 2002.

[16] R. Claus and S. Vanka. Multigrid calculations of a jet in crossflow. *Journal of Propulsion and Power*, 8(2):425–431, 1992.

[17] S. L. Coelho and J. Hunt. Dynamics of the near field of strong jets in crossflows. *Journal of Fluid Mechanics*, 200:95–120, 1989.

[18] L. Cortelezzi and A. Karagozian. On the formation of the counter-rotating vortex pair in transverse jets. *Journal of Fluid Mechanics*, 446:347–373, 2001.

[19] S. Dahlström and L. Davidson. Large Eddy Simulation applied to a High-Reynolds flow around an airfoil close to stall. In *41st AIAA Aerospace Sciences Meeting and Exhibit, 6-9 January 2003, Reno, NV, AIAA 2003-0776.*

[20] L. Davidson. Large-Eddy Simulations : A dynamic one-equation subgrid model for three-dimensional recalculating flows. *In 11th International Symposium on Turbulent Shear Flow*, 3:26.1–26.6, 1997.

[21] J. W. Deardorff. A numerical study of three-dimensional turbulent channel flow at large Reynolds numbers. *Journal of Fluid Mechanics*, 41(2):453–480, 1970.

[22] A. Demuren. Characteristics of three-dimensional turbulent jets in crossflow. *International Journal of Engineering Science*, 31(6):899–913, 1993.

[23] J. den Toonder and F. Nieuwstadt. Reynolds number effects in a turbulent pipe flow for low to moderate Re. *Physics of Fluids*, 9(11):3398–3409, 1997.

[24] J. A. Domaradzki and E. M. Saiki. Backscatter models for Large-Eddy Simulations. *Theoretical and Computational Fluid Dynamics*, 9:75–83, 1997.

[25] J. A. Domaradzki and E. M. Saiki. A subgrid scale model based on the estimation of unresolved scales of turbulence. *Physics of Fluids*, 9:1–17, 1997.

[26] F. Durst and M. Schafer. A parallel block-structured multigrid method for the prediction of incompressible flows. *International Journal for Numerical Methods in Fluids*, 22(6): 549–565, 1996.

[27] H. Eckelman. Structure of viscous sublayer and adjacent wall region in a turbulent channel flow. *Journal of Fluid Mechanics*, 65:439–459, 1974.

[28] J. Eggels, F. Unger, M. Weiss, J. Westerweel, R. Adrian, R. Friedrich, and F. Nieuwstadt. Fully developed turbulent pipe flow: A comparison between direct numerical simulation and experiment. *Journal of Fluid Mechanics*, 268:175–209, 1994.

[29] H. Fernholz and D. Warnack. Effects of a favourable pressure gradient and of the Reynolds number on an incompressible axisymmetric turbulent boundary layer. Part 1. The turbulent boundary layer. *Journal of Fluid Mechanics*, 359:329–356, 1998.

[30] T. Fric and A. Roshko. Vortical structure in the wake of a transverse jet. *Journal of Fluid Mechanics*, 279:1–47, 1994.

[31] J. Frohlich, C. P. Mellen, W. Rodi, L. Temmerman, and M. A. Leschziner. Highly resolved large-eddy simulation of separated flow in a channel with streamwise periodic constrictions. *Journal of Fluid Mechanics*, 526:19–66, 2005.

[32] M. Germano, U. Piomelli, P. Moin, and W. H. Cabot. A dynamic subgrid-scale eddy viscosity model. *Physics of Fluids A (Fluid Dynamics)*, 3(7):1760–1765, 1991.

[33] S. Ghoasal, T. S. Lund, P. Moin, and K. Akselvoll. A dynamic localization model for Large-Eddy Simulations of turbulent flow. *Journal of Fluid Mechanics*, 286:229–255, 1995.

[34] S. Ghosal. An analysis of numerical errors in Large-Eddy Simulations of turbulence. *Journal of Computational Physics*, 125:187–206, 1996.

[35] S. Gopalan, B. M. Abraham, and J. Katz. The structure of a jet in cross flow at low velocity ratios. *Physics of Fluids*, 16(6):2067–2087, 2004.

[36] J. Gullbrand and F. Chow. The effect of numerical errors and turbulence models in large-eddy simulations of channel flow, with and without explicit filtering. *Journal of Fluid Mechanics*, 495:323–341, 2003.

[37] C. Hartel and L. Kleiser. Analysis and modelling of subgrid-scale motions in near-wall turbulence. *Journal of Fluid Mechanics*, 356:327–352, 1998.

[38] B. Haven and M. Kurosaka. Kidney and anti-kidney vortices in crossflow jets. *Journal of Fluid Mechanics*, 352:27–64, 1997.

[39] J. Hinze. *Turbulence 2'nd edition*. McGraw-Hill, 1975.

[40] P. Holmes, J. Lumley, and G. Berkooz. *Turbulence, coherent structures, dynamical systems and symmetry*. Cambridge University Press, 1998.

[41] J. C. R. Hunt, A. A. Wray, and P. Moin. Eddies, stream and convergence zones in turbulent flows. In *Proceedings of the 1988 Summer Program, Report CTR-S88*, pages 193–208. Center for Turbulence Research, 1988.

[42] T. B. Jensen. Eksperimental og numerisk studium af turbulent grænselæg hen over en cylindersektion. Master's thesis, Department of Mechanical Engineering, MEK - DTU, 1992.

[43] J. Jeong and F. Hussain. On the identification of a vortex. *Journal of Fluid Mechanics*, 285:69–94, 1995.

[44] P. S. Johansson and H. I. Andersson. Generation of inflow data for inhomogeneous turbulence. *Theoretical and Computational Fluid Dynamics*, 18(5):371–389, 2004.

[45] W. Jones and M. Wille. Large-Eddy Simulations of a plane jet in a cross-flow. *International Journal of Heat and Fluid Flow*, 17:269–306, 1996.

[46] R. Kelso and A. Smits. Horseshoe vortex systems resulting from the interaction between a laminar boundary layer and a transverse jet. *Physics of Fluids*, 7(1):153–158, 1995.

[47] R. Kelso, T. Lim, and A. Perry. An experimental study of round jets in cross-flow. *Journal of Fluid Mechanics*, 306:111–144, 1996.

[48] J. Kim. The effect of rotation on turbulence structure. In *Symposium on Turbulent Shear Flows, 4th, Karlsruhe, West Germany, September 12-14, 1983, Proceedings (A85-14326 04-34)*, pages 6.14–6.19, 1983.

[49] J. Kim and H. J. Sung. Wall pressure fluctuations and flow-induced noise in a turbulent boundary layer over a bump. *Journal of Fluid Mechanics*, 558:79–102, 2006.

[50] J. Kim, P. Moin, and R. Moser. Turbulence statistics in fully developed channel flow at low Reynolds number. *Journal of Fluid Mechanics*, 177:133–166, 1987.

[51] M. Klein. An attempt to assess the quality of large eddy simulations in the context of implicit filtering. *Flow, Turbulence and Combustion*, 75(1-4):131–147, 2005.

[52] R. Kristoffersen and H. Andersson. Direct simulations of low-Reynolds-number turbulent flow in a rotating channel. *Journal of Fluid Mechanics*, 256:163–197, 1993.

[53] A. Krothapalli and C. Shih. Separated flow generated by a vectored jet in a crossflow. In *Computational and Experimental Assessment of Jets in CrossFlow, AGARD-CP-534*, Nov. 1993.

[54] A. Krothapalli, L. Lourenco, and J. Buchlin. Separated flow upstream of a jet in a crossflow. *AIAA Journal*, 28(3):414–420, 1990.

[55] A. Leonard. On the energy cascade in Large-Eddy Simulations of turbulent fluid flows. *Rep. TF-1, Thermosciences Div., Stanford University, Dept. Mech. Eng., Stanford, CA 94305*, 1973.

[56] N. Li, E. Balaras, and U. Piomelli. Brief communications - inflow conditions for large-eddy simulations of mixing layers. *Physics of Fluids*, 12(4):935–938, 2000.

[57] D. K. Lilly. A proposed modification of Germano subgrid-scale closure method. *Physics of Fluids A (Fluid Dynamics)*, 4(3):633–635, 1992.

[58] T. Lim, T. New, and S. Luo. On the development of large-scale structures of a jet normal to a cross flow. *Physics of Fluids*, 13(3):770–775, 2001.

[59] N. Liu and X. Lu. Large eddy simulation of turbulent flows in a rotating concentric annular channel. *International Journal of Heat and Fluid Flow*, 26(3):378–392, 2005.

[60] J. Lumley. The structure of inhomogeneous turbulent flows. In A. Yaglom and V. Tatarsky, editors, *Atmospheric Turbulence and Radio Wave Propagation*, pages 166–178, 1967.

[61] T. Lund and H. Kaltenbach. Experiments with explicit filtering for LES using a finite difference method. *Annual Research Briefs, Center for Turbulence Research, NASA Ames-Stanford University*, pages 91–105, 1995.

[62] T. Lund, X. Wu, and K. Squires. Generation of turbulent inflow data for spatially-developing boundary layer simulations. *Journal of Computational Physics*, 140(2):233–258, 1998.

[63] R. J. Margason. Analysis of the Flow Field of a Jet in a Subsonic Crosswind. In *Analytic methods in Aircraft Aerodynamics, NASA-SP-228*, pages 683–702, 1969.

[64] R. J. Margason. Fifty years of Jet in CrossFlow research. In *Computational and Experimental Assessment of Jets in CrossFlow, AGARD-CP-534*, Nov. 1993.

[65] A. L. Marsden, O. V. Vasilyev, and P. Moin. Construction of commutative filters for LES on unstructured meshes. *Center for Turbulence Research Annual Research Briefs*, page 179, 2000.

[66] H. McMahon, D. Hester, and J. Palfery. Vortex shedding from a turbulent jet in a crosswind. *Journal of Fluid Mechanics*, 48:73–80, 1971.

[67] O. J. McMillan and J. H. Ferziger. Direct testing of subgrid-scale models. *AIAA*, 17 (12):1340–1346, 1979.

[68] F. Menter. Performance of popular turbulence models for attached and separated adverse pressure gradient flows. *AIAA Journal*, 30(8):2068–2072, 1992.

[69] K. E. Meyer, J. Pedersen, and O. Özcan. Turbulent Jet in Cross Flow Analyzed with Proper Orthogonal Decomposition . *Submitted to Journal of Fluid Mechanics.*

[70] K. E. Meyer, O. Özcan, P. S. Larsen, and C. H. Westergaard. Stereoscopic PIV measurements in a jet in crossflow. In *Proceedings of Second International Symposium on Turbulence and Shear Flow Phenomena*, 27-29 June, Stockholm - Sweden, 2001.

[71] K. E. Meyer, O. Özcan, and C. H. Westergaard. Flow mapping of a jet in crossflow with stereoscopic PIV. *Journal of Visualization*, 5(3):225–31, 2002.

[72] J. A. Michelsen. Block structured Multigrid solution of 2D and 3D elliptic PDE's. Technical Report AFM 94-06, Technical University of Denmark, 1994.

[73] P. Moin and J. Kim. Numerical investigation of turbulent channel flow. *Journal of Fluid Mechanics*, 118:341–377, 1982.

[74] B. R. Morton and A. Ibbetson. Jets deflected in a crossflow. *Experimental Thermal and Fluid Science*, 12(2):112–133, 1996.

[75] R. Moser, J. Kim, and N. Mansour. Direct numerical simulation of turbulent channel flow up to $Re_\tau = 590$. *Physics of Fluids*, 11(4):943–945, 1999.

[76] Z. M. Moussa, J. W. Trischka, and S. Eskinazi. Near field in the mixing of a round jet with a cross-stream. *J Fluid Mech*, 80:49–80, 1977.

[77] O. Özcan and P. S. Larsen. An experimental study of a turbulent jet in cross-flow by using LDA. Technical Report MEK-FM 2001-02, Department of Mechanical Engineering, Technical University of Denmark - DTU, 2001.

[78] O. Özcan, K. E. Meyer, and P. S. Larsen. Measurement of mean rotation and strain-rate tensors by using stereoscopic PIV. *Experiments in Fluids*, 39(4):771–783, 2005.

[79] J. Pallares and L. Davidson. Large-eddy simulations of turbulent flow in a rotating square duct. *Physics of Fluids*, 12(11):2878–2894, 2000.

[80] V. C. Patel and F. Sotiropoulos. Longitudinal curvature effects in turbulent boundary layers. *Progress in Aerospace Sciences*, 33(1-2):1–70, 1997.

[81] J. M. Pedersen. *Analyses of Planar Measurements of Turbulent Flows.* PhD thesis, Danish Technical University, DTU, 2003.

[82] U. Piomelli and E. Balaras. Wall-layer models for large-eddy simulations. *Annual Review of Fluid Mechanics*, 34:349–374, 2002.

[83] U. Piomelli and J. Liu. Large-Eddy Simulations of rotating channel flow using a localized dynamic model. *Physics of Fluids*, 7(4):839–848, 1995.

[84] U. Piomelli, J.-L. Balint, and J. Wallace. On the validity of Taylor's hypothesis for wall-bounded flows. *Physics of Fluids A (Fluid Dynamics)*, 1(3):609–611, 1989.

[85] S. B. Pope. *Turbulent Flows.* Cambridge University Press, 2000.

[86] M. Reck. *Computational fluid dynamics, with detached eddy simulation and the immersed boundary technique, applied to oscillating airfoils and vortex generators.* PhD thesis, Department of Mechanical Engineering, MEK - DTU, 2005.

[87] D. Rempfer and H. F. Fasel. Evolution of three-dimensional coherent structures in a flat-plate boundary layer. *Journal of Fluid Mechanics*, 260:351–375, 1994.

[88] A. Rivero, J. Ferre, and F. Giralt. Organized motions in a jet in crossflow. *Journal of Fluid Mechanics*, (444):117–149, 2001.

[89] M. Rudman. Simulation of the near field of a jet in a cross flow. *Experimental Thermal and Fluid Science*, 12(2):134–141, 1996.

[90] P. Sagaut. *Large Eddy Simulation for Incompressible Flows, An Introduction.* Springer-Verlag, 1998.

[91] P. Sagaut. Numerical simulations of separated flows with subgrid models. *Rech. Aero.*, pages 51–63, 1996.

[92] P. Sagaut, E. Montreuil, O. Labbe, and C. Cambon. Analysis of the near-wall behaviour of some self-adaptive subgrid-scale models in finite-differenced simulations of channel flow. *International Journal for Numerical Methods in Fluids*, 40(10):1275–1302, 2002.

[93] J. J. Schmidt. *Experimental and Numerical Investigation of Separated Flows.* PhD thesis, Department of Mechanical Engineering, MEK - DTU, 1997.

[94] U. Schumann. Subgrid-scale model for finite difference simulations of turbulent flow in plane channels and annuli. *Journal of Computational Physics*, 18:376–404, 1975.

[95] C. Seal, C. Smith, O. Akin, and D. Rockwell. Quantitative characteristics of a laminar, unsteady necklace vortex system at a rectangular block-flat plate juncture. *Journal of Fluid Mechanics*, 286:117–135, 1995.

[96] J. Shang, D. McMaster, N. Scaggs, and M. Buck. Interaction of jet in hypersonic cross stream. *AIAA Journal*, 27(3):323–329, 1989.

[97] R. L. Simpson. Turbulent boundary-layer separation. *Annual Review of Fluid Mechanics*, 21:205–234, 1989.

[98] L. Sirovich. Turbulence and the dynamics of coherent structures. PART I: Coherent structures. *Quarterly of Applied Mathematics*, 45(3):561–570, 1987.

[99] J. Smagorinsky. General circulation experiments with primitive equations. *Monthly Weather Review*, 91:99–165, 1963.

[100] S. Smith and M. Mungal. Mixing, structure and scaling of the jet in crossflow. *Journal of Fluid Mechanics*, 357:83–122, 1998.

[101] P. Spalart and J. Watmuff. Experimental and numerical study of a turbulent boundary layer with pressure gradients. *Journal of Fluid Mechanics*, 249:337–371, 1993.

[102] P. R. Spalart. Direct simulation of a turbulent boundary layer up to $Re_\Theta = 1410$. *Journal of Fluid Mechanics*, 187:61–98, 1988.

[103] C. Speziale. Galilean invariance of subgrid-scales stress models in the Large-Eddy Simulation of turbulence. *Journal of Fluid Mechanics*, 156:55–62, 1985.

[104] A. Spille-Kohoff and H.-J. Kaltenbach. Generation of turbulent inflow data with a prescribed shear-stress profile. *Third AFOSR International Conference on DNS/LES, Arlington, TX, 5-9, August, 2001, in DNS/LES Progress and challenges, edited by C. Liu, L. Sakell, T. Beutner*, pages 319–326.

[105] N. N. Sørensen. *General Purpose Flow Solver Applied to Flow over Hills.* PhD thesis, Risø National Laboratory, Roskilde, Denmark, 1995.

[106] S. Stolz and N. A. Adams. An approximate deconvolution procedure for Large-Eddy Simulation. *Physics of Fluids*, 11:1699–1701, 1999.

[107] S. Stolz, N. A. Adams, and L. Kleiser. An approximate deconvolution model for Large-Eddy Simulation with application to incompressible wall-bounded flows. *Physics of Fluids*, 13:997–1015, 2001.

[108] R. I. Sykes, W. S. Lewellen, and S. F. Parker. On the vorticity dynamics of a turbulent jet in a crossflow. *Journal of Fluid Mechanics*, 168:393–413, 1986.

[109] D. Tafti and S. Vanka. A numerical study of the effects of spanwise rotation on turbulent channel flow. *Physics of Fluids A (Fluid Dynamics)*, 3(4):642–656, 1991.

[110] O. V. Vasilyev, T. S. Lund, and P. Moin. A general class of commutative filters for LES in complex geometries. *Journal of Computational Physics*, 146:105, 1998.

[111] L. P. K. Voigt. *Navier-Stokes Simulation of Airflow in Rooms and around Human Bodies.* PhD thesis, Danish Technical University, DTU, 2001.

[112] D. Warnack and H. Fernholz. Effects of a favourable pressure gradient and of the Reynolds number on an incompressible axisymmetric turbulent boundary layer. Part 2. The boundary layer with relaminarization. *Journal of Fluid Mechanics*, 359:357–381, 1998.

[113] D. Webster, D. DeGraaff, and J. Eaton. Turbulence characteristics of a boundary layer over a two-dimensional bump. *Journal of Fluid Mechanics*, 320:53–69, 1996.

[114] G. Winckelmans and H. Jeanmart. Assessment of some models for LES without/with explicit filtering. *In Direct and Large-Eddy Simulation IV*, pages 55–66, 2001.

[115] X. Wu and K. D. Squires. Numerical investigation of the turbulent boundary layer over a bump. *Journal of Fluid Mechanics*, 362:229–271, 1998.

[116] A. Yoshizawa. A statistically-derived model for the large-eddy simulation of turbulence. *Physics of Fluids*, 25(9):1532–1538, 1982.

[117] L. L. Yuan, R. L. Street, and J. H. Ferziger. Large-Eddy Simulations of a round jet in crossflow. *Journal of Fluid Mechanics*, 379:71–104, 1999.

[118] S. Zahrai, F. Bark, and R. Karlsson. On anisotropic subgrid modeling. *European Journal of Mechanics, B/Fluids*, 14(4):459–486, 1995.

[119] Y. Zang, R. L. Street, and J. R. Koseff. A dynamic mixed subgrid-scale model and its applications to turbulent recalculating flows. *Physics of Fluids A (Fluid Dynamics)*, 5: 3186–3196, 1993.

Appendix A

Numerical Investigations of the R=3.3 Velocity Ratio Case

A computational study, where effects of different numerical parameters on the computed results of the JICF flow for the $R = 3.3$ case were investigated, has been conducted in the course of this project. In this section the results of those numerical investigations are presented and analyzed.

A.1 Outline of Computational Details

A summary, covering various aspects of numerical investigations presented in the following, is outlined in Table A.1. Note that the Table caption provides the basic explanation for most of the abbreviations used in it.

In Table A.1 fourteen different and representative computations of the analyzed JICF flow case are presented. They are denoted as cases LES 1 - LES 14 and are generally covering the essential findings of this computational study. It should be mentioned that some additional computations of this flow have been conducted in the course of this project, but as they do not add any new information regarding the computed JICF flow, they are not included in this presentation.

From Table A.1 it can be observed that in 10 out of 14 cases, the grids - refereed to as 4.7 million and 5.9 million (cells) grids are utilized. These grids represent the basic numerical set-up used in this study. The spanwise and wall-normal distributions of grid points in the the mentioned meshes are identical; the difference between them basically lies in a variation of the streamwise domain extension employed in the computations, so additional 1.2 million cells in the 5.9 million (cells) grid is actually used to cover the streamwise region $12D < x < 25D$ (see Table A.1). The grid referred to as 4.3 million (cells) grid (Case LES 4) follows the described pattern as well; here the streamwise domain extension is shortened to $10D$, so number of cells used in LES 4 case compared to cases LES 5, 6, 10, 11 and 13 is diminished by app. 400 000, while the basic grid distribution in y and z directions is kept unchanged.

Case	L_{x_1}	Inlet (L_{x_1})	L_{z_D}	L_{x_2}	Outl. (L_{x_2})	Model	Grid Size	$\frac{t_a}{t_{FLT}}$	$\frac{\Delta t U_\infty}{D}$	R	Code	Diff. Scheme	CFL_{max}
LES 1	$5D$	Mean U, V	$3D$	$25D$	Z.G.	DSM	5.9 mil.	9(16)	0.0313	3.24	EllipSys	Quick	11.6
LES 2	$5D$	Mean U, V	$3D$	$25D$	Z.G.	Mix (Ω)	5.9 mil.	4(7)	0.0025	3.24	EllipSys	Cds4	1.12
LES 3	$5D$	Mean U, V	$3D$	$25D$	Z.G.	Mix (Ω)	5.9 mil.	10(17.5)	0.0025	3.24	EllipSys	Quick	1.07
LES 4	$5D$	Turbulent	$3D$	$10D$	Conv.	SM	4.3 mil.	20(18)	0.0063	3.35	Fastest	Cds	4.23
LES 5	$5D$	Turbulent	$3D$	$12D$	Conv.	DSM	4.7 mil.	60(−)	0.0313	3.37	EllipSys	Cds4/Quick	14.9
LES 6	$5D$	Turbulent	$3D$	$12D$	Conv.	Mix (Ω)	4.7 mil.	60(−)	0.0313	3.31	EllipSys	Quick	8.20
LES 7	$5D$	Turbulent	$3D$	$25D$	Z.G.	Mix (Ω)	5.9 mil.	60(105)	0.0313	3.22	EllipSys	Quick	12.7
LES 8	$10D$	Turbulent	$6D$	$12D$	Conv.	Mix (Ω)	8.0 mil.	20(26)	0.0313	3.30	EllipSys	Quick	14.6
LES 9	$5D$	Mean U, V	$3D$	$25D$	Z.G.	Mix (Ω)	14.8 mil.	6.5(11.5)	0.0013	3.27	EllipSys	Cds4	0.55
LES 10	$5D$	Turbulent	$3D$	$12D$	Conv.	Mix (Ω)	4.7 mil.	8(−)	0.0313	3.41	EllipSys	Quick	8.15
LES 11	$5D$	Turbulent	$3D$	$12D$	Conv.	Mix (Ω)	4.7 mil.	16(−)	0.0313	3.61	EllipSys	Quick	7.61
LES 12	$10D$	Turbulent	$6D$	$12D$	Conv.	Mix (Ω)	12.9 mil.	9(11.5)	0.0063	3.23	EllipSys	Cds4	2.33
LES 13	$5D$	Turbulent	$3D$	$12D$	Conv.	Mix (Ω)	4.7 mil.	9(−)	0.0063	3.34	EllipSys	Cds4/Quick	2.07
LES 14	$5D$	Turbulent	$3D$	$25D$	Conv.	Mix (Ω)	5.9 mil.	14(25)	0.0063	3.34	EllipSys	Cds4/Quick	2.11

Table A.1: Summary of the computations - t_a : averaging time; t_{FLT} : flow-through time $t_{FLT} = (L_{x_1} + L_{x_2})/U_\infty$. Due to different streamwise domain extensions employed in various computations, values in parentheses are introduced and they refer to the baseline grid with $L_{x_1} = 5D$ and $L_{x_2} = 12D$. These values are used as overall averaging time reference.; Conv.: Convective OutFlow BC; Z.G.: Zero-Gradient (Neumann) BC; DSM: Dynamic Smagorinsky Model; SM: Smagorinsky Model; Mix(Ω) : Mixed Scale (Ω) based Eddy Viscosity (Sagaut [91]) Model; Mean U, V : Steady Experimental mean inlet profiles; Turbulent: UnSteady pre-computed turbulent inlet data; Cds: 2nd order Central Difference Scheme; Cds4: 4th order deferred corrected Central Difference Scheme; Quick: 3rd order Upwind based Scheme; Cds4/Quick: A wiggle-detecting scheme of Dahlström and Davidson [19] is implemented in order to stabilize the computations. Underlying scheme is Cds4, which in case of detected wiggle is locally replaced by the Quick scheme; R: The velocity ratio; L_{n_m} : Domain extensions described on Figure 4.2 on page 37.

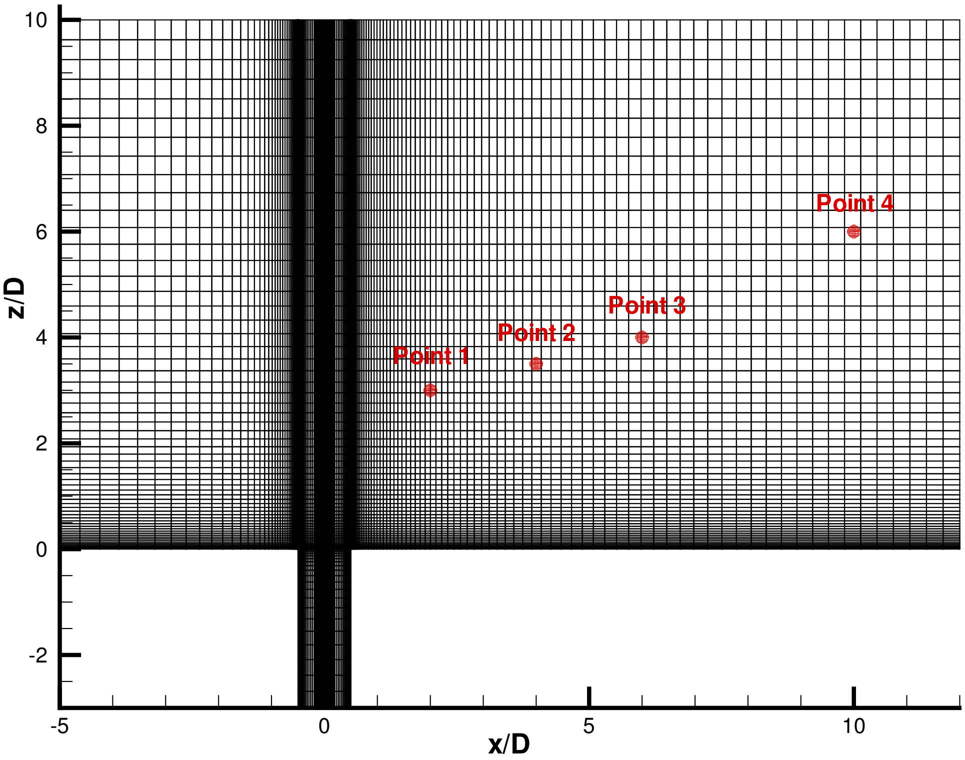

(a)

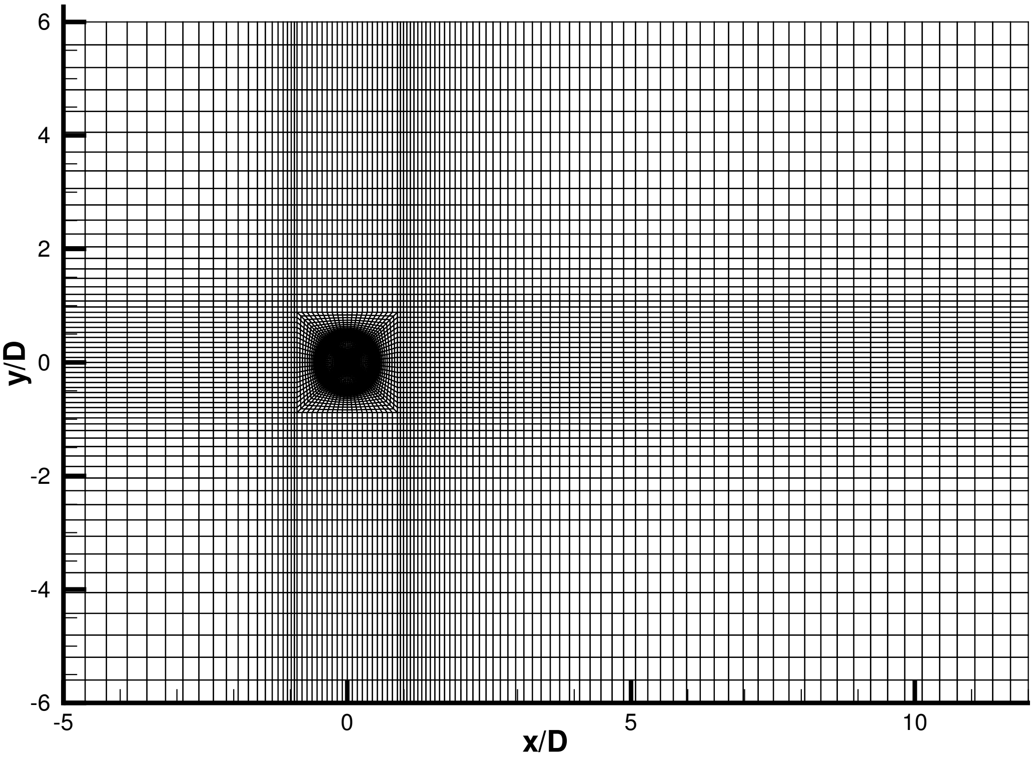

(b)

Figure A.1: Cross sections of the 4.7 million (cells) grid. Note that only every second grid point is depicted on the subfigures. Indicators of points in subfigure (a) refer to positions where a time series of all velocity components have been recorded - see Figure A.21.

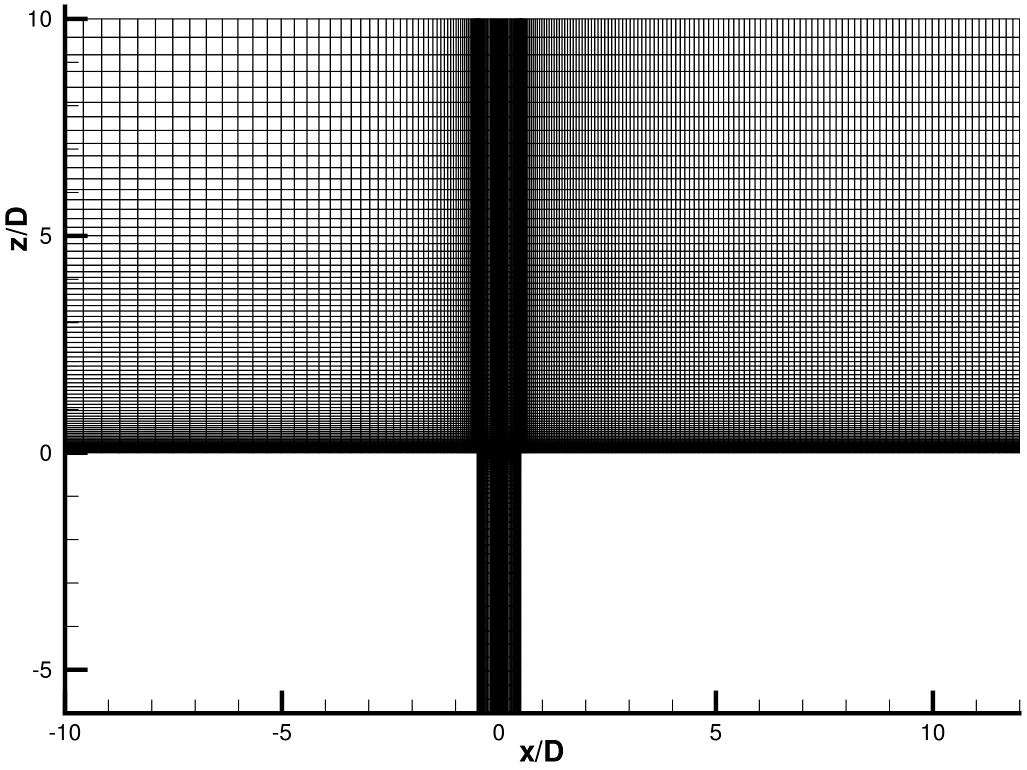

(a)

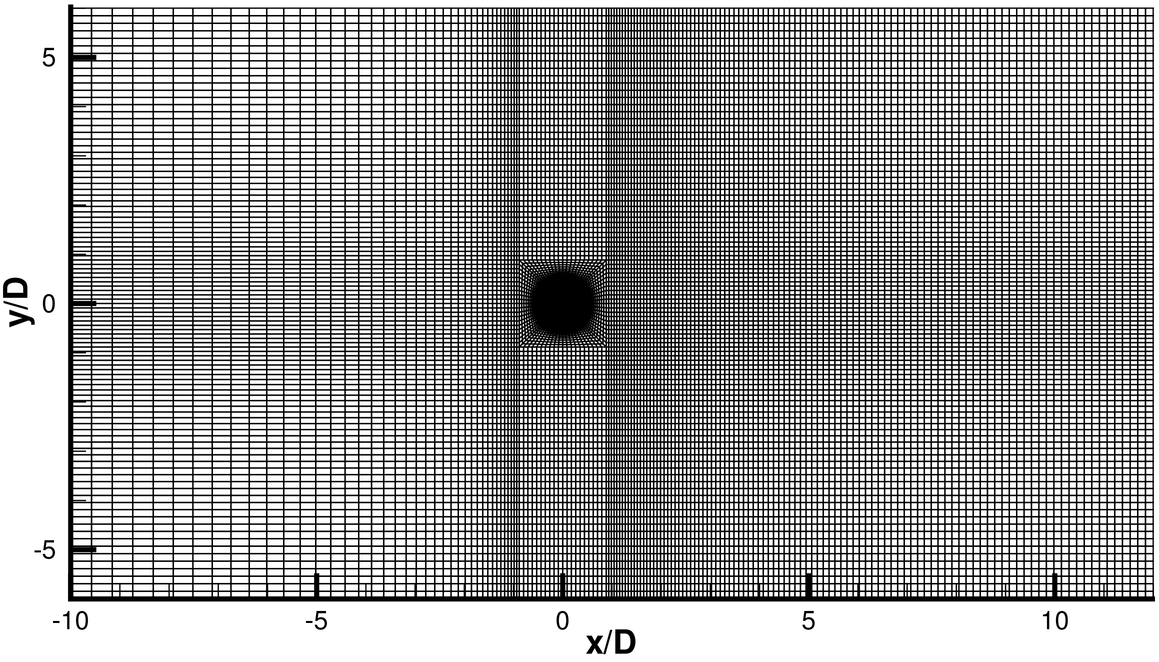

(b)

Figure A.2: Cross sections of the 12.9 million (cells) grid. Note that only every second grid point is depicted on the subfigures.

Two cross sections of the 4.7 million (cells) grid, corresponding to planes $y/D = 0$ and $z/D = 5$ are presented in Figure A.1. Disregarding the "*direct jet zone*" ($-D \lesssim x,\ y \lesssim D$) this computational mesh can be described as 200 x 120 x 120 cells mesh - (in the streamwise, spanwise and wall-normal directions respectively - app. 2.9 million cells), whereas the *"jet zone"*, extending throughout the whole wall-normal direction (see Figure A.1), is additionally covered[1] by 1.8 million cells. The grid used in case LES 12, representative for cases LES 8 and LES 9 where grid refinement was considered, is presented in Figure A.2. Using the same analogy this grid can be denoted as 320 x 200 x 160 mesh in L_x x L_y x L_z directions (app. 10.2 million cells), whereas the *"jet zone"*, has additional 2.7 million cells in this case.

It should be noted that numerical blocks consisting of 40^3 cells were used for generation of both the presented grids. In the case LES 9 numerical blocks consisting of 48^3 cells were used. Whereas in the LES 12 case the jet itself has not been refined, in the LES 9 case 40% more cells, compared to the other cases, are located directly in the jet area. The refined grid of LES 8 case has 25% more cells placed in the streamwise and wall-normal directions, compared to the baseline case (LES 6).

In the LES 4 case a different flow solver (FASTEST - see Appendix C and Durst and Schafer [26] for reference) has been utilized. In this case a most general numerical LES set-up has been employed, where the 2nd order central difference scheme for convective terms was combined with the 2nd order Crank-Nicholson time discretisation and the Smagorinsky SGS model (without wall-damping). As practically the same mesh is utilized here as in the baseline (LES 6) case, the LES 4 computation can directly be used to additionally assess quality of the computed results.

Besides variations in the grid size, different spatial extensions of the considered computational domain were considered in this study. This was done for two basic reasons: 1) to investigate whether the position of inflow boundary influences the computed flow significantly and 2) to allow different types of outflow boundary conditions to be used. As the jet flow is considered to be fully developed, extending the domain (L_{z_D} from $3D$ to $6D$ - see Figure 4.2 on page 37) should not influence the quality of the jet inflow data used. On the wind tunnel side where the turbulent and time resolved spatially developing boundary layer flow is used as inlet condition, extending the domain in the jet-upstream direction (L_{x_1} from $5D$ to $10D$) in principle changes the state of the boundary layer flow existing at the inlet position. This effect was not considered/included in the present investigation, as it was assumed that it does not influence the overall flow configuration used in this study significantly. However it was considered important to investigate whether the inlet BC position of $L_{x_1} = 5D$ (corresponding to app. $1.7\,\delta_0$ - δ_0 is the experimental BL thickness at inlet) is sufficient to allow development of proper boundary layer flow impacting the jet. Positioning inlet BC at $L_{x_1} = 10D$ (app. $3.5\,\delta_0$) can directly give an indication of the BL flow development state in the jet-upstream region. Convective Outflow BC was implemented in the EllipSys code in the course of this project. It allowed use of a shorter domain in the streamwise direction without compromising quality of the obtained results. This means that the grid used in the LES 12 case can basically be regarded as the highest quality grid used in this study, in spite of the fact that the grid in LES 9 case includes (overall) more computational points.

As one of the main ideas behind this project is comparison of flow dynamics in the experimentally and numerically obtained JICF flow fields, an important issue regarding the use of Upwind based QUICK scheme vs. the central difference CDS(4) schemes for the convective term in the N-S equations is investigated in this study too. Initial calculations showed a

---

[1] 0.2 million cells are already included in the *"jet zone"*.

high level of unphysical oscillations (wiggles) in the instantaneous flow fields obtained using the CDS schemes, which made the POD analysis of the synthetic LES flow quite unfeasible. Additionally the time step size effects on the computed results have been addressed in this numerical investigation as well. Ideally the CFL number should not exceed 1 during the computations anywhere in the domain, but fulfilling this demand impacts the computational costs tremendously, as the number of time steps needed to achieve the convergence of statistics increases enormously - e.g. a 150 000 time steps (each take app. 25 seconds on 34 P4 2.4 GHz PCs) in the LES 9 case correspond to only 6.5 FLTs (CFL_{max} demand satisfied i.e. $CFL_{max} < 1$), while the same amount of time steps will correspond to 285 FLTs in the LES 6 case (CFL_{max} demand not satisfied - see Table A.1). Regarding the general computational costs it is noted that 60 FLTs in LES 6 case (30 sec. pr. time step, app. 33 000 steps needed) took about 12 days to complete on 37 P4 2.4 GHz PCs.

In the EllipSys code the 2nd order iterative dual-time stepping method is used for time advancement of the solution. In the present study the number of (sub)iterations utilized (pr. time step) in order to achieve a sufficient convergence has been adjusted significantly in various computations, as different sizes of time steps were considered. As a minimum demand in all cases the drop of residuals in order of app. 10^{-2} during a time step was required and in many cases residuals actually dropped beyond 10^{-3}.

In most of the presented computations the turbulent inflow on the wind tunnel boundary layer side was used. In the initial phase of this project, where neither convective outflow BC was implemented nor boundary layer simulation was performed, some results were obtained by using the mean experimental profiles at inlet boundary on the wind tunnel side. They are also included in this presentation.

A note on how the effective velocity ratio R is determined should be given. Normally R represents the ratio of mean jet velocity U_{jet} and free-stream velocity U_∞. This might be a good way in determining it in cases where laminar boundary layer flow[2] on the wind tunnel side is considered, but it turns out to be difficult to use in present cases where turbulent boundary layer inflow was utilized in the computations. As data interpolation at inflow boundary was necessary, a much more important quantity than U_∞, which should be directly controlled, is the effective mass flow rate on the wind tunnel boundary layer inlet side. The velocity ratio in the present study is therefore determined in the following way: Based on the mean experimental streamwise velocity profile the mean flow rate corresponding to the used numerical set-up (cross section of 12D x 10D) is determined. This mean flow rate combined with the mean experimental jet velocity was than considered to correspond to the velocity ratio of $R = 3.3$. Velocity ratios presented in Table A.1 are determined based on relative differences of the mean flow rates computed in each considered case (jet and BL side) and the corresponding mean flow rates determined based on experimental results.

The time step in LES 9 case was 25 times lower than in e.g. LES 6 case. As inflow data were originally created to fit the time step requirements of the baseline cases (like LES 6), a generation of a new inflow data set was necessary in order to be able to perform computations in the LES 9 case. Therefore a new database, consisting of 100 000 files representing instantaneous snapshots of a pipe flow cross section have been created in order to perform JICF flow analysis with a better time resolution. This huge number of files was assumed to be sufficient to obtain a statistically reasonable (Li et al. [56]) inflow dataset. In general two datasets of both the pipe flow (created at $\Delta t U_\infty / D = [0.0313,\ 0.000625]$) and and boundary

---

[2] It actually worked fine in this study in cases where non-turbulent BL flow was applied at inlet.

layer flow (created at $\Delta tU_\infty/D = [0.0313,\ 0.0063]$) were generated in order to to perform all presented computations.

In cases LES 1 and LES 5 the Dynamic Smagorinsky (DSM) SGS model was used. Initial computations with this model broke down, apparently due to inherit instability of the DSM model and the fact that no homogeneous directions, which could be used to stabilize the Smagorinsky constant C_s, exist in this flow. In order to stabilize the constant C_s and thereby the computations two approaches were utilized in this study. In the LES 1 case the relaxation of the dynamically computed C_s constant with its default value of 0.1 was performed and in the LES 5 case the constant was averaged for 100 time steps in each domain point before it was applied in the computations.

In all conducted calculations at least one turbulent inlet boundary condition (jet) was used. In order to reach a statistically steady state in the flow domain, calculations were initially carried out for a period of at least 5 FLTs[3] before any statistics have been sampled. In many cases the initially taken statistics were restarted, so the initial computational phase consisted of 10-15 FLTs in those cases.

Lastly it is noted that the pressure is corrected utilizing the PISO algorithm in the EllipSys code and SIMPLE algorithm in the FASTEST code.

A.2 Results and discussions

In the following part results of different computations conducted in the course of this study are presented. As whole 14 cases are considered here it is necessary to subdivided the analyses in some parts, in order to get a general idea about the quality of the conducted computations. Therefore the results are presented in 5 parts. Each part consists of three Figures, where same quantities as ones illustrated in the main rapport at the same domain positions as there, are compared against each other and the measurements. This means that cases LES 1, 2 and 3 are presented in the first part - Figures A.3-A.5, cases LES 4, 5 and 7 are presented in the second part - Figures A.6-A.8, cases LES 8, 9 and 12 are presented in the third part - Figures A.9-A.11, cases LES 10 and 11 are presented in the fourth part - Figures A.12-A.14 and cases LES 13 and 14 are presented in the fifth part - Figures A.15-A.17. Note that velocities, r.m.s. fluctuations and shear stress are rescaled with an appropriate factor on many subfigures in order to accommodate a better comparison basis between various LES computations and experiment. The scale is adjusted at the first four ($x/D = [-1.00,\ -0.83,\ -0.67,\ -0.5]$) positions in the case of mean wall-normal velocity W, the first three positions ($x/D = [-1.00,\ -0.83,\ -0.67]$) are adjusted in the case of the r.m.s fluctuations and uw shear stress, while only the first position ($x/D = -0.67$) is adjusted in the case of v_{rms} velocity fluctuation. In all subsequent Figures results from case LES 6, which corresponds to results presented in the main rapport, are included. Thereby a comparison of this baseline case against all other computed cases can directly be made. Some differences between measurements and practically all conducted computations can be observed from Figures A.3-A.17, especially in region $-0.5 < x/D < 0.5$ and $0 < z/D < 5$. They are analyzed and discussed in the main rapport - section 4.4 on page 48. In this section the main focus is directed on differences in the obtain results between various computations performed and they will be primarily discussed in the following. Actually most of the computations are able to predict trends in the experimentally measured profiles reasonably well, so only areas where some distinct differences are observed will be assessed.

---

[3] Due to extreme computational costs the initial phase period was only 1.5 FLTs in the LES 9 case.

The subdivision in groups is made in such a way that cases where a certain property/properties was/were investigated and correspondingly varied are placed together - e.g. cases LES 1, 2 and 3 have an identical geometrical set-up and identical boundary conditions. So in this part influence of the SGS modeling strategy (DSM vs. Mix Eddy Viscosity model of Sagaut [91]), influence of the discretisation scheme (QUICK vs. CDS4) and influence of the time step size on the obtained results are investigated. The results are presented on Figures A.3-A.5.

Generally comparing the mean streamwise and wall- normal velocity profiles - Figure A.3, only a miner differences between the computations can be observed, probably caused by a difference in the velocity ratios between cases LES 1, 2, 3 and case LES 6 (see Table A.1 and jet trajectories in Figure A.5) and discrepancies caused by use of different inlet databases in cases LES 2, 3 vs. cases LES 1, 6 (to be further discussed in the following). The biggest difference actually occurs at position $x/D = -0.5$ where case LES 2 predicts the gradient in the W velocity profile in the near-wall region correctly (both peak in the first measurement point and immediate following peak away from the wall), whereas in all other cases the first peak is overpredicted while the second peak is considerably underpredicted. Considering the turbulence quantities at the same position, the similar trends are visible there too (Figure A.4). Actually both Mixed Eddy Viscosity (SGS) based cases LES 2 and 3, at this position approach the measurements much better than DSM based case LES 1 and the baseline case LES 6. On the other hand it should be noted that case LES 2 overpredicts the measured w_{rms} profile in the near-wall region $1.17 \leq x/D \leq 1.83$ and corresponding measured v_{rms} profile at $x/D = 0.67$, $1.5 < z/D < 3$ considerably, while its predictions of uw shear stress in region $-0.5 \leq x/D \leq 0.5$ are closest to the measurements. Generally it is noted that influence of the non-turbulent boundary layer flow at inlet is practically localized to poor predictions of the turbulence quantities in the jet-upstream region. It is furthermore seen that no general improvement of the results is obtained by complying with the CFL_{max} demand. It is noted that no more the 5 cells in the whole computational domain had a CFL value $CFL > 1$ in cases LES 2 and 3. Moreover it is observed that SGS modeling strategy has a very limited (insignificant) impact on the computed results. A certain impact of the discretization scheme on the computations can be observed from Figures A.3-A.5, comparing cases LES 2 and 3. Actually at almost all positions but $x/D = -0.5$ the QUICK based case LES 3 has a better predictions of the measured properties, but the general impact of the discretization scheme on the results seems to be very small.

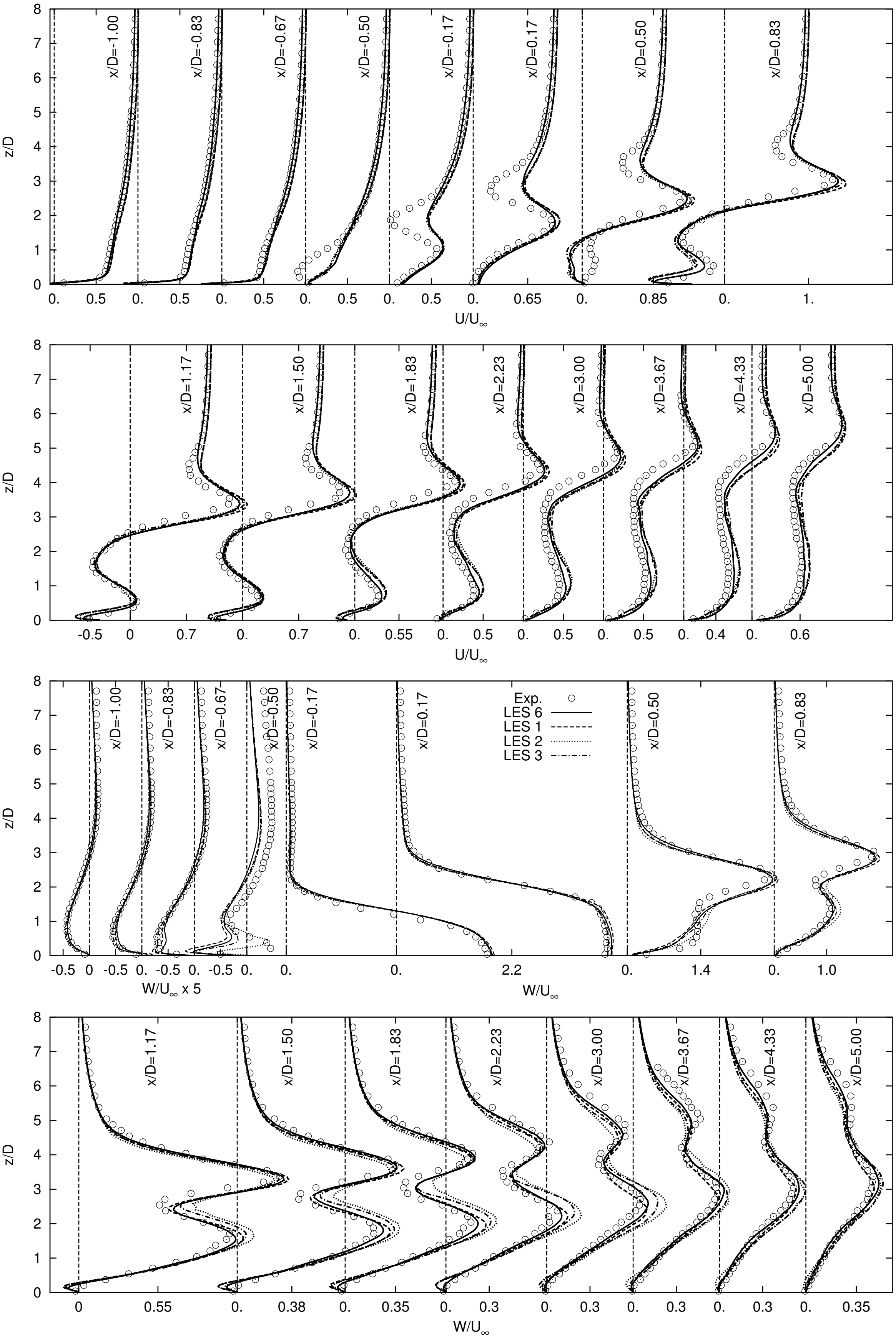

Figure A.3: U/U_∞ and W/U_∞ for $R = 3.3$ case, at $y/D = 0$ plane. Cases LES 1, 2, 3 and 6. Open circles refer to the experiment of Özcan and Larsen [77].

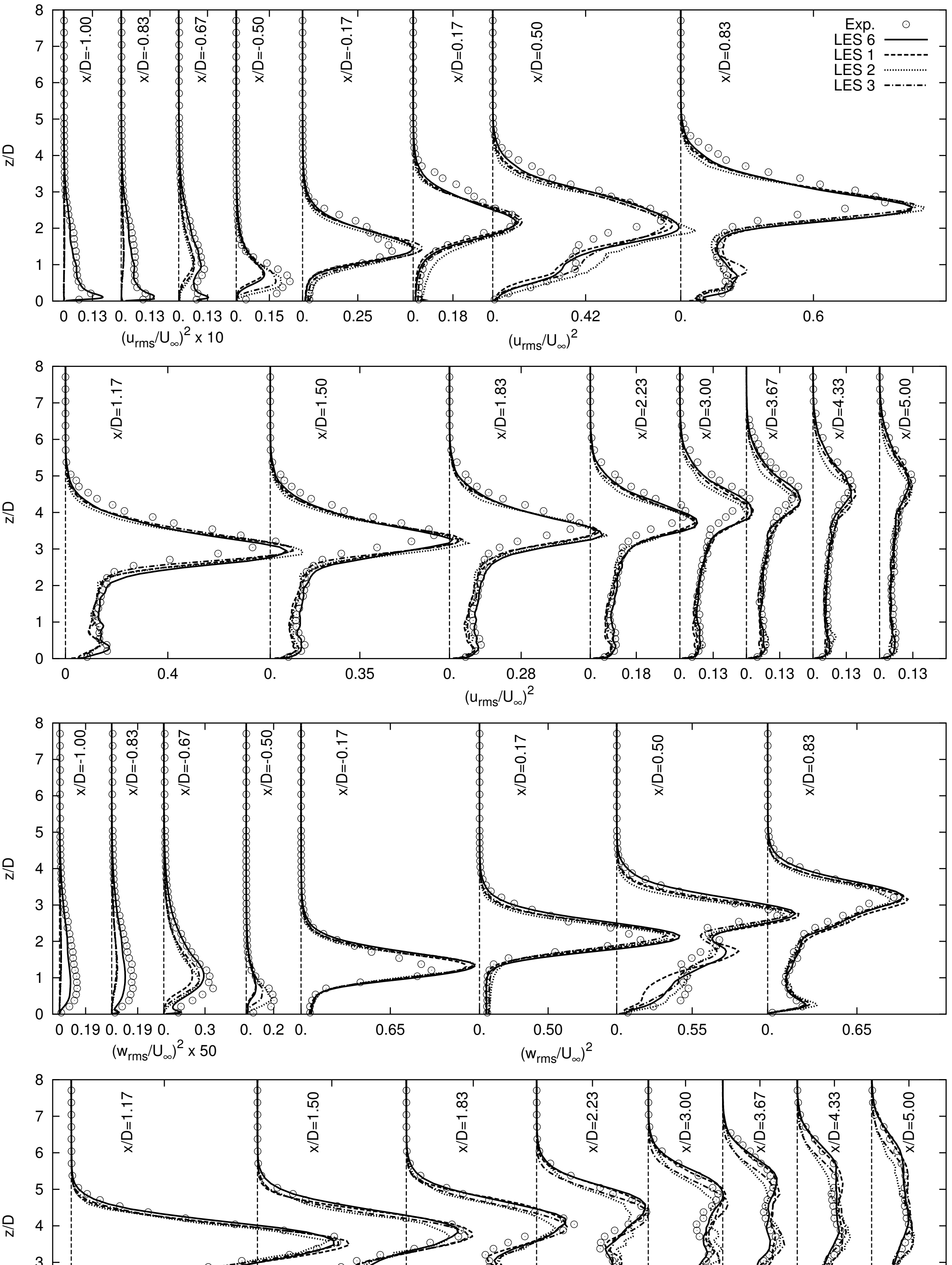

Figure A.4: $(u_{rms}/U_\infty)^2$ and $(w_{rms}/U_\infty)^2$ for $R = 3.3$ case, at $y/D = 0$ plane. Cases LES 1, 2, 3 and 6. Open circles refer to the experiment of Özcan and Larsen [77].

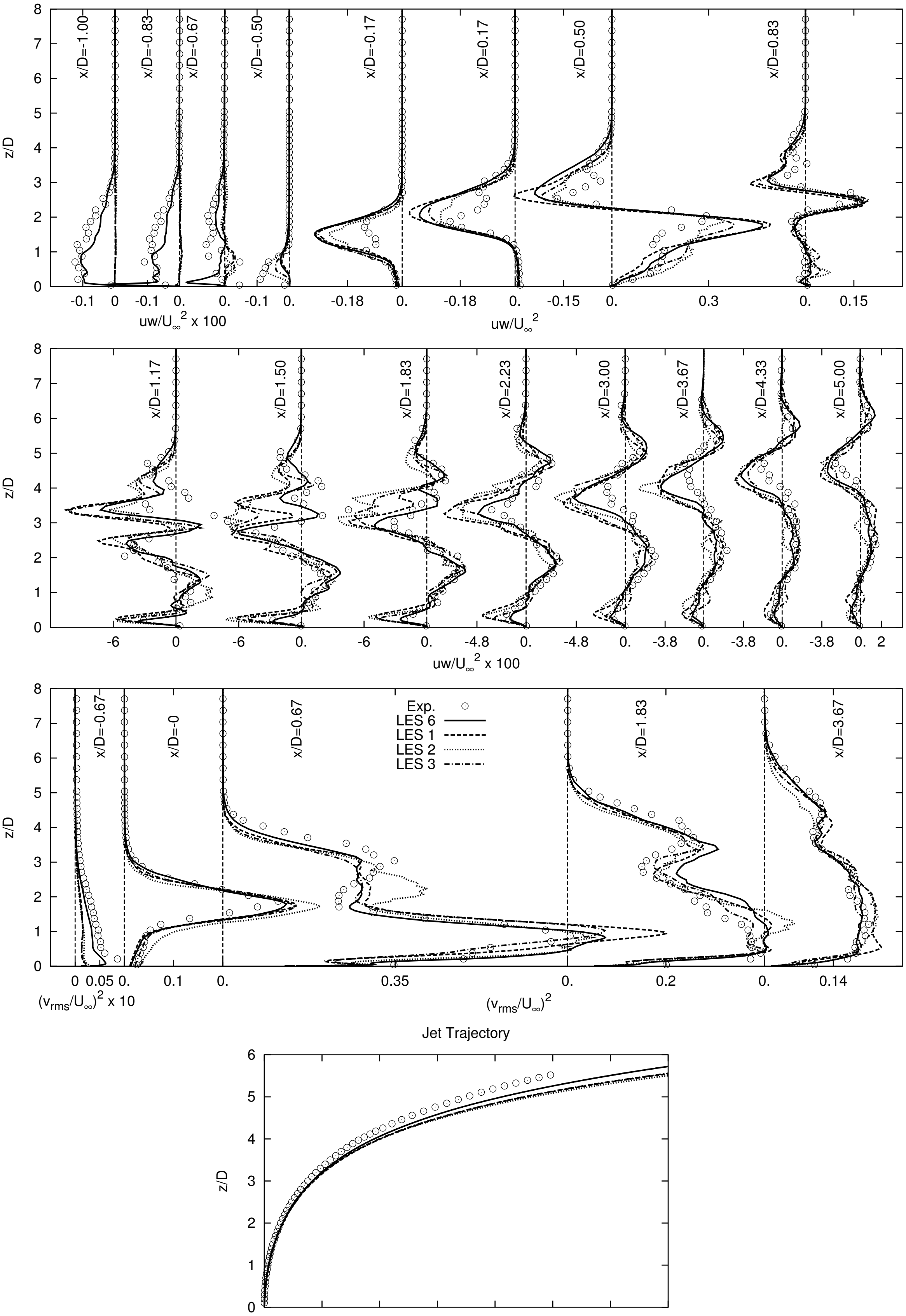

Figure A.5: $(v_{rms}/U_\infty)^2$, uw/U_∞^2 and jet-trajectories for $R = 3.3$ case, at $y/D = 0$ plane. Cases LES 1, 2, 3 and 6. Jet-trajectories are estimated as mean streamlines emerging from the point $x/D = z/D = 0$ in the symmetry plane following the definition of Yuan et al. [117]. Open circles refer to the experiment of Özcan and Larsen [77].

In cases LES 4, 5 and 7 the turbulent inlet conditions are applied on both jet- and boundary layer- inlet. Three different SGS models are used, 2 CFD codes are utilized and different discretization schemes are applied. Influence of the sampling time on the obtained results can be addressed here too, as LES 7 is the case where the largest amount of samples is included into the statistics. The results are presented on Figures A.6-A.8.

The biggest difference which can be observed from Figure A.6 is between case LES 4 and all other cases in region $x/D > 0.5$, where case LES 4 predicts U velocity profiles slightly better than other cases, but at the same time predicts W velocity profiles significantly worse than other cases in the same region. Regarding the turbulence quantities (u_{rms} and w_{rms} - Figure A.7) the only noticeable difference is again between case LES 4 and other cases at same locations as previously. It will become apparent later that some of the observed differences between results of case LES 4 and other cases presented in Figures A.6-A.8 is due to different inlet databases used to compute them. Some general differences between all calculations in the case of uw shear stress (Figure A.8) in region $x/D \geq 0.5$ can be observed too. Note also a similar shape of the v_{rms} profile from case LES 4 and LES 2 - (Figure A.5) at position $x/D = 0.67$, $1.5 < z/D < 3$. Considering all the mentioned Figures and comparing the results of cases LES 6 and 7, one can conclude that sampling time corresponding to 60 FLTs (case LES 6) is sufficient to produce reliable computational results. Again results from cases presented in Figures A.6-A.8 indicate no noteworthy influence of the SGS modeling strategy on the quality of the obtained results, as discrepancies between case LES 4 and other cases shown here are apparently caused by other influence factors than SGS model utilized - to be discussed further, later in this section. The same conclusion can be drawn with regards to the use of different discretization schemes.

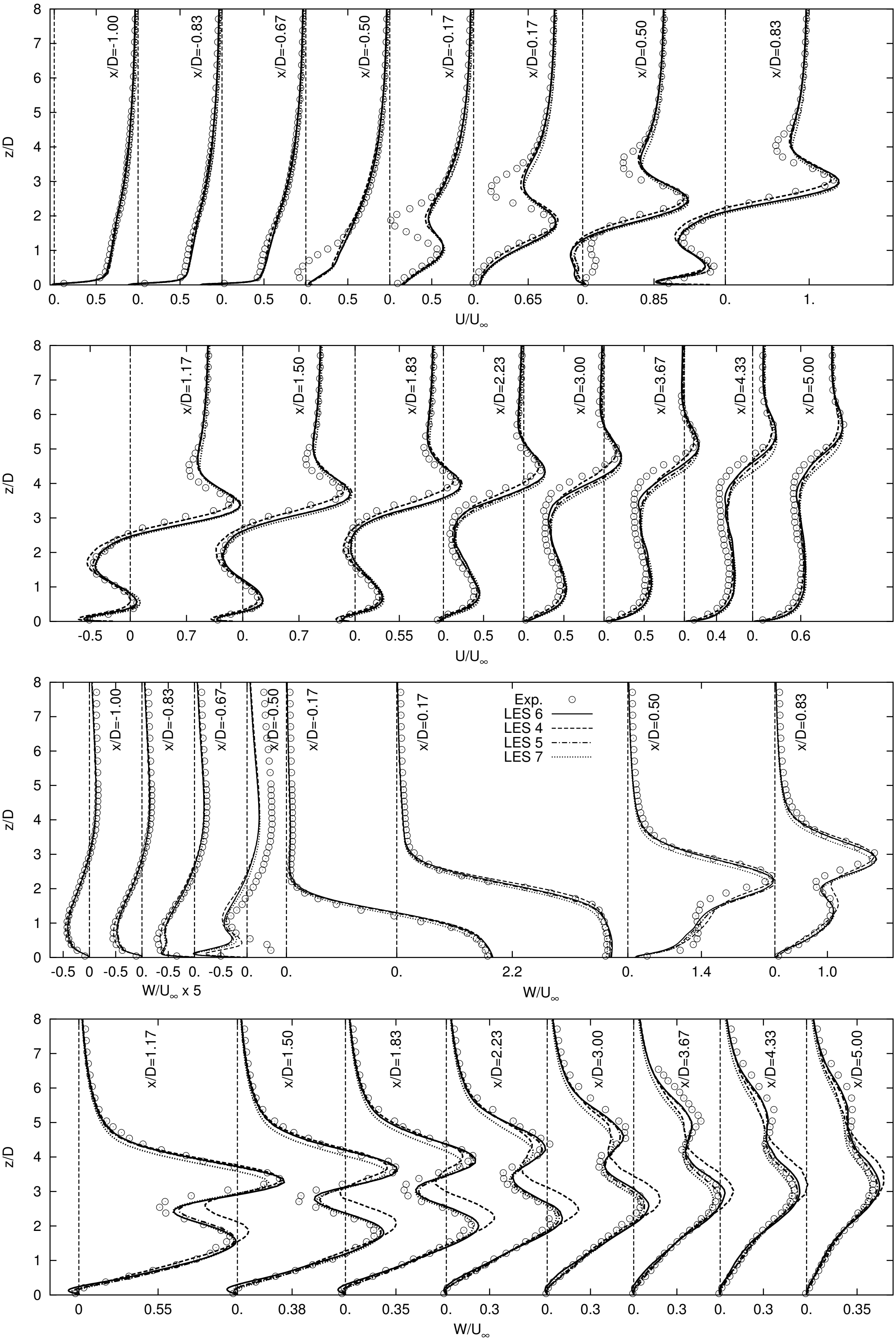

Figure A.6: U/U_∞ and W/U_∞ for $R = 3.3$ case, at $y/D = 0$ plane. Cases LES 4, 5, 6 and 7. Open circles refer to the experiment of Özcan and Larsen [77].

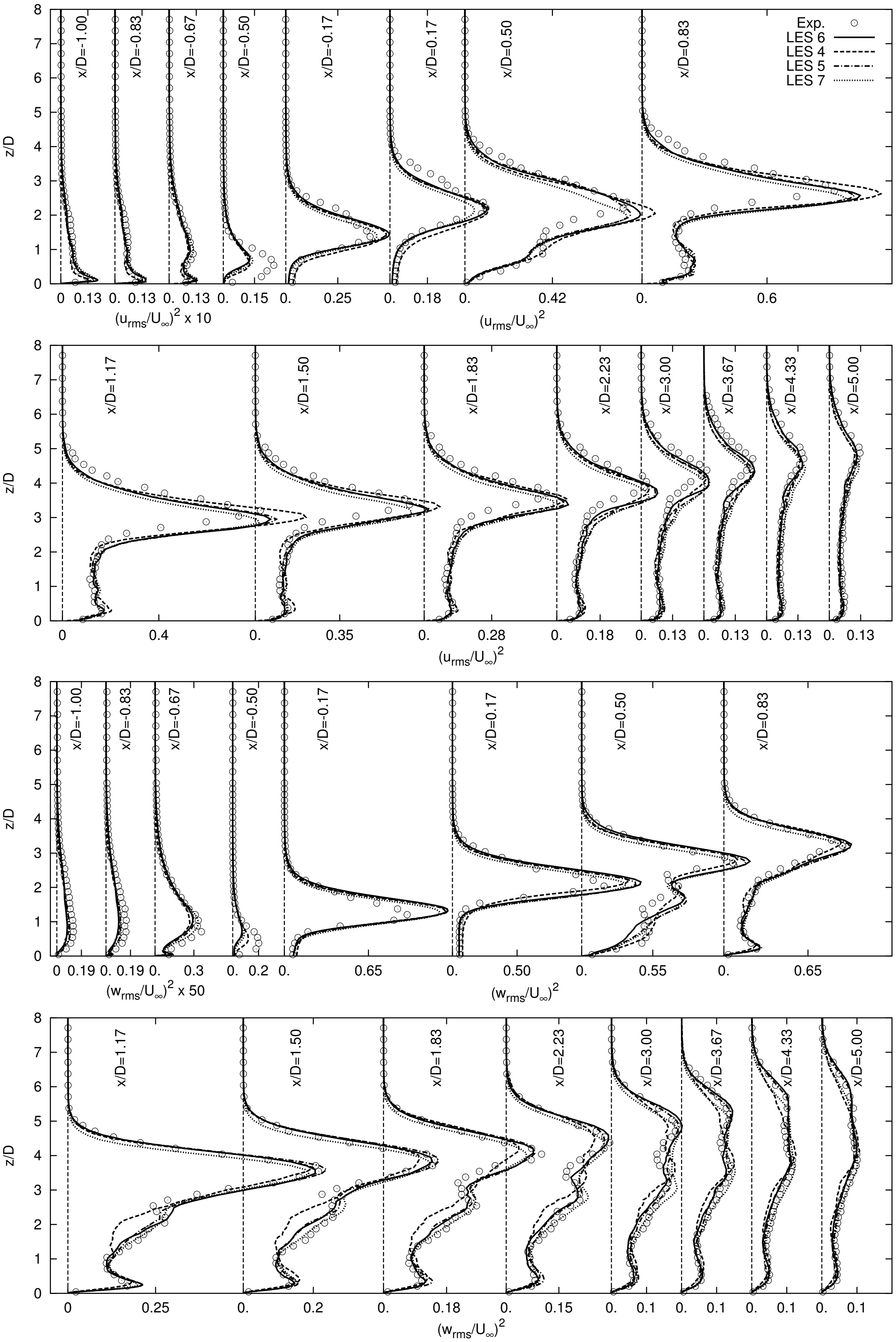

Figure A.7: $(u_{rms}/U_\infty)^2$ and $(w_{rms}/U_\infty)^2$ for $R = 3.3$ case, at $y/D = 0$ plane. Cases LES 4, 5, 6 and 7. Open circles refer to the experiment of Özcan and Larsen [77].

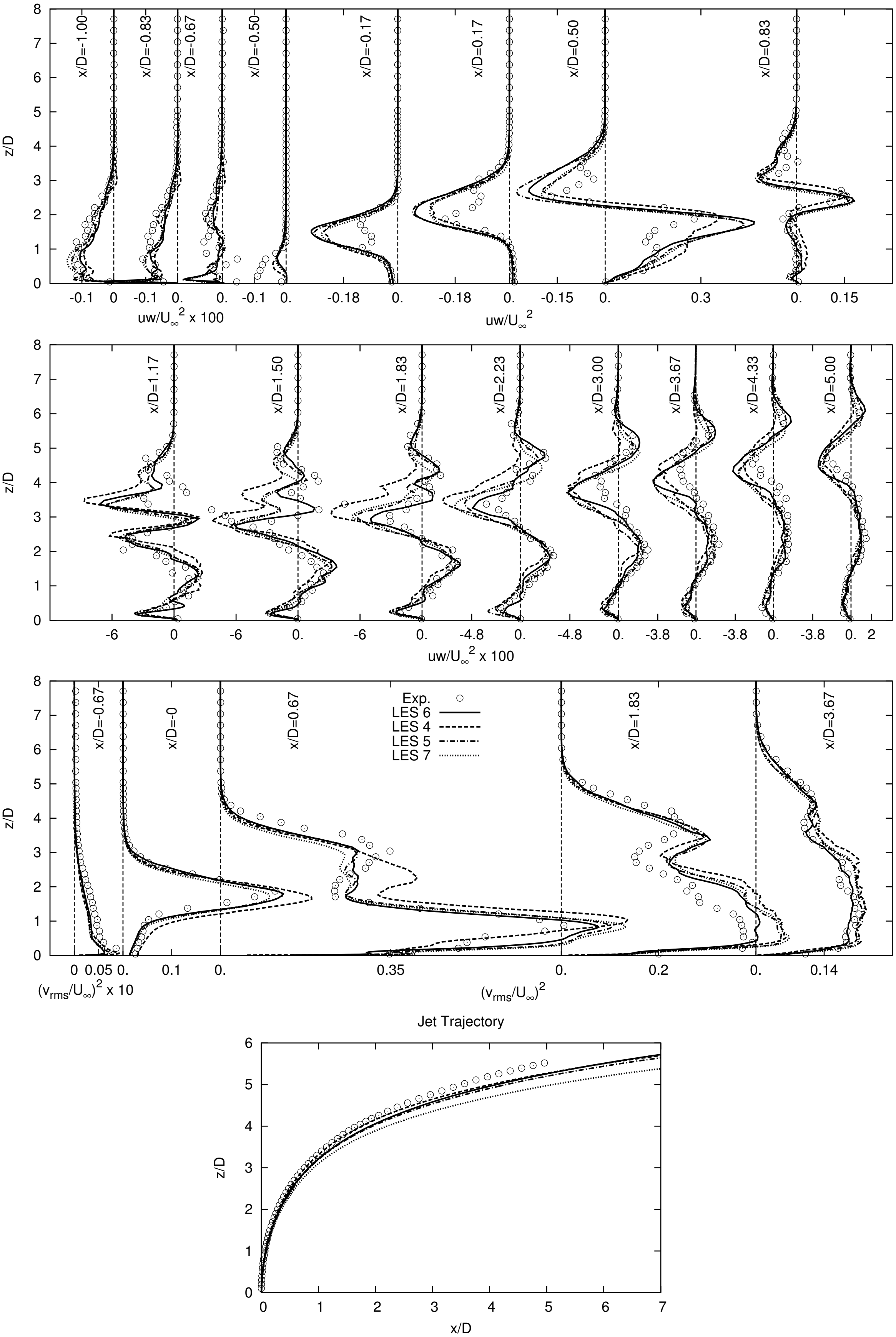

Figure A.8: $(v_{rms}/U_\infty)^2$, uw/U_∞^2 and jet-trajectories for $R = 3.3$ case, at $y/D = 0$ plane. Cases LES 4, 5, 6 and 7. Jet-trajectories are estimated as mean streamlines emerging from the point $x/D = z/D = 0$ in the symmetry plane following the definition of Yuan et al. [117]. Open circles refer to the experiment of Özcan and Larsen [77].

In cases LES 8, 9 and 12 influence of the grid size on the computed results is basically studied. Note that case LES 9 have a non-turbulent boundary layer inlet and a smallest time step size used in all computations ($CFL_{max} < 0.6$). The results are presented on Figures A.9-A.11.

First thing one can note from the mentioned Figures is the similarity between results from case LES 9 (and partially LES 12) with cases LES 2 and to some extent LES 3 at position $x/D = -0.5$. Comparing the results on all presented Figures A.3-A.17, a clear tendency of a good profile predictions at this position, for cases where a non-turbulent boundary layer inlet is used and the time step size utilized was lower than the nominal one[4] of $\Delta t U_\infty/D = 0.0313$, can be established. Actually, of all cases with the turbulent BL inlet, only a refined grid of case LES 12 reproduces the measurement (in fact only turbulence quantities) at this position reasonably well. One should also note a similar tendency of overpredictions of mean wall-normal W and w_{rms} profiles in the case LES 9 and case LES 2 (Figure A.4). Note also that some general differences between all models in the case of uw shear stress (Figure A.11) in region $x/D \geq 0.5$ can be observed here as well and that the similar profile shapes are produced by cases LES 9, 12 and case LES 4 at various streamwise positions in the flow field. As profile shapes of practically all measured quantities are well reproduced by each presented computation, the magnitude differences at various positions are likely to be attributed to small variations in velocity ratios used in the calculations - see jet trajectories in Figure A.11 and Table A.1). Considering the presented computational predictions of the JICF flow from Figures A.9-A.11, one can clearly observe that a better agreement between measurements and computations is not achieved by a significant increase in the grid size used (comparing refined grids of cases LES 8, 9, 12 vs. baseline LES 6 case and 4.7 million (cells) grid). It is noted furthermore that extending both inlet boundary positions further away from the impact zone between the jet and boundary layer (case LES 12) does not have a considerable (positive) effect on the computed results.

---

[4] This implies that a different inlet database is used

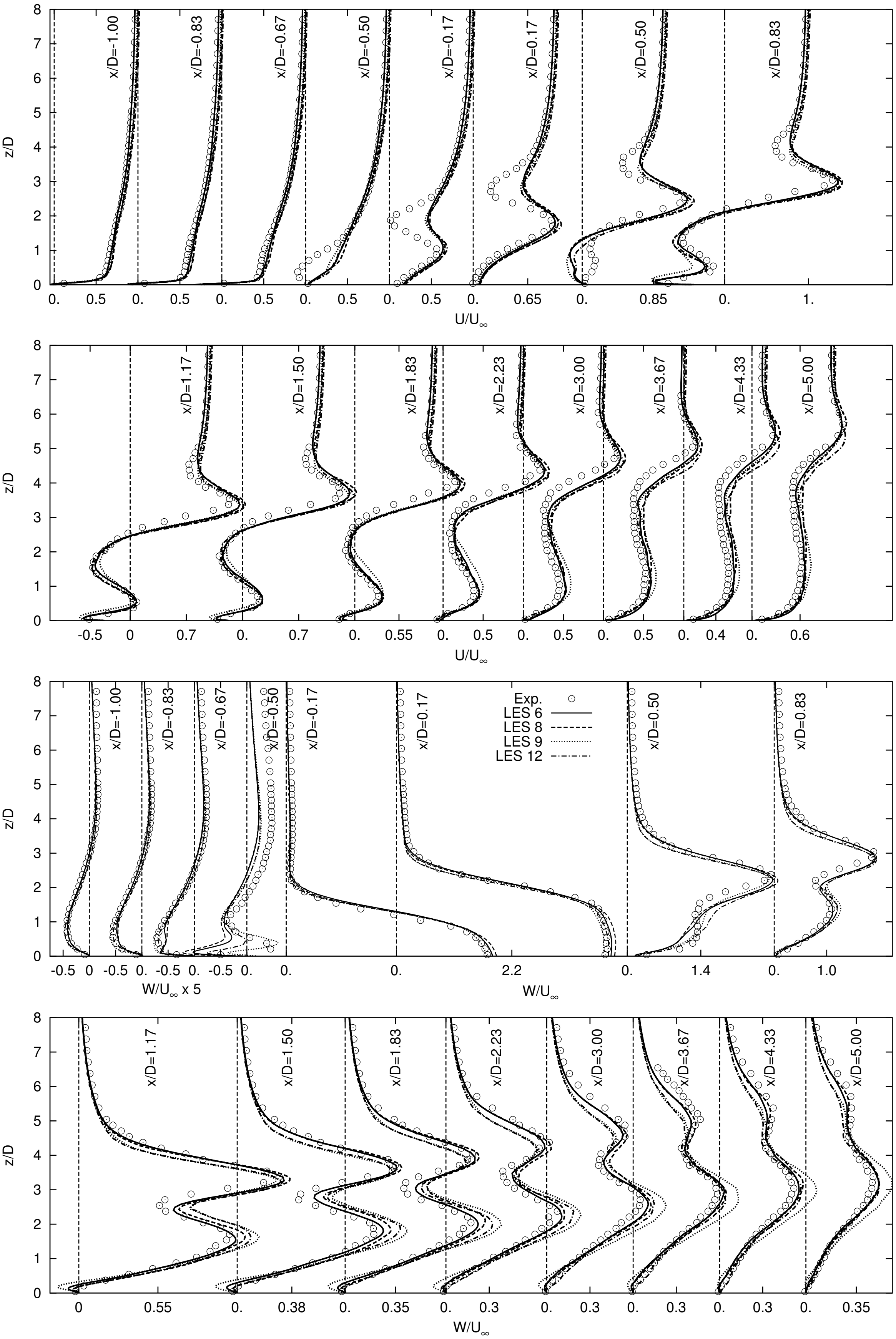

Figure A.9: U/U_∞ and W/U_∞ for $R = 3.3$ case, at $y/D = 0$ plane. Cases LES 6, 8, 9 and 12. Open circles refer to the experiment of Özcan and Larsen [77].

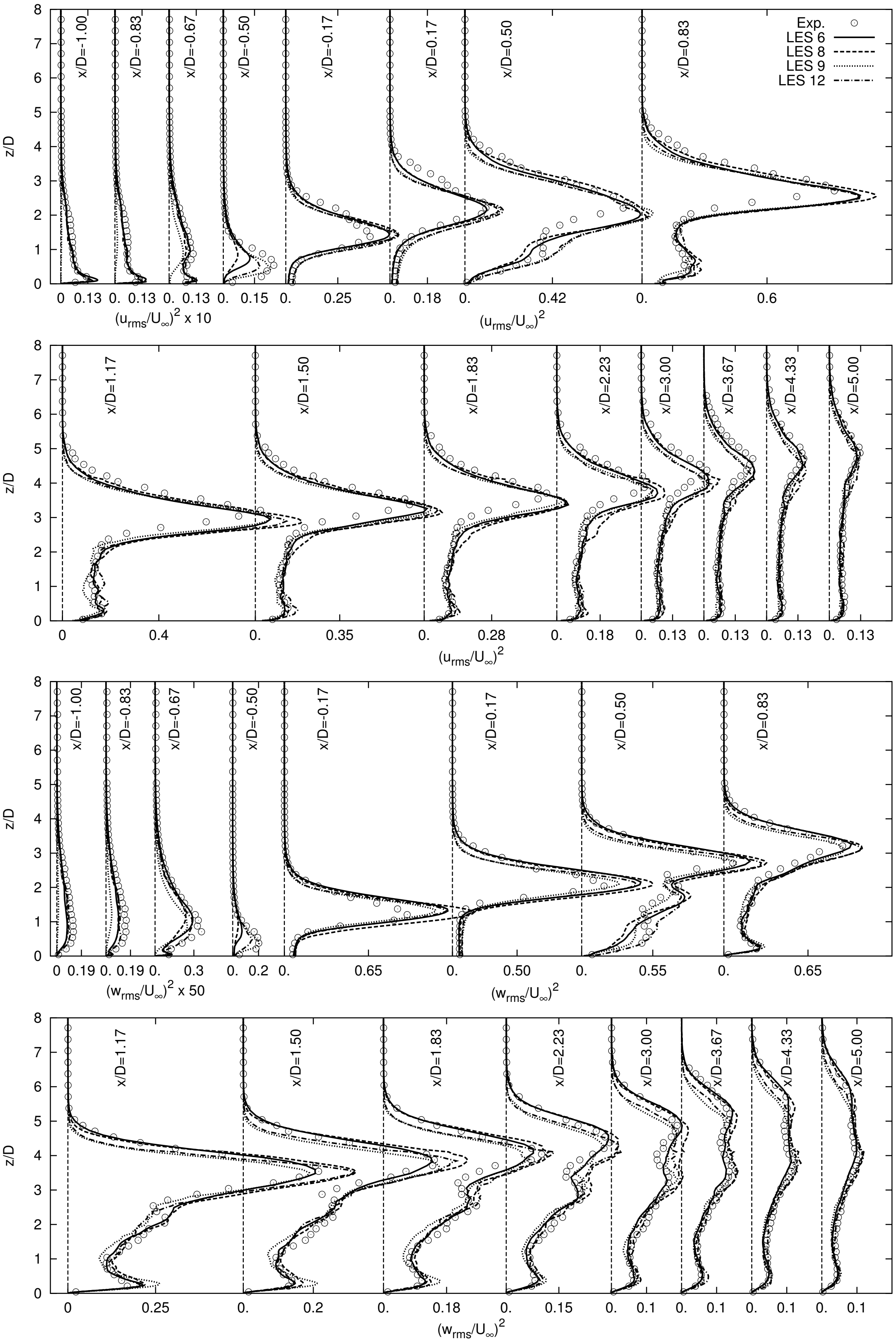

Figure A.10: $(u_{rms}/U_\infty)^2$ and $(w_{rms}/U_\infty)^2$ for $R = 3.3$ case, at $y/D = 0$ plane. Cases LES 6, 8, 9 and 12. Open circles refer to the experiment of Özcan and Larsen [77].

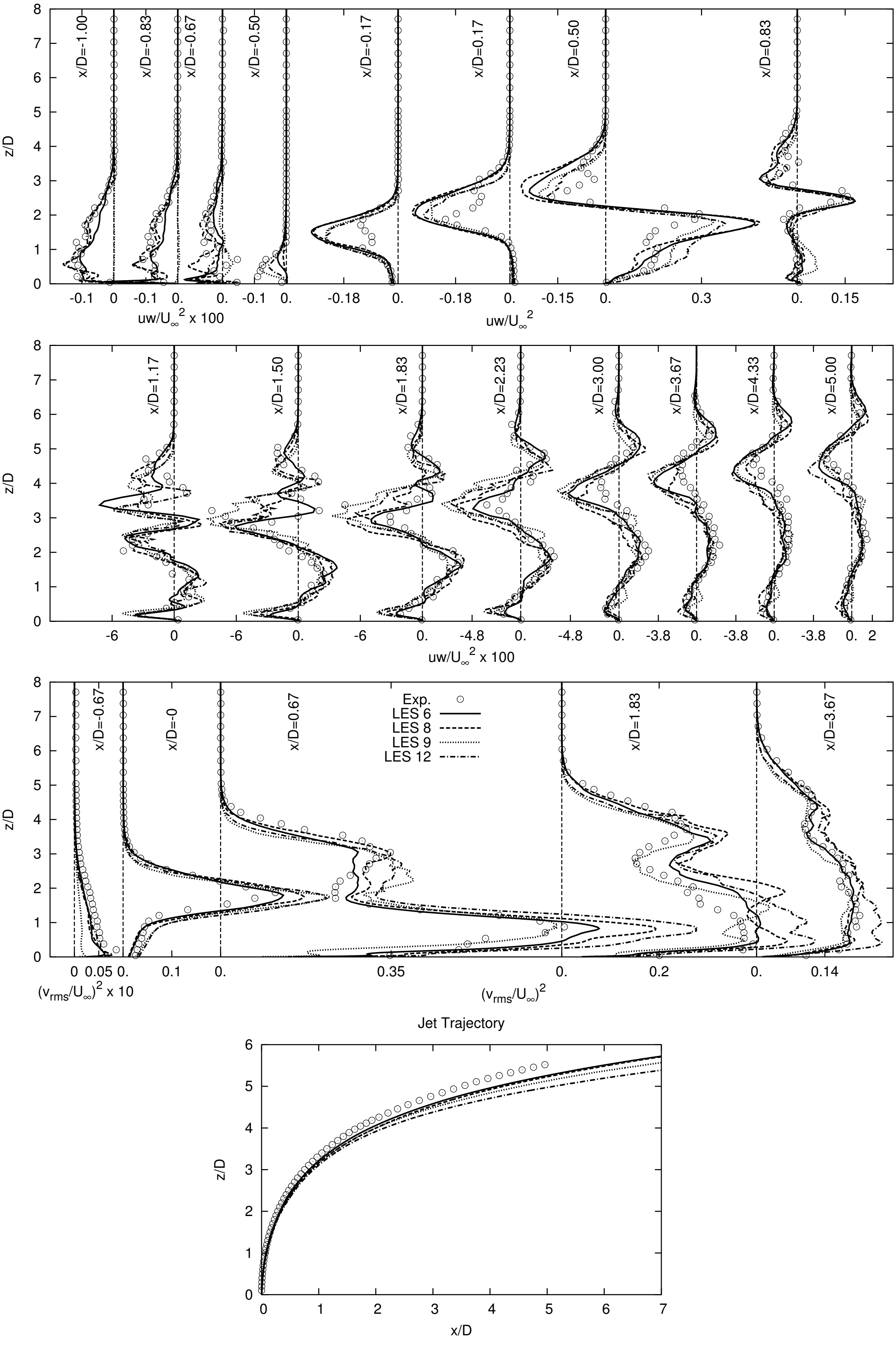

Figure A.11: $(v_{rms}/U_\infty)^2$, uw/U_∞^2 and jet-trajectories for $R = 3.3$ case at $y/D = 0$ plane. Cases LES 6, 8, 9 and 12. Jet-trajectories are estimated as mean streamlines emerging from the point $x/D = z/D = 0$ in the symmetry plane following the definition of Yuan et al. [117]. Open circles refer to the experiment of Özcan and Larsen [77].

In cases LES 6, 10 and 11 influence of a moderate increase of the velocity ratio on the computed results is studied. This implies that a computational set-up in all three cases investigated here is completely identical (see Table A.1) so an influence of the velocity ratio increase on the computed results can directly be assessed. The results are presented on Figures A.12-A.14.

Based on the presented results in the mentioned Figures, it seems that effects of the velocity ratio increase on the computed results are pretty obvious. The shapes of all calculated profiles are very similar; the only distinct difference between them is the general upward shift in profile magnitudes caused by the velocity ratio increase. One should note that the best fit with the measured jet trajectory (Figure A.14) is obtained for the case LES 10 ($R = 3.41$) but the best overall agreement with the measurements is clearly obtained for the case LES 6 ($R = 3.31$). The results presented here can actually put a perspective on many of the observed discrepancies between various cases studied, where profile shapes considered were relatively well predicted but the measured profile magnitudes were to a certain extent over/under predicted. As seen here, some of these differences can directly be linked to relatively small differences in the velocity ratios utilized in various computations.

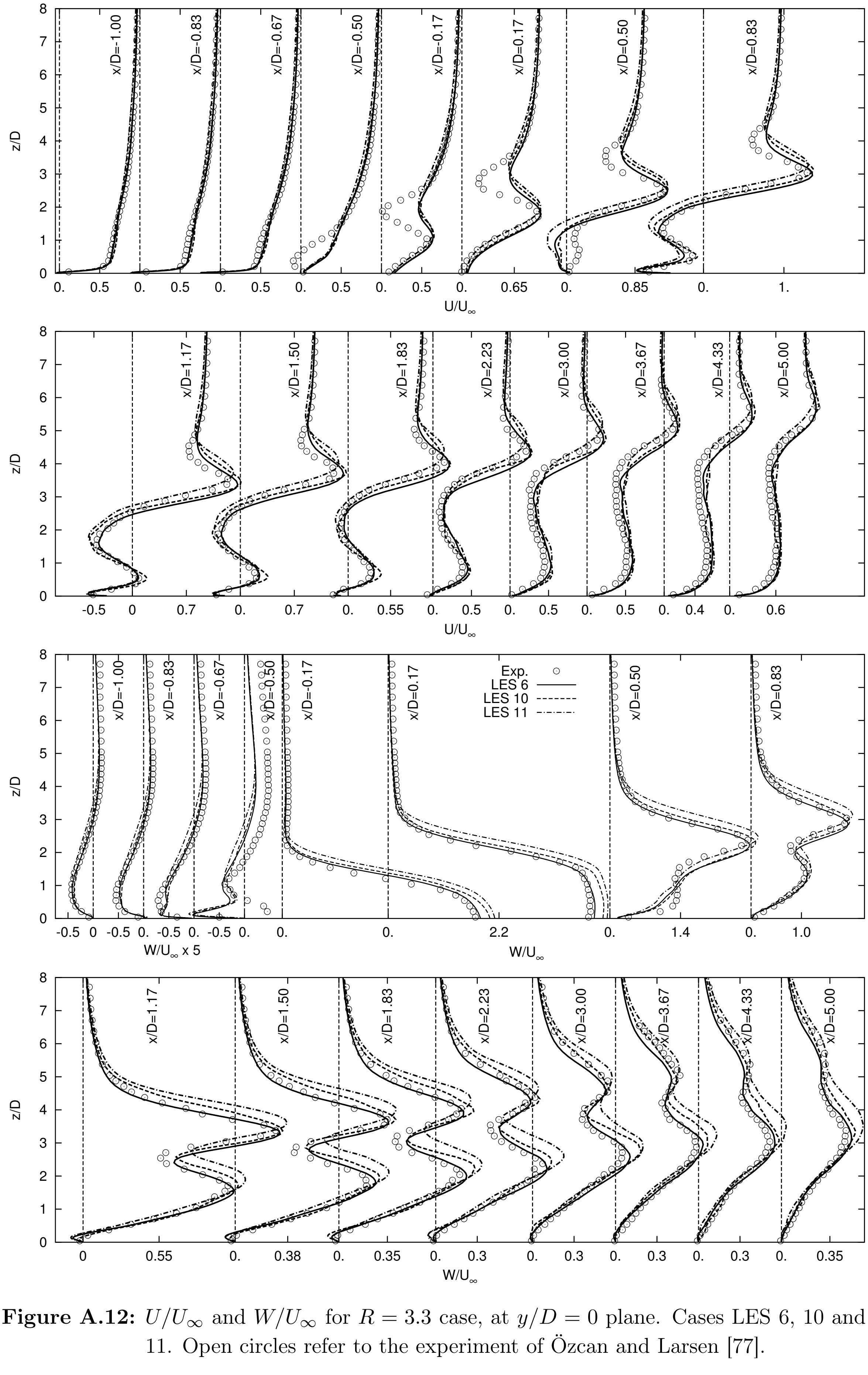

Figure A.12: U/U_∞ and W/U_∞ for $R = 3.3$ case, at $y/D = 0$ plane. Cases LES 6, 10 and 11. Open circles refer to the experiment of Özcan and Larsen [77].

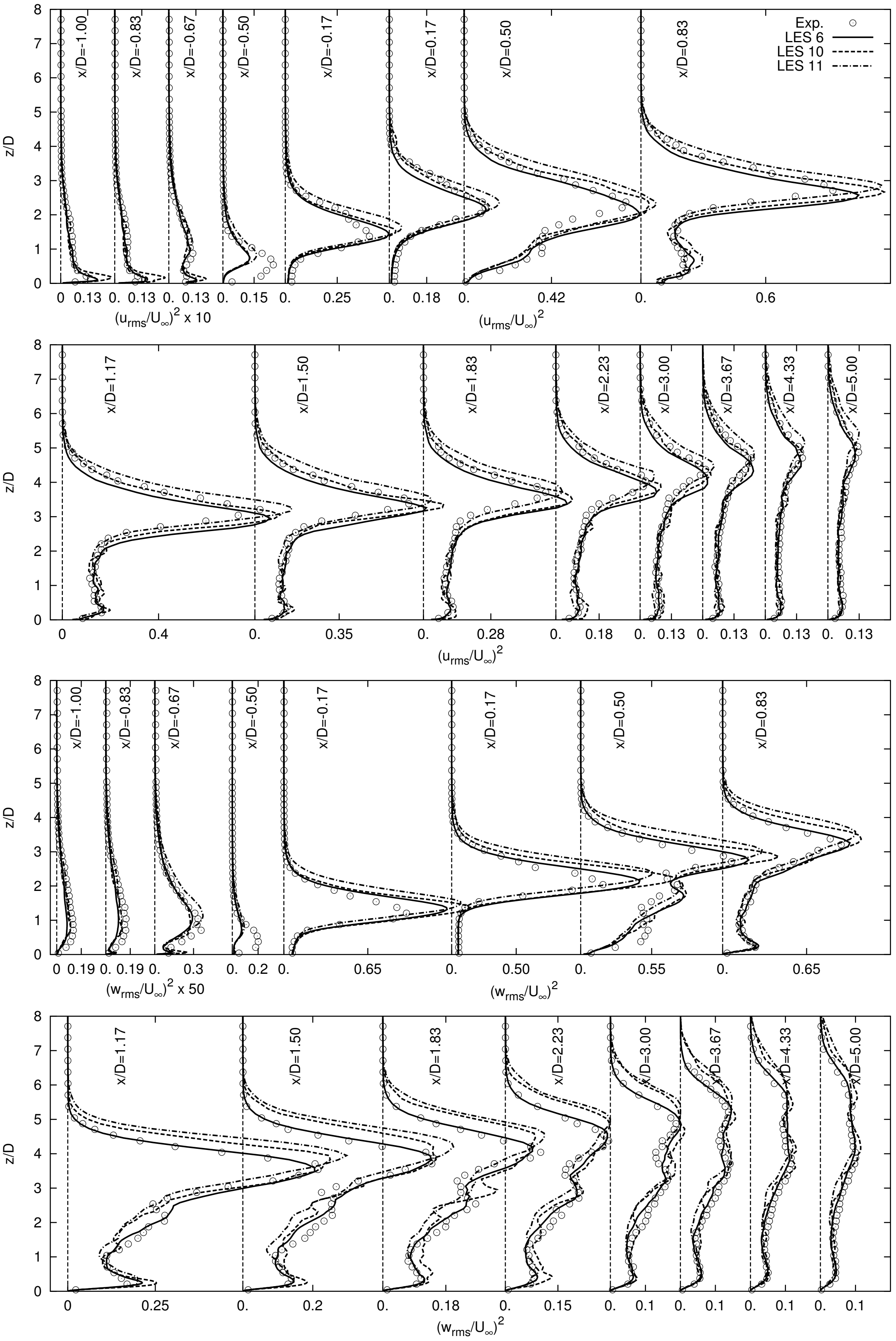

Figure A.13: $(u_{rms}/U_\infty)^2$ and $(w_{rms}/U_\infty)^2$ for $R = 3.3$ case, at $y/D = 0$ plane. Cases LES 6, 10 and 11. Open circles refer to the experiment of Özcan and Larsen [77].

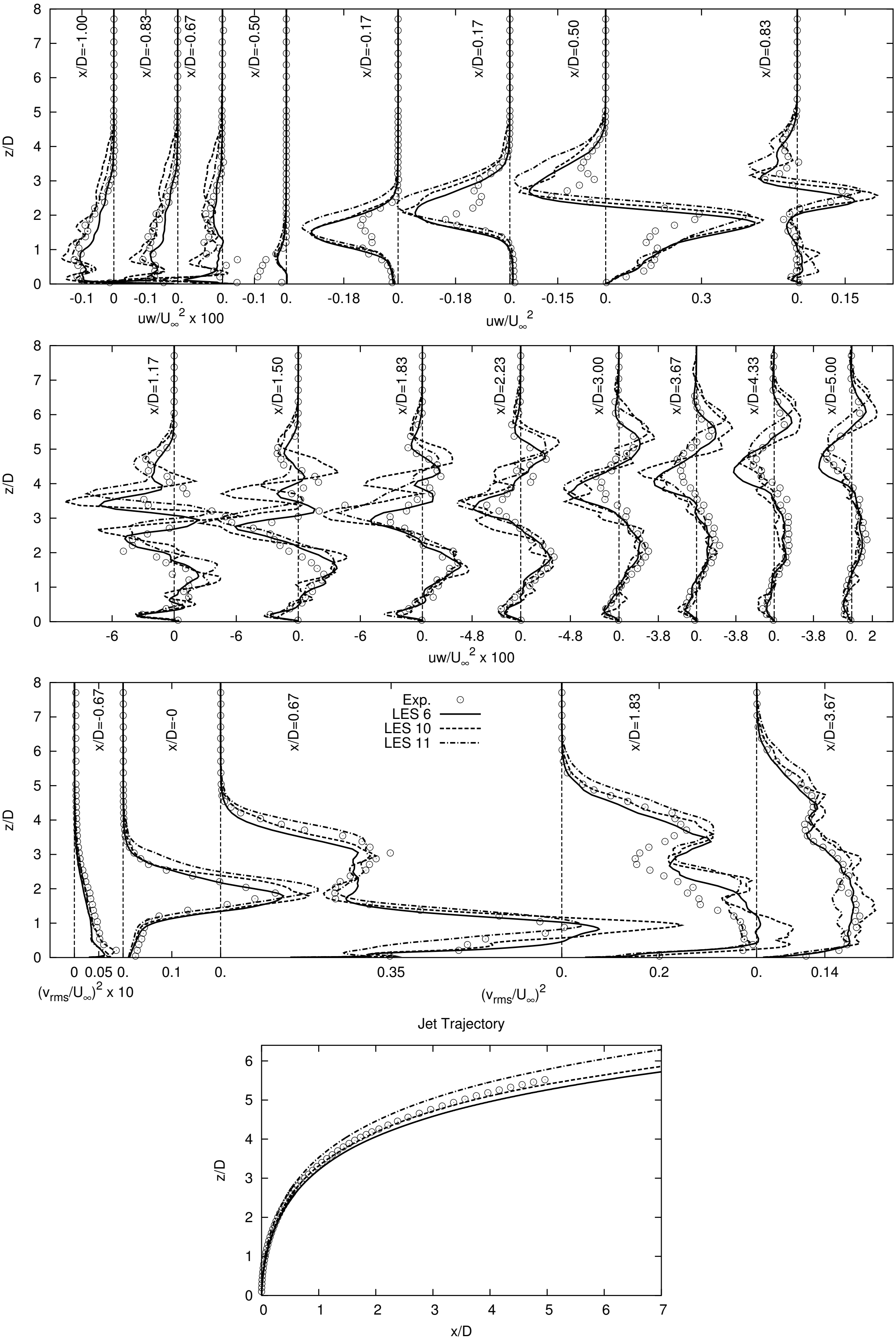

Figure A.14: $(v_{rms}/U_\infty)^2$, uw/U_∞^2 and jet-trajectories for $R = 3.3$ case, at $y/D = 0$ plane. Cases LES 6, 10 and 11. Jet-trajectories are estimated as mean streamlines emerging from the point $x/D = z/D = 0$ in the symmetry plane following the definition of Yuan et al. [117]. Open circles refer to the experiment of Özcan and Larsen [77].

Finally in cases LES 13 and 14 an influence of the time step size (and compliance to the CFL_{max} criterion - see Table A.1), in cases where two turbulent inlets are utilized, is investigated. It is noted that maximum CFL value in cases LES 13 and 14 (and generally in all cases) is reached in the immediate vicinity of the jet entrainment position into the cross flow, where grid size in the wall-normal (z) direction is basically adjusted to resolve the boundary layer flow (see e.g. Figure A.1). Actually a full compliance with CFL_{max} criterion is obtained for cases LES 2, 3 and 9 (non-turbulent BL inflow). In cases LES 13 and 14 some 5000 cells in the immediate vicinity of the jet entrainment position are allowed to exceed the CFL_{max} criterion i.e. $CFL > 1$. The results are presented on Figures A.15-A.17.

As it can be seen from the mentioned Figures, no basic improvement of the computed results vs. measurements is achieved by lowering the time step and almost complying with the CFL demand. In fact all important differences between results of cases LES 13, 14 and case LES 6 have previously been observed for some other analyzed cases and correspondingly discussed there. However it is noted that influence of the outflow boundary position ($L_{x_1} = 12\,D$ vs. $L_{x_1} = 25\,D$), based on comparison of results from cases LES 13 and 14, when convective outflow BC was employed at both instances, is practically negligible.

On the other hand some interesting conclusions from cases LES 13 and 14, compared to all other cases where a similar inlet database was used, can actually be deduced. Comparing results from cases LES 13 and 14 with cases LES 2, 3, 4, 9 and 12 - Figures A.3 - A.17, one can observe that they produce very similar profile shapes at positions $x/D \neq -0.5$. At $x/D = -0.5$ position, cases where a non-turbulent BL inlet is utilized perform better than all other cases. Of course the same is not true for $x/D < -0.5$ positions. As it can be seen from Table A.1, in these 7 cases (LES 2, 3, 4, 9, 12, 13 and 14) the same inlet database is used (created at $\Delta t U_\infty/D = 0.0063$ - for the boundary layer flow[5], $\Delta t U_\infty/D = 0.000625$ - for the pipe flow). In all other cases the inlet database used was the one directly created to match the time step requirements of the baseline cases - $\Delta t U_\infty/D = 0.0313$. As differences between non-turbulent vs. turbulent BL inlet is localized to positions $x/D \leq -0.5$, differences in the computed profiles at positions $x/D > -0.5$ indicate that the pipe database created to fulfill the constraints of case LES 9 and used in cases LES 2, 3, 4, 9, 12, 13 and 14 may consist of an insufficient overall number of samples (data files). This database consist of 100 000 files representing 3.5 FLTs on the $L_{x_1} = 12D$ based grids and only 2 FLTs $L_{x_1} = 25D$ based grids. As the computational set-up used to create both the pipe (jet) database with $\Delta t U_\infty/D = 0.0313$ and database with $\Delta t U_\infty/D = 0.000625$ is identical, these findings indicate that the database size in the latter case may be inadequate to provide a good basis for obtaining a reliable LES results.

---

[5] Not applicable to cases LES 2, 3 and 9

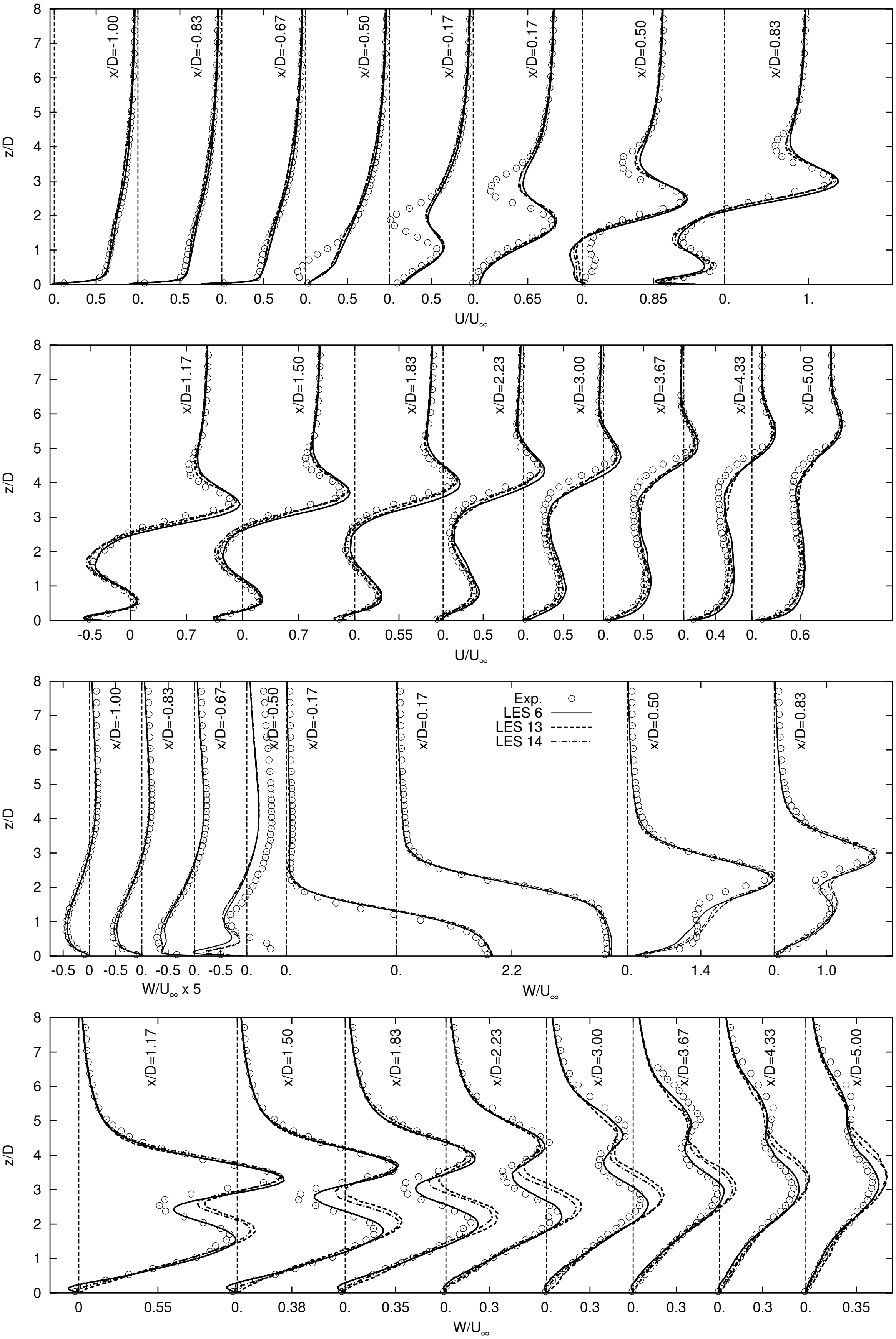

Figure A.15: U/U_∞ and W/U_∞ for $R = 3.3$ case, at $y/D = 0$ plane. Cases LES 6, 13 and 14. Open circles refer to the experiment of Özcan and Larsen [77].

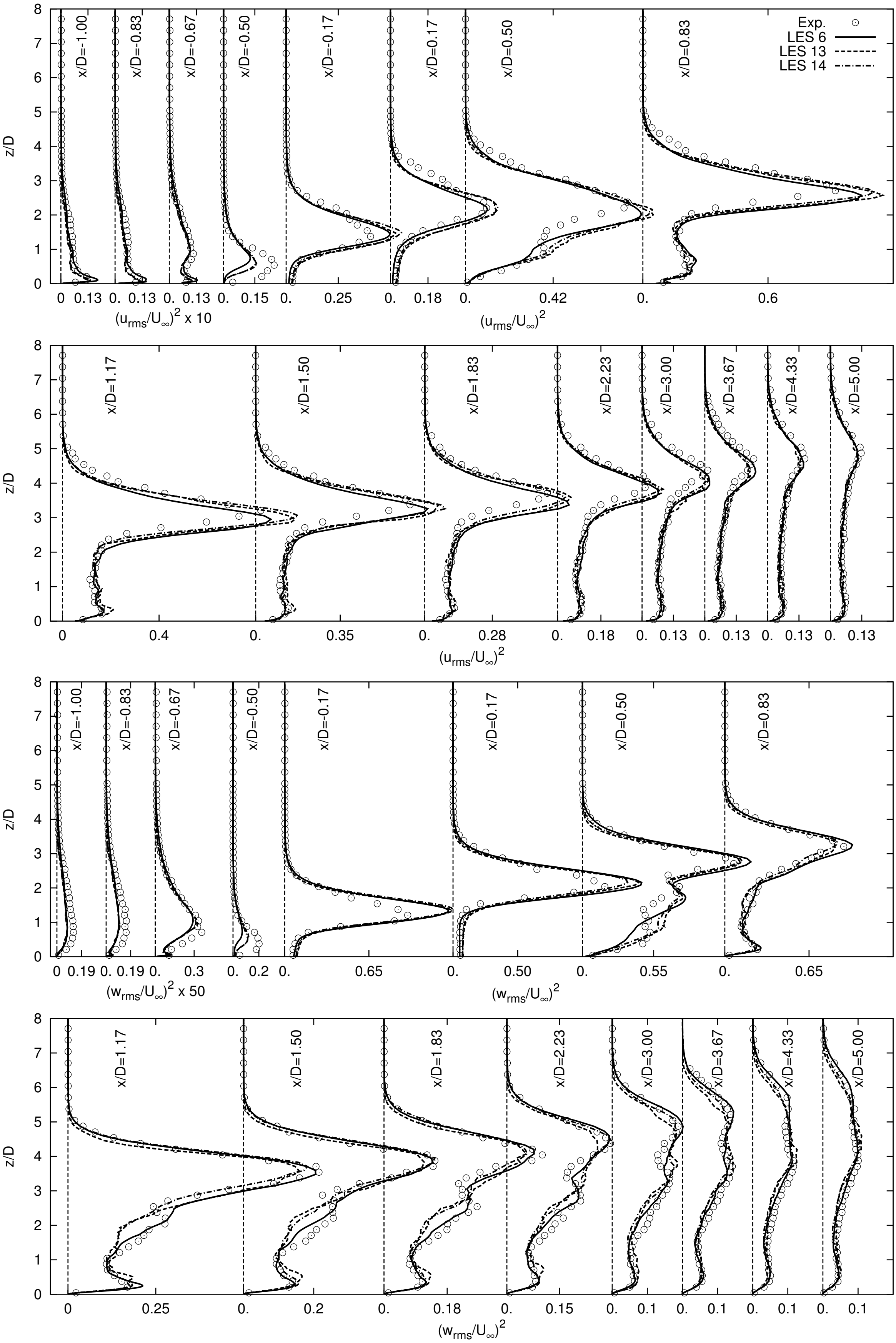

Figure A.16: $(u_{rms}/U_\infty)^2$ and $(w_{rms}/U_\infty)^2$ for $R = 3.3$ case, at $y/D = 0$ plane. Cases LES 6, 13 and 14. Open circles refer to the experiment of Özcan and Larsen [77].

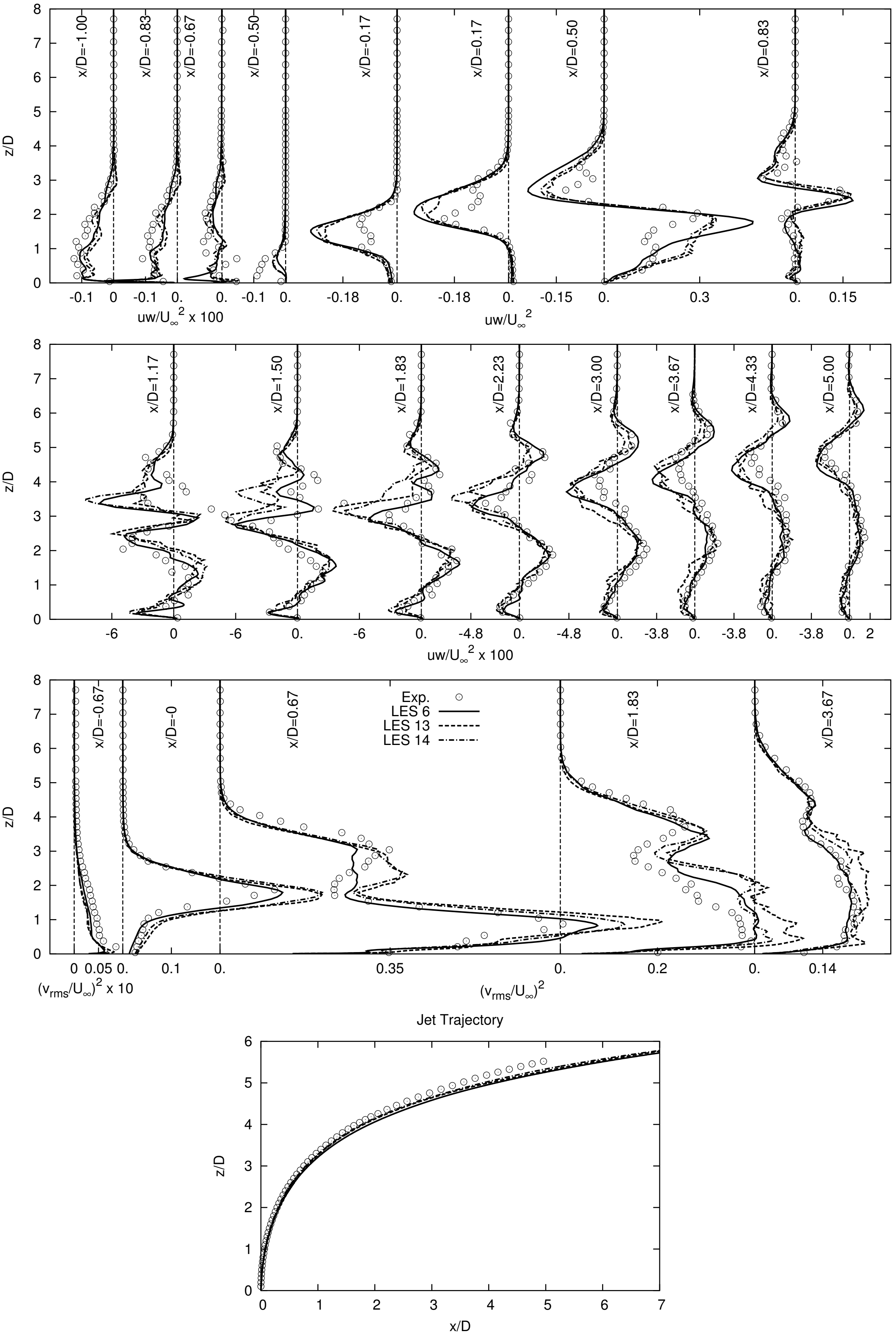

Figure A.17: $(v_{rms}/U_\infty)^2$, uw/U_∞^2 and jet-trajectories for $R = 3.3$ case, at $y/D = 0$ plane. Cases LES 6, 13 and 14. Jet-trajectories are estimated as mean streamlines emerging from the point $x/D = z/D = 0$ in the symmetry plane following the definition of Yuan et al. [117]. Open circles refer to the experiment of Özcan and Larsen [77].

Finally summarizing all the presented comparisons, some clear tendencies in the calculated results can be observed. It is seen that practically every change in the numerical set-up used in the calculations has an impact on the computed results. A certain impact of the discretization scheme is visible directly from e.g. cases LES 2 and 3; an impact of a locally large CFL number on results can as well be seen from the presented comparisons etc., but none of the previously discussed influence factors is sufficiently large to claim that any other case than numerical set-up and results obtained using the case LES 6, can better reproduce the experimentally measured quantities.

For those reasons, results of the case LES 6 are included in the main rapport and further analyzed there. It is noted that this has a very positive impact on an ability to use the present LES results in context of POD analysis presented in section on 4.6 on page 73, as use of the QUICK scheme practically removes the wiggles from the instantaneous flow realizations, apparently without compromising quality of the result.

Before proceeding further, some general estimates of the statistical uncertainties pertinent to the LES computations (for case LES 6 in particular) are given. Using the same kind of uncertainty estimates as ones utilized in experimental work of Özcan and Larsen [77], assuming Gaussian distribution of the measured quantities and confidence interval of 95 percent, the uncertainties in determination of U, u_{rms} and uw can be estimated based on the following equations:

$$S(U) = \pm 1.96\frac{u_{rms}}{\sqrt{N}},\ S(u^2_{rms}) = \pm 1.96\sqrt{\frac{2}{N}}u^2_{rms},\ \text{and}\ S(uw) = \pm 1.96\sqrt{\frac{1+R^2_{uw}}{N}}u_{rms}w_{rms}, \tag{A.1}$$

with N being the number of uncorrelated samples and $R_{uw} = uw/(u_{rms}w_{rms})$.

For points indicated in Figure A.1, where a time series has been recorded at a frequency of f = 2 kHz, the integral time scale is determined to be app. 3 D/U_∞ at Point 1 and 12 D/U_∞ at Point 4. As most of the positions where comparisons with the measurement are conducted is in the jet near-field, to simplify the analysis it is assumed in the following that 2× the integral time scale correspond to app. 6 D/U_∞. Based on this estimate the computation corresponding to case LES 6 (60 FLTs) contains app. $N = 170$ statistically uncorrelated samples. Inserting this number in eq. (A.1) the corresponding uncertainties can be calculated. The uncertainties are typically presented as relative deviations from a certain maximum value. Here, local maximum values are calculated at each considered streamwise position. Based on these assumptions the relative uncertainties for mean velocities (U, V and W), normal stresses (u^2_{rms}, v^2_{rms} and w^2_{rms}) and shear stresses (uv, uw and vw) are determined to be 11, 21 and 37 percent respectively. The corresponding experimental uncertainties are estimated to be 4, 6 and 15 percent - cf. Özcan and Larsen [77].

As illustrated, the estimates of uncertainties connected with the obtained LES results seem to be quite high. However, the values presented here should be considered cautiously in the context of present LES computations. To illustrate this, the calculated mean streamwise velocity U and u^2_{rms} profiles at streamwise position of $x/D = 0.17$ from cases LES 13 and 14 are presented in Figure A.18, together with the corresponding estimate of uncertainties relevant to these two computations, at positions corresponding to two profile-peeks. As cases LES 13 and 14 are conducted on almost identical numerical setups, with only major difference being expressed in form of the time utilized for sampling the statistics (25 FLTs case LES 14 vs. 9 FLTs case LES 13 - see Table A.1) the difference in the computed profiles corresponding to a substantial increase in the sampling time of the statistical quantities can be directly visualized. From eq. (A.1) it is seen that the uncertainty interval is proportional to $1/\sqrt{N}$ for both U and u^2_{rms}. Performing the uncertainty analysis for the case LES 13 the uncertainties in U and u^2_{rms} can be estimated as app. 35 and 60 percent respectively. The uncertainty interval in case LES 14 is correspondingly reduced by a factor of $\sqrt{9/25} = 0.6$. The errorbars presented in Figure A.18 correspond to the described values.

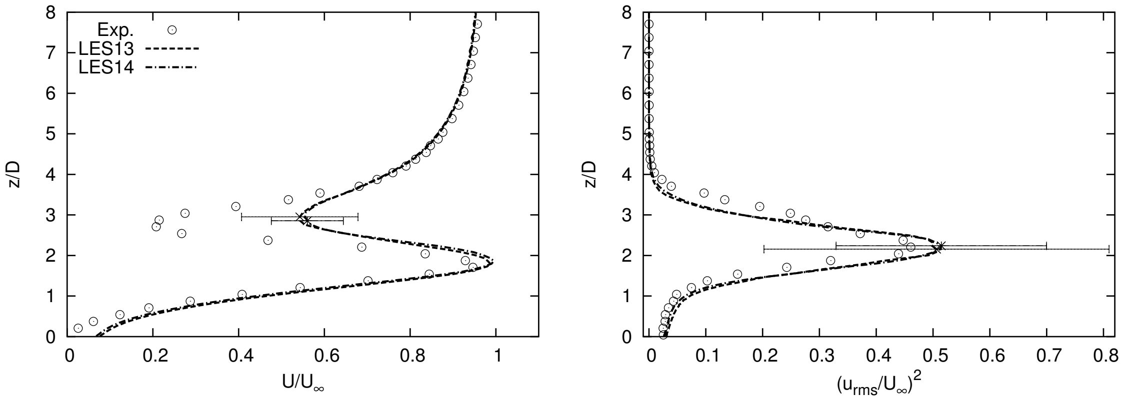

Figure A.18: Comparison of mean streamwise velocity profiles U and u^2_{rms} between cases LES 13 and 14. Errorbars corresponding to uncertainties pertinent to the analyzed cases are given for one point on each of the profiles. Errorbars are placed on two slightly displaced points on the corresponding profiles in order to better visualize their relative sizes.

As clearly seen from the Figure, general changes in profile shapes between cases LES 13 and 14 are very small. This indicates that a further increase in the sampling time will most probably introduce changes in profile shapes of similar order. So despite the fact that sizes of relative uncertainties pertinent to the considered computations are quite high, it is generally difficult to justify a continuation of LES computation corresponding to case like LES 14 (which cost 30 sec. of computational time pr. time step (statistical sample) on 37 P4 CPUs - i.e. 24 hours of computations pr. FLT in the present case) just in order to significantly lower general levels of relative uncertainties, which at the end may not necessarily bring any noteworthy improvement in agreements between measurements and computations.

All the conducted numerical tests can be used to evaluate quality of the results obtained from the case LES 6. On the other hand it is interesting to directly assess the resolution characteristics of the grid utilized in case LES 6 and thereby estimate how well the used grid is capable of producing reliable results. In previously discussed cases (channel flow etc.), where resolution demand of the near wall-region was the dominating factor, some well established requirements of the grid spacing (expressed in wall units) do exist (Piomelli and Balaras [82]) and they can be used as direct indicators of the grid quality. In cases where flow is not dominated by wall structures it is not feasible to use the same criteria. Following Frohlich et al. [31], who investigated 2D periodic hill flow, the resolution in the interior of a given flow can be assessed by comparing the size of a local grid spacing Δ and an estimate of the Kolmogorov length η scale, which characterizes the length scale of the dissipative motion. The Kolmogorov scale is defined by the following expression:

$$\eta = \left(\frac{\nu^3}{\varepsilon}\right)^{\frac{1}{4}}, \tag{A.2}$$

where ε is the dissipation rate and ν is the kinematic viscosity. Assuming that $\varepsilon_{sgs} \approx \varepsilon$ - an estimate of the ε_{sgs} can be obtained from (see e.g. Pope [85]):

$$\varepsilon \approx \varepsilon_{sgs} = \frac{C_E k_{sgs}^{3/2}}{\Delta}, \tag{A.3}$$

where k_{sgs} is the SGS kinetic energy and C_E is an empirical constant $C_E = 0.7$. Furthermore an estimate of k_{sgs} is typically calculated from (Pope [85]):

$$k_{sgs} = \left(\frac{\nu_{sgs}}{C_v \Delta}\right)^2, \tag{A.4}$$

where ν_{sgs} is the computed SGS viscosity and C_v is another empirical constant. It should be noted that some dispute on the reasonable magnitude of the C_v constant do exist in the literature; $C_v = 0.094$ is used in e.g. Klein [51] and $C_v = 0.05$ is suggested by Yoshizawa [116]. In the presently considered case LES 6, estimate of the k_{sgs} is an integral part of the utilized Mixed scale (Ω) based eddy viscosity model of Sagaut [91]. Therefore the grid size quality estimate presented here is calculated both directly - based on the k_{sgs} from the Sagaut's model and based on eq. (A.4) with $C_v = 0.05$ and $C_v = 0.094$ respectively. It is noted that $\eta\,(C_v = 0.094) \approx 1.6\,\eta\,(C_v = 0.05)$ meaning that the more conservative estimate of the Δ/η ratio is obtained by utilizing $C_v = 0.05$.

Results showing the computed Δ/η ratio for two planes $y/D = 0$ and $x/D = 1$ are presented on Figures A.19 and A.20. From the mentioned Figures it can be directly observed that C_v value of $C_v = 0.05$ is an adequate C_v choice in the currently investigated JICF flow, as $C_v = 0.05$ based results are very similar to results obtained directly utilizing the k_{sgs} calculated from the model of Sagaut [91]. Furthermore it is argued in Pope [85] that in an isotropic turbulence the maximum dissipation takes place at length scales of about $24\,\eta$. As at least two points are necessary to resolve any flow feature, a grid spacing of $12\,\eta$ is needed to resolve the scale of $24\,\eta$. Thereby, any flow region discretized by cells with $\Delta/\eta \leq 12$ can be considered as very well resolved (Frohlich et al. [31]). Inspecting the results presented in Figures A.19 and A.20 it can be seen that maximum Δ/η ratio does exceed 13 (max. value is 13.3 in $x/D = 1$ plane) only in a very limited region, indicating that the presently used grid resolution is very good.

An additional assessment of the grid quality can be done by inspecting the one dimensional power spectra. The power spectra, based on a time series recorded at frequency of f = 2 kHz and consisting of 30 000 samples, for four different points in the $y/D = 0$ plane - see Figure A.1) are presented in Figure A.21. Note the decrease in grid density, moving from Point 1 to Point 4 - Figure A.1. Inspecting the results from Figure A.21 it is seen that decay in the one dimensional power spectrum with a slope of app. -5/3 can be observed at all considered positions for all velocity components. Existence of this region in all presented points signify that the inertial subrange can be identified at all these flow positions in the computational domain, indicating further that effective LES filtering does occur in the inertial subrange region, which is one of the basic demands for a well resolved LES calculation.

Finally, the grid quality can be assessed by comparing the computed turbulent viscosity $\nu_{t\,(sgs)}$ and the kinematic viscosity ν. The ratio of ν_t/ν for two previously considered planes is illustrated in Figure A.22. It is seen that ν_t/ν ratio does not exceed value of 1.6 in any of the presented planes, indicating once more very good capabilities of the utilized grid.

Thereby, the performed a posteriori tests of the grid quality presented here confirm that the basic numerical configuration utilized in the LES 6 should be capable of producing reliable LES results.

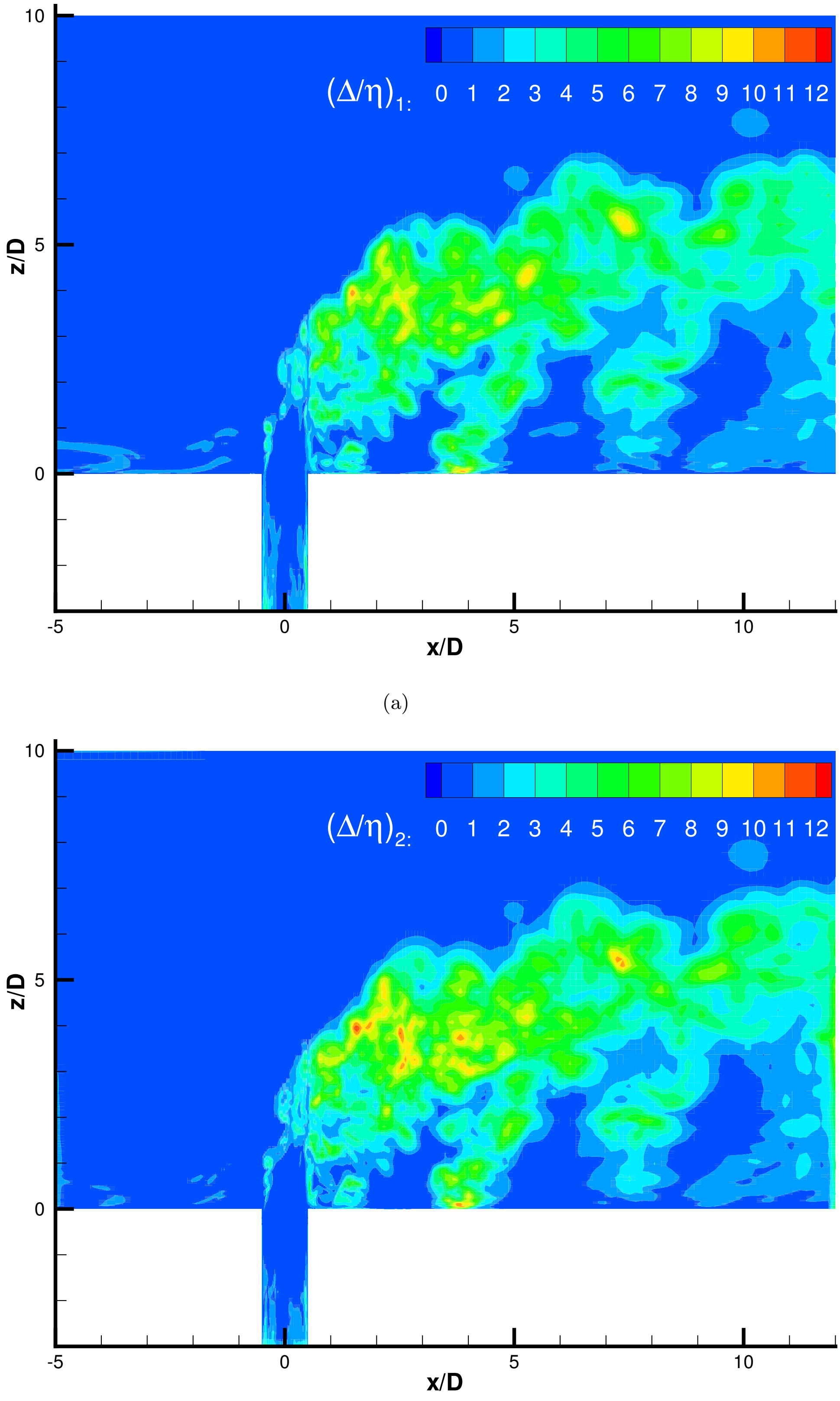

(a)

(b)

Figure A.19: Estimate of the Δ/η ratio in the $y/D = 0$ plane. (a) based on k_{sgs} from Eddy Viscosity model of Sagaut [91] and equations (A.2), (A.3) (b) based on equation (A.4) with $C_v = 0.05$ and equations (A.2), (A.3).

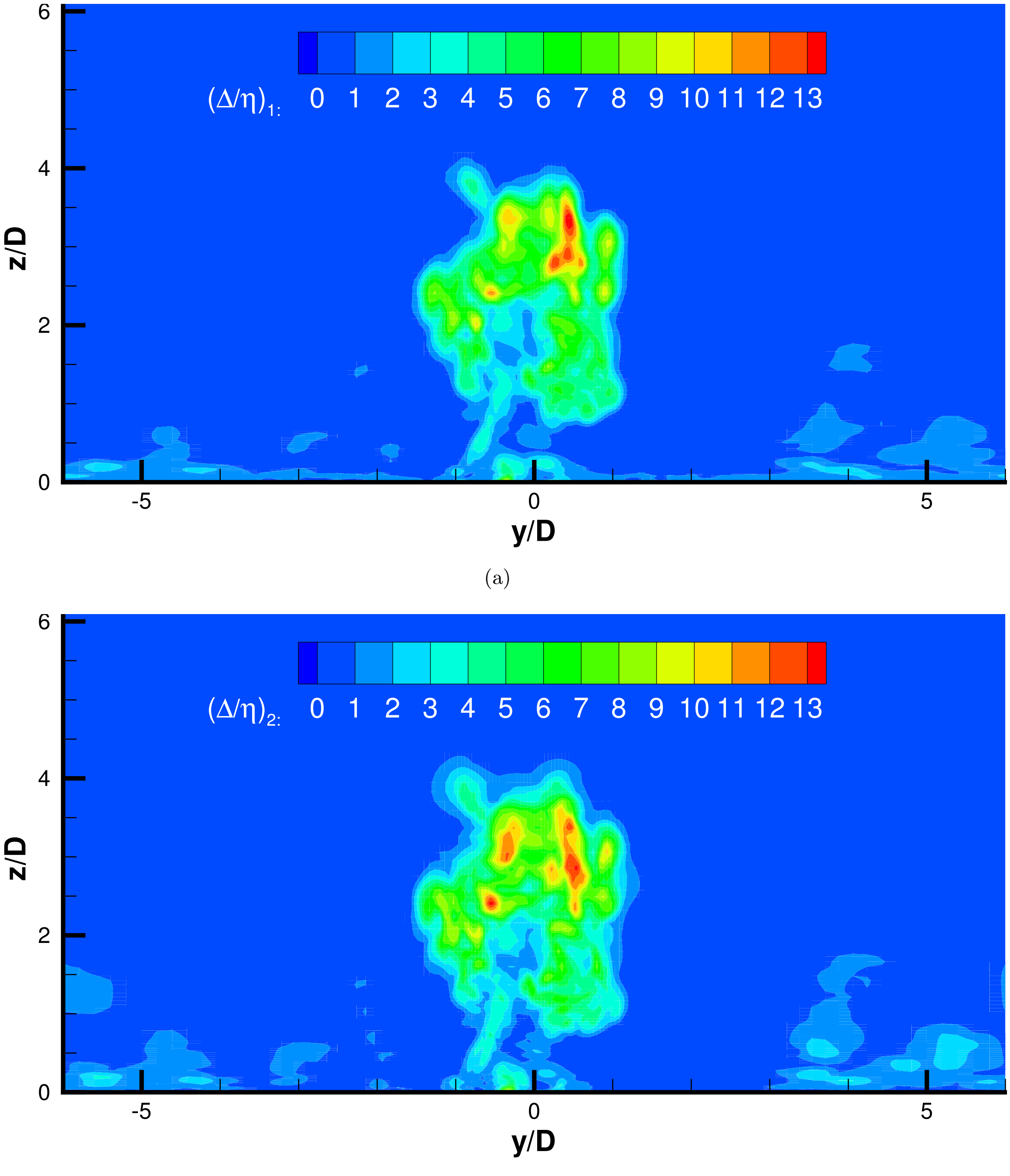

(a)

(b)

Figure A.20: Estimate of the Δ/η ratio in the $x/D = 1$ plane. (a) based on k_{sgs} from Eddy Viscosity model of Sagaut [91] and equations (A.2), (A.3) (b) based on equation (A.4) with $C_v = 0.05$ and equations (A.2), (A.3).

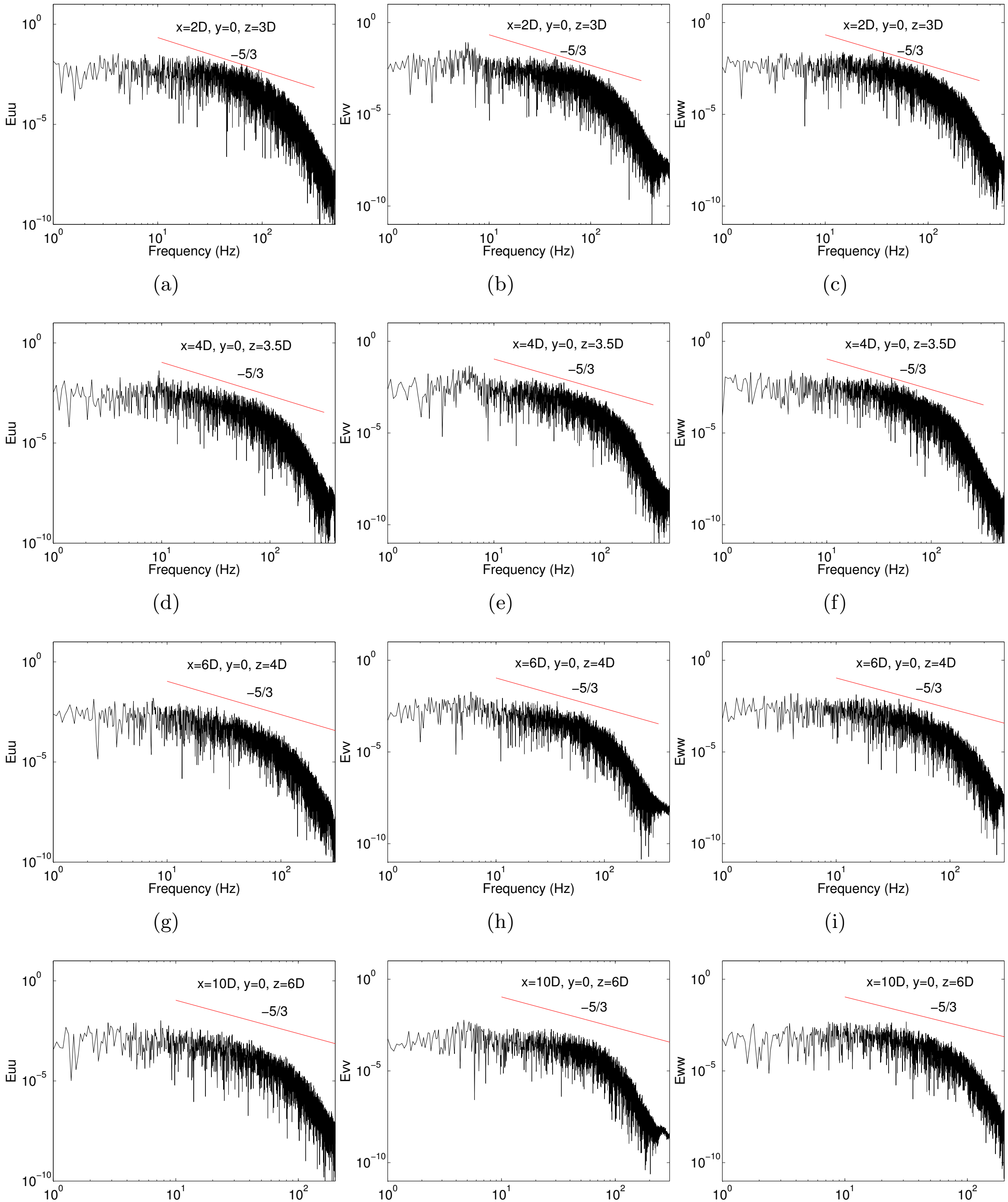

(a) (b) (c)

(d) (e) (f)

(g) (h) (i)

(j) (k) (l)

Figure A.21: One dimensional power spectrum densities of all three velocity components (E_{uu}, E_{vv} and E_{ww}) calculated based on time series obtained at points with domain positions indicated in Figure A.1.

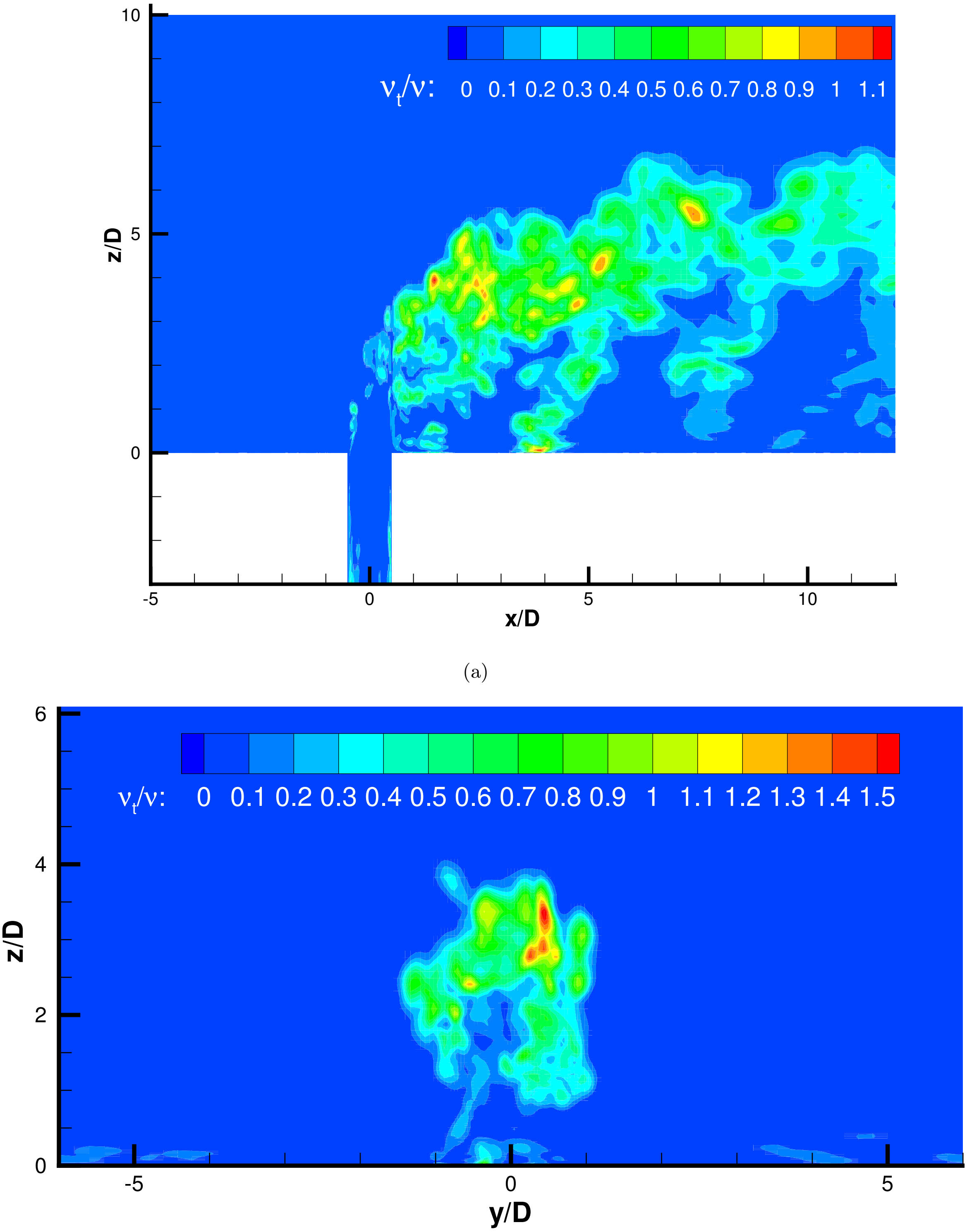

(a)

(b)

Figure A.22: Ratio of the instantaneous subgrid-scale viscosity ν_t and the kinematic viscosity ν in (a) $y/D = 0$ (b) $x/D = 1$ planes.

Appendix B

Numerical Investigations of the R=1.3 Velocity Ratio Case

A considerable amount of computational time has been used on various numerical investigations in the case of a higher ($R = 3.3$) velocity ratio. The gathered experience was in a way directly transferred to this case, so only limited number of runs were conducted here. Based on findings of the $R = 3.3$ case it was decided to directly reuse the numerical set-up corresponding to case LES 6 (Appendix A) and base the $R = 1.3$ related calculations on it. As velocity ratio is decreased in the present case and correspondingly the grid resolution demands for this particular flow are reduced, the utilized grid is assumed to be at least as suitable for use in this $R = 1.3$ case as it was for the $R = 3.3$ case. A decrease in extension of the wall-normal (z) direction, in the grid used for $R = 1.3$ case compared to $R = 3.3$ case, was actually considered but not applied into the calculations, as influence of the upper domain chosen becomes practically negligible in the $R = 1.3$ case, if the domain extension in z direction is kept on $z/D = 10$.

The preliminary results, conducted utilizing the described numerical configuration, showed some distinct discrepancies between measurements and computations which necessitated a more detailed velocity ratio related analysis. Even though the numerical set-up used in this case is considerably simplified compared to the $R = 3.3$ case, it is chosen to present results here in a similar way as previously, simply in order to keep the presentation level of the illustrated material on the comparable levels.

Therefore the outline of the performed computations in the $R = 1.3$ case is presented in Table B.1. As practically only one parameter is varied throughout this study (with the exception of $R = 1.45$ case) the cases are named after the effective velocity ratio R obtained from the calculations. Note that R is calculated in this numerical study in the same way as previously (see Appendix A).

In the following part, results of the computations conducted in the $R = 1.3$ case are presented - Figures B.1-B.6. It is emphasized one more time that velocities, r.m.s. fluctuations and shear stress are rescaled with an appropriate factor on many subfigures, in order to accommodate a better comparison basis between various LES computations and measurements. The scale is adjusted at the first four ($x/D = [-1.00,\ -0.83,\ -0.67,\ -0.5]$) positions in the case of mean wall-normal velocity W, the first three positions ($x/D = [-1.00,\ -0.83,\ -0.67]$) are adjusted in the case of the r.m.s fluctuations and uw shear stress, while only the first position ($x/D = -0.67$) is adjusted in the case of v_{rms} velocity fluctuation.

Case	L_{x_1}	Inlet (L_{x_1})	L_{z_D}	L_{x_2}	Outl. (L_{x_2})	Model	Grid Size	$\frac{t_a}{t_{FLT}}$	$\frac{\Delta t\, U_\infty}{D}$	Code	Diff. Scheme	CFL_{max}
$R = 1.53$	$5\,D$	Turbulent	$3D$	$12\,D$	Conv.	Mix (Ω)	4.7 mil.	15($-$)	0.0313	EllipSys	Quick	2.51
$R = 1.44$	$5\,D$	Turbulent	$3D$	$12\,D$	Conv.	Mix (Ω)	4.7 mil.	15($-$)	0.0313	EllipSys	Quick	2.62
$R = 1.33$	$5\,D$	Turbulent	$3D$	$12\,D$	Conv.	Mix (Ω)	4.7 mil.	15($-$)	0.0313	EllipSys	Quick	2.44
$R = 1.24$	$5\,D$	Turbulent	$3D$	$12\,D$	Conv.	Mix (Ω)	4.7 mil.	15($-$)	0.0313	EllipSys	Quick	2.49
$R = 1.45$	$5\,D$	Turbulent	$3D$	$25\,D$	Conv.	Mix (Ω)	5.9 mil.	12(21)	0.0063	EllipSys	Cds4/Quick	0.52

Table B.1: Summary of the $R = 1.3$ computations. For detailed explanation of the used abbreviations and symbols see caption of Table A.1.

It is underlined here also that the main focus in discussions related to the presented material is directed upon differences in the obtain results between various computations, while the general agreement between computations and measurements is discussed in the main rapport.

It is noted moreover that results presented here are based on two inlet databases (pipe and BL flow) created at $\Delta t U_\infty / D = 0.0063$. For further details regarding the numerical flow configuration used in the present study the interested reader is referred to Appendix A.

Comparison of results corresponding to the first four cases in Table B.1 are illustrated in Figures B.1-B.3. Comparing the obtained jet trajectories from the computational case corresponding to $R = 1.33$ (Figure B.3) and the experimental one, together with the general agreement between computed results of this case and measurements, some considerable disagreements can be observed and a reason for conducting the (computational) velocity ratio sensitivity study can be seen.

Turning the focus on the mean velocity profiles (Figure B.1) a clear tendencies in profile shapes, caused by moderate changes in velocity ratios utilized, can be seen. For example in regions close to the first near-wall peak in profiles of both mean velocity components U and W (positions $x/D \geq 1.5$) the lowest velocity ratio computation ($R = 1.24$) predicts the measured profiles best, while almost the opposite is true in regions after the second (negative) peak in profiles of both velocity components. In the case of mean wall-normal velocity W, the $R = 1.53$ case seems to be furthest away from the measurements at practically all streamwise positions. Regarding the profiles of various turbulence quantities presented in Figures B.2 and B.3 it is seen that all computations predict similar profile shapes but the scaling factor differences, originating from velocity ratio variations, cause the upward shift in the profile magnitudes, visible on the mentioned Figures.

From the presented results it can be clearly deduced that no ideal computational velocity ratio, which will be able to correctly predict the measured profile magnitudes, exist on the currently utilized numerical configuration. As the numerical set-up used here proved to be sufficient to produce reliable LES results in the more demanding (in terms of grid resolution requirements) $R = 3.3$ case (see Appendix A), the inability of the current numerical set-up to produce better results in the $R = 1.3$ case can indicate that a certain basic difference between the computational set-up utilized in the calculations of the present JICF flow and the experiment (e.g. difference in the boundary conditions, especially BL inlet) might exist. This issue is further elaborated on in the main rapport.

From the results presented in Figures B.1-B.3 it is concluded that the best overall predictions of the measured quantities, utilizing the given numerical set-up, are obtained using the case with computational velocity ratio of $R = 1.44$.

To put some perspective on the quality of the obtained numerical results, an additional case, with computational velocity ratio of $R = 1.45$ is included in this study. The numerical set-up of this case is somewhat different, as a prolonged grid in streamwise direction combined with a lover time step size and different discretization scheme is used - see Table B.1.

Comparison of cases $R = 1.44$ and $R = 1.45$ is presented on Figures B.4-B.6. It is seen that only noticeable and distinct difference in profile shapes between those computations exist in the case of uw shear stress at position $x/D = 0.50$, where case $R = 1.45$ predicts measurements better. Some other differences in magnitudes can be observed at various streamwise positions too (like for w_{rms} profiles at $x/D = 0.50$), but the profile shapes remain similar when results are compared between the considered cases at these locations.

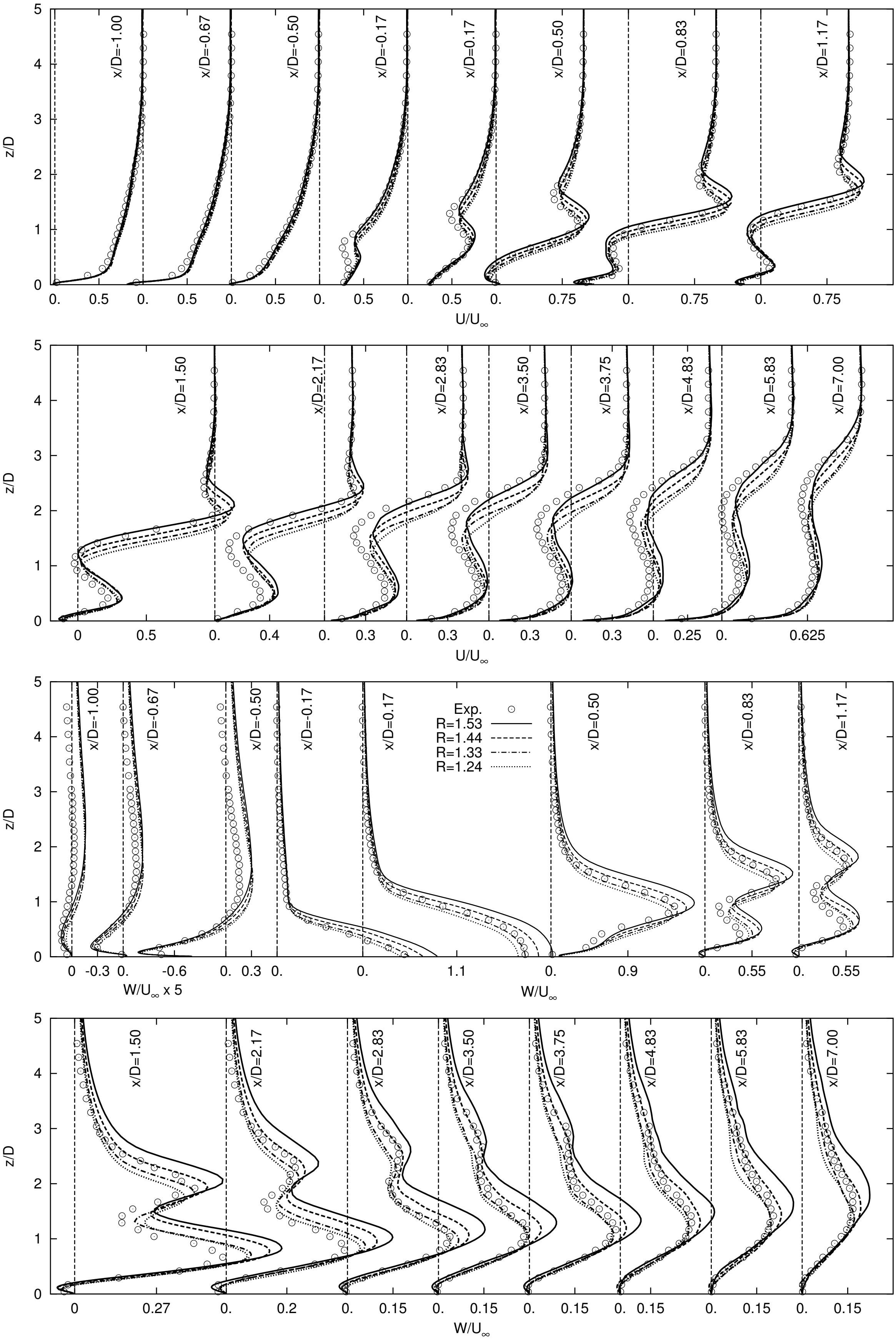

Figure B.1: U/U_∞ and W/U_∞ for experimental $R = 1.3$ case, at $y/D = 0$ plane presented for first four cases from Table B.1. Open circles refer to the experiment of Özcan and Larsen [77].

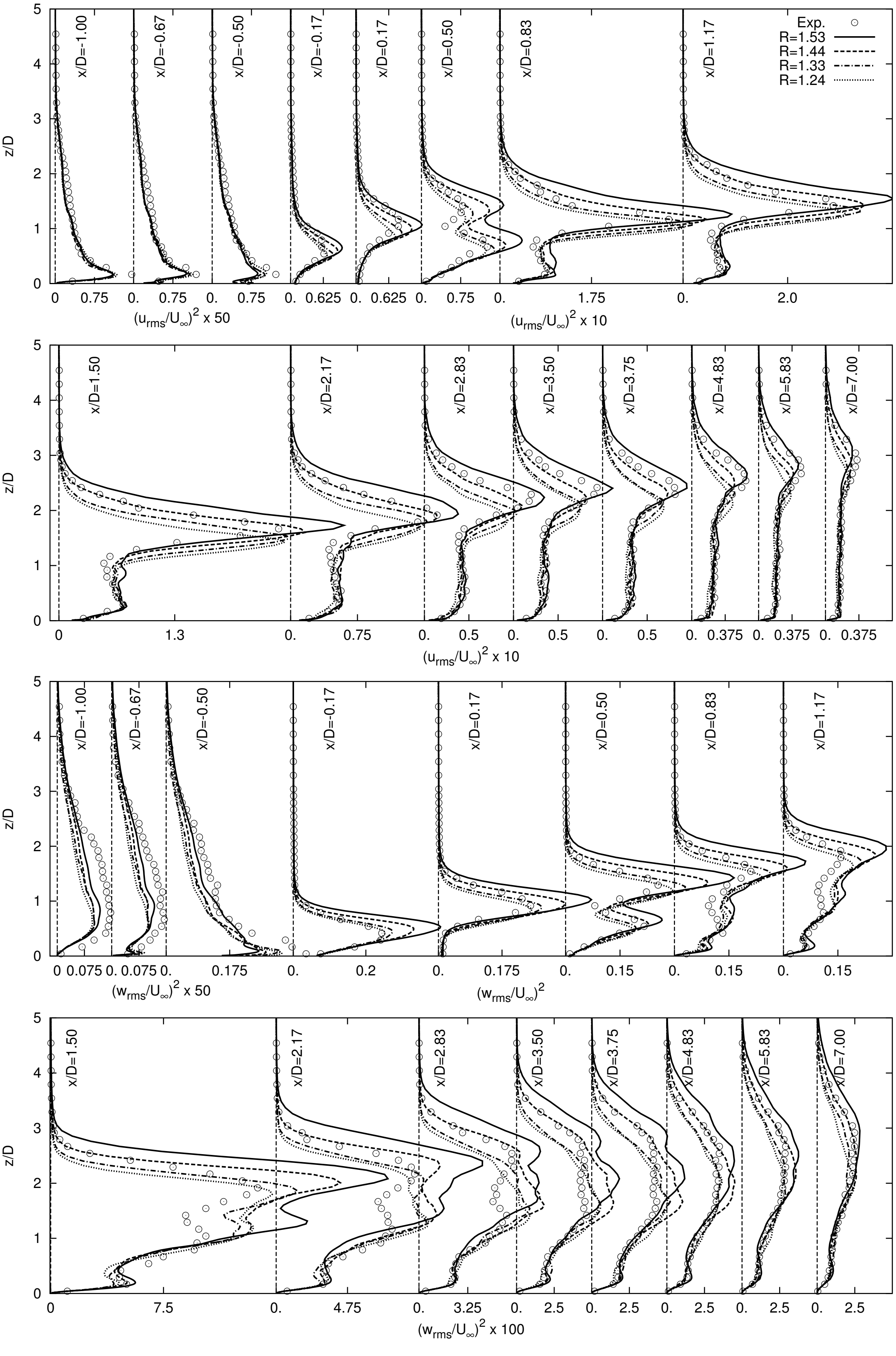

Figure B.2: $(u_{rms}/U_\infty)^2$ and $(w_{rms}/U_\infty)^2$ for experimental $R = 1.3$ case, at $y/D = 0$ presented plane for first four cases from Table B.1. Open circles refer to the experiment of Özcan and Larsen [77].
]

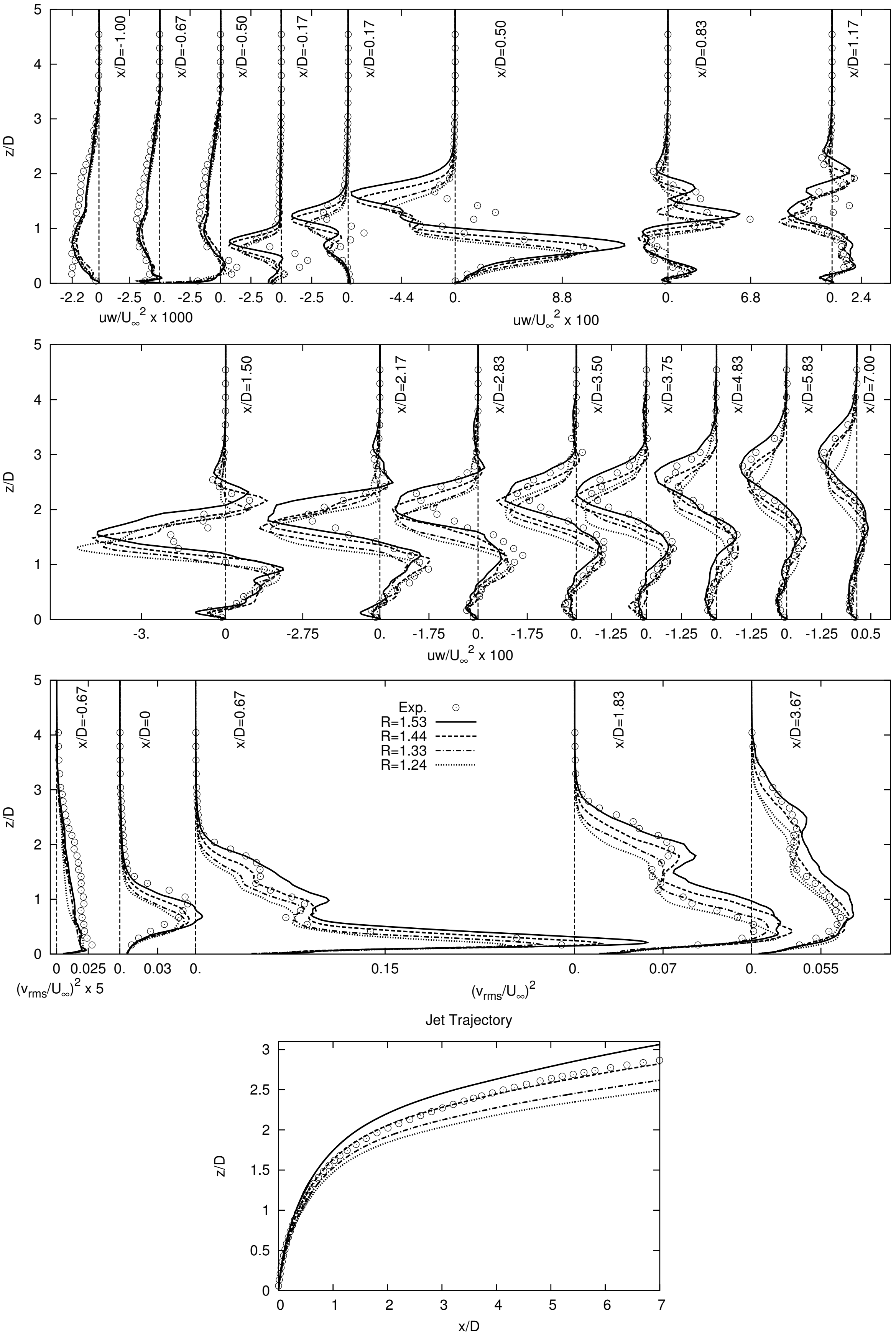

Figure B.3: $(v_{rms}/U_\infty)^2$, uw/U_∞^2 and jet-trajectories for experimental $R = 1.3$ case, at $y/D = 0$ plane presented for first four cases from Table B.1. Jet-trajectories are estimated as mean streamlines emerging from the point $x/D = z/D = 0$ in the symmetry plane following the definition of Yuan et al. [117]. Open circles refer to the experiment of Özcan and Larsen [77].

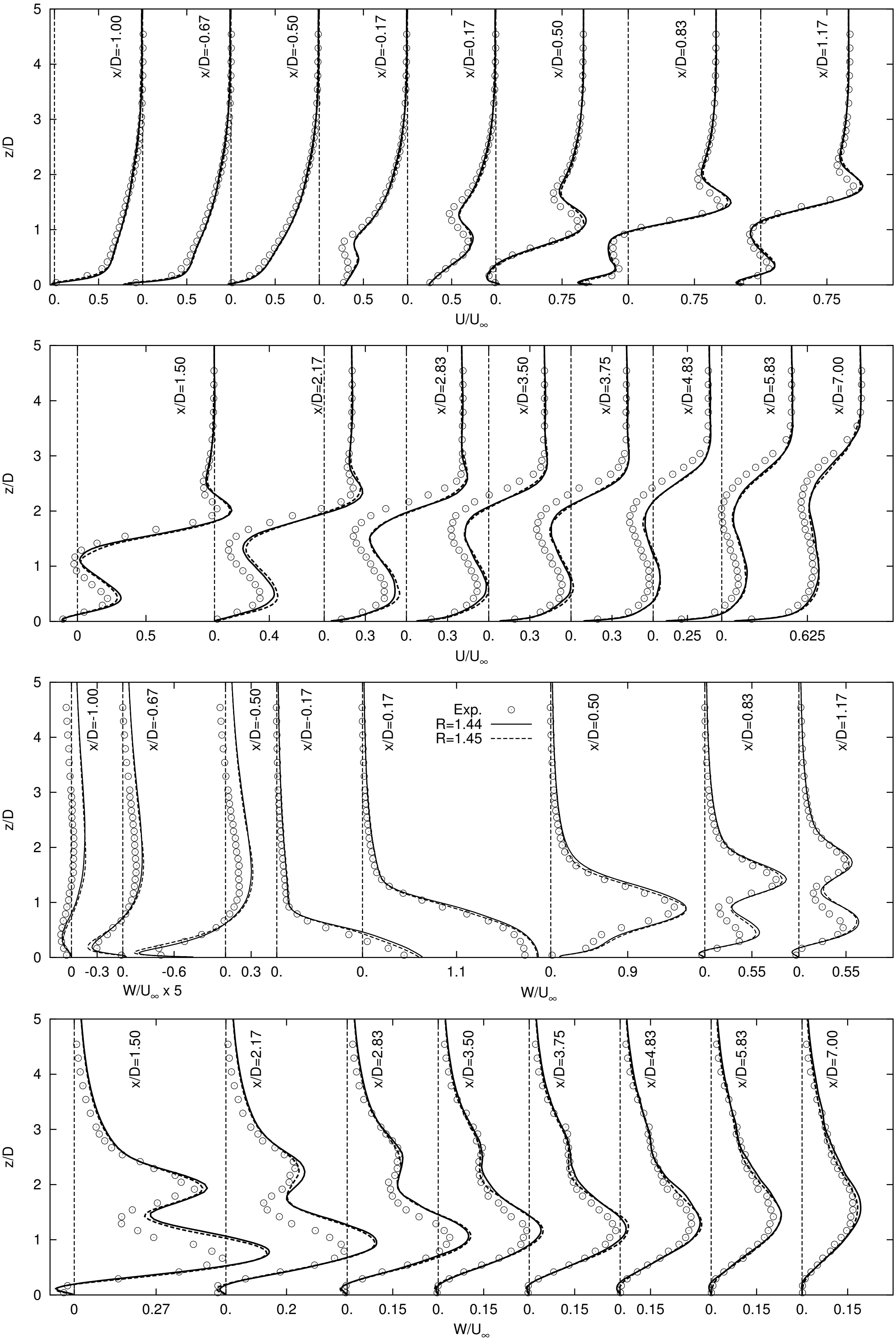

Figure B.4: U/U_∞ and W/U_∞ for experimental $R = 1.3$ case, at $y/D = 0$ plane - cases $R = 1.44$ and $R = 1.46$. Open circles refer to the experiment of Özcan and Larsen [77].

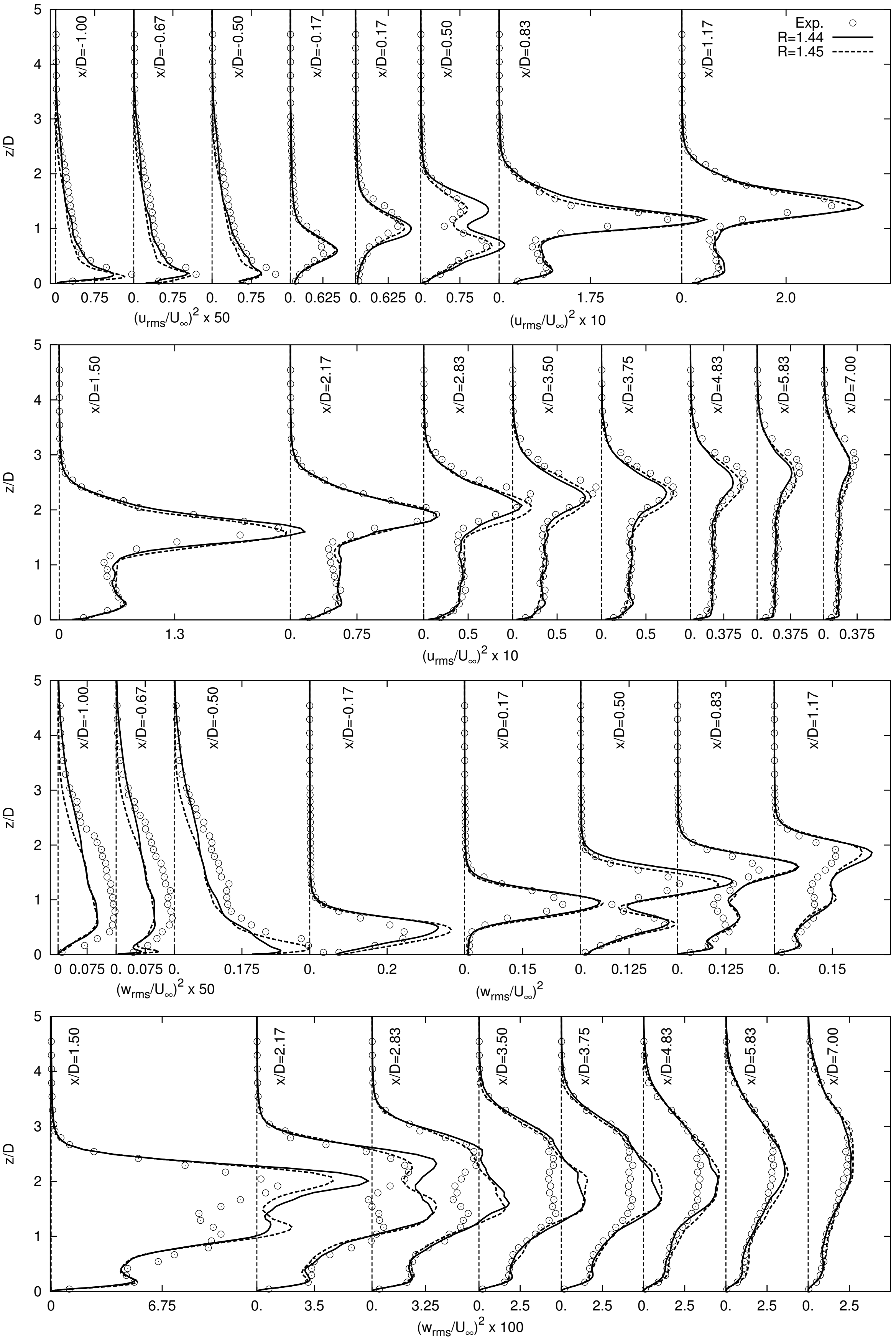

Figure B.5: $(u_{rms}/U_\infty)^2$ and $(w_{rms}/U_\infty)^2$ for experimental $R = 1.3$ case, at $y/D = 0$ - cases $R = 1.44$ and $R = 1.46$. Open circles refer to the experiment of Özcan and Larsen [77].

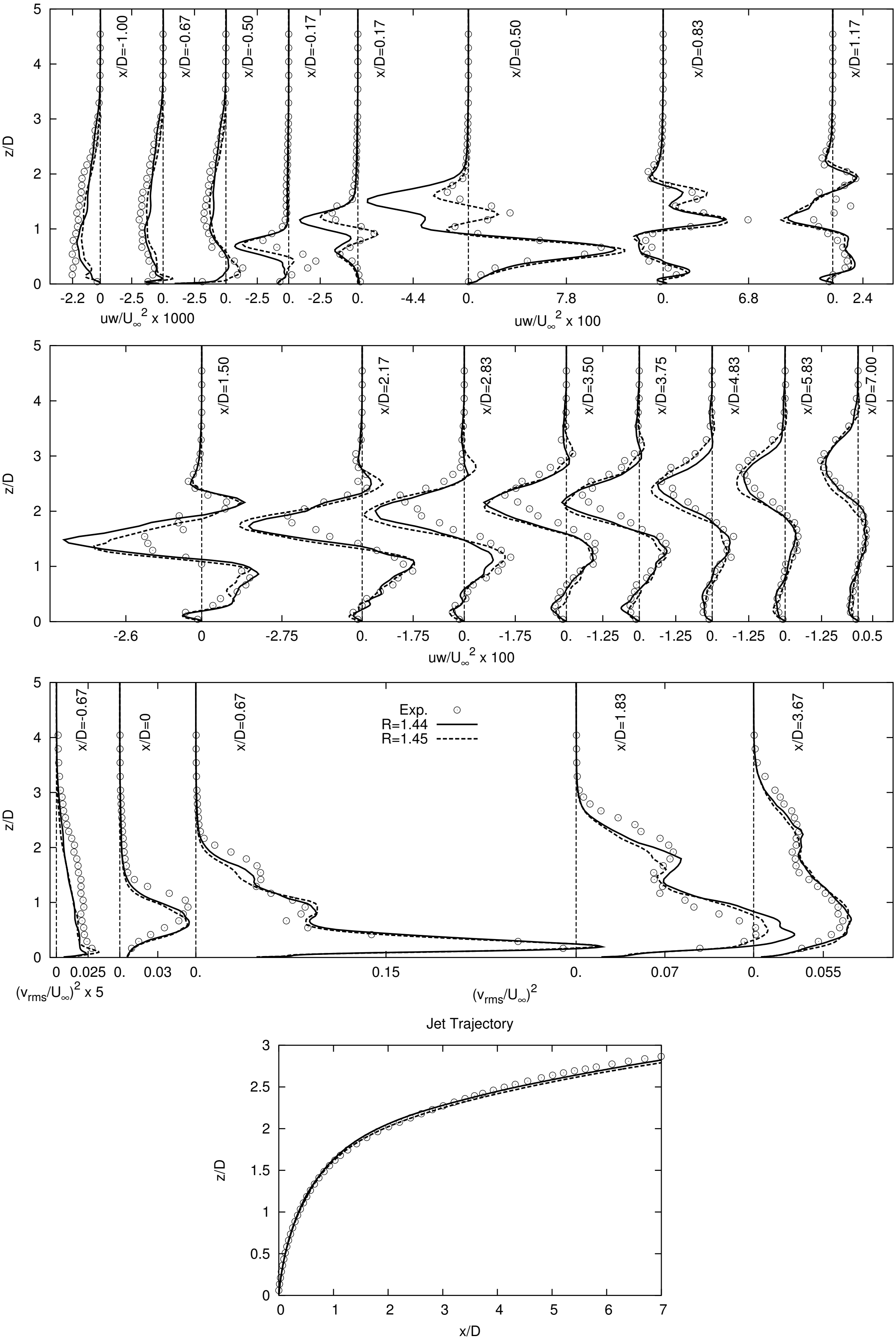

Figure B.6: $(v_{rms}/U_\infty)^2$, uw/U_∞^2 and jet-trajectories for experimental $R = 1.3$ case, at $y/D = 0$ plane - cases $R = 1.44$ and $R = 1.46$. Jet-trajectories are estimated as mean streamlines emerging from the point $x/D = z/D = 0$ in the symmetry plane following the definition of Yuan et al. [117]. Open circles refer to the experiment of Özcan and Larsen [77].

Based on all presented calculations of the JICF flow for the (experimental) $R = 1.3$ case, it is clear that computational case with the ratio of $R = 1.45$ produces the best overall predictions of the measured quantities. For that reason this case is included and further analyzed in the main rapport.

Appendix C

Numerical Codes and Implementations

Practically all numerical results obtained in this study are based on the in-house flow solver **EllipSys**, developed in co-operation between the Department of Mechanical Engineering at DTU and The Department of Wind Energy at Risø National Laboratory - see Michelsen [72] and Sørensen [105] for reference.

The EllipSys code is a multiblock finite volume solver of the incompressible Navier-Stokes equations in general curvilinear coordinates. The code uses a collocated variable arrangement, where revised Rhie/Chow interpolation is used to avoid odd/even pressure coupling. In the present study the PISO algorithm is used to enforce the pressure/velocity coupling. The EllipSys code is parallelized with MPI for executions on distributed/shared memory machines, using a non-overlapping domain decomposition technique.

The solution is advanced in time using a 2nd order iterative time-stepping (or dual time-stepping) method. In each global time-step the equations are solved in an iterative manner, using under-relaxation. First, the momentum equations are used as a predictor to advance the solution in time. At this point in the computation the flow field will not fulfil the continuity equation. The rewritten continuity equation (the so called pressure correction equation) is used as a corrector making the predicted flow field satisfy the continuity constraint. This two step procedure corresponds to a single sub-iteration, and the process is repeated until a convergent solution is obtained for the time step. When a convergent solution is obtained, the variables are updated and solution process continues with the next time step.

The convective terms in this study are discretized using the deferred corrected 4th order central difference scheme or 3rd order upwind based QUICK scheme. Central differences are used for the viscous terms, in each sub-iteration only the normal terms are treated fully implicit, while the terms from non-orthogonality are treated explicitly.

The three momentum equations are solved decoupled using a red/black Gauss-Seidel point solver. The solution of the Poisson system arising from the pressure correction equation is accelerated using a Schwartz Alternating Method (SAM). In order to accelerate the overall algorithm, a three level grid sequence and local time stepping are used.

The grids accepted by EllipSys solver have to be block structured. They can include any number of blocks, but each of them has to contain n^3 cells, which puts some considerable constraints on the mesh generation process.

An another code - **FASTEST-3D** (Flow Analysis Solving Transport Equations Simulating Turbulence) - see Durst and Schafer [26] for reference, is the code used on a single occasion (case LES 4 in Appendix A) in order to further assess the quality of the attained results. The code is based on a finite–volume numerical method for solving both three-dimensional filtered and Reynolds-Averaged Navier-Stokes equations on block-structured, body-fitted, non-orthogonal meshes. Block interfaces are treated in a conservative manner, consistent with the treatment of inner cell-faces. A cell-centered (collocated) variable arrangement and Cartesian vector and tensor components are used. The well-known SIMPLE algorithm is applied for coupling the velocity and pressure fields. The convective and diffusive transport of all variables is discretized by a second-order central differencing scheme, whose stability is enhanced through the so-called deferred correction approach.

Time discretization is accomplished by applying the 2nd order implicit Crank-Nicolson method. FASTEST-3D is parallelized based on domain decomposition in space using the MPI message passing library. This enables an efficient parallel computation on PC clusters which usually contain a number of processors with the same speed and available memory.

Implementations in EllipSys Code

Besides many small changes (like mass flow rate control at inlet boundary, etc.) applied in the EllipSys code in order to enhance its ability to produce reliable LES results, the major implementations comprises of:

- ▷ Three new SGS models are implemented/tested/validated in the EllipSys solver - (general).
- ▷ Ability to perform simulation of Boundary Layer flows is added - (specific).
- ▷ Convective Outflow boundary condition is added - (general).
- ▷ Ability to perform on-line averaging in homogeneous directions is added - (specific).

As indicated two of those implementations have a general character (can be applied on any problem utilizing LES), while two of them refer to some specific issues addressed in this study.

Recent Ph.D.-dissertations in Fluid Mechanics

Sørensen, J.N. Three-Level, Viscous-Inviscid Interaction Technique for the Prediction of Separated Flow Past Rotating Wing, AFM 86-03, 1986

Michelsen, J.A. Modelling of Laminar Incompressible Rotating Fluid Flow, AFM 86-05, and Modelling of Turbulent Incompressible Rotating Fluid Flow, AFM 86-07, 1986

Sørensen, L.S. Three-Dimensional Electro-Fluid-Dynamics in Tuft Corona Wire-Plate Precipitators, AFM 89-03, 1989

Gervang, B. Numerical Simulations of 3-Dimensional Flow in Straight and Curved Ducts of Rectangular Cross Section, AFM 89-09, 1989

Andresen, E. Statistical Approach to Continuum Models for Turbulent Gas Particles Flows, AFM 90-04, 1990

Nielsen, N.F. Low Reynolds Number Fluid Dynamics with Applications to Suspending Feeding Animals, AFM 91-10, 1991

Zamany, J. Modelling of Particle Transport in Commercial Electrostatic Precipitators, Ph.D under ATV, EF316, 1992

Christensen, E.A. Laminar-Turbulent Transition in the Rotating Driven Cavity Problem, AFM 93-12, 1993

Trinh, C.M. Turbulence Modelling of Confined Swirling Flows, Risø-R-647,1993

Mayer, K.E. Experimental and Numerical Modelling of Turbulent Flows and Heat Transfer in Staggered Tube Bundles, AFM 94-03, 1994

Mayer, S. Particle Motion in Unsteady Three-Dimensional Flow at Low Reynolds Numbers , AFM 94-04, 1994

Hansen, M.O.L. Vorticity-Velocity Formulation of Navier-Stokes Equations for Aerodynamic Flows, AFM 94-07, 1994

Hvid, S.L. Curvature Based Smoothing of Plane Cubic B-spline Curves, AFM 93-08, Surface Description using Bicubic B-splines, AFM 93-10, QM3D, 3D Netgenerering, Brugermanual, AFM 94-02 and Three-Dimensional Algebraic Grid Generation, AFM 94-08 1993-94

Walther, J.H. Discrete Vortex Method for Two-Dimensional Flow past Bodies of Arbitrary Shape Undergoing Prescribed Rotary and Translational Motion, AFM 94-11, 1994

Nim, E. Energidissipation og Masseoverførsel af Gas i og Omkring Statiske Miksere med Boblestrømning, Ph.D. under ATV, EF410, 1994

Sørensen, N.N. General Purpose Flow Solver Applied to Flow over Hills, Risø-R-827(EN), 1995

Filippone, A. Interaction of Potential Flow Model with the Navier-Stokes Equations for Rotor Aerodynamics, AFM 95-07, 1995

Jensen, E. Optimization of the Electromagnetic Flowmeter, AFM 95-09, 1995

Schmidt, J.J. Experimental and Numerical Investigation of Separated Flows, ET-PHD 97-01 1997

Nygreen, P. A Vorticity-Streamfunction Formulation of the Navier-Stokes Equations for Predicting Unsteady Flow past Bodies in Arbitrary Movement, ET-PHD 97-02, 1997

Sørensen, D.N. Aerodynamic Modelling and Optimization of Axial Fans, ET-PHD 98-01, 1998

Lennart, A.S. Experimental and Theoretical/Numerical Study of Evaporation from Shallow Pools of Organic Liquids, at Simulated Work Conditions, ET-PHD 98-02, 1998

Johansen, J. Unsteady Airfoil Flows with Application to Aeroelastic Stability, Risø-R-1116(EN), 1999

Ullum, U. Imaging Techniques for Planar Velocity and Concentration Measurements, ET-PHD 99-03,1999

Jørgensen, B.H. Low-Dimensional Modelling and Dynamics of the Flow in a Lid Driven Cavity with a Rotating Rod, ET-PHD 2000-02, 2000

Myllerup, L. Turbulence Models for Complex Flows, ET-PHD 2000-03, 2000

Pedersen, N. Experimental Investigation of Flow Structures in a Centrifugal Pump Impeller using Particle Image Velocimetry, ET-PHD 2000-05, 2000

Voigt, L.P.K. Navier-Stokes Simulations of Airflows in Rooms and Around a Human Body, ET-PHD 2001-00, 2001

Gaunaa, M. Unsteady Aerodynamic Forces on NACA 0015 Airfoil in Harmonic Translatory Motion, MEK-FM-PHD 2002-02, 2002

Pedersen, J.M. Analysis of Planar Measurements of Turbulent Flows, MEK-FM-PHD 2003-01, 2003

Mikkelsen, R. Actuator Disc Methods Applied to Wind Turbines, MEK-FM-PHD 2003-02, 2003

Ullum, T.U. Investigation of Turbulence and Flow Structures in Electrostatic Precipitator, MEK-FM-PHD 2003-03, 2003

Hjort, S. Incompressible Boundary Layer Instability and Transition, MEK-FM-PHD 2004-01, 2004

Reck, M. Computational Fluid Dynamics, with Detached Eddy Simulation and the Immersed Boundary Technique, Applied to Oscillating Airfoils and Vortex Generators, MEK-FM-PHD 2005-01, 2005